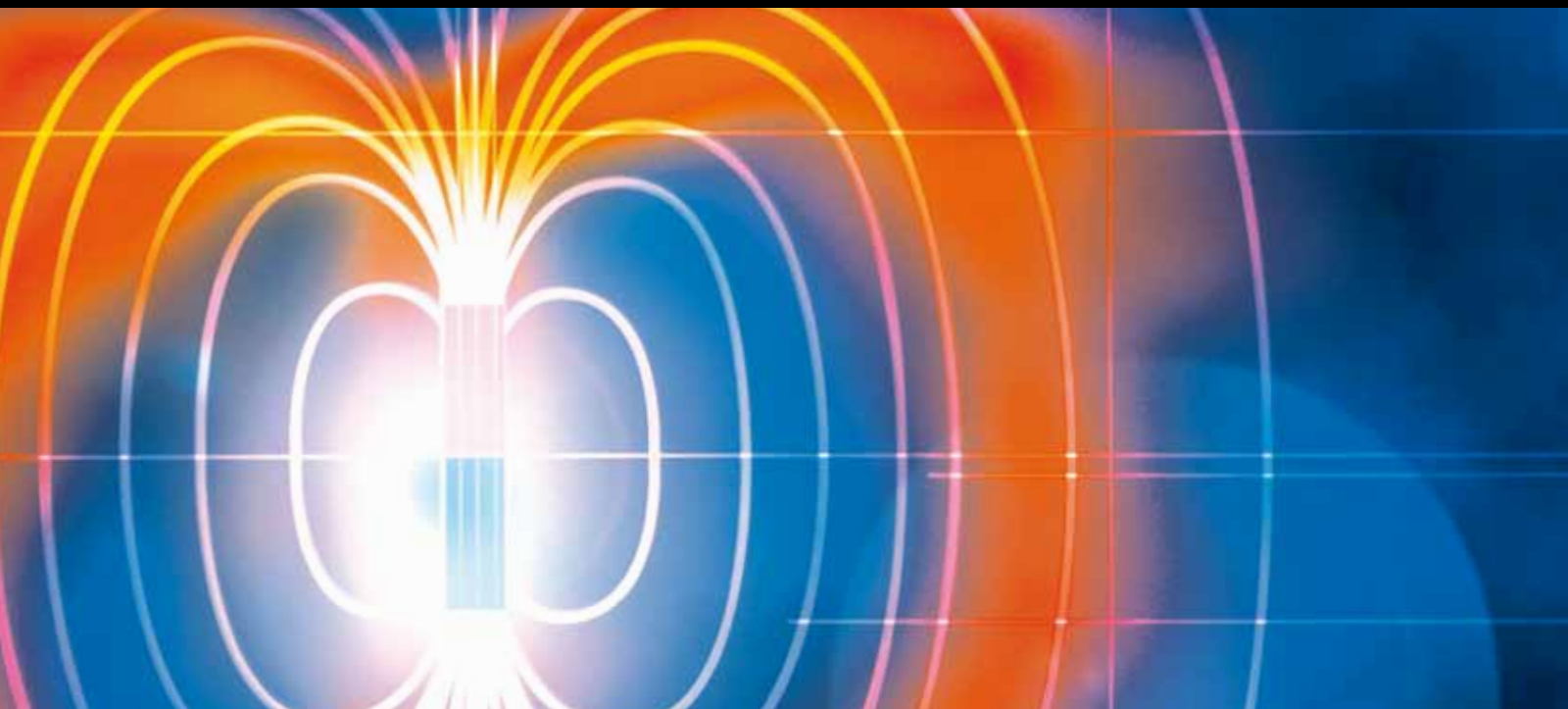


ADVANCES IN NOVEL OPTICAL MATERIALS AND DEVICES

GUEST EDITORS: MICHAEL R. GLEESON, YASUO TOMITA, SERGI CALLEGO, AND ROBERT MCLEOD





Advances in Novel Optical Materials and Devices

Physics Research International

Advances in Novel Optical Materials and Devices

Guest Editors: Michael R. Gleeson, Yasuo Tomita,
Sergi Gallego, and Robert McLeod



Copyright © 2013 Hindawi Publishing Corporation. All rights reserved.

This is a special issue published in “Physics Research International.” All articles are open access articles distributed under the Creative Commons Attribution License, which permits unrestricted use, distribution, and reproduction in any medium, provided the original work is properly cited.

Editorial Board

F. Aguilera-Granja, Mexico
Rajeev Ahuja, Sweden
N. P. Bigelow, USA
Peter Blunden, Canada
W. Niel Brandt, USA
Sean Cadogan, Australia
Maria G. Castellano, Italy
Arthur E. Champagne, USA
Ashok Chatterjee, India
W. Y. Ching, USA
Anil R. Chourasia, USA
Debashish Chowdhury, India
Bart Cleuren, Belgium
Thomas D. Cohen, USA
Mike Cottam, Canada
G. Das, India
Avishai Dekel, Israel
Jerry P. Draayer, USA
Ehud Duchovni, Israel
Douglas J. Durian, USA
Dipankar Dutta, USA
Simon I. Eidelman, Russia
Faramarz Farahi, USA
Israel Felner, Israel
Yuan Ping Feng, Singapore
Lee Samuel Finn, USA
Moshe Gai, USA
Lian Gao, China
Luis Gimeno, Spain
Nikos D. Giokaris, Greece
Leonardo Golubovic, USA
David Goodstein, USA
Christoph Grab, Switzerland

Robert D. Guenther, USA
Atul Gurtu, India
Robert B. Hallock, USA
Yilong Han, Hong Kong
Shlomo Havlin, Israel
Ernest M. Henley, USA
Juan Jose Hernandez-Rey, Spain
Alfred C. Huan, Singapore
Nathan Ida, USA
Martin Kröger, Switzerland
Pablo Laguna, USA
Shaun Lovejoy, Canada
David Lowe, USA
Yuli Lyanda-Geller, USA
Zhiqiang Mao, USA
Thomas G. Mason, USA
Grant J. Mathews, USA
P. V. E. McClintock, UK
Paul J. Meakin, USA
Baruch Meerson, Israel
Ernst Meyer, Switzerland
Sergey B Mirov, USA
Andre Mischke, The Netherlands
W. B. Mori, USA
Franco Nori, USA
K. Alexander Nugent, Australia
Jeremy O'Brien, UK
Hans Rudolf Ott, Switzerland
Ravindra R. Pandey, USA
Byungwoo Park, Korea
Jeevak M. Parpia, USA
Anand Pathak, India
Lorenzo Pavesi, Italy

A. John Peter, China
Jean-François Pinton, France
Viktor Podolskiy, USA
Han Pu, USA
Rajeev K. Puri, India
B. Raveau, France
Ali H. Reshak, Czech Republic
Slava V. Rotkin, USA
Angel Rubio, Spain
James A. Sauls, USA
Nir J. Shaviv, Israel
Steven Sherwood, Australia
Bellave Shivaram, USA
Theo Siegrist, USA
Ved Ram Singh, India
Roman Sobolewski, USA
H. E. Stanley, USA
Neil S. Sullivan, USA
Uwe Claus Tauber, USA
Ichiro Terasaki, Japan
Frank Tsui, USA
Jack Adam Tuszynski, Canada
Gautam Vemuri, USA
Donepudi V. Rao, India
Jacobus Verbaarschot, USA
Bennie F. L. Ward, USA
Yue Wu, USA
Fahrettin Yakuphanoglu, Turkey
Weitao Yang, USA
Harold Zandvliet, The Netherlands
Jianhui Zhong, USA

Contents

Advances in Novel Optical Materials and Devices, Michael R. Gleeson, Yasuo Tomita, Sergi Gallego, and Robert McLeod
Volume 2013, Article ID 430947, 2 pages

A Minireview of the Natures of Radiation-Induced Point Defects in Pure and Doped Silica Glasses and Their Visible/Near-IR Absorption Bands, with Emphasis on Self-Trapped Holes and How They Can Be Controlled, David L. Griscom
Volume 2013, Article ID 379041, 14 pages

Modeling of Optical Nanoantennas, Bedir B. Yousif and Ahmed S. Samra
Volume 2012, Article ID 321075, 10 pages

Quantitative Comparison of Five Different Photosensitizers for Use in a Photopolymer, Yue Qi, Michael R. Gleeson, Jinxin Guo, Sergi Gallego, and John T. Sheridan
Volume 2012, Article ID 975948, 11 pages

Coaxial Self-Trapping of White and Gray Regions of an Incandescent Field: A Bright Core with a Dark Cladding, Kailash Kasala and Kalaichelvi Saravanamuttu
Volume 2012, Article ID 798906, 5 pages

Development of Laser-Produced Tin Plasma-Based EUV Light Source Technology for HVM EUV Lithography, Junichi Fujimoto, Tsukasa Hori, Tatsuya Yanagida, and Hakaru Mizoguchi
Volume 2012, Article ID 249495, 11 pages

Design and Analysis of a THz Metamaterial Structure with High Refractive Index at Two Frequencies, Zan Lu, Bruno Camps-Raga, and N. E. Islam
Volume 2012, Article ID 206879, 9 pages

Closed-Aperture Z-Scan Analysis for Nonlinear Media with Saturable Absorption and Simultaneous Third- and Fifth-Order Nonlinear Refraction, Xiangming Liu and Yasuo Tomita
Volume 2012, Article ID 161572, 9 pages

Zero Spatial Frequency Limit: Method to Characterize Photopolymers as Optical Recording Material, Sergi Gallego, Andrés Márquez, Manuel Ortuño, Cristian Neipp, Inmaculada Pascual, and Augusto Beléndez
Volume 2012, Article ID 352681, 9 pages

A Review of the Optimisation of Photopolymer Materials for Holographic Data Storage, Jinxin Guo, Michael R. Gleeson, and John T. Sheridan
Volume 2012, Article ID 803439, 16 pages

Editorial

Advances in Novel Optical Materials and Devices

Michael R. Gleeson,¹ Yasuo Tomita,² Sergi Gallego,³ and Robert McLeod⁴

¹ *Optoelectronic and Communications, Research Centre, University College Dublin, Dublin 4, Ireland*

² *Department of Engineering Science, University of Electro-Communications, 1-5-1 Chofugaoka, Chofu, Tokyo 182-8585, Japan*

³ *University Institute of Physics Applied to Sciences and Technologies, University of Alicante, Ap. De Correos 99, 03080 Alicante, Spain*

⁴ *Department of Electrical, Computer and Energy Engineering, University of Colorado at Boulder, ECEE 1B47, Boulder, CO, UCB 425, USA*

Correspondence should be addressed to Michael R. Gleeson; michael.gleeson@ucd.ie

Received 25 February 2013; Accepted 25 February 2013

Copyright © 2013 Michael R. Gleeson et al. This is an open access article distributed under the Creative Commons Attribution License, which permits unrestricted use, distribution, and reproduction in any medium, provided the original work is properly cited.

This special issue highlights the continuous growth and advancement in the field of optical materials and optical devices. Extensive research carried out in these areas has led to the development of novel applications and uses in a range of areas, including biomedical devices, imaging, optical communication networks, optical storage media, and photovoltaics. In order to maintain the successful growth and diversity in these areas, a better understanding of optical materials and their behaviour is required. Achieving this will then enable improvements in material performance and material functionality and potentially yield more innovative devices and applications.

The research contributions presented here illustrate recent significant efforts undertaken throughout the field of optical materials and optical devices. A variety of works are provided, encompassing many research areas within the field. The following is a brief introduction to the scope of the research which is offered with this special issue.

The paper provided by Z. Lu et al. extends the concept of a single frequency band, single high-refractive-index metamaterial and then applies it to the simulation and design of dual frequency band, dual high-refractive-index metamaterial in the THz regime. The resulting metamaterial designed with gold structures embedded with polyimide film effectively exhibits high refractive index at two frequency bands. These results indicate that through modification of the geometry and design of these structures, a higher refractive index can be achieved at the second resonant frequency, thus leading

to a single structure multifrequency, multiple high-refractive-index metamaterial, which could be used in a variety of practical applications.

J. Fujimoto et al. report on their continued development of their first generation extreme-ultraviolet (EUV) light source for high volume manufacturing (HVM) “GL200E.” They review some of their latest data and describe their system and the various original concepts that they have proposed, including (1) highly efficient Sn plasma generation, driven by pulsed CO₂ laser (2) double pulse irradiation scheme for Sn plasma generation (3) Sn debris mitigation by a magnetic field and small Sn droplet size and (4) hybrid CO₂ laser system using a combination of a short pulse oscillator and commercial cw-CO₂ amplifiers.

The paper by B. B. Yousif and A. S. Samra provides a detailed investigation of the optical properties of plasmonic nanoantennas using a finite integration technique, with particular emphasis on near-field resonances and far-field radiation properties. They also report on the role that geometrical parameters such as antenna length and gap dimension have on the field enhancement and spectral response. Field enhancement can lead to resolution improvements in applications such as microscopy and optical lithography, therefore increasing optical data storage capacity and offering potential improvements in sample detection and medical imaging.

X. Liu and Y. Tomita developed a closed-aperture Z-scan theory capable of characterising nonlinear optical materials such as novel QD-polymer nanocomposite materials.

They show that the observed large nonlinear refraction and induced transparency as well as the capability of holographic nanoparticle assembling make QD-polymer nanocomposite materials promising for nonlinear photonics applications (e.g., optical switching, limiting, and signal processing) by use of holographic Bragg grating structures that provide the electromagnetic nonlinear feedback mechanism.

A literature review provided by D. L. Griscom discusses the nature of radiation-induced point defects in silica-based optics. He discusses and argues the role that self-trapped holes play in transient radiation-induced red/near IR optical absorption in these silica-based photonics and also provides methods which can be utilised to permanently minimize the numbers of environmentally or operationally created self-trapped holes. In particular, he emphasises the importance of utilising fractal kinetics as a means of extrapolating the results of dose-rate-dependence studies backward into time regimes and forward into supra-high-dose-rate regimes.

In a very interesting piece of work, K. Kasala and K. Saravanamuttu explore the generation of self-trapped incoherent hybrid beams in a photocrosslinkable organosiloxane. The temporal and spatial variations in the refractive index of the material caused the encapsulation of the incoherent light. Subsequently, this encapsulation gradually increases the light confinement giving these filaments similar characteristics to optical fibres, protecting each filament from interactions with other nearby self-trapped filaments. This work offers new possibilities for the manipulation and confinement of self-trapped beams.

J. Guo et al. presents a comprehensive review of works in the literature on the optimisation of photopolymer materials for holographic applications. This work highlights the major advancements made in the area and indicates a number of outstanding developmental issues. It is proposed that to overcome these issues, an accurate theoretical representation of the various photokinetic behaviour which occur in these photopolymers is required. This would allow potential trends to take advantage of improving photopolymer performance.

S. Gallego et al. present work on the development of a method based on a zero spatial frequency recording and interferometric techniques to determine quantitative values of shrinkage, polymerization rate, polymer refractive index, and the relation between intensity and polymerization. They also present some simple models used to extract these various parameters from a number of photopolymer materials. This work offers techniques to characterise the viability of photopolymers for diffractive and holographic applications.

Y. Qi et al. present recent advances in the nonlocal photopolymerisation driven diffusion (NPDD) model, including a generic representation for photosensitiser kinetics during and after illumination. They analyse a number of different photosensitisers and indicate trends from their resulting theory which enable material optimisation for the application required.

The scope of the works presented in this special issue offers a real insight into the progress made across a wide range of areas within the field of optical materials and optical devices. It is clear that from this continued pursuit of

knowledge many exciting new applications and devices will be on the horizon.

Acknowledgment

On behalf of the guest editors, we would like to thank all those who have contributed to the production of this very interesting and informative special issue.

*Michael R. Gleeson
Yasuo Tomita
Sergi Gallego
Robert McLeod*

Review Article

A Minireview of the Natures of Radiation-Induced Point Defects in Pure and Doped Silica Glasses and Their Visible/Near-IR Absorption Bands, with Emphasis on Self-Trapped Holes and How They Can Be Controlled

David L. Griscom

Impact Glass Research International, San Carlos, SON, Mexico

Correspondence should be addressed to David L. Griscom; david_griscom@yahoo.com

Received 9 May 2012; Accepted 19 October 2012

Academic Editor: Robert McLeod

Copyright © 2013 David L. Griscom. This is an open access article distributed under the Creative Commons Attribution License, which permits unrestricted use, distribution, and reproduction in any medium, provided the original work is properly cited.

The natures of most radiation-induced point defects in amorphous silicon dioxide ($a\text{-SiO}_2$) are well known on the basis of 56 years of electron spin resonance (ESR) and optical studies of pure and doped silica glass in bulk, thin-film, and fiber-optic forms. Many of the radiation-induced defects intrinsic to pure and B-, Al-, Ge-, and P-doped silicas are at least briefly described here and references are provided to allow the reader to learn still more about these, as well as some of those defects not mentioned. The metastable self-trapped holes (STHs), intrinsic to both doped and undoped silicas, are argued here to be responsible for most *transient* red/near-IR optical absorption bands induced in *low-OH* silica-based optical fibers by ionizing radiations at ambient temperatures. However, accelerated testing of $a\text{-SiO}_2$ -based optical devices slated for space applications must take into account the highly supralinear dependence on ionizing-dose-rate of the *initial* STH creation rate, which if not recognized would lead to false negatives. Fortunately, however, it is possible to permanently reduce the numbers of environmentally or operationally created STHs by long-term preirradiation at relatively low dose rates. Finally, emphasis is placed on the importance and utility of rigorously derived fractal-kinetic formalisms that facilitate reliable extrapolation of radiation-induced optical attenuations in silica-based photonics recorded as functions of dose rate backward into time domains unreachable in practical laboratory times and forward into dose-rate regimes for which there are no present-day laboratory sources.

1. Introduction

Optical fibers and metal-oxide-semiconductor (MOS) devices based on amorphous forms of SiO_2 ($a\text{-SiO}_2$) are components of many photonic devices and systems that require hardness against nuclear and/or space radiations. Development of radiation-hardened optical fibers based on glassy silica, as well as MOS devices with amorphous SiO_2 gate insulators, is dependent on a fundamental understanding of radiation-induced defect formation in the $a\text{-SiO}_2$ component. The multitude of relevant radiation damage processes are schematically illustrated in Figure 1, which is taken from [1] where these processes are discussed in considerable detail. The present paper will limit its focus to the natures of the radiation-induced point defects—also termed “color centers”—that are known to absorb light in

the wavelength range ~ 500 to ~ 2000 nm in silica-based optical fibers and other photonic devices. A concise review of radiolytic trapped-oxide charges in $a\text{-SiO}_2$ -based MOS structures and their relation to interface-state formation can be found in [2].

The molecular-scale structures of those point defects that are paramagnetic (i.e., possessing an unpaired electron) have been determined primarily by the technique of electron spin resonance (ESR) spectrometry. The most commonly measured ESR parameters are the g values and hyperfine coupling constants, which will be mentioned in passing below but will not be defined here. Rather, the reader is referred to [3] for the meanings of these terms, as well as a highly condensed review of the theory and application of ESR to both insulating crystals and glasses, and/or to [4] for a more comprehensive review of both the theory and practice of ESR

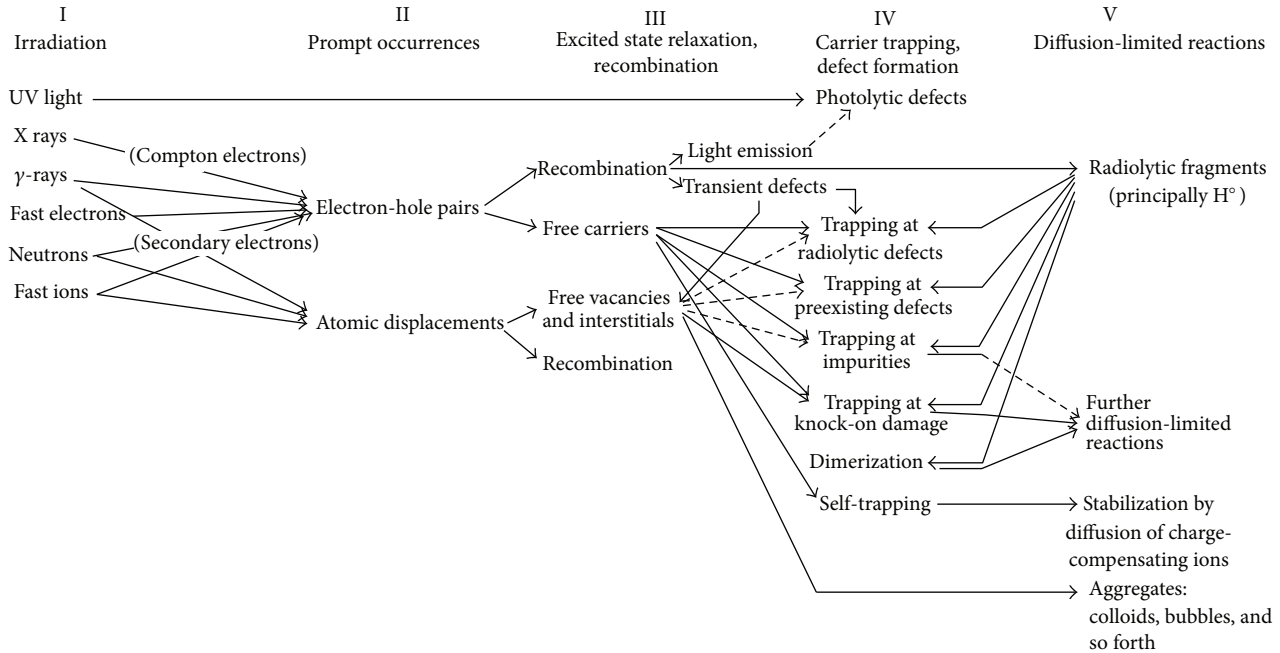


FIGURE 1: Modes of defect formation in insulators subjected to various types of ionizing radiations and/or particles of sufficiently high energy to create “knock-on” damage. See [1] for discussions of the indicated processes.

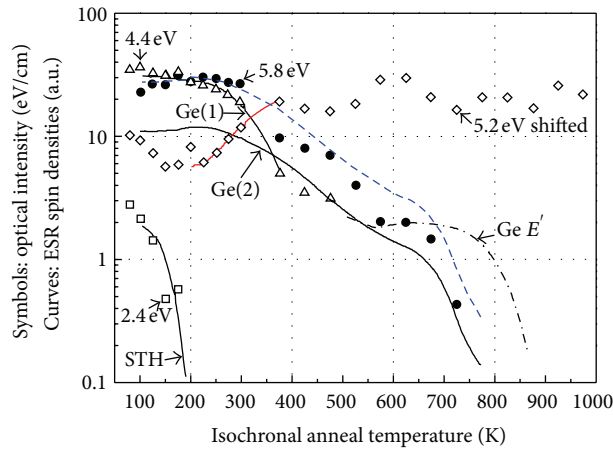


FIGURE 2: ESR-determined number densities (bold curves, relative units) and independently determined optical-band intensities (symbols, eV/cm) for X-ray-induced defect centers in separate samples of a Ge-doped-silica fiber-optic perform following irradiations to the same dose at 100 and 77 K, respectively, and subsequent 5-minute isochronal anneals to the higher temperatures. (The ESR data were also recorded at discrete temperatures but are displayed here as continuous curves as an aid to the eye). It is seen here that the self-trapped holes (STHs) and the Ge(1) trapped-electron centers correlate well with optical absorption bands centered near 2.4 and 4.4 eV, respectively (and have identical oscillator strengths [5, 6]). The upshifted Ge(2) number-density curve (dashed blue curve relating to Ge(2)’s higher oscillator strength) strongly matches the 5.8 eV optical data below 300 K and is cryptically correlated with those data above 300 K. The diamonds, representing a 5.2-eV band not associated with any ESR-detectable defect, are shown here displaced upward by a factor of 2.4 from their originally recorded optical intensities in order to discover their perfect match with the red curve in the range 200–370 K, which comprises the sum of the changes of the Ge(1) and Ge(2) number densities in the range 200–370 K multiplied by negative 0.5. This figure—adapted from [5]—was recently published in [6], where full explanations of the meanings and implications of these data can be found.

as applied to paramagnetic ions and radiation-induced point defects in (mostly silica-based) oxide glasses.

The associations of ESR-determined defect-center structures with specific optical absorption bands are generally

established by ESR-optical correlations obtained, for example, by means of postirradiation isochronal thermal annealing experiments. Figure 2 provides an example of such a parallel set of ESR and optical isochronal anneal sequences

recorded for a germanium-doped silica glass initially x-irradiated at ~ 100 K and annealed for 5 minutes at each sequence of higher temperatures [5, 6].

During the past half century many trapped-hole-type point defects in *pure* silicas have been identified by ESR (see, for example, [4]), in most cases unambiguously. (It should be noted however that silicas containing minor amounts of technological impurities such as OH, CO, Cl, or O₂ are often termed “pure,” whereas these impurities frequently take part in the formation of defect centers extrinsic to the pure glass.) By contrast, many of the counterpart trapped-*electron*-type defects in pure silicas have historically appeared to be ESR silent. Very recently, I reviewed in considerable detail what is presently known about radiation-induced trapped-electron centers in both pure and B-, Al-, Ge-, and P-doped silica glasses [7]. Among many other conclusions in [7], I was forced to reject and to replace certain models that I myself had posited earlier [4, 8] for radiation-induced defects in otherwise high-purity silicas containing high concentrations of chloride ions.

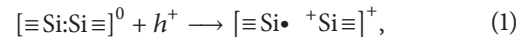
2. What We Know for Certain about Point Defects in Glassy Silica

2.1. Pure Silica. Among the best understood *intrinsic* defects in glassy silica is a family of oxygen-vacancy defects termed E' centers [9], which have been found to occur in a number of distinctly different variations termed $E'_{\alpha, \beta, \gamma, \text{ and } \delta}$ (e.g., [8, 10–13]). Until very recently all of these were regarded as trapped-hole centers. However, there is substantial evidence [7, 12] that the low-temperature version of E'_{α} , $E'_{\alpha LT}$ (nomenclature proposed in [7]) may be a trapped-*electron* center, whereas the high-temperature version of E'_{α} , $E'_{\alpha HT}$ has been unambiguously shown to be a trapped hole center [13]. The historical confusion owes to both E'_{α} versions sharing approximately the same g values—which is a necessary, but far from sufficient, condition for their being sterically and electronically identical.

Still, the majority of all E' centers result from trapping of holes (h^+) at a neutral oxygen vacancies in pure-silica-glass networks otherwise comprising SiO₄ tetrahedra linked at the corners; (the notation “ \emptyset ” indicates that in a hypothetically defect-free silica glass each oxygen, O, forms a bridge between, and is thus shared by, the central Si and one of its four nearest-neighbor silicons). The most famous exception is E'_{β} , which was originally proposed to involve an unpaired electron delocalized over four silicons [8], has since been widely argued by theorists to involve just two silicons, but has finally been experimentally proven to involve at least four virtually equivalent silicon neighbors and possibly five [14]. Some other recently proposed exceptions involve E'_{γ} centers induced in silicas with high Cl contents (now regarded in [7] to have been misinterpreted in [8]) and E' -type centers associated with oxygen “pseudo vacancies,” to be explained in Section 2.2.

In the simplest case of preexisting neutral oxygen *mono*-vacancies in the pure-silica glass structure, the

radiolytic process of E' center creation can be represented as



where “ \equiv ” represents bonds to 3 bridging oxygens, “ \emptyset ”, in the glass network, “ $:$ ” represents a pair of electrons shared between the two silicons on opposite sides of the vacancy, and “ \cdot ” is an unpaired electron localized in a dangling sp^3 orbital of a single silicon, as determined by ESR studies of irradiated samples. Most commonly, the defect structure “ $\equiv \text{Si}\cdot$ ” on the right-hand side of (1) is an E'_{γ} center although in certain cases it may be an E'_{α} or E'_{β} center signaled by small but easily discernable differences between their respective spin Hamiltonian parameters [3, 4, 13] and often depending on their respective modes of creation and/or thermal stabilities [8, 10–13]. In general, these variants are believed to correspond to different distortions or relaxations of the structure $\equiv \text{Si}\cdot$ and/or the structure of the surrounding glass in which this unit is embedded (see especially [11]).

In addition there are nonbridging-oxygen hole centers (NBOHCs: “ $\equiv \text{Si}-\text{O}\cdot$ ”, see, e.g., [4]), peroxy radicals (PORs: “ $\equiv \text{Si}-\text{O}-\text{O}\cdot$ ”, see, e.g., [4]) and two types of self-trapped holes (STH₁ and STH₂ [15, 16], the structures of which will be elucidated in Section 3). The literature is enormous, but references [1, 4, 12] are recommended entry points.

2.2. Doped Silicas. The best understood defects in *doped* glassy silica are those for which Si is substituted by B, Al, Ge, or P. This is because the radiation-induced aluminum-oxygen hole center (Al-OHC), the so-called Ge(1) and Ge(2) centers, and the P₂ trapped-electron center in the respectively-doped glasses have each been shown to be virtually identical with a doppelganger in similarly-doped crystalline α quartz, as discussed in detail in [7]. These α -quartz doppelgangers are unambiguously understood thanks to tedious, highly specialized, and meticulously performed, single-crystal ESR angular dependence studies carried out by John Weil and his students and colleagues (see [17] for a listing of reviews). It should be noted that the boron-oxygen hole center (B-OHC) has no doppelganger in α quartz; however it is isomorphous with the Al-OHC.

2.2.1. Ge-Doped Silica. As seen in Figure 2, the correspondences of the ESR data (curves) and optical measurements (data points) show that the Ge(1) and Ge(2) centers in Ge-doped silica glass have optical absorption bands at 4.4 eV and 5.8 eV, respectively.

Of particular importance to understanding the natures of these Ge(1) and Ge(2) defects are the remarkable interrelationships (described in greater detail in [6, 7]) between the Ge(1) and Ge(2) centers in Ge-doped silica glass and the Ge(II) and Ge(I) centers, respectively, in α quartz.

- (A) Given that the Ge(1) center in Ge-doped silica glass [5–7, 18] is characterized by virtually the same g values and mean hyperfine coupling constant as those of the Ge(II) center in quartz [19, 20], it must be concluded that (i) “ α -quartz-crystal-like” GeO₄

tetrahedra preexist in the glass and (ii) Ge(1) shares the Ge(II) property of being an electron trapped in a *Ge sp* orbital *parallel* to the twofold axis of symmetry of this tetrahedron.

- (B) Given that the Ge(I) center in α quartz [19, 20] is characterized by *g* values only slightly different from, and mean hyperfine coupling constant virtually identical to, those of the Ge(2) center in silica glass [5–7, 18]—and it is known [19, 20] that Ge(I) is an electron trapped in symmetry-breaking orbitals perpendicular to the twofold axis a GeO_4 tetrahedron in the α -quartz lattice (thus making it an energetically different state of the same defect responsible for Ge(II) [19])—it must be concluded that (i) Ge(I) is a “glass like” defect even though it occurs in perfect crystal and (ii) the “default” interpretations of Ge(1) and Ge(2) are that they are two energetically different states of the same defect in Ge-doped silica glass.

Notwithstanding insights (A) and (B) above, observed variations in the Ge(1)-to-Ge(2) concentration ratios at room temperature continue to convince some researchers that Ge(1) and Ge(2) cannot be two energetically different states of the same precursor (e.g., [21]). For example, in Figure 2 the Ge(1):Ge(2) ratio is seen to be $\sim 2:1$ after x-irradiation at 100 K and a 5-min warming at 300 K [6], whereas this ratio has been found in [21] to be 0.8:1 for GeO_2 -doped silica optical fibers and preforms γ -irradiated at room temperature and stored at ambient temperatures for a full month before recording the data. However, this is hardly a serious contradiction, given that in Figure 2 it is seen that a further 5-min anneal at 370 K also results in a Ge(1):Ge(2) ratio of $\sim 0.8:1$.

Here below I will summarize and analyze a very different example—one that cannot be dismissed without further consideration: Nagasawa and coworkers [22] provided striking evidence of selective destruction of γ -ray-induced Ge(2) centers—but not Ge(1) centers—in Ge-doped-silica-core optical fibers by *postirradiation* ambient-temperature in-diffusion of molecular hydrogen. They also reported a linear relationship between (i) the numbers of Ge(2) centers recorded by ESR in five different samples immediately following γ -irradiation and (ii) the numbers of $[\text{Ge}^{\bullet}\text{-H}]^0$ defects *subsequently* created in these same samples by identical H_2 treatments.

The $[\text{Ge}^{\bullet}\text{-H}]^0$ defect, commonly termed the H(II) center, results when a charge-neutral twofold-coordinated germanium $[\text{Ge}]^0$ —commonly termed the Germanium Lone Pair Center (GLPC⁰)—reacts with a neutral hydrogen atom, H^0 , a process that has been extensively studied by Bobyshev and Radtsig on the surfaces of Ge-doped silica glasses [23]. (Confirmation of the structure of the analogous $[\text{Si}^{\bullet}\text{-H}]^0$ defect in pure bulk silica, denoted H(I), is given in [24].)

In order for H(II) centers to have formed in Nagasawa et al.’s [22] bulk glasses, both of the following processes must have taken place [23]: (i) two Ge- O bonds must have been broken at each of an equal number of tetrahedrally coordinated germanium sites and (ii) the introduced molecular H_2

must have been “cracked” into a pair of free hydrogen atoms. One possible cracking site could have been nonbridging-oxygen hole centers (NBOHCs) [25], if any were present. Conceivably, however, H_2 might have been cracked in the process of destroying Ge(2) centers:



where “[GeO_4]” denotes a substitutional germanium, “ \bullet ” a trapped electron, the superscript “ $-$ ” a negative electrostatic charge, and the subscript “2” a Ge(2)-type trapped-electron on the left-hand side of the reaction...and the “H” on the right-hand side is an H^0 bonded to this Ge(2)-type orbital.

Cracking reactions of H_2 dissolved in silica glass can be determined by its diffusion coefficient alone if the *reaction* coefficient pertaining to the entity upon which it cracks is more rapid than the diffusion time (an explicit example of this is given in [25]). Conversely, the reaction could be greatly slowed if the reaction coefficient should happen to be much slower than the diffusion coefficient. Thus, if Ge(1) and Ge(2) are “two energetically different manifestations of the same defect”—as it certainly appears that they are—it is not at all unreasonable to suggest from the results of [22] that Ge(1) has a much slower reaction coefficient for a cracking H_2 than does Ge(2).

Apropos, by tracing the ESR intensities of Ge(1) and Ge(2), together with the 5.2-eV optical intensity of GLPC⁰ in the range ~ 200 to 370 K in Figure 2, it was determined [6] that GLPC⁰s had trapped a number of holes equal to the combined number of electrons trapped at Ge(1) and Ge(2) sites. However, the number density of hole-trapping GLPC⁰s deduced in [6] was only 50% of this number [6]—thus proving that GLPC⁰s stably trap holes only in pairs (thereby becoming GLPC²⁺s). Because they possess no unpaired electrons, both GLPC⁰ and GLPC²⁺ are ESR silent. Moreover, it is empirically apparent that neither one has a strong optical band in the range 1 to 6 eV [5, 6].

2.2.2. Boron- and Aluminum-Doped Silicas. Boron does not substitute in α quartz. However, in a γ -irradiated binary $\text{B}_2\text{O}_3\text{-3SiO}_2$ glass, borons substituted for silicons were found to trap holes to form boron-oxygen hole centers (B-OHCs) [26]. This result is in perfect analogy to the Al-OHCs reported to occur in both Al-containing quartz [27] and Al-doped silica glass [28]. By contrast, *trapped-electron*-type B- E' centers [26] and Al- E' centers (reported by Brower in [29] and reviewed in [7]) are created upon irradiation of a binary $\text{B}_2\text{O}_3\text{-3SiO}_2$ glass and an Al-doped silica, respectively, whereas no counterparts to either of these trapped-electron defects exist in α quartz.

In [26] it was proposed that the radiation-induced B- E' centers $[\equiv\text{B}\bullet]^-$ in the binary $\text{B}_2\text{O}_3\text{-3SiO}_2$ glass result from electron trapping at the sites of preexisting oxygen “pseudo vacancies,” diagrammed as $[\equiv\text{B}^+\text{Si}\equiv]^+$. This model was extended in [7] to apply also to the Al- E' centers $[\equiv\text{Al}\bullet]^-$ in Al-doped silica. Thus



Note the similarity of the right-hand sides of (1) and (3). However, the paramagnetic defect on the right of (1) is a positively charged trapped-hole center, whereas the paramagnetic defect on the right of (3) is a charge-neutral trapped-electron center, as discussed in greater detail in [7]. Note that in this model the *unirradiated* glasses must maintain charge neutrality by assuring that the numbers of negatively charged substitutional $[B\text{O}_4]^-$ and $[Al\text{O}_4]^-$ tetrahedra exactly equal the numbers of $[\equiv B^+Si\equiv]^+$ and $[\equiv Al^+Si\equiv]^+$ “pseudo vacancies,” respectively.

It has recently been shown [30] that subband-gap-excited luminescence bands at 2.8 and 4.4 eV recorded for a silica sample to which was added 0.015 wt% elemental silicon (introducing *true* oxygen vacancies) are virtually identical to those recorded for silica doped to the same degree with Al_2O_3 . This particular luminescence is *unambiguously* attributed to charge-neutral twofold-coordinated silicons ($[=Si:]^0$, an ESR-silent oxygen-vacancy defect; see [7] and references therein), and its strength in the 0.015 wt%-Si-doped sample is ~ 50 to 100 times greater than that of undoped silica [30]. Therefore, the results of the experiment of [30] imply that a commensurate degree of Al_2O_3 doping somehow creates the same high number and *type* of oxygen vacancies (specifically involving twofold coordinated *silicons*) as does doping with elemental Si. The only conceivable way that this could happen must somehow relate to the presence of Al “pseudo vacancies” [7, 26] in the as-quenched alumina-rich glass, that is, in the form of $[\equiv Al^+Si\equiv]^+$ units. Although the explanation for the appearances of *twofold*-coordinated silicons under these conditions is necessarily more complicated (as is also the case of silica doped only with elemental Si), a possible model explaining the results of both of these cases is proffered in [7].

3. Space Applications Narrow the Subject Mostly to Self-Trapped Holes

The facts are that (i) the most radiation-hard *nonlaser* silica-based optical fibers employ little or no cationic dopants, (ii) the commonly used fluorine dopants appear *not* to take part in color-center formation [31] (though chloride impurities are problematic [31]), and (iii) for dose rates ~ 6 Gy/s the *transient* optical absorption near 660 nm induced at short times in low-OH pure-silica fibers (due to STHs; see below) is ~ 3 orders of magnitude greater than that of the concomitantly induced 620 nm band of (nondecaying) NBOHCs following a total dose of 10^7 Gy [31]. It therefore follows that the true “elephant in the room” with respect to nuclear and space applications of glassy silica would seem to be the STHs [15, 16]. Metastable STHs are *always* created in *low-OH* glassy silica by ionizing radiation, so long as there are no strongly competing hole-trapping dopants or impurities present. As will be explained in greater detail in Section 3.5, STHs in *high-OH* silicas are instantly quenched by reaction with atomic hydrogen released by radiolysis of OH groups [2, 32, 33].

The discovery and ESR characterization of the STHs are extensively discussed in [15, 16], so most of the details will not be reprised here. However, it can be stated that two

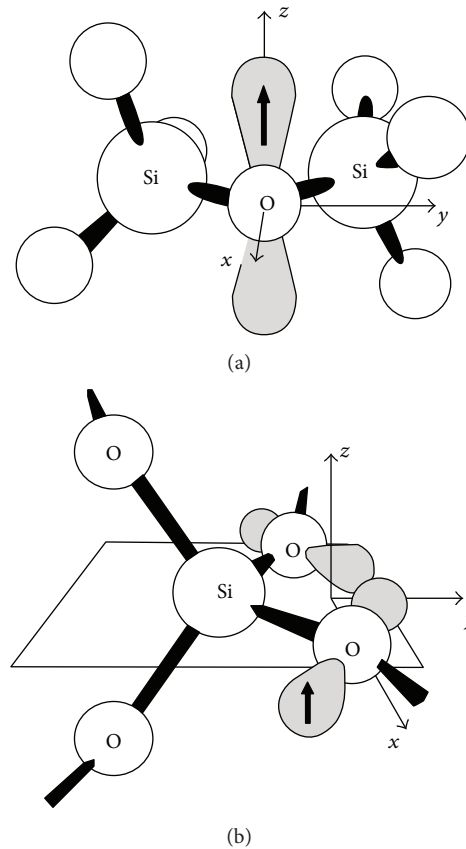


FIGURE 3: Models for self-trapped holes in silica-based glasses: (a) STH_1 and (b) STH_2 . These structures were deduced experimentally on the basis of a highly detailed ESR study [15] involving both g -value distributions and ^{29}Si hyperfine splittings (and theories thereof) and have since been successfully calculated by *ab initio* methods, for example, [35, 36]. Here, the shaded “balloons” represent the orbitals of the unpaired electron spins (denoted by vertical arrows).

distinct variants of STHs, termed STH_1 and STH_2 , have been identified in irradiated silica glasses as the local structures portrayed in Figure 3. In principle, the potential hole trapping sites leading to STH_1 formation can be virtually anywhere in the glass network. By contrast, the sites that become STH_2 upon hole trapping are likely to be relatively rare, since these precursor sites have been shown [15, 16] to have α -quartz-like local structure, whereas a comparison of X-ray-diffraction radial-distribution functions of glassy silica with those the α quartz, cristobalite, and tridymite crystalline polymorphs of SiO_2 has shown quartz to be the least similar to structure to silica glass (correlation coefficient of only 0.26, versus 0.69 and 0.82 for cristobalite and tridymite, respectively [34]).

The ideal “defect-free” [37] structures of inorganic glasses are best determined by means of carefully controlled X-ray and neutron diffraction methods followed by data analyses governed by a branch of materials science termed “amorphography” [38]. It is stated in [37] that

“...since the ideal structure (of an inorganic glass) is disordered, departures from normality

can occur in the direction of both decreased and increased order, the former leading to what are commonly known as defects.”

However, in light of the quartz-like Ge(1) and Ge(2) trapped electron centers in Ge-doped silicas discussed in Section 2.2 and the quartz-like precursor structures deduced for STH_2 in pure silica glasses [15, 16], it appears that departures from normality in the direction of *increased* order can *also* serve as electron- or hole-trapping sites which are termed defects in such silica-based glasses when they trap electrons or holes loosed by ionizing radiations.

3.1. Optical Spectra of Self-Trapped Holes. Self-trapped holes in silica were first identified in bulk silica glasses by ESR studies, the initial results of which I reported in 1989 [39]. The first STH -related optical band was reported practically simultaneously by Chernov et al. [40] and pertained to low-OH, pure-silica-core *fibers* irradiated at 77 K. This band, termed by its discoverers “low-temperature infrared absorption (LTIRA)” [40], consisted of a broad absorption beginning in the visible and increasing with increasing wavelength until peaking near 1800 nm. Its isochronal annealing characteristics were found to be very similar to a component of trapped positive charge in an $\alpha\text{-SiO}_2$ thin film as reported by Harari et al. [41]. However, to my knowledge no follow-up studies of 1800 nm band have since been published.

Similarly, soon after completing my main paper on the ESR-determined properties of STH s [15] for publication in the proceedings of the International Seminar Point Defects in Glasses (Riga, Latvia, July -August, 1991), my activities at the Naval Research Laboratory (NRL) were redirected toward radiation hardening of fiber optics for ITER diagnostics under a contract from the U.S. Department of Energy (DOE). Due to this redirection, I found no opportunity to look for optical manifestations of STH s in bulk silicas. Indeed, I had nearly forgotten about STH s when five years later I began to think that the intense absorption bands at 660 and 760 nm (originally reported by Nagasawa and coworkers [42, 43]) that leaped up in my aluminum-jacketed low-OH pure-silica-core and F-doped-silica-core test fibers immediately upon inserting the sample coils into the NRL “swimming pool” γ -ray source might be due to STH s [44, 45].

It was another five years later, and a year after my January 2001 retirement from NRL, when I finally devised a means to obtain isochronal anneal data for the 660 and 760 nm fiber-optic bands following γ -irradiation at 77-K. And I managed to carry out the experiment during the final two weeks of my 10 month invited professorship of research at Tokyo Institute of Technology. Then two more years passed before I became sufficiently inspired to analyze those very convoluted data sets and publish the results in [46]. These results indeed agreed quite well with my previously published isochronal anneal curves for STH_1 and STH_2 in *bulk silica* [15, 16, 39], as well as with Harari et al.’s trapped positive charge curve [41].

In the meantime, Sasajima and Tanimura [47] had reported *both* ESR and *dichroic* optical spectra of a well selected suite of *bulk* silica samples subjected to 1-Mev, 20-nsec-duration electron pulses at 77 K. They reported that their

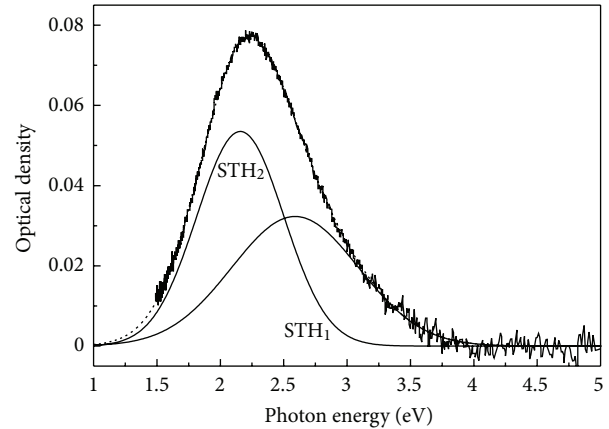


FIGURE 4: Optical bands of STH_2 and STH_1 induced in a low-OH, low-Cl *bulk* fused silica by pulsed electron irradiation at 77 K. These bands were separated from a series of bands peaking at successively higher energies (not shown) by means dichroic red-light bleaching, and it was these dichroic bands (shown here) that correlated with the ESR spectra recorded for the very same samples. This figure is replotted from [47] using the original data and fitted curves kindly provided in digital form by Tanimura.

lowest-OH, lowest-Cl bulk samples yielded the strongest STH ESR signals. Notably, my lowest-OH, lowest-Cl optical fibers yielded the strongest 760 and 660 nm bands (1.63 and 1.88 eV, resp.) during ambient-temperature 1.5 Mev ^{60}Co γ -irradiation. However, I have never recorded ESR spectra for my irradiated fibers, whereas Sasajima and Tanimura *unambiguously* associated their induced optical bands at 2.16 and 2.60 eV (Figure 4) with the classical [15] ESR signals of STH_2 and STH_1 , respectively, *recorded for the very same samples as used for their optical studies*. So if I have correctly interpreted the 1.63 and 1.88 eV bands induced in my pure-silica core fibers [16, 31, 44–46] as being due to STH s, the natures of these optical-fiber STH s must differ considerably from those in bulk silica.

In my recent review article on STH s [16] I cited data in the literature for STH spin densities per unit dose increasing with increasing fictive temperature and remarked that fictive temperatures of silica-core optical fibers are much higher than those of bulk glasses, thus invoking fictive temperature as a possible reason for the difference between 2.16 and 2.60 eV STH optical bands in bulk silica [47] and the 1.63 and 1.88 eV bands in silica fibers [31, 44–46]. However, in retrospect it might also be considered that the structures of silica glasses drawn into fibers surely have residual uniaxial strains superposed on the SiO_2 random network. And these strains would affect the Si–O–Si bond angles anisotropically, thereby changing the properties of STH s created therein relative to those in isotropic bulk glasses studied under similar experimental conditions.

3.2. Yet Another Difference between the Optical Spectra of Self-Trapped Holes in Bulk and Optical-Fiber-Form Silicas. Sasajima and Tanimura [47] determined that the STH_1 absorption band peaking at 2.60 eV in *bulk silica* glass, though

Gaussian in shape, is homogeneously broadened—meaning that bleaching just a small part of the band destroys the entire band rather than burning a hole in it. Thus, at least in the case of the STH_1 band, the bulk-silica bands cannot be decomposed into sums of component subbands. By contrast, as illustrated in Figure 5, the putative STH bands including prominent peaks at 1.63 eV (760 nm) and 1.88 eV (660 nm) recorded for irradiated low-OH F-doped and pure-silica core fibers [44] are clearly much narrower and more numerous than those in bulk silicas [47]. The reasons for this remain unknown, but are surely related to one or more of the issues raised in Section 3.1.

3.3. Growth and Decay Kinetics of Self-Trapped Holes in Pure-Silica-Core Optical Fibers. Figure 6 [44] illustrates the intensities at 760 nm of the spectra (including those of Figure 5(a)) recorded during in-the-dark ^{60}Co γ -irradiation at 1 Gy/s, using the CCD-camera-based prism spectrometer described in [31] (light on for ~ 2 to 5 s per screen grab) at time intervals varying by factors of ~ 3 and ranging from 32 sec to 24 days. This process was briefly interrupted to record ambient-temperature ex situ thermal bleaching and subsequent recovery when this Al-clad fiber coil was returned to its original position in the source [48]. The in situ optical bleach and recovery spike in this figure was taken from an earlier experiment using the same fiber type and radiation dose rate.

The crosses in Figure 6 represent a classical second-order kinetic fit to the data recorded at times above 10^4 s. Accepting this fit as the correct representation of reality, a t^{-1} decrease in induced absorption is to be expected at still longer irradiation times, t . I later determined that this decline in induced loss during continued irradiation is *permanent*. Specifically, in [45] I found that upon reirradiation at 1 Gy/s of a pure-silica-core fiber that 3 months previously had been subjected to the same dose rate for 10^7 s, the *incremental* optical absorption-versus-time curve was two orders of magnitude weaker at $t \sim 200$ s than observed during the initial irradiation, ~ 20 times weaker than the original curve recorded near 10^4 s, and about one order of magnitude weaker at 10^6 s. Describing the same data from a different perspective, this fiber had been radiation hardened to such a degree by the original irradiation that the results of re-irradiation 3 months later at the same dose rate resulted in *newly induced absorption* that was generally less than the *final* value at the end of the first irradiation. Moreover, I discovered in [44] that this Radiation Stimulated Reconfiguration (RSR) process (a terminology that I introduced in [48]) is *purely a function of time*—not of dose—for dose rates ranging between 0.15 Gy/s and 5.5 Gy/s.

One additional experiment reported in [45] involved pulling the irradiated sample coils out of the “swimming pool” γ -ray source, rapidly recording a spectrum at room temperature and immediately afterward thrusting the coil into liquid nitrogen and then recording a second spectrum. Taking the difference between these two spectra revealed the 77-K spectrum to be characterized by (i) an added gray absorption, (ii) a shift of the principle peak position downward from 660 nm to ~ 630 nm, and (iii) a component

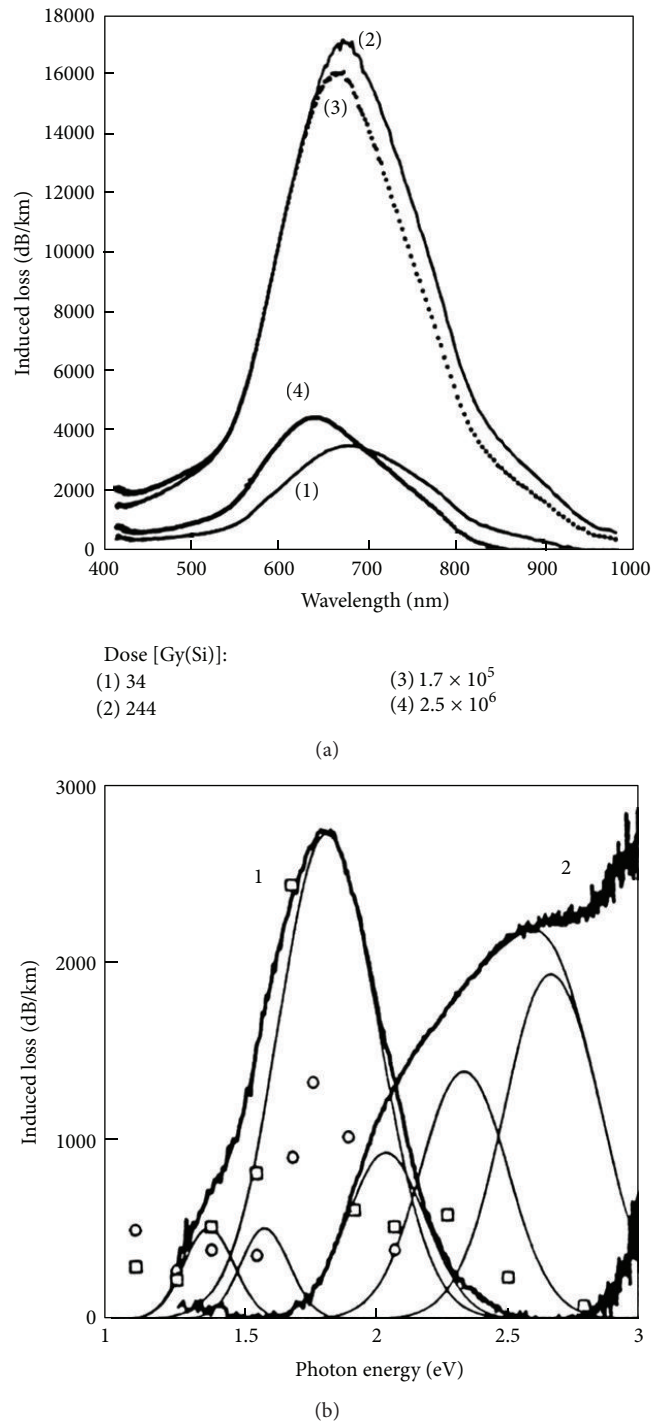


FIGURE 5: (a) Visible/near-IR spectra of a low-OH F-doped-silica-core optical fiber at selected times during continuous γ -irradiation at 1 Gy/s in the dark. (b) A decomposition of similar spectra of a low-OH high-purity-silica-core fiber concomitantly irradiated and recorded under identical conditions. This decomposition was achieved by first separating the red/near-IR peaks (1) from the induced absorptions at higher energies (2) by means of cut-and-try subtractions of several members of the full set of recorded spectra, of which the four displayed in (a) are corresponding examples (adapted from [44]). Superposed circles and squares in (b) represent in arbitrary units optically stimulated release of trapped positive charge from an X-irradiated α - SiO_2 thin film (data from [41]).

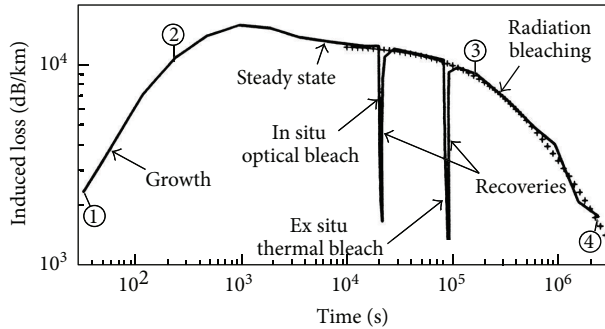


FIGURE 6: Kinetics of the γ -ray-induced optical absorption measured at 760 nm in an F-doped-silica-core, Al-jacketed optical fiber as a function of irradiation time at 1 Gy/s at ambient temperature (~ 27 C) in the dark, except for ~ 3 seconds of probe light for each frame grab. The illustrated in situ optical bleach spike was taken from a separate experiment at the same dose rate and was “grafted” onto the present data for comparison purposes. Circled numbers 1, 2, 3, and 4 correspond to the numbered spectra of Figure 5(a). Figure from [44].

monotonically increasing with increasing wavelength up to maximum value measurable at that time, 1000 nm. I speculated in [45] that the latter may be the high-energy tail of Chernov et al.’s LTIRA (cf. Section 3.1). This speculation could be tested by repeating this experiment with an instrument capable of recording spectra out to ~ 2000 nm.

3.4. If STHs Are the Problem, Accelerated Testing Can Easily Lead to False Positives. Figure 7, adapted from [48], exhibits optical absorption data picked off at 900 nm from complete spectra of the type shown in Figure 5(a) recorded as functions of γ -irradiation time for two virgin lengths of fiber taken from the same spool of aluminum-clad, low-OH/low-Cl KS4V pure-silica-core optical fiber subjected to dose rates of 0.15 Gy/s and 1.02 Gy/s. Note in Figure 7 the confluence of the two data sets (solid squares and circles) at times longer than $\sim 10^6$ s. The large hollow symbols are not data points; rather they have been added to connect arbitrarily selected points on the two curves which share identical radiation doses. Clearly, if the 1.02 Gy/s curve had been an accelerated test and 0.15 Gy/s was the anticipated mission dose rate, the accelerated test would be seriously lying about the vulnerability of this fiber to mission conditions.

3.5. Radiation Hardening by the Presence of Hydroxyl Groups or Interstitial Hydrogen. In [33] the influence of pulsed x-irradiation on the optical transmission of a pair of high-purity-silica-core optical fibers was investigated at room temperature. Transient exposures employed a ~ 1 MeV pulsed X-ray generator with doses varying between 1 and 300 Gy(SiO_2) and dose rates > 1 MGy/s. One of these fibers had a high OH content and the other an extremely low OH content. Figure 8 shows the resulting induced absorption in the low-OH-silica-core sample at times 0.5 and 16 s after that pulse as the black curves with peaks near 1.6 eV. These curves are compared with the (magnified to fit above 2.3 eV) spectra of

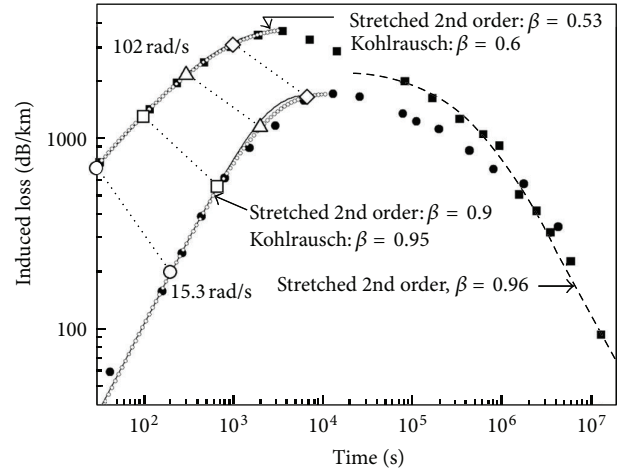


FIGURE 7: Growth and radiation-stimulated destruction of optical bands sampled at 900 nm for an identical virgin pair of low-OH/low-Cl, aluminum-clad pure-silica-core (KS4V) optical fibers continuously subjected to two different γ -ray dose rates. Large hollow symbols link points on the two growth curves receiving equal accumulated doses. This is an adaptation of a figure in [48], where further information about the data collection and curve fitting can be found.

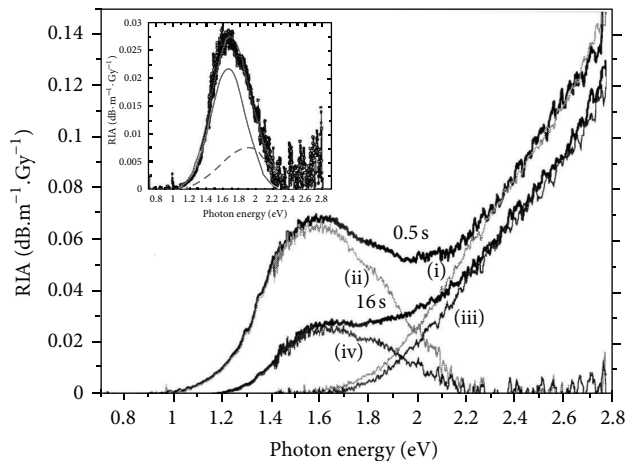
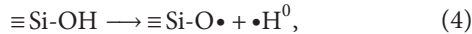


FIGURE 8: Pulsed-X-ray-induced spectra of a pair of optical fibers with pure silica cores, one with high-OH and the other with low-OH, decomposed to emphasize bands centered near 1.6 eV unique to low-OH fiber [33]. Note rapid room-temperature decay of these metastable visible/near-IR bands.

the similarly irradiated and measured high-OH fibers (curves i and iii, resp.). Subtraction of curves i and iii from the respective spectra of the low-OH fiber resulted in curves ii and iv, respectively, which have been decomposed in the inset into a pair of bands centered near 1.63 and 1.88 eV—virtually identical to the bands that I have assigned to STHs induced in low-OH-silica-core fibers continuously γ -irradiated at dose rates in the range of ~ 0.15 to ~ 5 Gy/s [44–46, 48].

In order to better understand the results of Figure 8, it should be understood that γ -rays [49], X-rays [50], and 6.4 eV laser photons [50] have each been shown to create free

hydrogen atoms in OH-containing silica glasses by radiolytic dissociation of hydroxyl groups in according to:



where “ $\equiv\text{Si-O}\cdot$ ” is a nonbridging-oxygen hole center (NBOHC) and the dots “ \cdot ” indicate unpaired electrons, which in these particular cases have both been monitored by ESR. When such irradiations are carried out at 100 K or lower, the numbers of $\cdot\text{H}^0$ s found in high-OH silicas before warming are typically ~ 2 to 3 times more numerous than any other paramagnetic defect [25, 49, 50]. Warming briefly to ~ 150 K (or sometimes only to ~ 130 K) results in the disappearance of all $\cdot\text{H}^0$ s due at least partially to the back reaction of (4). Those $\cdot\text{H}^0$ s that neither back react nor immediately react with STHs or defect center precursors in the glass have been demonstrated to dimerize into ESR-silent H_2 molecules, some of which subsequently diffuse in the temperature range ~ 190 – 290 K to the sites of NBOHCs where they are “cracked” according to the reaction [25]:



The released hydrogen atom, $\cdot\text{H}^0$ commonly reacts with precursors to form E_β' centers [10, 25, 32] (or formyl radicals in the rare case of silica glasses containing traces of carbon monoxide [49]).

STHs have never been observed in high-OH glasses, presumably because the initially created $\cdot\text{H}^0$ s immediately react with STHs to form ESR-silent protons (which in *a*- SiO_2 gate oxides of MOS structures drift toward the SiO_2/Si interface under positive gate bias to form deleterious P_b centers [2]). Thus, the experiment of [33] becomes additional evidence that radiation-induced optical bands centered near 1.63 and 1.88 eV in *low-OH* pure-silica-core optical fibers are truly attributable to STHs—even though these optical-fiber STHs differ from the bands at 2.16 and 2.60 eV that *unambiguously* characterize STH_2 and STH_1 , respectively, in irradiated *bulk silica* [47].

4. Superiority of Fractal Kinetics for Assessing the Kinetics of Radiation-Induced Defects in Glasses

In [48] I reported my derivations of first- and second-order fractal kinetic processes relevant to radiation-induced defect creation in glasses and their *thermally induced decays* at ambient temperature. These relations cannot be applied to situations where decays are *radiation induced*. Fortunately, however, Vladimir Mashkov has derived the fractal kinetic equations for the growth and *radiolytic decay* of defects in glasses [51]. Indeed, Vladimir’s work preceded mine and inspired and guided me to do my own derivations for the case of thermally decaying defects [48].

So why are fractal kinetic formalisms superior to the “stretched exponential” Kohlrausch function, given that in both cases the solutions are functions of $(kt)^\beta$, where k is an effective rate constant, t is time, and $0 < \beta < 1$? Well, my

answer is that the parameterizations of the fractal formalisms that I obtained by changing the dimensionless variable $kt \rightarrow (kt)^\beta$ for *both* the classical first-order and classical second-order kinetic equations (i) explicitly pertain to the *thermal decay* of the radiation-induced defects, (ii) result in solutions that have been found to fit the experimental data much better than by any other means, and (iii) have also revealed some striking, totally unexpected, and potentially valuable empirical rules [48], which the ad hoc parameterizations of the strictly first-order Kohlrausch function conceal. Indeed, Klafter and Shlesinger [52] have shown that three very different theoretical models leading to same Kohlrausch law all have a common underlying mathematical structure, whereas in the present case the mathematical structures are particular to the specific models.

Figure 9 illustrates the most striking empirical rule that I discovered [48] by using my new fractal formalisms to fit the growth in optical attenuation at 1300 nm recorded for four spools each of two sets of Ge-doped-silica-core optical fibers—one of the sets being multimode (MM) and the other single-mode (SM)—during γ -irradiations at 0.0045, 0.17, and 3.4 Gy/s, and either an 8.8×10^{-6} Gy/s nuclear-reactor irradiation or a 1×10^{-4} Gy/s γ -irradiation. All of the spectral data that I fitted were acquired by Joe Friebele and his group at the Naval Research Laboratory and had been previously reported in [53]. The stunning features of Figure 9 are the facts that (i) the fractal rate coefficients k in both first- and second-order are essentially coincident and (ii) they turn out to define a single linear function of dose rate over six orders of magnitude in dose rate! Needless to say, this outcome offers genuine hope that it should be possible to safely extrapolate these parameters into dose-rate regimes greater than 4 Gy/s (for which sources are generally unavailable), as well as backwards into the realm of dose rates lower than 10^{-5} Gy/s (in which case complete growth curves such as those of Figure 10 could not be obtained in practical laboratory times).

4.1. *There Are Two Other Fractal Kinetic Parameters Besides k .* Figure 9 is only a part of a much longer story [48], which I will attempt only to outline here. Most importantly, I must confess that there are two additional fractal measurables derivable from the fitting functions, which also depend on the experimental dose rate \dot{D} :

- (A) β is the exponent of the dimensionless variable, (kt) , that appears in both the first- and second-order fractal-kinetic differential equations and their solutions, wherein k is the deduced fractal rate coefficient plotted on the ordinate of Figure 9 and t is the running time of the irradiation in seconds. The maximum irradiation times, t_{\max} , were arranged in [53] to achieve as nearly as possible the same total doses, $\check{D}_i \times t_{\max(i)}$, for each of the four experimental dose rates, \check{D}_i , where $i = 1, 2, 3, \text{ or } 4$. (However, this ideal objective was not quite achieved for the two lowest dose rates in Figure 10.) By means of fitting the experimental growth curves, I found β to vary

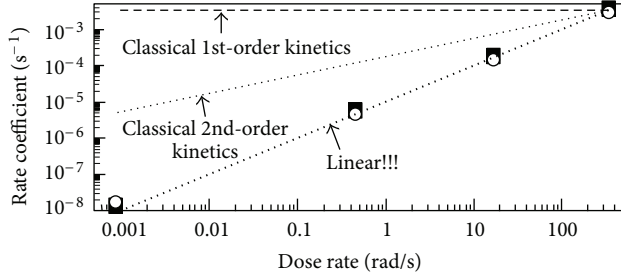


FIGURE 9: Fractal-kinetic rate coefficients k determined as functions of dose rate \dot{D} by fitting [48] growth curves comprising induced losses at 1300 nm as functions of accumulated dose from ~ 7 Gy to $\sim 10^4$ Gy in four virgin samples (one curve for each dose rate) of the MM Ge-doped-silica-core fiber of [53]. The fractal first-order (open circles) and second-order (solid squares) fitting functions (described in detail in [48]) were employed here without taking into account a small population of dose-rate-independent (nondecaying) defects inferred to be copresent. When corrections were made to account for such nondecaying defect populations, the data points collapsed onto the slope-1 line almost perfectly. (Note that Figure 10 shows the similarly fitted curves for the corresponding SM fibers, each of which takes into account the non-decaying components.)

(concave downward) from ~ 1.0 at the lowest dose rates to ~ 0.5 at the highest dose rate [48].

- (B) N_{sat} is the saturation defect concentration at infinite time ($t \rightarrow \infty$) which, though formulated differently in the two kinetic orders considered, was found to behave nearly identically when each was plotted versus the dose rates, \dot{D}_i . By means of my fits, I found N_{sat} to increase by a factor of ~ 100 as \dot{D} increased by ~ 6 orders of magnitude [48], with an average slope $\sim \beta/2$ (vis-à-vis the slope of 1.00 determined for k in Figure 9).

4.2. Major Differences between Classical-Kinetic Constants and Fractal-Kinetic Coefficients. In my fractal derivations [48] both k and N_{sat} are expressed in terms of the dose rates, \dot{D} , in combination with the radiation-induced-creation and thermal-decay-rate coefficients, K and R , respectively, which are *constants* in the *classical* rate equations upon which they are based.

In my 1st-order fractal-kinetic rate equation I found that $k = R$ (which was no longer a constant; see below) while in its solution I found that $N_{\text{sat}} = (K\dot{D}/R)^\beta$.

In my 2nd-order fractal-kinetic rate equation I found that $k = (K\dot{D}R)^{1/2}$ and in its solution I found that $N_{\text{sat}} = (K\dot{D}/R)^{\beta/2}$.

Given these strikingly different formulae for the two fractal-kinetic orders, it was surprising to find that the calculated values of k (see Figure 9), as well as those of β and N_{sat} (cf. [48]) for each of these two fractal-kinetic orders coincided rather accurately for every sampled dose rate. Again, all values of k , β , and N_{sat} were derived from *independent fits* of my first- and second-order fractal solutions for two sets (MM and SM) of four experimental growth curves corresponding

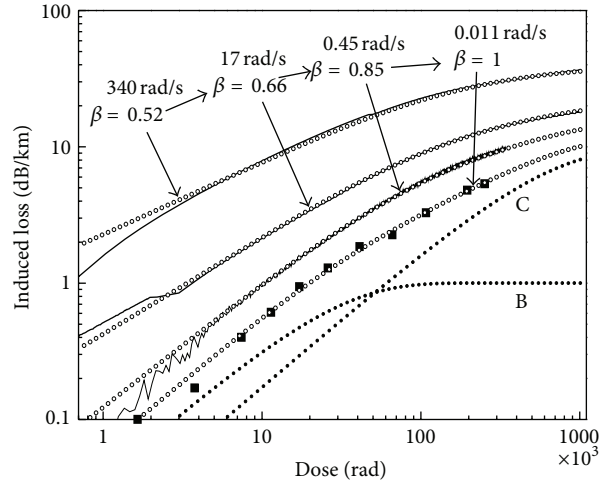


FIGURE 10: Growth of induced attenuation at 1300 nm in lengths of Corning single mode (SM) Ge-doped-silica-core optical fibers separately subjected to γ -ray irradiations at dose rates of 0.011, 0.45, 17, and 340 rad/s at 50°C (continuous solid curves and black squares) [53]. The small open circles are best fits to these four data sets based *primarily* on the fractal second-order-kinetic growth solutions given as (equation (17) of [48]) for defects (termed “Population A”) that *thermally decay at ambient temperature*. However, after the best-fit Population-A simulations were accomplished and found to be less than perfect, these fits were improved upon by cut-and-try additions of first one, and finally two *nondecaying* (dose-rate independent) populations, termed B and C. The finally optimized Population B and C growth curves are illustrated here by the correspondingly labeled dotted curves. Because these additional populations were independent of dose rate by design, the very same pair of curves had to be added to *each* of the four fractal-kinetic simulations comprising the *dose-rate-dependent parts* of the four growth curves in order to achieve the final fits, such as the ones depicted here. Figure from [48].

to four different dose rates \dot{D} (Figure 10 shows the second-order fits of the SM data).

Another surprising outcome turned out to be the empirical rules [48]. In the 1st-order case, $R \propto \dot{D}$ and $K \propto \dot{D}^{1/2}$, whereas in the 2nd-order case, K/R is independent of \dot{D} while $K \times R \propto \dot{D}$.

4.3. What Are the Defects Responsible for the Radiation-Induced Losses at 1300 nm? After a long period of time thinking about it, I am finally convinced that the “Population A” attenuations must be manifestations of the long-wavelength tails of the optical bands of self-trapped holes, which peak near 1.63 and 1.88 eV in low-OH silica-based optical fibers [44–46] (see Figure 11). If I am right about this, then it should be possible to radiation harden low-OH pure silica-core optical fibers, or fiber devices, against photo darkening at 1300 nm by pre-irradiation at a relatively low dose rate (cf. Section 3.3).

Populations B and C in the Ge-doped-silica fibers discussed above make much smaller (but permanent) contributions to the radiation-induced losses at 1300 nm. Clearly, they

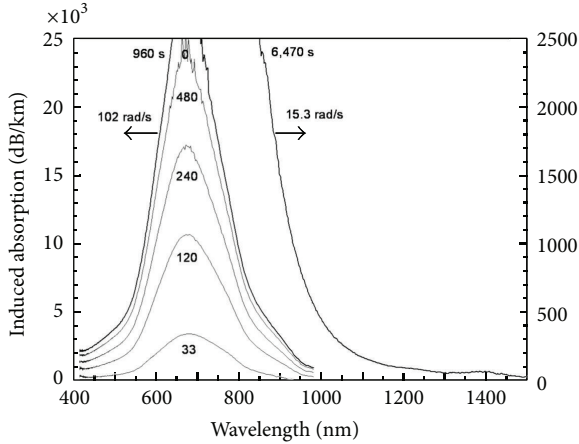


FIGURE 11: γ -ray-induced optical absorption bands attributable to metastable self-trapped holes in separate lengths of an aluminum-clad, low-OH, F-doped-silica-core optical fiber at 27°C in the dark. The short-wavelength spectra were recorded in situ using a 1 m length of fiber and a prism-based CCD-camera spectrometer [48]; whereas long-wavelength spectrum was recorded in situ using a 10 m length and an optical signal analyzer. Dose rates in rad/s and irradiation times in seconds are indicated in the figure. The dose delivered to the 10 m length was about the same as for the 960 s exposure of the 1 m length (note that the right-hand scale is expanded by a factor of 10). Figure from [48].

must comprise the long-wavelength tails of the nearest (non-STH) bands at shorter wavelengths. These would be the Ge(1) [5, 6] and GeX [54, 55] trapped-electron centers centered at 4.4 eV and 2.6 eV, respectively, and perhaps also the 2.0 eV band (e.g., [56]) due to NBOHCs.

The nomenclature “GeX” was introduced by Anokin and his coworkers [54] to express its unknown place in the Pantheon of Ge-doped-silica-glass defects. However, there was one clue. By rerecording the optical spectra of their γ -irradiated polymer-clad, Ge-doped-silica-core fibers one year later, they found that the number density of Ge(1) centers had diminished by about 70% while GeX had increased by an amount approximately equal to the number of Ge(1) centers lost. Accordingly, I speculate that GeX may be a Ge(1) that has reacted with atmospheric hydrogen that penetrated their polymer jackets. If my guess is right, then Ge(2) should have been completely destroyed in less than a year’s time (cf. Section 2.2.1). However, Anokin et al. [54] did not record their spectra to energies higher than 3.2 eV, so further research will be needed to find out what happens to the 5.8 eV band (associated with Ge(2); see Figure 2) in irradiated polymer-clad fibers subsequently exposed to the atmosphere for extended periods of time.

4.4. Fractal-Kinetic Isothermal Decay Curves. Postirradiation decay curves were measured only for the MM and SM Ge-doped fiber coils exposed to the highest dose of 1 Mrad at a dose rate of 340 rad/s [53]. My study of these curves yielded some good news and some bad news.

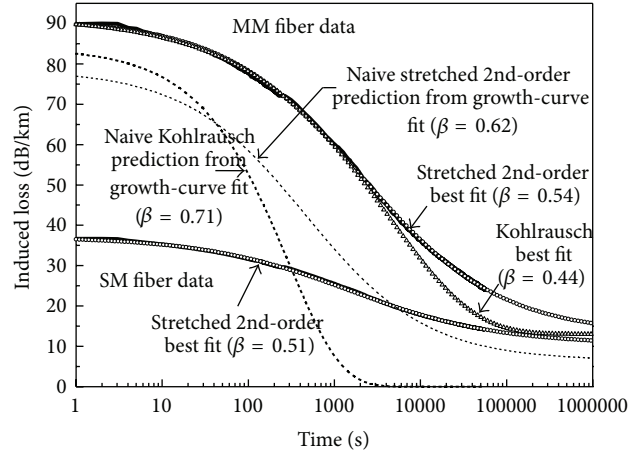


FIGURE 12: Thermal decay curves of MM and SM Ge-doped-silica-core optical fibers following a 1-Mrad irradiation at 340 rad/s (bold black curves) [53]. The SM data correspond to the upper curve of the growth data of Figure 10. Other features are explained in the figure from [48]. Although virtually impossible to discern in the figure above, the experimental data terminate at 60,000 s; thus, the open circles at longer times are solely extensions of the fits to the data at shorter times.

The good news is that the existence of nondecaying (dose-rate independent) defect centers was confirmed, and the unambiguous numbers of these nondecaying centers were found to agree rather well with the sum of the high-dose ends of the “Populations B and C” growth curves that I had iterated into my simulations of the growth curves of Figure 10. This verification came in the form of the time-independent induced losses ~ 10 dB/km that I was forced to add to my fractal-kinetic decay-equation simulations in order to match the actual decay curves shown as the bold black lines in Figure 12.

The “bad news” was that the fractal decay-rate constants R that I used so successfully to simulate the dose-rate-dependent growth curves of Figure 10 were too large by factors of ~ 15 to fit the actual decay curves of Figure 12. The naïveté of my notion that they should match exactly is illustrated by the light dashed curves in Figure 12. My successful fits using substantially larger values of R in my fractal-kinetic second-order decay solution (Equation (20) of [48]) are shown in Figure 12 as the small hollow circles. My fractal first-order-kinetic best-fit (“Kohlrausch best fit”: small hollow triangles) is clearly inferior. In fact, this bow toward the second-order solution is good news for my fractal-kinetic formalisms, given that the recombination of electrons and holes is a second-order kinetic process.

Appropos of predicting the decay curve from the parameters of the growth curve, it has been proven possible to dissect power-law growth curves into a succession of classical n th-order-kinetic solutions wherein the dominant subpopulations are characterized by growth and thermal decay rate constants $K(D)$ and $R(D)$, respectively, both of which decline in magnitude with increasing dose D according to rigorously derived rules [57]. Then for power laws $0 < \beta < 1$, kinetic orders n , and experimental irradiation times t_{irrad} ,

the characteristic postirradiation decay time constants τ_c are predicted to be

$$\tau_c = \frac{t_{\text{irrad}}}{[(n-1)(1-\beta)]} \quad \text{for } n > 1, \quad (6)$$

$$\tau_c = \frac{t_{\text{irrad}}}{[1-\beta]} \quad \text{for } n = 1.$$

This prediction has actually worked out nicely in one experimental case [57]. However, the caveat here is that (6) have succeeded only when applied to *pure power-law growth curves*. Whether or not an analogous system can ever be worked out for continuously curved growth curves such as those in Figure 10 is uncertain.

5. Conclusions

It is clear that a half century of electron-spin-resonance and optical studies of radiation-induced point defects in pure and doped silica glasses has been an immense boon for understanding the performances of both bulk and fiber-optic forms of these materials in radiation environments ranging from the Large Hadron Collider and the International Thermonuclear Experimental Reactor to outer space. Fortunately these studies are continuing, given the virtual infinity of trace impurities, manufacturing methods, environmental conditions, and end-user requirements to which these essential materials and devices will continue to be subjected. Hopefully, the body of knowledge incorporated into this paper and the references provided will stimulate future studies in areas that still remain unsettled while averting “reinvention of the wheel” in areas that are solidly established.

In particular, I hope that the reader will recognize from Section 4 that *fractal kinetics* is much more than just a systematized study of dose-rate-dependent attenuations induced in silica-based fiber optics by ionizing radiations. Rather, it is a rigorous mathematical formalism that perfectly matches the model pertaining to the experimental data and serendipitously provides a reliable means for extrapolating the results of dose-rate-dependence studies backward into time regimes so extended that the experiments cannot be completed in practical laboratory times and forward into suprahigh-dose-rate regimes for which no laboratory sources are likely to become available in the near future.

Acknowledgments

The author thanks Katsumi Tanimura for kindly providing his original data and curve fits, which he has replotted in Figure 4, and Ed Taylor for inviting him to speak on this theme at the SPIE 2011 Optics + Photonics Conference 8164, thereby inspiring an early version of this paper. He composed this paper without outside funding.

References

- [1] D. L. Griscom, “Nature of defects and defect generation in optical glasses,” *Proceedings of SPIE*, vol. 541, pp. 38–59, 1985.
- [2] D. L. Griscom, “Hydrogen model for radiation-induced interface states in SiO₂-on-Si Structures: a review of the evidence,” *Journal of Electronic Materials*, vol. 21, no. 7, pp. 763–767, 1992.
- [3] D. L. Griscom, “Amorphous materials: electron spin resonance,” in *Encyclopedia of Materials: Science and Technology*, pp. 179–186, Elsevier Science, 2001.
- [4] D. L. Griscom, “Electron spin resonance,” in *Glass Science and Technology*, vol. 4B of *Advances in Structural Analysis*, pp. 151–251, Academic Press, New York, NY, USA, 1990.
- [5] E. J. Friebele and D. L. Griscom, “Color centers in glass optical fiber waveguides,” in *Defects in Glasses*, vol. 61 of *MRS Proceedings*, pp. 319–331, 1986.
- [6] D. L. Griscom, “On the natures of radiation-induced point defects in GeO₂-SiO₂ glasses: reevaluation of a 26-year-old ESR and optical data set,” *Optical Materials Express*, vol. 1, pp. 400–412, 2011.
- [7] D. L. Griscom, “Trapped-electron centers in pure and doped glassy silica: a review and synthesis,” *Journal of Non-Crystalline Solids*, vol. 357, no. 8-9, pp. 1945–1962, 2011.
- [8] D. L. Griscom and E. J. Friebele, “Fundamental radiation-induced defect centers in synthetic fused silicas: atomic chlorine, delocalized e centers, and a triplet state,” *Physical Review B*, vol. 34, no. 11, pp. 7524–7533, 1986.
- [9] R. A. Weeks, “Paramagnetic resonance of lattice defects in irradiated quartz,” *Journal of Applied Physics*, vol. 27, no. 11, pp. 1376–1381, 1956.
- [10] D. L. Griscom, “Characterization of three E′-center variants in X- and γ-irradiated high purity α-SiO₂,” *Nuclear Instruments and Methods in Physics Research B*, vol. 1, no. 2-3, pp. 481–488, 1984.
- [11] D. L. Griscom and M. Cook, “²⁹Si superhyperfine interactions of the E′ center: a potential probe of range-II order in silica glass,” *Journal of Non-Crystalline Solids*, vol. 182, no. 1-2, pp. 119–134, 1995.
- [12] D. L. Griscom, “The natures of point defects in amorphous silicon dioxide,” in *Defects in SiO₂ and Related Dielectrics: Science and Technology*, G. Pacchioni, L. Skuja, and D. L. Griscom, Eds., pp. 117–159, Kluwer Academic Publishers, Dordrecht, The Netherlands, 2000.
- [13] G. Buscarino, S. Agnello, and F. M. Gelardi, “²⁹Si hyperfine structure of the E′_α center in amorphous silicon dioxide,” *Physical Review Letters*, vol. 97, no. 13, Article ID 135502, 2006.
- [14] M. Jivanescu and A. Stesmans, “Multi-frequency ESR analysis of E′_δ defect in α-SiO₂,” in *Proceedings of the 8th Symposium SiO₂, Advanced Dielectrics and Related Devices*, Varenna, Italy, 2010.
- [15] D. L. Griscom, “Electron spin resonance characterization of self-trapped holes in amorphous silicon dioxide,” *Journal of Non-Crystalline Solids*, vol. 149, no. 1-2, pp. 137–160, 1992.
- [16] D. L. Griscom, “Self-trapped holes in pure-silica glass: a history of their discovery and characterization and an example of their critical significance to industry,” *Journal of Non-Crystalline Solids*, vol. 352, no. 23-25, pp. 2601–2617, 2006.
- [17] J. A. Weil, “A demi-century of magnetic defects in α quartz,” in *Defects in SiO₂ and Related Dielectrics: Science and Technology*, pp. 197–212, Kluwer Academic, London, UK, 2000.
- [18] E. J. Friebele, D. L. Griscom, and G. H. Sigel, “Defect centers in a germanium-doped silica-core optical fiber,” *Journal of Applied Physics*, vol. 45, no. 8, pp. 3424–3428, 1974.
- [19] J. Isoya, J. A. Weil, and R. F. C. Claridge, “The dynamic interchange and relationship between germanium centers in α-quartz,” *The Journal of Chemical Physics*, vol. 69, no. 11, pp. 4876–4884, 1978.

- [20] R. J. McEachern and J. A. Weil, " ^{17}O hyperfine interaction for the $[\text{GeO}_4]_{\text{I,II}}^-$ and $[\text{GeO}_4/\text{Li}]_{\text{A,C}}^0$ centers in an enriched crystal of α -quartz," *Physical Review B*, vol. 49, no. 10, pp. 6698–6709, 1994.
- [21] A. Alessi, S. Girard, M. Cannas, S. Agnello, A. Boukenter, and Y. Ouerdane, "Evolution of photo-induced defects in Ge-doped fiber/preform: influence of the drawing," *Optics Express*, vol. 19, no. 12, pp. 11680–11690, 2011.
- [22] K. Nagasawa, T. Fujii, Y. Ohki, and Y. Hama, "Relation between Ge(2) center and 11.9 mT hyperfine structure of ESR spectra in Ge-doped silica fibers," *Japanese Journal of Applied Physics*, vol. 27, no. 2, pp. 240–243, 1988.
- [23] A. A. Bobyshev and V. A. Radtsig, "EPR study of the centers of chemisorption of certain gases on a GeO_2 surface," *Kinetics and Catalysis*, vol. 22, pp. 1229–1235, 1982.
- [24] T. E. Tsai and D. L. Griscom, "On the structures of hydrogen-associated defect centers in irradiated high-purity a- $\text{SiO}_2\text{:OH}$," *Journal of Non-Crystalline Solids*, vol. 91, no. 2, pp. 170–179, 1987.
- [25] D. L. Griscom, "Thermal bleaching of x-ray-induced defect centers in high purity fused silica by diffusion of radiolytic molecular hydrogen," *Journal of Non-Crystalline Solids*, vol. 68, no. 2-3, pp. 301–325, 1984.
- [26] D. L. Griscom, G. H. Sigel, and R. J. Ginther, "Defect centers in a pure-silica-core borosilicate-clad optical fiber: ESR studies," *Journal of Applied Physics*, vol. 47, no. 3, pp. 960–967, 1976.
- [27] M. G. Jani, R. B. Bossoli, and L. E. Halliburton, "Further characterization of the E'_1 center in crystalline SiO_2 ," *Physical Review B*, vol. 27, no. 4, pp. 2285–2293, 1983.
- [28] R. Schnadt and A. Rauber, "Motional effects in the trapped-hole center in smoky quartz," *Solid State Communications*, vol. 9, no. 2, pp. 159–161, 1971.
- [29] K. L. Brower, "Electron paramagnetic resonance of $\text{Al E}'_1$ centers in vitreous silica," *Physical Review B*, vol. 20, no. 5, pp. 1799–1811, 1979.
- [30] A. N. Trukhin, A. Sharakovski, J. Grube, and D. L. Griscom, "Sub-band-gap-excited luminescence of localized states in SiO_2 -Si and SiO_2 -Al glasses," *Journal of Non-Crystalline Solids*, vol. 356, no. 20-22, pp. 982–986, 2010.
- [31] D. L. Griscom, " γ and fission-reactor radiation effects on the visible-range transparency of aluminum-jacketed, all-silica optical fibers," *Journal of Applied Physics*, vol. 80, no. 4, pp. 2142–2155, 1996.
- [32] D. L. Griscom, D. B. Brown, and N. S. Saks, "Nature of radiation-induced point defects in amorphous SiO_2 and their role in SiO_2 -on-Si structures," in *The Physics and Chemistry of SiO_2 and the Si- SiO_2 Interface*, pp. 287–297, Plenum, New York, NY, USA, 1988.
- [33] S. Girard, D. L. Griscom, J. Baggio, B. Brichard, and F. Berghmans, "Transient optical absorption in pulsed-X-ray-irradiated pure-silica-core optical fibers: influence of self-trapped holes," *Journal of Non-Crystalline Solids*, vol. 352, no. 23-25, pp. 2637–2642, 2006.
- [34] J. H. Konnert, P. D'Antonio, and J. Karle, "Comparison of radial distribution function for silica glass with those for various bonding topologies: use of correlation function," *Journal of Non-Crystalline Solids*, vol. 53, no. 1-2, pp. 135–141, 1982.
- [35] G. Pacchioni and A. Basile, "Calculated spectral properties of self-trapped holes in pure and Ge-doped SiO_2 ," *Physical Review B*, vol. 60, no. 14, pp. 9990–9998, 1999.
- [36] A. V. Kimmel, P. V. Sushko, and A. L. Shluger, "Structure and spectroscopic properties of trapped holes in silica," *Journal of Non-Crystalline Solids*, vol. 353, no. 5-7, pp. 599–604, 2007.
- [37] A. C. Wright, "Defect-free vitreous networks: the idealized structure of SiO_2 and related glasses," in *Defects in SiO_2 and Related Dielectrics: Science and Technology*, pp. 1–35, Kluwer Academic Publishers, London, UK, 2000.
- [38] A. C. Wright, "Neutron and x-ray amorphography," in *Experimental Techniques of Glass Science*, pp. 205–314, The American Ceramic Society, Westerville, Ohio, USA, 1993.
- [39] D. L. Griscom, "Self-trapped holes in amorphous silicon dioxide," *Physical Review B*, vol. 40, no. 6, pp. 4224–4227, 1989.
- [40] P. V. Chernov, E. M. Dianov, and V. N. Karpechev, "Spectroscopic manifestations of self-trapped holes in silica," *Physica Status Solidi B*, vol. 155, pp. 633–640, 1989.
- [41] E. Harari, S. Wang, and B. S. H. Royce, "Low-temperature irradiation effects in SiO_2 -insulated MIS devices," *Journal of Applied Physics*, vol. 46, no. 3, pp. 1310–1317, 1975.
- [42] K. Nagasawa, M. Tanabe, K. Yahagi, A. Iino, and T. Kuroha, "Gamma-ray induced absorption band at 760 nm in pure silica core optical fibers," *Japanese Journal of Applied Physics*, vol. 23, no. 5, pp. 606–611, 1984.
- [43] K. Nagasawa, M. Tanabe, and K. Yahagi, "Gamma-ray-induced absorption bands in pure-silica-core fibers," *Japanese Journal of Applied Physics*, vol. 23, no. 12, pp. 1608–1613, 1984.
- [44] D. L. Griscom, "Visible/infrared absorption study in fiber geometry of metastable defect states in high-purity fused silicas," *Materials Science Forum*, vol. 239–241, pp. 19–24, 1997.
- [45] D. L. Griscom, "Radiation hardening of pure-silica-core optical fibers: reduction of induced absorption bands associated with self-trapped holes," *Applied Physics Letters*, vol. 71, no. 2, pp. 175–177, 1997.
- [46] D. L. Griscom, " γ -Ray-induced visible/infrared optical absorption bands in pure and F-doped silica-core fibers: are they due to self-trapped holes?" *Journal of Non-Crystalline Solids*, vol. 349, no. 1-3, pp. 139–147, 2004.
- [47] Y. Sasajima and K. Tanimura, "Optical transitions of self-trapped holes in amorphous SiO_2 ," *Physical Review B*, vol. 68, no. 1, Article ID 014204, pp. 142041–142047, 2003.
- [48] D. L. Griscom, "Fractal kinetics of radiation-induced point-defect formation and decay in amorphous insulators: application to color centers in silica-based optical fibers," *Physical Review B*, vol. 64, no. 17, Article ID 174201, 2001.
- [49] D. L. Griscom, M. Stapelbroek, and E. J. Friebele, "ESR studies of damage processes in X-irradiated high purity a- $\text{SiO}_2\text{:OH}$ and characterization of the formyl radical defect," *The Journal of Chemical Physics*, vol. 78, no. 4, pp. 1638–1651, 1983.
- [50] D. L. Griscom, "Growth and decay kinetics of defect centers in high-purity fused silicas irradiated at 77 K with X-Rays or 6.4-eV laser light," *Nuclear Instruments and Methods in Physics Research B*, vol. 46, no. 1-4, pp. 12–17, 1990.
- [51] V. A. Mashkov, W. R. Austin, L. Zhang, and R. G. Leisure, "Fundamental role of creation and activation in radiation-induced defect production in high-purity amorphous SiO_2 ," *Physical Review Letters*, vol. 76, no. 16, pp. 2926–2929, 1996.
- [52] J. Klafter and M. F. Shlesinger, "On the relationship among three theories of relaxation in disordered systems," *Proceedings of the National Academy of Sciences of the United States of America*, vol. 83, pp. 848–851, 1986.
- [53] E. J. Friebele, G. M. Williams, and W. D. Mack, "Qualified parts list optical fibers in radiation environments," in *Optical Fiber Reliability and Testing*, vol. 3848 of *Proceedings of SPIE*, pp. 232–239, September 1999.

- [54] E. V. Anokin, V. M. Mashinsky, V. B. Neustruev, and Y. S. Sidorin, "Effects of exposure to photons of various energies on transmission of germanosilicate optical fiber in the visible to near IR spectral range," *Journal of Non-Crystalline Solids*, vol. 179, pp. 243–253, 1994.
- [55] D. L. Griscom, " γ -ray-induced optical attenuation in Ge-doped-silica fiber image guides," *Journal of Applied Physics*, vol. 78, no. 11, pp. 6696–6704, 1995.
- [56] L. Skuja, "Section 1. Defect studies in vitreous silica and related materials: optically active oxygen-deficiency-related centers in amorphous silicon dioxide," *Journal of Non-Crystalline Solids*, vol. 239, no. 1–3, pp. 16–48, 1998.
- [57] D. L. Griscom, M. E. Gingerich, and E. J. Friebele, "Model for the dose, dose-rate and temperature dependence of radiation-induced loss in optical fibers," *IEEE Transactions on Nuclear Science*, vol. 41, no. 3, pp. 523–527, 1994.

Research Article

Modeling of Optical Nanoantennas

Bedir B. Yousif¹ and Ahmed S. Samra²

¹ *Electrical Engineering Department, Faculty of Engineering, Kafrelsheikh University, Kafrelsheikh 35514, Egypt*

² *Electronics and Communications Department, Faculty of Engineering, Mansoura University, Mansoura 35516, Egypt*

Correspondence should be addressed to Bedir B. Yousif, bedir.yousif@gmail.com

Received 11 May 2012; Accepted 3 October 2012

Academic Editor: Sergi Gallego

Copyright © 2012 B. B. Yousif and A. S. Samra. This is an open access article distributed under the Creative Commons Attribution License, which permits unrestricted use, distribution, and reproduction in any medium, provided the original work is properly cited.

The optical properties of plasmonic nanoantennas are investigated in detail using the finite integration technique (FIT). The validity of this technique is verified by comparison to the exact solution generalized Mie method (GMM). The influence of the geometrical parameters (antenna length, gap dimension, and shapes) on the antenna field enhancement and spectral response is discussed. Localized surface plasmon resonances of Au (gold) dimers nanospheres, bowtie, and aperture bowtie nanoantennas are modeled. The enhanced field is equivalent to a strong light spot which can lead to the resolution improvement of the microscopy and optical lithography, thus increasing the optical data storage capacity. Furthermore, the sensitivity of the antennas to index changes of the environment and substrate is investigated in detail for biosensing applications. We confirm that our approach yields an exact correspondence with GMM theory for Au dimers nanospheres at gap dimensions 5 nm and 10 nm but gives an approximation error of less than 1.37% for gap dimensions 1 nm and 2 nm with diameters approaching 80 nm. In addition, the far-field characteristics of the aperture bowtie nanoantenna such as directivity and gain are studied. The promising results of this study may have useful potential applications in near-field sample detection, optical microscopy, and so forth.

1. Introduction

The study of optical phenomena related to the electromagnetic response of metals has been recently termed plasmonics or nanoplasmonics. This rapidly growing field of nanoscience is mostly concerned with the control of optical radiation on the subwavelength scale [1]. The interaction of light with metal nanostructures is hidden in the frequency dependence of the metal's complex dielectric function. Properly designed nanostructures are known to produce the so-called hot spots where the incident electromagnetic field is enhanced by several orders of magnitude. The plasmonic resonances observed in such structures open the possibility to build antennas operating in the visible [2, 3]. Their hot spots can be used to trigger nonlinear effects and to couple electromagnetic radiation efficiently between the antennas and dipole emitters. Experimental techniques such as tip-enhanced Raman spectroscopy or surface-enhanced Raman spectroscopy demonstrate the potential of such hot spots to detect radiative emitters with sensitivity down to a single molecule [4–10]. The enhancement of the fluorescence of molecules placed near a plasmonic nanostructure has been

observed recently, tuning the plasmon resonance either to the excitation or the emission of the molecules [11–14].

In recent years, a variety of schemes taking advantage of localized near fields generated by metallic nanoparticles have been proposed to use them as optical nanoantennas [2, 3, 15–22]. Optical antennas consisting of nanometer size metallic particle can be used to improve the size mismatch between the diffraction limited spot of the excitation light and fluorescent molecules that are much smaller than the excitation wavelength [19]. Optical antennas can produce very high near-field intensities when they are optically excited with a wavelength suitably matched to the antenna size due to their localized surface plasmon resonances [3]. Passive optical antennas were first demonstrated in the microwave regime by Grober and coworkers [23]. Also, mid-infrared (mid-IR) passive antennas [15] and bowtie antenna-based bolometers [24, 25] have been implemented.

Near-field enhancement generated by optical antennas is useful for surface-enhanced Raman spectroscopy (SERS) [4, 5, 18, 26]. Recently, metallic nanoparticles have been utilized in biosensing [27], cancer treatment [28], spectral imaging [29], solar applications [30], and near-field probes [31].

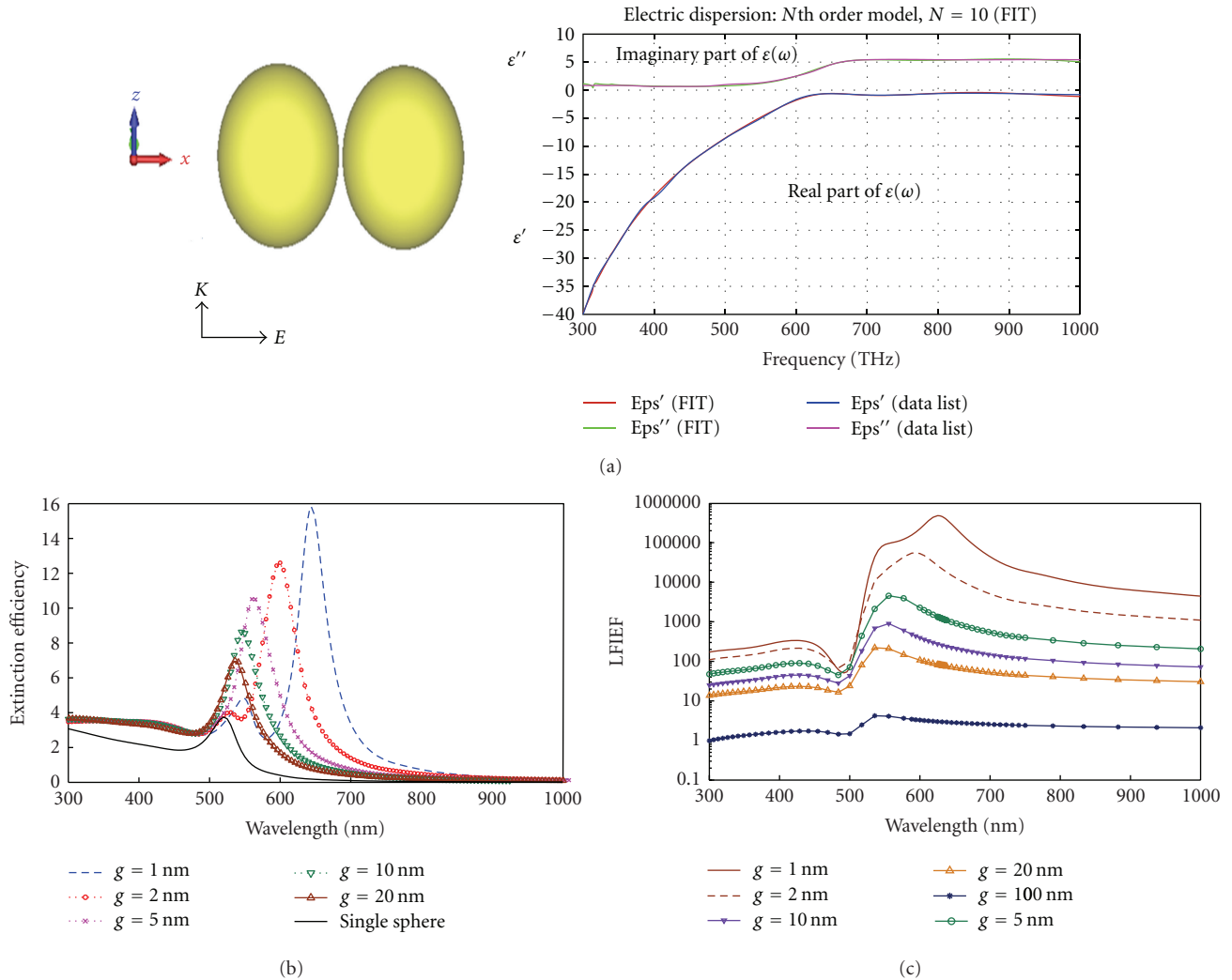


FIGURE 1: Simulation of gold dimer nanoantenna with FIT. (a) Schematic configuration of a gold dimer nanoantenna and its dielectric function $\epsilon(\omega)$. (b) Extinction coefficients for varying gaps as functions of incident wavelength. (c) The local field intensity enhancement factor (LFIEF) inside the gap (g) of gold dimer nanoantenna.

Optical nanoantennas can also increase the excitation and emission rates of fluorescent molecules [11, 32]. The aim of this paper is to provide a detailed analysis and design of plasmonic nanoantennas for the near-field and spectral response enhancement.

The outline of this paper is as follows. Section 2 explains optical antenna design and modeling. Section 3 discusses the response of plasmonic nanoantennas with the validation of the results by comparison to the exact solution generalized Mie method (GMM) and the other published papers. Section 4 summarizes our observations and discuss potential future extensions of the research.

2. Optical Antenna Design and Modeling

The finite integration technique (FIT) using computer simulation technology (CST) microwave studio was used for the simulations to calculate the optical response of plasmonic nanoantennas. The microwave studio (MWS) developed

based on the FIT exhibits helpful functions especially suitable for simulating nanoantennas. It was adopted for modeling of monopole, dipole, bowtie, and nanooptical Yagi-Uda antennas [33–40]. The real and imaginary parts of the gold dielectric function are obtained from experimental data [41, 42]. The structures are illuminated from below, perpendicular to the antenna long axis. The gap between the nanostructure represents an essential feature of the antenna structure. To characterize the spectral response of the antenna and its intensity enhancement, we therefore calculate the field intensity inside this gap in relative units to the illumination intensity.

2.1. Au Dimer Nanoantenna. We first investigated plasmonic resonances and the local field intensity enhancement factor (LFIEF) inside the gap (g) of dimer gold nanospheres as shown in Figure 1(a). A dimer formed by two identical spheres (with radius $R = 40$ nm) of dielectric function $\epsilon(\omega)$, separated by a gap g , and embedded in a nonabsorbing

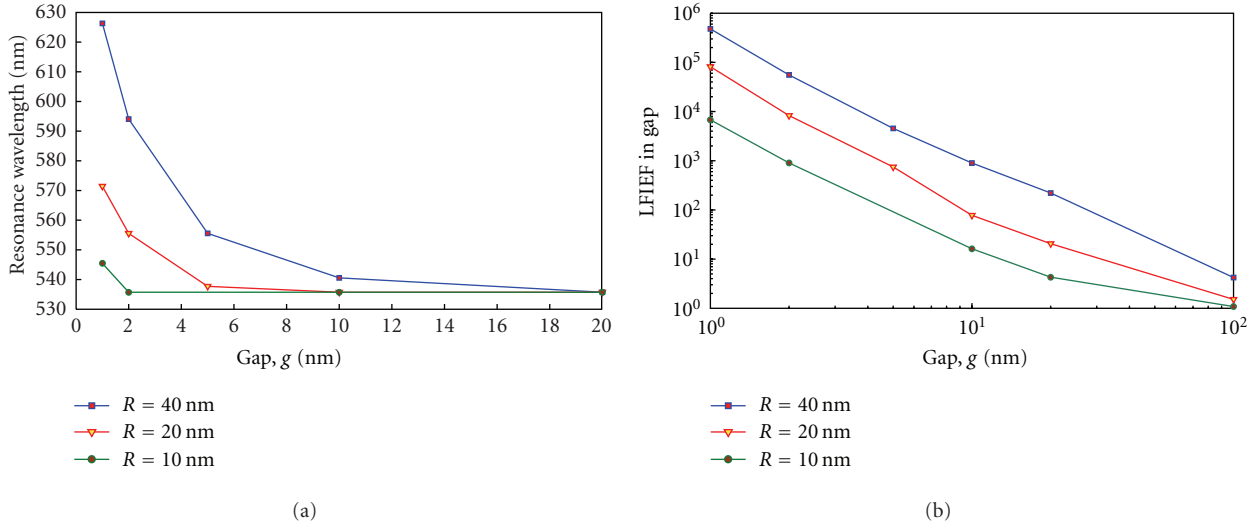


FIGURE 2: Gap dependence of the main coupled-LSPR. (a) Resonance wavelength and (b) LFIEF at the “hot spot” in the gap.

dielectric with $\epsilon_M \approx 1$). The geometry of the antenna strongly influences its optical properties as indicated in Figures 1(b) and 1(c), which shows the calculated intensity spectra in the antenna gap of the dimer nanoantenna. In the spectral range of the calculation, the dimer nanoantenna at $g = 1$ nm has two resonances at 540 nm and 635 nm as shown in Figure 1(b) extinction efficiency spectrum, where the field intensity (LFIEF) in the gap is about 100000 and 479200 times larger than the intensity of the illumination field as indicated in Figure 1(c). It is clear that the dimer gold spheres nanoantenna is essentially single mode for all gaps dimensions except only at $g = 1$ nm, which has two modes due to the strong interaction coupling of the two nanospheres.

Stronger field enhancements can be achieved by decreasing the width of the gap and this is observed for the gap dimension 1 nm and the sphere diameter 80 nm in Figure 1(c). Note the presence of a dominant red-shifted localized surface plasmon resonance (LSPR) that moves further to the red for smaller gaps. Decreasing the gap width increases the antenna sensitivity as shown in Figure 2. We assume that this sensitivity is related to the spectral position of the antenna resonance at the maximum LFIEF. The main properties of the coupled-LSPR are characterized by its resonance wavelength and the LFIEF at the hot-spot (on the metal surface along the dimer axis in the gap). The gap dependence of these two quantities is summarized in Figures 2(a) and 2(b) for a gold dimer in air for different radius spheres ($R = 40, 20,$ and 10 nm). It is worth stressing the fact that the resonance wavelength and the LFIEF at the hot-spot are plotted on semilog and log-log scales, respectively. A sharp change is seen for both for gap distances g below 20 nm. Actually, we can use this information as an “empirical” rule to establish in this case a characteristic distance beyond which the spheres can be considered as “independent.” Spheres can be effectively considered as electromagnetically independent if they are separated by more than 20 nm in the gap. For shorter distances, the interaction starts playing a role, and the main LSPR red

shifts with a concomitant steep increase in the hot-spot LFIEF at that wavelength. From Figure 2, it is also noted that decreasing the sphere radius decreases the antenna sensitivity and blue-shifted localized surface plasmon resonance (LSPR) that moves further.

Much more interesting is the antenna sensitivity to changes of the environmental index of refraction n_{env} . As shown in Figure 3 the spectral positions of the dipole resonances strongly depend on n_{env} . Increasing the refractive index of surrounding medium increases the antenna sensitivity and red-shifted localized surface plasmon resonance (LSPR) that moves further. Figure 3(b) shows a linear increase of the resonance wavelength for increasing n_{env} for different gap widths. The sensitivity is related to the spectral position of the antenna resonance. The further the resonance wavelength is shifted to the red, the higher the antenna sensitivity on index changes.

This section explains the effects of the polarization direction of the incident light on the optical properties of a gold dimer nanoantenna. By keeping the wave propagating in the z -direction, two cases with the polarization directions in the x - and y -directions are carefully considered. That is, the light is incident upon the antenna from the bottom side. The results are shown in Figure 4, where E_x and E_y polarizations are for Figures 4(a) and 4(b), respectively.

The light intensity is calculated and recorded at the origin in the middle of the dimer, through our interested optical region. It is found that both cases show a resonant behavior varying with wavelength in the light intensity’s spectra. Single resonance occurs in the optical range in both cases of polarization while two resonances appear in the visible light range at 555.56 nm for x -polarization and 517.24 nm for y -polarization. This can be explained by the strong interaction between the nanoantenna and the light through plasmon resonance when light polarized in x -direction. However, the variation magnitudes of E_x polarization (900.12) in Figure 4(a) are much larger than those of E_y polarization (0.831) in Figure 4(b). On the other hand, it can be

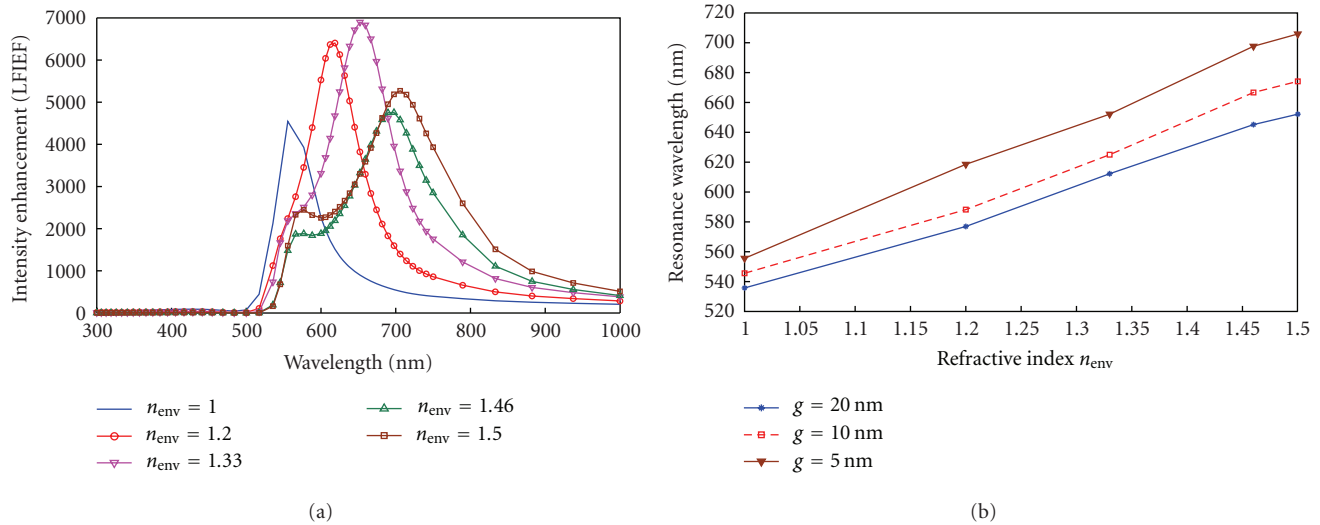


FIGURE 3: (a) Relative field intensity enhancement in the gap for a gold dimer nanoantenna with diameter 80 nm and gap width 5 nm as a function of the illumination wavelength for different refractive indexes n_{env} is used for the cover material. (b) Sensitivity of a gold dimer nanoantenna with sphere diameter 80 nm and various gap widths as a function of the environment index n_{env} .

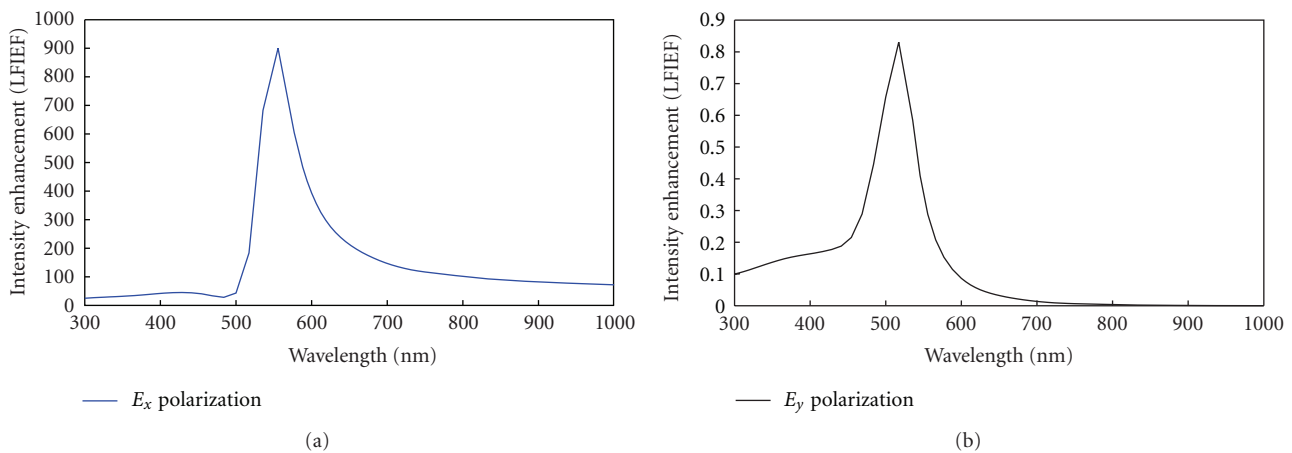


FIGURE 4: Light intensity as a function of incident wavelength for gold dimer nanoantenna with 80 nm sphere diameter and 10 nm gap width in air under different excitations. E_x polarization in (a) and E_y polarization in (b).

observed from the Figure 4 that the polarization is able to achieve much higher light intensity than the polarization at corresponding wavelengths. The reason is that for the coupling between two nanoparticles, a polarization along the longitudinal direction connecting them is preferable for a dipole-like excitation.

At microwave or radio frequencies, the substrate index n_s has a strong influence on the resonance spectrum of the antenna [43]. This dependence is in general used to design small antennas with dimensions well below the half wavelength condition. The same effect can be observed in Figure 5 for optical resonant antennas: an increasing substrate index leads to a red shift of the antenna resonance. At optical frequencies the antenna dimensions are as small as a few tens of nanometers, that is, below the half wavelength condition [44] and at the limit of today's fabrication techniques. Hence, designing smaller antennas by using high-index materials as substrate does not seem to be of great practical interest

presently. From Figure 5 it is clear that at n_s equal to 2.5 or 3 the response of the nanoantenna transfers from single mode to double mode, and this is similar or equivalent to increases in the size of the nanoantenna as stated above. The direction of propagation is also investigated with the effect of the substrate for a gold dimer with sphere diameter 80 nm and gap width 5 nm in air. The field enhancements which obtained in $+z$ direction are much stronger than those of $-z$ direction as shown in Figure 6. This is due to the strong interaction between the SPR in metallic nanoparticles and the substrate when the light incident from the bottom of substrate, in contrary when light illuminated from above where SPR is little or weakly interact with light as illustrated in Figure 6.

2.2. *Au Bowtie and Bowtie Aperture Nanoantennas.* Another way of increasing the near fields is to engineer the antenna

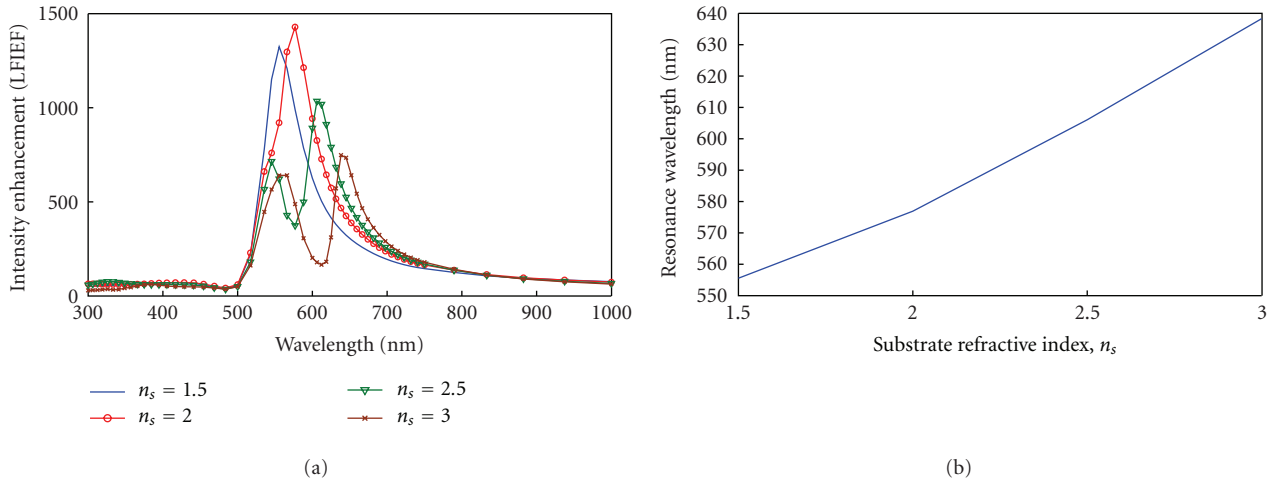


FIGURE 5: (a) Relative field intensity enhancement in the gap for a gold dimer nanoantenna with diameter 80 nm and gap width 10 nm as a function of the illumination wavelength for different refractive indexes n_s of substrate. (b) Sensitivity of nanoantenna as a function of the refractive indexes n_s of substrate.

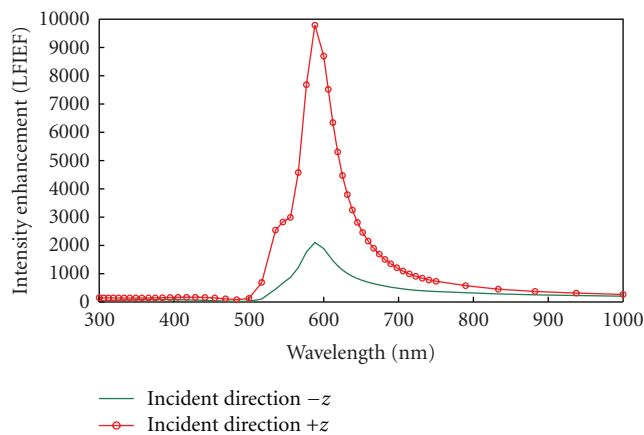


FIGURE 6: Relative field intensity enhancement in the gap for a gold dimer nanoantenna with diameter 80 nm and gap width 5 nm as a function of the illumination wavelength for wavevector k in $-z$ and $+z$ directions.

terminations and shapes. Bowtie optical antenna was also proven to be effective in reaching the spatial resolution well below the diffraction limit [23]. Similarly, metallic apertures like C-shaped aperture were also investigated because they can prove high transmission [45]. Moreover, the enhanced field via the strong light spot produced by the nanoantenna is highly dependent on its structure. Thus, considerable investigations were carried out based on different structural designs ranging from single nanoparticles of various shapes [46, 47] to delicately arranged nanoparticles including pairs and arrays [16, 48]. Bowtie antennas, namely, a pair of coupled triangular gold particles, offer higher near-field enhancements and better spatial confinement. When two triangular particles are placed side by side with the apices facing one another, the capacitive coupling between them will generate even higher fields than those generated by an isolated particle. Another typical design of the nanoparticle

pairs with good field confinement is the aperture bowtie nanoantenna. It was successfully fabricated in experiment, and there were wide studies exploring its controllable geometric effects on its optical properties, such as length and gap effects [16]. These studies are meaningful because bowtie nanoantenna has tunable characteristics. Bowtie-shaped aperture nanoantenna also attracts our recent research interests. Researchers have found that bowtie-shaped aperture can offer higher optical transmission than other apertures with regular shapes under the same resolution [49]. But recent studies provide little information about either its near-field resonant properties within a continuous wideband frequency spectrum or its far-field antenna performance. Such information is, however, quite important for optical communications. Therefore, it is worthwhile to extend both theoretical and experimental studies.

Here, we first clear that the near-field enhancement using the coupled triangular particles (bowtie antenna) as a function of incident wavelength for gold bowtie nanoantenna. The antennas are illuminated by a plane wave polarized along the x -axis and the substrate refractive index is 1.46, same boundary conditions as the above sections. The near-field response curve for the bowtie antenna is shown in Figure 7. When two triangular particles are placed side by side with the apices facing one another, the capacitive coupling between them will generate even higher fields than those generated by an isolated particle. Compared to the other antenna designs, bowties seem to offer the largest near-field enhancements and the smallest spatial extent for the field, that is, a single sharp optical spot. As shown in Figure 7, most of the electromagnetic energy is localized in the gap of the antenna. This property of bowties is crucial for applications requiring a very intense spatially confined optical spot.

In this section, both the near-field optical resonant properties and the far-field antenna characteristics are investigated for the bowtie shaped aperture nanoantenna. The nanoantenna consists of two fan-shaped hollow apertures

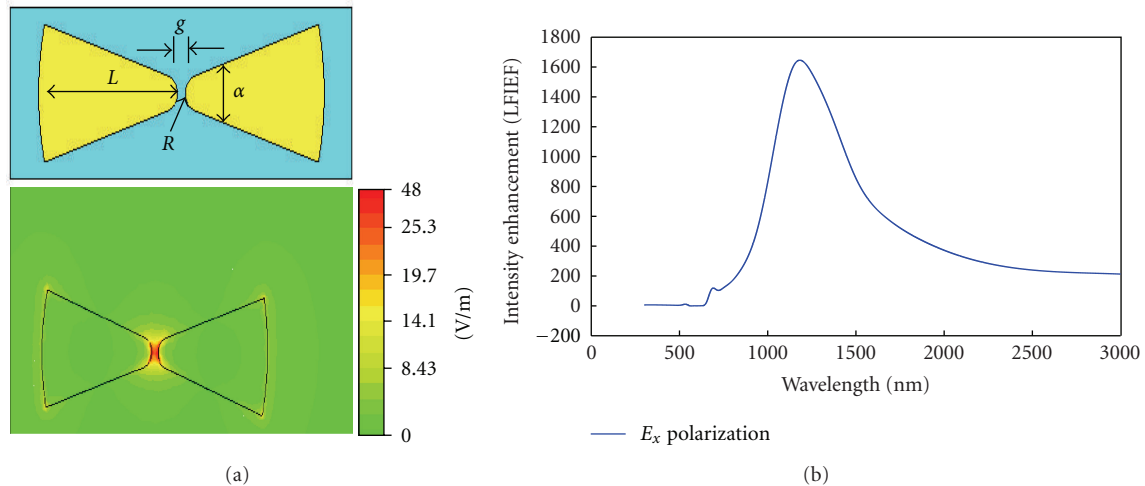


FIGURE 7: Near-field intensity distribution (a) around a triangular bowtie gold nanoantenna near the resonance wavelength (1363 nm) and (b) local field intensity enhancement in the middle of the gap with $L = 240$ nm, gap of 20 nm, tip radius 20 nm, flare angle 30° , and $n_s = 1.46$.

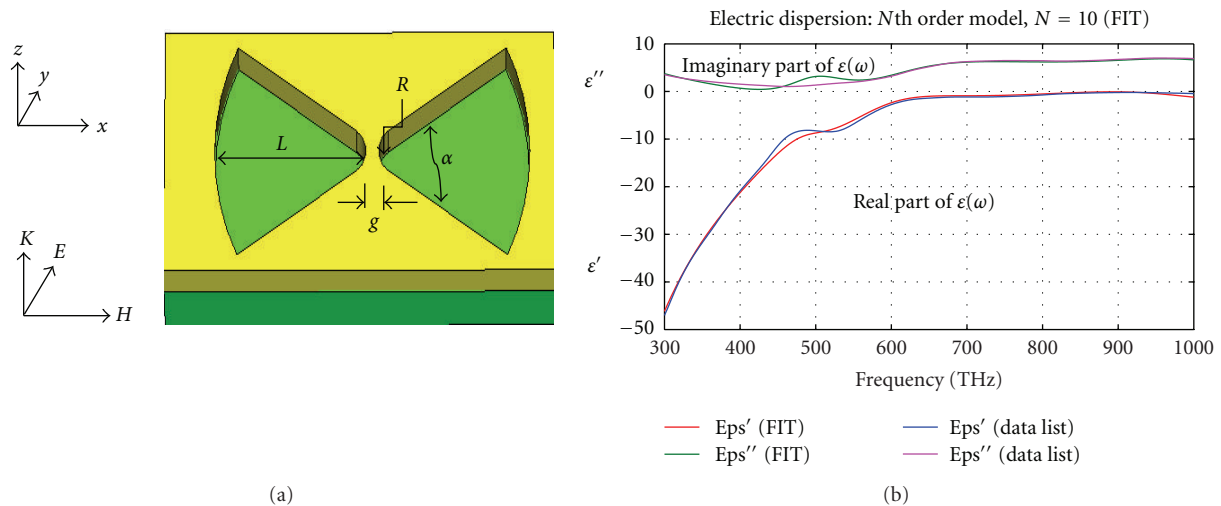


FIGURE 8: Simulation of bowtie shaped aperture nanoantenna with FIT. (a) Schematic configuration of bowtie aperture nanoantenna and its dielectric function $\epsilon(\omega)$.

mounted on a gold thin film. Configurations under consideration are depicted in Figure 8. Two tip-to-tip placed fan-shaped nanoapertures are mounted onto the gold thin film. Each has a length of 240 nm and a gap of 20 nm. The fan shape is more preferable than a triangle shape because it avoids the sharp corner which can cause undesirable singularity issues in design and because it is difficult to have its fabrication of high precision. Due to the same reasons, the tip of each fan-shaped aperture is rounded off with a radius of curve. Such a gold bowtie aperture nanoantenna is mount-integrated on the top of a substrate of silicon dioxide with a refractive index of 1.46. The nanoantenna with finite substrate is surrounded by the air. The coordinates in the figure are schematic and its origin is located in the middle of the nanoantenna. There are four geometric parameters of major concerns shown in Figure 8: length (L), flare angle (α), radius of curve of each nanoaperture (R), and distance between the two nanoapertures (g). These parameters can

be used to optimize their effects on the optical properties of nanoantennas.

The effects of the polarization direction of the incident light on the optical properties of a gold aperture nanoantenna. The results are shown in Figure 9, where E_x and E_y polarization are for Figures 9(a) and 9(b), respectively. It is found that both cases show a resonant behavior varying with wavelength in the light intensity's spectra. Single resonance occurs in the optical range in the case of x -polarization while two resonances appear in the near infrared range in the case of y -polarization. This can be explained by the strong interaction between the nanoantenna and the light through plasmon resonance. However, the variation magnitudes of E_x polarization in Figure 9(a) are much smaller than those of E_y polarization in Figure 9(b).

Figure 10 shows how the light intensity changes with different radii of curvature. For each change, the flare angle, length, and gap separation of the aperture nanoantenna

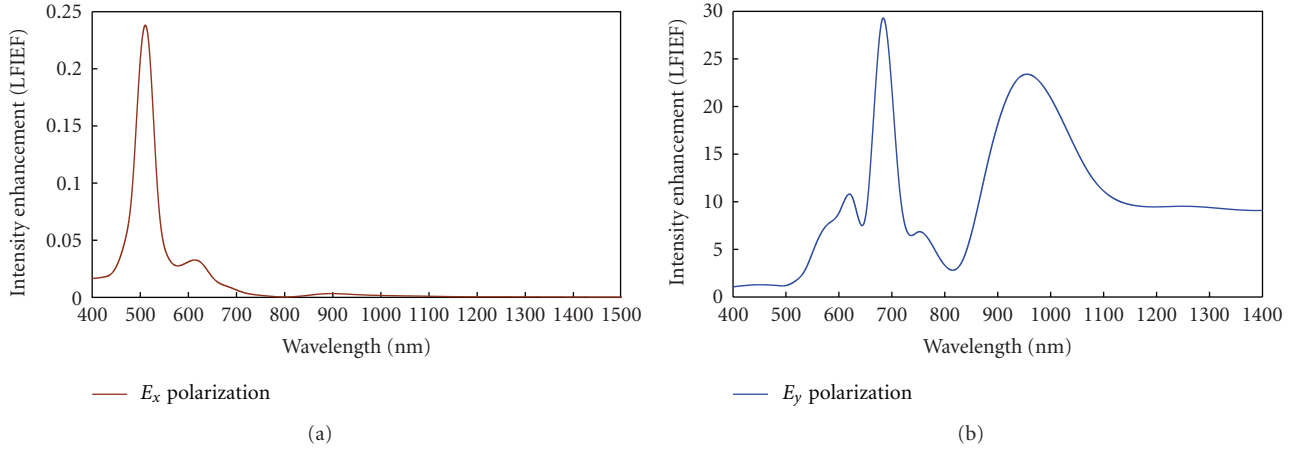


FIGURE 9: Light intensity as a function of incident wavelength for bowtie aperture nanoantenna different excitations. E_x polarization in (a) and E_y polarization in (b) at tip radius 30 nm, gap 20 nm, antenna length 240 nm, and flare angle 60° .

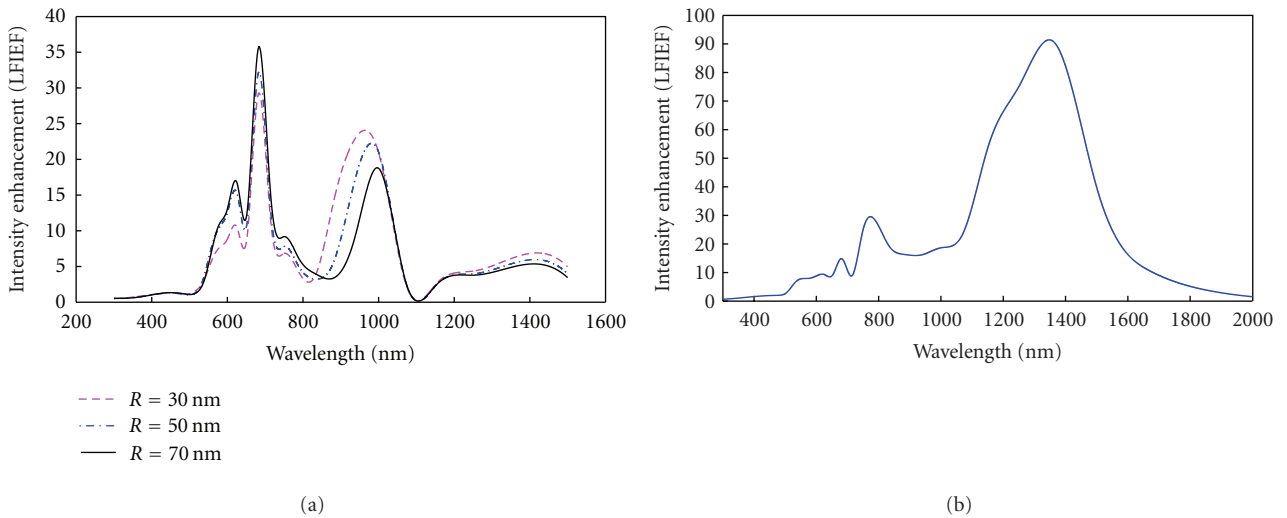


FIGURE 10: Light intensity enhancement as a function of incident wavelength for gold bowtie shaped aperture nanoantenna under different radii of curvature of nanoapertures.

are 60° , 240 nm, and 20 nm, respectively. From Figure 10, it can be observed that as R becomes smaller from 70 nm to 30 nm (i.e., the apex of the nanoaperture becomes sharper), the light intensity at both resonances turns higher at the second mode and the resonances move toward greater wavelength side, which means a red shift in the spectrum. As a result, if stronger enhancement is needed the bowtie aperture nanoantenna can be designed with appropriately sharper tip to meet such a requirement as shown in Figure 10(b), for the following design parameters $R = 20$ nm, $g = 20$ nm, $\alpha = 30^\circ$, $L = 240$ nm, and substrate refractive index $= 1.46$. From Figure 10(b), the stronger enhancement is observed and larger than in Figure 10(a) about three times.

In the far-field computation, the field patterns in the E -plane and H -plane of are plotted in Figures 11(a) and 11(b) for the bowtie-shaped aperture nanoantenna with a radius 30 nm of curvature and a flare angle of 60° at a wavelength of 500 nm (600 THZ). The patterns of the nanoantenna imply that a good directivity is achievable by the bowtie aperture.

From Figure 11, it is found that the half power bandwidths obtained are 37.5 and 54.1 in both planes, respectively. The following approximation formulation for a directional pattern is used [43]:

$$D_0 = \frac{41253}{(\Theta_{1d}\Theta_{2d})}, \tag{1}$$

where Θ_{1d} and Θ_{2d} stand for the half power bandwidths in degrees in two respective perpendicular planes. The directivity calculated is 20.334, equivalent to 13.1 dB. In the same fashion, the gain for antenna satisfies the following empirical equation [43]:

$$G_0 = \frac{30000}{(\Theta_{1d}\Theta_{2d})}. \tag{2}$$

From (2), the gain of nanoantenna calculated is 11.7 dB. It should be noted that the directivity is obtained by the formula based on some approximations. Equation (1)

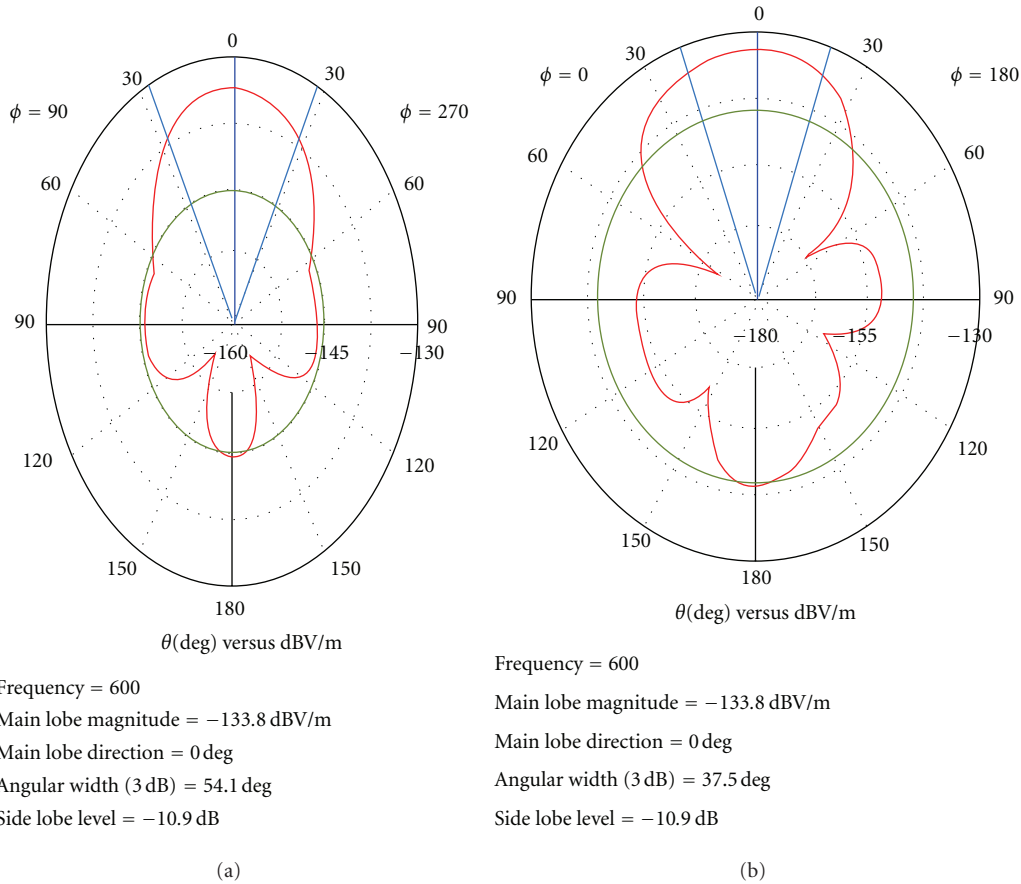


FIGURE 11: Field pattern of bowtie-shaped aperture nanoantenna. (a) *E*-plane. (b) *H*-plane (frequency in THZ).

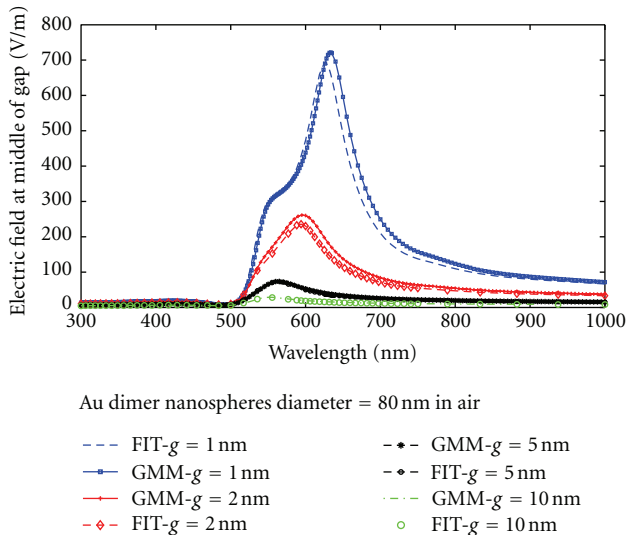


FIGURE 12: Comparison of electric field spectra calculated in middle of the gap using the FIT and GMM for various gaps of gold dimer nanoantenna in air.

suggests one narrow major lobe and very negligible minor lobes. Hence, it might be not adequately exact in our case with larger side lobes. Even so, the results could serve as a fair reference for nanoantenna designs.

3. Validity of FIT

As a numerical method, it is necessary to judge and review the validity of the FIT method before its application in optical nanoantenna. For this purpose, we performed FIT simulations for gold dimer nanospheres with diameter 80 nm in air surrounding medium and compared the results with exact solution generalized Mie method (GMM) [50–52] calculations for the same system. The results are shown in Figure 12, we observe an exact correspondence between the two models for the gaps width that are 5 nm and 10 nm, respectively. From Figure 12 at gap width 1 nm and nanospheres diameter 80 nm, the peak of electric field is 720 V/m as published in the papers [35, 53] and the resonance wavelength 634 nm.

4. Conclusion

In this paper, we investigate plasmonic gold dimer bowtie and bowtie aperture nanoantennas, with particular emphasis on near-field resonances and far-field radiation properties. Such properties have been explored numerically in detail based on the FIT algorithm. It is found that this antenna can exhibit a resonant behavior in the optical and near-infrared regions. In addition, SPR resonances can occur at different positions, depending on the polarization directions of incident light, refractive index of surrounding medium,

substrate, and geometric parameters of the nanoantenna (length, gap width, and shapes). Polarization along antenna axis can give better efficiency of enhancement in dimer sphere and bowtie nanoantenna, in contrast to bowtie aperture nanoantenna, where the enhancement field occurred in the direction of minor axis of the antenna (y -polarization) as explained previously. Moreover, the field enhancement produced is related to the geometric parameters including the radius of nanospheres, tip radius, and the gap width between the nanoparticles. A nanoantenna with a smaller gap supports higher light intensity at resonance and red-shifts the resonances at the same time. The results of this paper should be useful for choosing the best suited antenna geometry for a given application.

References

- [1] L. Novotny and B. Hecht, *Principles Of Nano-Optics*, Cambridge University Press, 1st edition, 2006.
- [2] D. P. Fromm, A. Sundaramurthy, P. James Schuck, G. Kino, and W. E. Moerner, "Gap-dependent optical coupling of single "bowtie" nanoantennas resonant in the visible," *Nano Letters*, vol. 4, no. 5, pp. 957–961, 2004.
- [3] P. Mühlischlegel, H. J. Eisler, O. J. F. Martin, B. Hecht, and D. W. Pohl, "Resonant optical antennas," *Science*, vol. 308, no. 5728, pp. 1607–1609, 2005.
- [4] S. Nie and S. R. Emory, "Probing single molecules and single nanoparticles by surface-enhanced Raman scattering," *Science*, vol. 275, no. 5303, pp. 1102–1106, 1997.
- [5] K. Kneipp, Y. Wang, H. Kneipp et al., "Single molecule detection using surface-enhanced Raman scattering (SERS)," *Physical Review Letters*, vol. 78, no. 9, pp. 1667–1670, 1997.
- [6] H. Xu, E. J. Bjerneld, M. Käll, and L. Börjesson, "Spectroscopy of single hemoglobin molecules by surface enhanced Raman scattering," *Physical Review Letters*, vol. 83, no. 21, pp. 4357–4360, 1999.
- [7] N. Félidj, J. Aubard, G. Lévi et al., "Optimized surface-enhanced Raman scattering on gold nanoparticle arrays," *Applied Physics Letters*, vol. 82, no. 18, pp. 3095–3097, 2003.
- [8] W. Zhang, X. Cui, B. S. Yeo, T. Schmid, C. Hafner, and R. Zenobi, "Nanoscale roughness on metal surfaces can increase tip-enhanced raman scattering by an order of magnitude," *Nano Letters*, vol. 7, no. 5, pp. 1401–1405, 2007.
- [9] L. Rogobete, F. Kaminski, M. Agio, and V. Sandoghdar, "Design of plasmonic nanoantennae for enhancing spontaneous emission," *Optics Letters*, vol. 32, no. 12, pp. 1623–1625, 2007.
- [10] T. H. Taminiau, F. D. Stefani, F. B. Segerink, and N. F. Van Hulst, "Optical antennas direct single-molecule emission," *Nature Photonics*, vol. 2, no. 4, pp. 234–237, 2008.
- [11] S. Kuhn, U. Hakanson, L. Rogobete, and V. Sandoghdar, "Enhancement of single-molecule fluorescence using a gold nanoparticle as an optical nanoantenna," *Physical Review Letters*, vol. 96, 4 pages, 2006.
- [12] T. H. Taminiau, R. J. Moerland, F. B. Segerink, L. Kuipers, and N. F. Van Hulst, " $\lambda/4$ resonance of an optical monopole antenna probed by single molecule fluorescence," *Nano Letters*, vol. 7, no. 1, pp. 28–33, 2007.
- [13] P. Bharadwaj and L. Novotny, "Spectral dependence of single molecule fluorescence enhancement," *Optics Express*, vol. 15, no. 21, pp. 14266–14274, 2007.
- [14] F. Tam, G. P. Goodrich, B. R. Johnson, and N. J. Halas, "Plasmonic enhancement of molecular fluorescence," *Nano Letters*, vol. 7, no. 2, pp. 496–501, 2007.
- [15] K. B. Crozier, A. Sundaramurthy, G. S. Kino, and C. F. Quate, "Optical antennas: resonators for local field enhancement," *Journal of Applied Physics*, vol. 94, no. 7, pp. 4632–4642, 2003.
- [16] A. Sundaramurthy, K. B. Crozier, G. S. Kino, D. P. Fromm, P. J. Schuck, and W. E. Moerner, "Field enhancement and gap-dependent resonance in a system of two opposing tip-to-tip Au nanotriangles," *Physical Review B*, vol. 72, no. 16, Article ID 165409, 6 pages, 2005.
- [17] A. Sundaramurthy, P. J. Schuck, N. R. Conley, D. P. Fromm, G. S. Kino, and W. E. Moerner, "Toward nanometer-scale optical photolithography: utilizing the near-field of bowtie optical nanoantennas," *Nano Letters*, vol. 6, no. 3, pp. 355–360, 2006.
- [18] D. P. Fromm, A. Sundaramurthy, A. Kinkhabwala, P. J. Schuck, G. S. Kino, and W. E. Moerner, "Exploring the chemical enhancement for surface-enhanced Raman scattering with Au bowtie nanoantennas," *The Journal of chemical physics*, vol. 124, no. 6, Article ID 061101, 4 pages, 2006.
- [19] P. J. Schuck, D. P. Fromm, A. Sundaramurthy, G. S. Kino, and W. E. Moerner, "Improving the mismatch between light and nanoscale objects with gold bowtie nanoantennas," *Physical Review Letters*, vol. 94, no. 1, Article ID 017402, 4 pages, 2005.
- [20] J. N. Farahani, D. W. Pohl, H. J. Eisler, and B. Hecht, "Single quantum dot coupled to a scanning optical antenna: a tunable superemitter," *Physical Review Letters*, vol. 95, no. 1, Article ID 017402, 4 pages, 2005.
- [21] J. N. Farahani, H. J. Eisler, D. W. Pohl et al., "Bow-tie optical antenna probes for single-emitter scanning near-field optical microscopy," *Nanotechnology*, vol. 18, no. 12, Article ID 125506, 2007.
- [22] B. Hecht, P. Mühlischlegel, J. N. Farahani et al., "Prospects of resonant optical antennas for nano-analysis," *Chimia*, vol. 60, no. 11, pp. A765–A769, 2006.
- [23] R. D. Grober, R. J. Schoelkopf, and D. E. Prober, "Optical antenna: towards a unity efficiency near-field optical probe," *Applied Physics Letters*, vol. 70, no. 11, pp. 1354–1356, 1997.
- [24] J. Alda, J. M. Rico-García, J. M. López-Alonso, and G. Boreman, "Optical antennas for nano-photon applications," *Nanotechnology*, vol. 16, no. 5, pp. S230–S234, 2005.
- [25] F. J. González, B. Ilic, J. Aida, and G. D. Boreman, "Antenna-coupled infrared detectors for imaging applications," *IEEE Journal on Selected Topics in Quantum Electronics*, vol. 11, no. 1, pp. 117–120, 2005.
- [26] K. Kneipp, H. Kneipp, I. Itzkan, R. R. Dasari, and M. S. Feld, "Ultrasensitive chemical analysis by Raman spectroscopy," *Chemical Reviews*, vol. 99, no. 10, pp. 2957–2975, 1999.
- [27] D. Enders, S. Rupp, A. Küller, and A. Pucci, "Surface enhanced infrared absorption on Au nanoparticle films deposited on SiO₂/Si for optical biosensing: detection of the antibody-antigen reaction," *Surface Science*, vol. 600, no. 23, pp. L305–L308, 2006.
- [28] X. Huang, I. H. El-Sayed, W. Qian, and M. A. El-Sayed, "Cancer cells assemble and align gold nanorods conjugated to antibodies to produce highly enhanced, sharp, and polarized surface Raman spectra: a potential cancer diagnostic marker," *Nano Letters*, vol. 7, no. 6, pp. 1591–1597, 2007.
- [29] L. J. Steven, S. Ravikant, and C. Niloy, "Rapid spectral analysis for spectral imaging," *Biomedical Optics Express*, vol. 1, pp. 157–164, 2010.
- [30] S. Pillai, K. R. Catchpole, T. Trupke, G. Zhang, J. Zhao, and M. A. Green, "Enhanced emission from Si-based light-emitting

- diodes using surface plasmons,” *Applied Physics Letters*, vol. 88, Article ID 161102, 3 pages, 2006.
- [31] P. Anger, P. Bharadwaj, and L. Novotny, “Enhancement and quenching of single-molecule fluorescence,” *Physical Review Letters*, vol. 96, Article ID 113002, 4 pages, 2006.
- [32] M. Danckwerts and L. Novotny, “Optical frequency mixing at coupled gold nanoparticles,” *Physical Review Letters*, vol. 98, Article ID 026104, 4 pages, 2007.
- [33] Y. M. Wu, L. W. Li, and B. Liu, “Gold bow-tie shaped aperture nanoantenna: wide band near-field resonance and far-field radiation,” *IEEE Transactions on Magnetics*, vol. 46, no. 6, pp. 1918–1921, 2010.
- [34] K. J. Ooi, P. Bai, M. X. Gu, and L. K. Ang, “Design of a monopole-antenna-based resonant nanocavity for detection of optical power from hybrid plasmonic waveguides,” *Optics Express*, vol. 19, no. 18, pp. 17075–17085, 2011.
- [35] C. S. T. Microwave Studio, 2011, <http://www.cst.com/>.
- [36] E. Tatartschuk, E. Shamonina, and L. Solymar, “Plasmonic excitations in metallic nanoparticles: resonances, dispersion characteristics and near-field patterns,” *Optics Express*, vol. 17, no. 10, pp. 8447–8460, 2009.
- [37] T. H. Taminiau, F. B. Segerink, and N. F. van Hulst, “A monopole antenna at optical frequencies: single-molecule near-field measurements,” *IEEE Transactions on Antennas and Propagation*, vol. 55, no. 11 I, pp. 3010–3017, 2007.
- [38] A. E. Miroshnichenko, I. S. Maksymov, A. R. Davoyan, C. Simovski, P. Belov, and Y. S. Kivshar, “An arrayed nanoantenna for broadband light emission and detection,” *Physica Status Solidi*, vol. 5, no. 11 I, pp. 347–349, 2011.
- [39] T. Weiland, “A discretization method for the solution of maxwell’s equations for six-component fields,” *AEU-Archiv für Elektronik und Übertragungstechnik*, vol. 31, no. 3, pp. 116–120, 1977.
- [40] T. H. Taminiau, R. J. Moerland, F. B. Segerink, L. Kuipers, and N. F. Van Hulst, “Enhanced directional excitation and emission of single emitters by a nano-optical Yagi-Uda antenna,” *Optics Express*, vol. 16, no. 14, pp. 16858–16866, 2008.
- [41] P. B. Johnson and R. W. Christy, “Optical constants of the noble metals,” *Physical Review B*, vol. 6, Article ID 4370, 1972.
- [42] E. Palik, *Handbook of Optical Constants of Solids*, vol. 1, Academic, New York, NY, USA, 1985.
- [43] C. A. Balanis, *Antenna Theory: Analysis and Design*, Wiley-Interscience, Hoboken, NJ, USA, 2005.
- [44] L. Novotny, “Effective wavelength scaling for optical antennas,” *Physical Review Letters*, vol. 98, Article ID 266802, 4 pages, 2007.
- [45] X. Shi, L. Hesselink, and R. L. Thornton, “Ultrahigh light transmission through a C-shaped nanoaperture,” *Optics Letters*, vol. 28, no. 15, pp. 1320–1322, 2003.
- [46] C. Li, G. W. Kattawar, P. W. Zhai, and P. Yang, “Electric and magnetic energy density distributions inside and outside dielectric particles illuminated by a plane electromagnetic wave,” *Optics Express*, vol. 13, no. 12, pp. 4554–4559, 2005.
- [47] Z. Chen, X. Li, A. Taflove, and V. Backman, “Backscattering enhancement of light by nanoparticles positioned in localized optical intensity peaks,” *Applied Optics*, vol. 45, no. 4, pp. 633–638, 2006.
- [48] D. A. Genov, A. K. Sarychev, V. M. Shalaev, and A. Wei, “Resonant Field Enhancements from Metal Nanoparticle Arrays,” *Nano Letters*, vol. 4, no. 1, pp. 153–158, 2004.
- [49] L. Wang, S. M. Uppuluri, E. X. Jin, and X. Xu, “Nanolithography using high transmission nanoscale bowtie apertures,” *Nano Letters*, vol. 6, no. 3, pp. 361–364, 2006.
- [50] A. Bek, R. Jansen, M. Ringle, S. Mayilo, T. A. Klar, and J. Feldmann, “Fluorescence enhancement in hot spots of AFM-designed gold nanoparticle sandwiches,” *Nano Letters*, vol. 8, no. 2, pp. 485–490, 2008.
- [51] M. Ringle, A. Schwemer, M. Wunderlich et al., “Shaping emission spectra of fluorescent molecules with single plasmonic nanoresonators,” *Physical Review Letters*, vol. 100, no. 20, Article ID 203002, 2008.
- [52] L. Liu, B. Wang, X. Cao, X. Xu, and Y. Wang, “Comparison investigation of near- and far-field properties for plasmon resonance of silver nanosphere dimers,” *Photonics and Nanostructures*, vol. 10, no. 1, pp. 16–24, 2011.
- [53] J. Hoffman, C. Hafner, P. Leidenberger, J. Hesselbarth, and S. Burger, “Comparison of electromagnetic field solvers for the 3D analysis of plasmonic nano antennas,” in *Modeling Aspects in Optical Metrology II*, vol. 7390 of *Proceedings of the SPIE*, 2009.

Research Article

Quantitative Comparison of Five Different Photosensitizers for Use in a Photopolymer

Yue Qi,¹ Michael R. Gleeson,² Jinxin Guo,¹ Sergi Gallego,³ and John T. Sheridan¹

¹ School of Electrical, Electronic, and Communications Engineering, Communications and Optoelectronic Research Centre, The SFI-Strategic Research Cluster in Solar Energy Conversion, College of Engineering and Architecture, University College Dublin, Belfield, Dublin 4, Ireland

² Department of Computer Science, NUIM, Maynooth, Kildare, Ireland

³ Departamento de Física, Ingeniería de Sistemas y Teoría de la Señal, Universidad de Alicante, Apartado 99, 03080 Alicante, Spain

Correspondence should be addressed to John T. Sheridan, john.sheridan@ucd.ie

Received 2 May 2012; Accepted 19 July 2012

Academic Editor: Yasuo Tomita

Copyright © 2012 Yue Qi et al. This is an open access article distributed under the Creative Commons Attribution License, which permits unrestricted use, distribution, and reproduction in any medium, provided the original work is properly cited.

Several studies of the time varying photon absorption effects, which occur during the photoinitiation process involving in photopolymer materials, have been presented. Three primary mechanisms have been identified: (i) the dye absorption, (ii) recovery, and (iii) bleaching. Based on an analysis of these mechanisms, the production of primary radicals can be physically described and modelled. In free radical photopolymerization systems, the excited dye molecules induce the production of the primary radicals, R^* , which are key in determining how many monomers are polymerized. This, in turn, is closely related to the refractive index modulation formed during holographic recording. In this paper, to avoid the complexities involved in estimating the rate constant of intersystem crossing, k_{st} , in going from the excited singlet state dye to the excited triplet state dye, we introduce two rates, k_{aS} and k_{aT} these are the proposed rate constants of photon absorption in going from the ground state to the singlet and triplet states, respectively. Using the resulting model, four kinds of Xanthene dyes: Erythrosin B; Eosin Y; Phloxine B, Rose Bengal, and one Thiazine dye: Methylene Blue, are experimentally characterised for use in an AA/PVA photopolymer.

1. Introduction

Photopolymer materials and the photochemical kinetics associated with them [1–3] are being actively studied for practical applications [4–8] such as 3D hybrid optoelectronic circuits, holographic storage [9–13], photoembossing (including the manufacturing of refractive and diffractive optical elements), metrology, 3D displays, and the self-trapping of light [14].

During the photopolymerisation process, the initial step, which involves the absorption of light by a dye, eventually results in the generation of radicals, and this initiation process plays a critical role in grating formation. The theoretical model of the photochemical processes has been developed to include the effects of photosensitizer recovery and bleaching [15–18], in order to permit the accurate prediction of the resulting material behaviour.

In a previous model of this material, in order to simplify the modelling of intersystem crossing from the excited singlet state dye to the excited triplet state dye, a bulk parameter Ψ was introduced [18]. It was assumed that during exposure a constant fraction Ψ of the ground state molecules present was always available to be converted into the singlet state, while $(1 - \Psi)$ of them are available to be converted into the triplet excited state. In [19], a more physical representation of intersystem crossing, occurring at a rate constant, k_{st} , was introduced, but this rate is difficult to estimate by the method described in [19] in that the monomer will be quickly crystallised when triethanolamine is not included in the layer. In order to overcome the limitations of these models, in this paper, we simplify our approach by introducing two new rates, k_{aS} and k_{aT} , into the model, which are the rate constant of photon absorption from ground state to singlet state and triplet state, respectively. Then using this simplified

model, the behaviours of five different photosensitizers, in an acrylamide polyvinyl alcohol (AA/PVA) photopolymer material, are studied. Detailed experimental and theoretical analyses are presented.

The paper is organized as follows. In Section 2, we introduce the photochemical reactions that take place and the NPDD model, including descriptions of the processes of initiation, propagation, termination, and inhibition. In Section 3, the material preparation is presented. In Section 4, the photoabsorptive behaviours of four green-sensitive types photosensitizer: Erythrosine B (EB); Eosin Y (EY); Phloxine B (PB), Rose Bengal (RB), of the same molarity in equivalent PVA/AA layers, and one red-sensitive photosensitizer, Methylene Blue (MB), of a higher molarity (due to the weaker absorptivity at the wavelength of 633 nm), also in a PVA/AA layer, are experimentally examined. Based on these results, the recovery and bleaching behaviours of these dyes are also estimated. In Section 5, physical parameter values extracted by fitting the measured results using our model are presented and analysed. Finally, in Section 6, a brief conclusion is given.

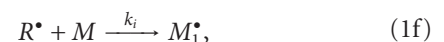
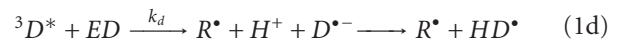
2. Theoretical Analysis of Photopolymer Material

In free radical photopolymerization systems, the excited dye molecules induce the production of the primary radicals, R^\bullet the concentration of which is key in determining how much monomers are polymerized. This, in turn, is closely related to the refractive index modulation formed during holographic recording.

In this paper, nonlocal photopolymerization driven diffusion (NPDD) model is developed. This model includes the effects of (a) the kinetics of the major photochemical processes; (b) the temporally and spatially varying photon absorption; (c) the nonlocal material response.

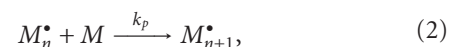
2.1. Photochemical Reactions. In the case of free radical photopolymerization systems, the kinetic model describing what takes place involves four main processes [2, 16, 20–23], (I) initiation, (II) propagation, (III) termination, and (IV) Inhibition. We note that each may involve several physicochemical reactions. We highlight the major chemical reactions in each process [3, 20, 24–27]. A summary of the discussion in this section is given in the flow chart in Figure 1. The excitation of the Xanthenes dyes is similar and is due to the breaking up of the C=O double bond when exposed to the green beam [28]. Since the structure of Methylene Blue is different from the Xanthene dye, the excitation is also different, that is, due to the breaking up of the C=N bond when exposed to the red beam [29]. However the reactions between Methylene Blue and the electron donor are similar to the case of Xanthenes dyes. The detailed chemical scheme of the photopolymerisation is described in [20, 28, 29]. The reactions highlighted within the dashed box will be studied experimentally in Section 4. In particular the introduction of k_{aS} and k_{aT} should be noted when comparing this model to previous models.

(I) *Initiation.* During illumination, the reaction between the photosensitiser and the electron donor (coinitiator) leads to the production of initiator radicals, R^\bullet , which can react with the monomers to produce chain initiators, M_1^\bullet .



where D represents the photosensitizer molecule, $h\nu$ indicates the energy absorbed from a photon, $k_{aS} = \varphi_S \times \varepsilon \times d \times I_0'$, $k_{aT} = \varphi_T \times \varepsilon \times d \times I_0'$ (φ_S and φ_T are the quantum efficiencies of the reactions in which the ground state dye is converted into the singlet ${}^1D^*$ and triplet ${}^3D^*$ dye states, ε is the dye molar absorptivity, d is the thickness of the layer, and I_0' Einstein's/cm³ s is the incident intensity [27]) are the rate constants of photon absorption in ground state, k_r is the recovery rate of the dye from singlet excited state to ground state, including the processes of (1) radiationless energy transfer to another molecule such as triethanolamine which acts as an electron donor (ED), (2) the emission of a photon by fluorescence [16, 18]. The recovery of triplet state dye is ignored for simplicity and also due to the even lower recovery rate in this process [18, 19], ED is the electron donor, and k_d is the rate constant of electron donation through which ED becomes a free radical, R^\bullet , HD^\bullet represents a radicalized dye, which abstracted a hydrogen ion from the electron donor, k_b is the rate constant of the photobleaching process, that is, the rate formation of dihydro dye, H_2D , ED_{int} is an intermediate form of the electron donor, k_i is the chain initiation kinetic constant, and M represents a monomer molecule. We note that (1a) and (1b) are new differing from the models proposed in [18, 19].

(II) *Propagation.* The chain initiator, M_1^\bullet will attach itself to another monomer molecule, M , by addition to the C=C bond yielding a growing polymer radical with an active tip. Through propagation polymer chain growth then follows [20].



where k_p is the rate constant of propagation and M_n^\bullet and M_{n+1}^\bullet are the growing macroradical chains of length n and $(n+1)$ repeat monomeric units ($n \geq 1$).

(III) *Termination.* Termination can occur in three ways. Two of these, disproportionation and combination, involve two

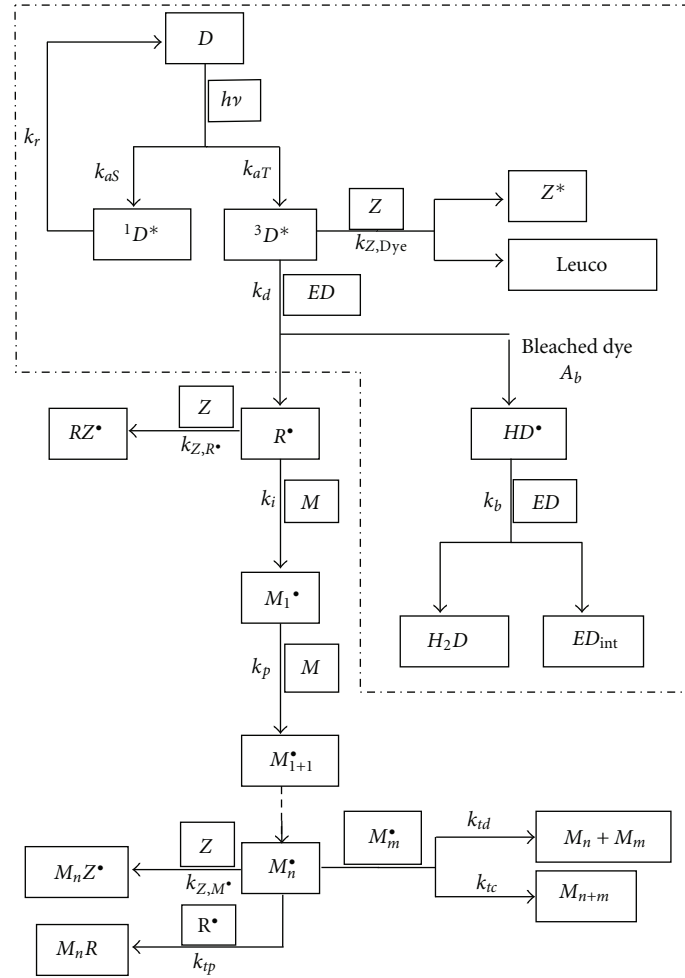
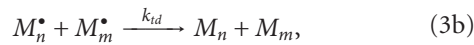


FIGURE 1: Flow chart of the photochemical process [16]. We note that the introduction of k_{aS} and k_{aT} is new. (All the parameters and variables are defined in the analysis in the text.)

growing macroradicals interacting, that is, the bimolecular termination mechanism.



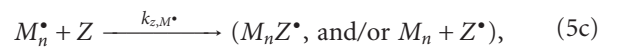
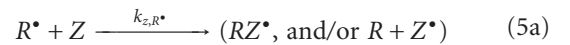
where k_{ic} and k_{td} are the rate constants of combination and disproportionation termination respectively. M_n^\bullet , M_m^\bullet , and M_{m+n}^\bullet represent terminated chains which have no radical tip, that is, a dead polymer. In this analysis, k_{ic} and k_{td} will be treated as a single lumped rate constant, $k_t = k_{ic} + k_{td}$ ($\text{cm}^3 \text{mol}^{-1} \text{s}^{-1}$), as the mode of termination does not effect the polymerization kinetics [25].

A third possible termination mechanism involves primary radical termination [19, 26].



where k_{ip} is the rate constant of primary radical termination. In this step, a growing macroradical chain reacts with a primary radical (initiator radical) leading once again to the production of inactive or dead polymer chains [25].

(IV) *Inhibition*. Inhibitors are chemicals which react with the initiating and propagating radical species by rapidly removing or scavenging these radicals. Polymerization is completely halted until they are all consumed [24]. Several possible inhibitor reaction mechanisms are listed in the following:



where Z is the inhibitor species, for example, oxygen, ${}^3D^*$ is the excited photosensitizer, Z^* is the concentration of singlet oxygen [21, 24, 27], and k_{z,R^\bullet} , k_{z,Dye^*} and k_{z,M^\bullet} are the rate constants of inhibition of the primary radicals [15–17, 21, 30], the photosensitizer and the macroradicals respectively. Inhibition leads to a dead band at the start of exposure, that is, stopping grating formation during the initial exposure. The effects of inhibitors are especially significant when lower exposure energies (dose) are used, for example, when large

areas must be exposed (low intensities) or short duration exposures must be used [27].

2.2. Inclusion in the NPDD Model. Based on the analysis present above and summarised in Figure 1, a set of coupled differential equations representing the spatial and temporal evolutions of the material concentrations associated with (1a)–(5c) can be derived using the same notation and following the same methodology as in references [24–26].

$$\frac{dD(x,t)}{dt} = k_r^1 D^*(x,t) - k_{aS}D(x,t) - k_{aT}D(x,t), \quad (6)$$

$$\frac{d^1 D^*(x,t)}{dt} = k_{aS}D(x,t) - k_r^1 D^*(x,t),$$

$$\begin{aligned} \frac{d^3 D^*(x,t)}{dt} &= k_{aT}D(x,t) - k_d^3 D^*(x,t)ED(x,t) \\ &\quad - k_{z,Dye^*}^3 D^*(x,t)Z(x,t), \end{aligned}$$

$$\frac{dED(x,t)}{dt} = -k_d^3 D^*(x,t)ED(x,t) - k_b ED(x,t)HD^*(x,t), \quad (7)$$

$$\begin{aligned} \frac{dR^*(x,t)}{dt} &= k_d^3 D^*(x,t)ED(x,t) - k_i R^*(x,t)u(x,t) \\ &\quad - k_{tp} M^*(x,t)R^*(x,t) - k_{z,R} R^*(x,t)Z(x,t), \end{aligned} \quad (8)$$

$$\frac{dHD^*(x,t)}{dt} = k_d^3 D^*(x,t)ED(x,t) - k_b ED(x,t)HD^*(x,t) \quad (9)$$

$$\begin{aligned} \frac{du(x,t)}{dt} &= \frac{d}{dx} \left[D_m(x,t) \frac{du(x,t)}{dx} \right] - k_i R^*(x,t)u(x,t) \\ &\quad - \int_{-\infty}^{\infty} k_p M^*(x',t)u(x',t)G(x,x')dx', \end{aligned} \quad (10)$$

$$\begin{aligned} \frac{dN(x,t)}{dt} &= \int_{-\infty}^{\infty} k_p M^*(x',t)u(x',t)G(x,x')dx' \\ &\quad - \frac{d}{dx} \left[D_N(x,t) \frac{dN(x,t)}{dx} \right], \end{aligned}$$

$$\begin{aligned} \frac{dM^*(x,t)}{dt} &= k_i R^*(x,t)u(x,t) - k_t [M^*(x,t)]^2 \\ &\quad - k_{tp} M^*(x,t)R^*(x,t) - k_{z,M} M^*(x,t)Z(x,t), \end{aligned}$$

$$\begin{aligned} \frac{dZ(x,t)}{dt} &= \frac{d}{dx} \left[D_z \frac{dZ(x,t)}{dx} \right] - k_{z,Dye^*}^3 D^*(x,t)Z(x,t) \\ &\quad - k_{z,R} R^*(x,t)Z(x,t) - k_{z,M} M^*(x,t)Z(x,t), \end{aligned} \quad (11)$$

where $u(x,t)$, $N(x,t)$, and $M^*(x,t)$ are the concentrations of free-monomer, polymer, and macroradical. $D_m(x,t)$, $D_N(x,t)$, and D_z are the diffusion rates of monomer, polymer, and inhibitor respectively. Equation (6) arises due to the new proposed reactions in (1a) and (1b). Furthermore,

TABLE 1: Composition of AA/PVA photopolymer material.

Component	Function	Amount per 100 ml
Poly-vinylalcohol (PVA)	Binder	70 cm ³ of 10% sol.
Acrylamide (AA)	Monomer	2.4 g
Bis-acrylamide	Cross-linker	0.8 g
Xanthene dyes/Methylene Blue	Dye	16 cm ³ of 1.25 × 10 ⁻⁴ M for Xanthene dyes and 16 cm ³ of 2 × 10 ⁻⁴ M for Methylene Blue
Triethanolamine (TEA)	Electron Donor (ED)	8 cm ³

we note that a rate equation governing the total bleached photosensitizer concentration can be obtained:

$$\frac{dA_b(x,t)}{dt} = k_{z,Dye^*}^3 D^*(x,t)Z(x,t) + k_b ED(x,t)HD^*(x,t), \quad (12)$$

where A_b denotes the total (leuco and dihydro) bleached photosensitizer concentration [19]. (see Figure 1).

In (10), $G(x,x')$ is the nonlocal material spatial response function given by [24]:

$$G(x,x') = \frac{1}{\sqrt{2\pi\sigma}} \exp \left[\frac{-(x-x')^2}{2\sigma} \right], \quad (13)$$

in which σ is the constant nonlocal response parameter [20, 31]. The nonlocal spatial response function represents the effect of initiation at a location x' on the amount of monomer polymerized at location x [31].

2.3. Summary. In this section, we have shown how the new dye model can be included in the NPDD model, in which the processes of initiation, propagation, termination and inhibition are included. A method to overcome the limitations of the use of the parameter Ψ in [18] and the intersystem crossing rate constant in the previous model [19] is presented. We introduce k_{aS} and k_{aT} into the model equations (1a) and (1b), which are the rate constant of photon absorption from ground state to singlet state and triplet state respectively. This leads to the coupled differential equation (6). This new model simplifies the modelling and data fitting of the experimental data in Section 4.

3. Material Preparation

Photopolymer materials are made sensitive to a particular wavelength using photosensitizing dye. The photosensitisers examined in this paper are that is, Xanthene dyes Erythrosin B (EB), Eosin Y (EY), Phloxine B (PB) and Rose Bengal (RB). These allow holographic recording to be carried out using a 532 nm Solid-State Crystal Laser. We have also sensitized our AA/PVA material in the red (HeNe 633 nm) using Methylene Blue (MB), which is a Thiazine dye.

Our PVA/AA material was made using the components listed in Table 1. The material was prepared as follows:

- (a) 10 g of PVA was added to 100 cm³ of deionised water and dissolved using a heater/stirrer. This solution is then allowed to cool and then 70 cm³ of this solution was transferred into a beaker.
- (b) 8 cm³ of Triethanolamine (ED) was added to the PVA solution and stirred thoroughly.
- (c) 2.4 g of Acrylamide and 0.8 g of Bis-acrylamide were added to the PVA solution under a fume cupboard and stirred until completely dissolved.
- (d) 16 cm³ of 1.25×10^{-4} M Xanthene dye (EB/EY/FB/RB) or 16 cm³ of 2×10^{-4} M Methylene Blue (MB) was then added to the beaker. As indicated in Section 1, a higher concentration of MB is used due to its weaker absorptivity at the wavelength of 633 nm. This step and subsequent steps were carried out under a safety light, as the material is now sensitive to green/red light.
- (e) The solution is then made up to 100 cm³ in a volumetric flask with de-ionised water.
- (f) The solution is then stored in the dark ready for plate preparation.

To prepare dry material layers for holographic exposure the solution prepared above is used as follows:

- (a) The microscope glass slice on which the material is to be deposited (75 mm × 25 mm) is cleaned thoroughly using de-ionised water and Acetone. Once cleaned the plates are placed on a level surface so that the photopolymer layers would adhere to the glass evenly, producing a layer of uniform thickness.
- (b) 1.3–1.4 mLs of the photopolymer solution is then deposited evenly over the area of the glass plate using a syringe.
- (c) Using this method the typical material thickness is 100 ± 10 microns. Different thicknesses can be obtained by depositing (drop casting) different quantities of material. The thickness and uniformity of these layers can be measured using a micrometer screw gauge.
- (d) The plates are then left in the dark for approximately 24 hours until dry. Drying times are dependent on the thickness of the material and the relative humidity.

4. Behaviors of the Five Photosensitizers in AA/PVA

4.1. Transmission Spectra. The dyes examined absorb light and act as photoinitiator, of the polymerization process. Figure 2 shows the transmittance of the four Xanthenes dyes, that is. EB, EY, PB, and RB over a range of visible wavelength.

The normalized transmittance $T(t)$ can be expressed as:

$$T(t) = T_{sf} \exp[-\varepsilon A(t)d], \quad (14)$$

where T_{sf} is the transmission fraction which corrects for the boundary and scatter losses, ε is the molar absorption of the

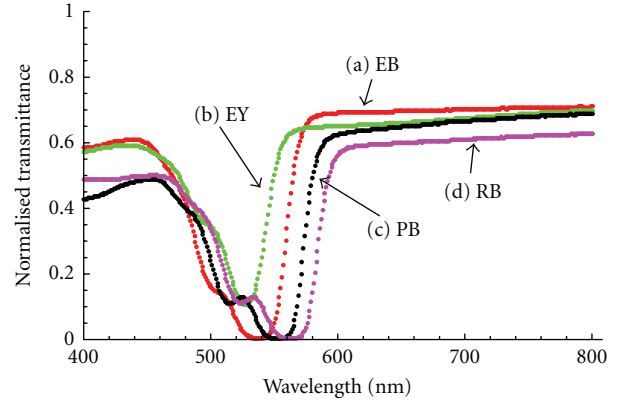


FIGURE 2: Spectrum for four different photosensitizers (a) EB (red curve), (b) EY (green curve), (c) PB (black curve), and (d) RB (pink curve) in AA/PVA photopolymer material.

dye, $A(t)$ is the time varying dye concentration, and d is the thickness of the material layer. Taking $t = 0$, (14) reduces to:

$$T_0 = T_{sf} \exp[-\varepsilon A_0 d], \quad (15)$$

where T_0 is the transmittance value for one particular wavelength, λ , $T_0(\lambda)$ is presented in Figure 2, for an initial dye concentration $A_0 = 1.22 \times 10^{-6}$ mol/cm³. We define T_{sf} to be the maximum transmittance value. Using this maximum value the molar absorption, ε , for a wavelength of $\lambda = 532$ nm, that is, the exposing wavelength in all the following experiments, can be estimated.

We also note that the transmittance at a wavelength of 633 nm, for all the dyes is over 59%, taking into account the increased scatter as a result of the crystallisation of the monomer with the time for this case and the thicker thickness of the layer, this means that 633 nm laser light can be used as the probe beam during recording. The resulting parameter values estimated are listed in Tables 2 and 3.

4.2. Transmission. In this subsection, we begin by examining the transmission process of the material. In all cases intensities of 10 mW/cm² (for EB, EY, PB, and RB), and 4.03 mW/cm² (for MB) are used to illuminate the layers. First, we need to examine the effects of adding different dyes to the standard AA/PVA material using simple experiments. In all cases the set-ups involve: uniform plane waves of wavelength 532 nm (for EB, EY, PB, and RB) or of 633 nm (for MB), pass normally through the material and the transmitted intensity is measured. The area of illumination is 0.25 cm². Normalised transmittance curve for the same dye concentrations for EB, EY, PB, and RB, and a higher dye concentration for MB, are given in Figure 3. Using the model proposed in Section 2 dye parameter values are estimated by fitting these curves. Table 4 lists the values of molar absorptivity, ε , and the quantum efficiency of the reactions in which the ground state dye is converted into the singlet $^1D^*$ and triplet $^3D^*$ dye states with the quantum efficiencies ϕ_S and ϕ_T respectively, as estimate by fitting the transmittance curves. We note that the transmittance curves all decrease once exposure ends. This

TABLE 2: Key parameters for four different Xanthene photosensitizers at a wavelength of 532 nm.

	Type of photosensitizer	Transmittance (%)	T_{sf} (%)	d (10^{-4}) (cm)	ϵ (10^8) (cm^2/mol)
a	Erythrosine B	0.6209	70.94360	200	1.942
b	Eosin Y	12.1757	69.82245	200	0.716
c	Phloxine B	9.4548	68.90019	200	0.814
d	Rose Bengal	12.8009	62.77100	200	0.652

TABLE 3: Transmittance values for four different Xanthene photosensitizers at 633 nm.

	Type of photosensitizer	Transmittance (%)
a	Erythrosine B (EB)	69.4110
b	Eosin Y (EY)	65.6761
c	Phloxine B (PB)	64.1600
d	Rose Bengal (RB)	59.4887

takes place due to the recovery process of the dye once the illuminating light is switched off [18]. $t_{\text{expa}} = 100$ s, $t_{\text{expb}} = 150$ s, $t_{\text{expc}} = 600$ s, $t_{\text{expd}} = 200$ s, and $t_{\text{expe}} = 50$ s are the times when illumination ends for: (a) EB, (b) EY, (c) PB, (d) RB, and (e) MB, respectively. It is worth noting that the values of molar absorptivity, ϵ , estimated here agree with those presented in Section 4.1. The value in Section 4.1 is calculated directly by measuring the spectrum and in Section 4.2 the numbers are estimated by fitting the experimental data. However given to the material and experimental environment difference, that is, temperature and humidity, the value could be slightly different. However we can see the agreement is still surprisingly good, and demonstrates that the absorptivity value extracted using our model is reasonable.

4.3. Recovery. In this section we estimate the rate, k_r , at which the photosensitizer recovers back to its initial ground state after it has been excited. In order to determine a value for k_r , a set of experiments is performed, which enables the photosensitizer concentration to be measured at any time, t , after a given exposure time, t_{exp} . To do so we use the results presented in Figure 4.

Using the same setup describe in Section 4.2, the recovery process is examined experimentally. The material is illuminated for t_{exp} , after t_{exp} the laser is switched off for time t_{off} . After t_{off} [19], the material is again illuminated and the transmittance immediately measured. This measurements repeat several times for different t_{off} values, so that we obtain the normalised transmission post-exposure, $T(t > t_{\text{exp}})$, which is related to the dye concentration post-exposure. As a result, by fitting the experimental data the recovery rate, k_r , can be estimated.

Based on the best fits achieved to the experimental results, using the model described in Section 2, Table 5 shows the estimated values of the recovery rate, k_r . The mean squared error (MSE) values achieved for the fitting procedure are also presented in the table.

4.4. Bleaching. In this section the estimation of the rate constant of photobleaching of the photosensitizer, k_b , the rate

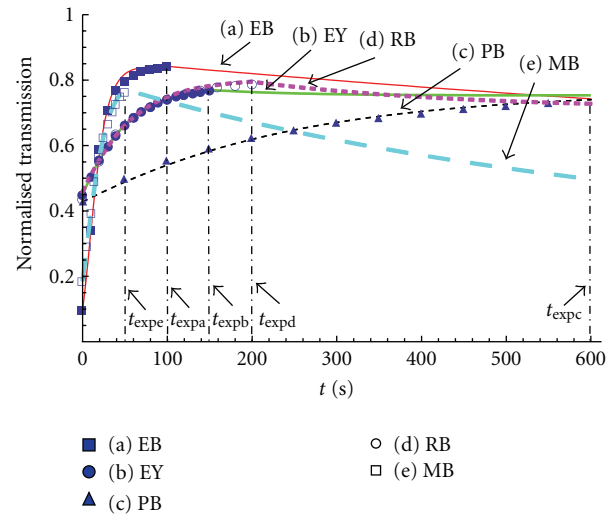


FIGURE 3: The normalised transmission characteristics of five different photosensitizers (a) EB (thin red curve and filled square) (b) EY (thick green curve and filled circle) (c) PB (thin short black dashed curve and filled triangle) (d) RB (thick pink short dashed curve and empty circle) (e) MB (thick blue long dashed curve and empty square) in AA/PVA photopolymer material. Both the experimental data points and theoretical fits for exposure intensities of $10 \text{ mW}/\text{cm}^2$ for (a), (b), (c), (d), and $4.03 \text{ mW}/\text{cm}^2$ for (e) are shown.

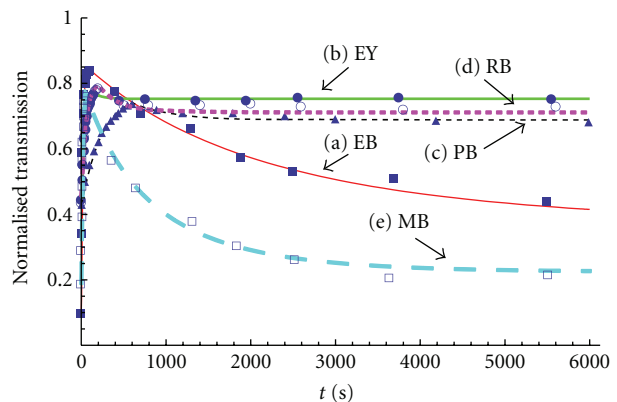


FIGURE 4: The recovery process for five different photosensitizers (a) EB (thin red curve and filled square) (b) EY (thick green curve and filled circle) (c) PB (thin black short dashed curve and filled triangle) (d) RB (thick pink short dashed curve and empty circle) (e) MB (thick blue long dashed curve and empty square) in AA/PVA photopolymer material. Both the experimental data points and theoretical fits for the exposure intensity of $10 \text{ mW}/\text{cm}^2$ for (a), (b), (c), (d), and $4.03 \text{ mW}/\text{cm}^2$ for (e) are shown.

TABLE 4: The values of dye absorption-related parameters extracted by fitting the experimental data in Figure 3 using the model in Section 2.

	Type of photosensitizer	λ (nm)	ϵ (10^8) (cm^2/mol)	φ_S (10^{-3}) (mol/Einstein)	φ_T (10^{-3}) (mol/Einstein)
a	Erythrosine B	532	1.720	6.00	9.10
b	Eosin Y	532	0.474	3.60	30.00
c	Phloxine B	532	0.525	1.53	4.30
d	Rose Bengal	532	0.470	8.40	19.00
e	Methylene Blue	633	0.824	57.00	7.30

TABLE 5: The parameter values associated with dye recovery extracted from fitting the experimental results in Figure 4 using model in Section 2.

	λ (nm)	Type of photosensitizers	k_r (10^{-3}) (s^{-1})	MSE
a	532	Erythrosine B	0.33	0.01021400
b	532	Eosin Y	10.00	0.00182489
c	532	Phloxine B	2.20	0.00644423
d	532	Rose Bengal	3.90	0.01056260
e	633	Methylene Blue	0.80	0.00838055

constant of electron donation (with which ED becomes a free radical, R^\bullet), k_d , and the rate constants of inhibition of the photosensitizer, k_z , dye^* , are discussed.

The setup for this experiment is the same as that used in Sections 4.2 and 4.3. The material is illuminated for t_{exp} , after t_{exp} the illumination is switched off for t_{OFF} . The material is left unilluminated for a long time, $t_{\text{OFF}} \rightarrow \infty$ in order to allow the dye to fully recover. In practise, we assume that the dye is fully recovered after $t_{\text{OFF}} = 12$ hours. After $t_{\text{OFF}} = 12$ hours the illumination is once again switched on and the transmittance measured. This procedure is repeated several times with different t_{exp} values for all the dyes.

The amount of photosensitizer concentration bleached by an exposure of duration, t_{exp} , can be estimated by taking the differences between the initial concentration A_0 and $A(t_{\text{OFF}} \rightarrow \infty)$,

$$A_b = A_0 - A(t_{\text{OFF}} \rightarrow \infty), \quad (16)$$

where A_0 is the initial photosensitizer concentration and $A(t_{\text{OFF}} \rightarrow \infty)$ is the final value. A typical set of experimental results are shown in Figure 5, and the resulting parameter values estimated are listed in Table 6.

4.5. Summary. In this section, the photoabsorptive behaviours of five photosensitizers, in almost equivalent PVA/AA layers, are examined using the model derived in Section 2. For each dye, the recovery and bleaching parameters are estimated by fitting reproducible experimental transmittance data.

It can be noted from the quality of the fitting results that the RB is not as well modelled as the other dyes, in that at a certain time t , the sum of the concentration of the recovered dye and the bleached dye is less than the original dye concentration value A_0 . Furthermore the quality of the fit is poorer as indicated by the fact that the MSE value is relatively higher. One possibility is that this could be a result of our neglect of the recovery of the triplet excited state dye, $^3\text{Dye}^*$ back into either the ground state, Dye , or the singlet state,

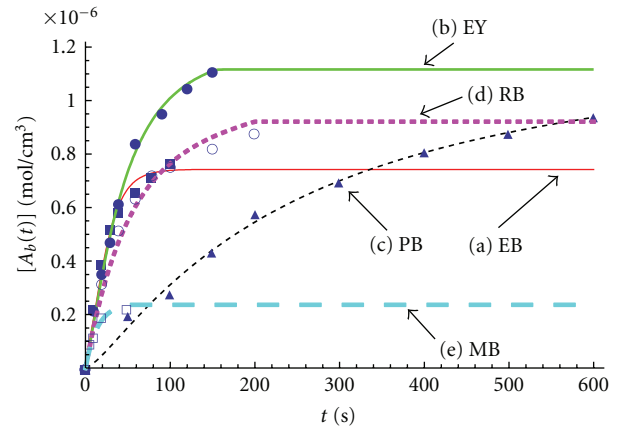


FIGURE 5: The bleaching process for five different photosensitizers (a) EB (thin red curve and filled square), (b) EY (thick green curve and filled circle), (c) PB (thin black short dashed curve and filled triangle), (d) RB (thick pink short dashed curve and empty circle), (e) MB (thick blue long dashed curve and empty square) in AA/PVA photopolymer material. All the experimental data points and theoretical fits for the exposure intensity of $10 \text{ mW}/\text{cm}^2$ for (a), (b), (c), and (d), and $4.03 \text{ mW}/\text{cm}^2$ for (e) are shown. In all the cases the illuminated area was 0.25 cm^2 .

$^1\text{Dye}^*$. However, following some analyses we note that even if such recovery mechanisms are included into the model the quality of the fit does not improve significantly. There is a connection between the recovery and the bleaching process. Using the same experiment data, as is presented in Figures 6 and 7 it is found that when we get the best fitting for the transmission and recovery of RB, the theoretical predicted values are higher than the experimental values for bleaching, especially for the longest values of time. Table 7 lists the parameter values extracted by applying this procedure. In conclusion, based on these observations, we expect that there are other reactions taking place in the RB system, which are of less significance for the other dyes studied.

TABLE 6: The values of bleaching-related parameters extracted by fitting experimental date in Figure 5 using the model in Section 2.

	Dye	λ (nm)	k_b (cm ³ /mol s)	k_{z,dye^*} (cm ³ /mol s)	k_d (10 ³) (cm ³ /mol s)	MSE ($\times 10^{-8}$)
a	EB	532	0.23×10^2	1.1×10^8	4.3	2.019090
b	EY	532	0.80×10^2	1.5×10^8	3.8	1.840540
c	PB	532	0.20×10^2	5×10^7	3.9	1.387100
d	RB	532	6.000×10^3	9×10^7	5.0	2.607790
e	MB	633	4.0×10^7	1.0×10^8	4.3	0.981322

TABLE 7: The parameters extracted by fitting experimental date in Figure 7 using the alternate model for RB.

ϵ (10 ⁸) (cm ² /mol)	φ_S (10 ⁻³) (mol/Einstein)	φ_T (10 ⁻³) (mol/Einstein)	k_r (10 ⁻³) (s ⁻¹)	MSE for recovery
0.510	8.40	17.90	9.10	0.00251136
k_b (cm ³ /mol s)	k_{z,dye^*} (cm ³ /mol s)	k_d (10 ³) (cm ³ /mol s)	MSE for bleaching ($\times 10^{-8}$)	
6.000×10^3	9×10^7	5.0	3.988450	

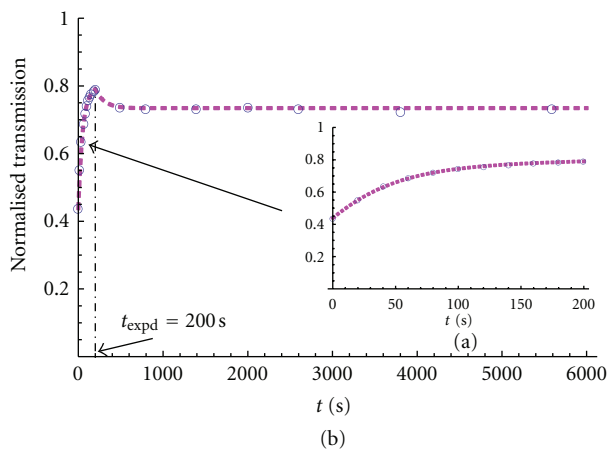


FIGURE 6: (a) The normalised transmission characteristics RB. (b) The recovery process for RB in AA/PVA photopolymer material. Both the experimental data points (circles) and theoretical fit (dashed line) for an exposure intensity of 10 mW/cm² are shown for the new fitting.

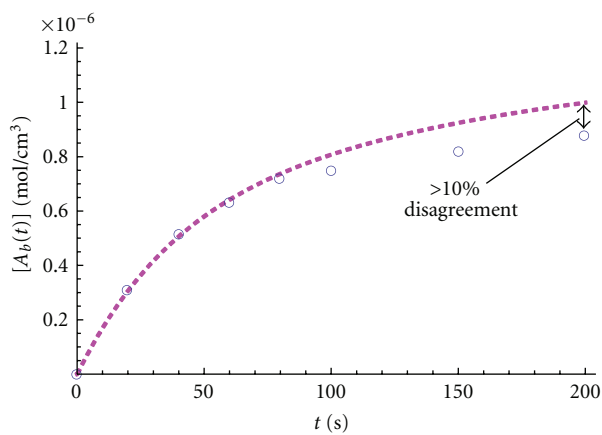


FIGURE 7: The bleaching process for RB in AA/PVA photopolymer material. Both the experimental data points and theoretical fits for the exposure intensity of 10 mW/cm² are shown with the new fitting. In all the cases, the illuminated area was 0.25 cm².

5. Simulation Model Predictions

Based on the theoretical analysis and experimental work presented in Sections 2 to 4, the temporal evolution of the primary radical concentration, ED^* (or R^*), can be predicted. It is found that the behaviours of the five dyes are significantly different.

From Section 2, we know that the primary radical concentration, ED^* , is produced by the reaction between ${}^3Dye^*$ and ED , at the rate constant of electron donation, k_d , see (1d). Simultaneously, ED^* is also being removed as it initiates photopolymer chains, see (1f), as it reacts with M_n^* , see (4), and is scavenged by the dissolved inhibitor, see (5a). Applying the full model of the photoinitiation process, using the parameter values estimated above, the temporal evolution of the concentration of the primary radicals, ED^* , for (a) EB, (b) EY, (c) PB, (d) RB, and (e) MB, can be predicted using (8).

The result is presented in Figure 8. As can be seen in the initial stages of the exposure, the generation of ED^* is significantly inhibited by the original dissolved oxygen, see (5a). Following the resulting initial inhibition period, the generation of ED^* progressively increases towards a maximum value. However, after this maximum the concentration value decreases gradually. This is due to the photoinitiation process described by (1f), and the reaction with M_n^* during the termination process described in (4).

From Figure 8 we can see that for the four Xanthene dyes examined, EB reaches the ED^* peak concentration value in a very short time and the ED^* peak concentration is also highest, which means that the inhibitor has less effect for the EB case. However the inhibition effect can be more accurately measured using lower exposure intensity, and this is a topic for future work. In addition, for the corresponding MB case, the general behaviour of the ED^* concentration is similar to that of the Xanthene dyes.

For PB and MB, since fewer ${}^3Dye^*$ molecules are generated, fewer are available to react with the electron donor, that is, φ_T (PB) and φ_T (MB) are smaller, thus less ED^* is produced. Therefore: (1) the inhibitor scavenging effect takes less time to end; (2) at the same corresponding time in Figure 8, the amount of dihydro dye formed is reduced, that

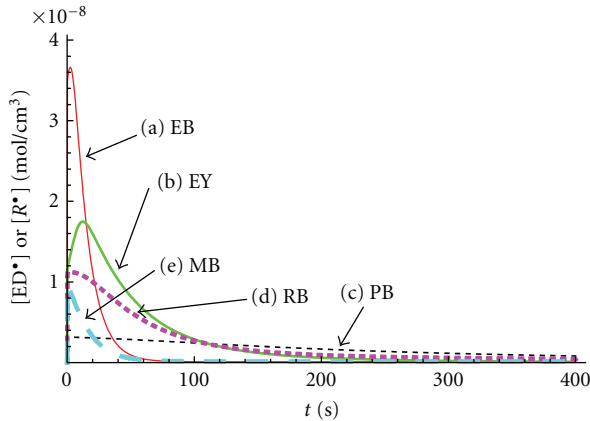


FIGURE 8: The predicted concentration of ED^* , or R^* , from (8) as a function of time for: (a) EB (thin red curve), (b) EY (thick green curve), (c) PB (thin black short dashed curve), (d) RB (thick pink short dashed curve), (e) MB (thick blue long dashed curve), in AA/PVA photopolymer material layer.

is, there is less bleaching of the PB and MB dyes for the same exposure time, see Figure 5.

Furthermore, comparing the results for these five types of photosensitizer, it is clear that the generation of primary radicals can be affected by the different reactivities between the ED molecules and the various excited dye molecules. This is important in the photoinitiation process, especially if one wishes to optimize the interaction between the electron donor and the photosensitizer. Therefore, and in agreement with previous results in the literature, in order to optimize a free-radical polymerization process [1, 16, 22, 25, 26, 32, 33], it is clear that a detailed model of dye kinetics, that is, photon absorption, photosensitizer recovery and bleaching is necessary. Once again we note that the behaviour of RB dye is different from that of the others, and once again this may be due to the presence of some other process.

6. Conclusion and Analysis

One of the aims of this paper has been the development of a new dye model which is both simple enough to use easily but also of practical value and sufficiently flexible to be used for different photosensitisers. In this paper, key dye parameter values for five photosensitisers, (i.e., molar absorptivity, ϵ , quantum efficiency of the reaction, ϕ_S and ϕ_T , recovery rate, k_r , and bleaching rate, k_b), have been extracted by fitting the experiment data using our new simplified dye model. This is achieved by measuring the transmission of the material layer, for certain exposure intensities. The recovery behaviours of the dyes are thus experimentally compared under identical conditions. Following this, the bleaching processes [19] were examined using the parameter values already estimated. In this way a full theoretical treatment of the photoinitiation processes was presented. The results are very useful, that is, PB should be used to record gratings with low energetic exposure, in that the inhibition has a less effect on it.

While significant progress has been made in the work presented here, much remains to be done. It appears that some

other reactions are taking place during and after-exposure in the RB system case, indicating that a more accurate model is needed. The resulting accurate description of the photoinitiation processes must then be incorporated into the full nonlocal photopolymerization driven diffusion (NPDD) model, allowing a more complete modelling of free radical photopolymerization to take place. Such a model can then be applied to the study of photopolymer use for such application as holographic data storage and 3D hybrid optoelectronic circuit fabrication.

A new dye model, which includes the effect of photosensitizer recovery and bleaching has been developed and compared to experimental results. The photoabsorptive behaviours of five types of photosensitizer: Erythrosine B (EB); Eosin Y (EY); Phloxine B (PB); and Rose Bengal (RB), of the same molarity in equivalent PVA/AA layers, and Methylene Blue (MB) of higher molarity in PVA/AA layers, are experimentally examined. We modify the previous dye model by introducing k_{aS} and k_{aT} into the model, which are the rate constant of photon absorption from ground state dye to singlet state and triplet state respectively. A description of how to incorporate this dye model into a full NPDD material model, in order to simulate photopolymer material behaviour, has been presented and discussed.

Future work must include characterising the spatial frequency response of the AA/PVA material. There is a large difference between the molecular weights between five dyes. It is reasonable to assume that, barring an unusual molecular structure, the smaller the molecule, the quicker it will diffuse through a given polymer matrix [34]. It is expected that the faster the rate of diffusion, the more total polymerisation that can take place in the exposed areas. This should lead to a larger saturation value of refractive index modulation and a stronger material response. In summary the effect of the five different polarities, shapes and size of the Xanthene and Thiazine dyes on the spatial frequency response of the AA/PVA material must be quantitatively examined [35, 36]. Since the existence and diffusion of oxygen is non-ignorable in low intensity exposure cases, the inhibition process will be studied by using low exposure intensity in the future.

Acknowledgments

The authors would like to acknowledge the funding support of the EU ERUSMAS Mundus fund. They would also like to acknowledge the support of Enterprise Ireland and Science Foundation Ireland under the national development fund and the Irish Research Council for Science, Engineering and Technology (IRCSET) through the EMPOWER postgraduate and postdoctoral fellowship schemes and the Ministerio de Economía y Competitividad of Spain under Project FIS2011-29803-C02-01 as well.

References

- [1] M. R. Gleeson, D. Sabol, S. Liu, C. E. Close, J. V. Kelly, and J. T. Sheridan, "Improvement of the spatial frequency response of photopolymer materials by modifying polymer chain length," *Journal of the Optical Society of America B*, vol. 25, no. 3, pp. 396–406, 2008.

- [2] C. H. Bamford, A. D. Jenkins, and R. Johnston, "Termination by primary radicals in vinyl polymerization," *Transactions of the Faraday Society*, vol. 55, pp. 1451–1460, 1959.
- [3] G. Manivannan and R. A. Lessard, "Trends in holographic recording materials," *Trends in Polymer Science*, vol. 2, pp. 282–290, 1994.
- [4] A. Márquez, C. Neipp, A. Beléndez, S. Gallego, M. Ortuño, and I. Pascual, "Edge-enhanced imaging with polyvinyl alcohol/acrylamide photopolymer gratings," *Optics Letters*, vol. 28, no. 17, pp. 1510–1512, 2003.
- [5] S. Harbour, J. V. Kelly, T. Galstian, and J. T. Sheridan, "Optical birefringence and anisotropic scattering in acrylate based holographic polymer dispersed liquid crystals," *Optics Communications*, vol. 278, no. 1, pp. 28–33, 2007.
- [6] S. M. Schultz, E. N. Glytsis, and T. K. Gaylord, "Design, fabrication, and performance of preferential-order volume grating waveguide couplers," *Applied Optics*, vol. 39, no. 8, pp. 1223–1232, 2000.
- [7] A. Sato, M. Scepanovic, and R. K. Kostuk, "Holographic edge-illuminated polymer Bragg gratings for dense wavelength division optical filters at 1550 nm," *Applied Optics*, vol. 42, no. 5, pp. 778–784, 2003.
- [8] M. Straub, L. H. Nguyen, A. Fazlic, and M. Gu, "Complex-shaped three-dimensional microstructures and photonic crystals generated in a polysiloxane polymer by two-photon microstereolithography," *Optical Materials*, vol. 27, no. 3, pp. 359–364, 2004.
- [9] A. C. Sullivan, M. W. Grabowski, and R. R. McLeod, "Three-dimensional direct-write lithography into photopolymer," *Applied Optics*, vol. 46, no. 3, pp. 295–301, 2007.
- [10] J. V. Kelly, M. R. Gleeson, C. E. Close, and J. T. Sheridan, "Optimized scheduling for holographic data storage," *Journal of Optics A*, vol. 10, no. 11, Article ID 115203, 2008.
- [11] L. Dhar, A. Hale, H. E. Katz, M. L. Schilling, M. G. Schnoes, and F. C. Schilling, "Recording media that exhibit high dynamic range for digital holographic data storage," *Optics Letters*, vol. 24, no. 7, pp. 487–489, 1999.
- [12] R. R. McLeod, A. J. Daiber, M. E. McDonald et al., "Micro-holographic multilayer optical disk data storage," *Applied Optics*, vol. 44, no. 16, pp. 3197–3207, 2005.
- [13] F. Bruder and T. Faেকে, "Materials in optical data storage," *International Journal of Materials Research*, vol. 101, pp. 199–215, 2010.
- [14] J. Zhang, K. Kasala, A. Rewari, and K. Saravanamuttu, "Self-trapping of spatially and temporally incoherent white light in a photochemical medium," *Journal of the American Chemical Society*, vol. 128, no. 2, pp. 406–407, 2006.
- [15] M. R. Gleeson, J. V. Kelly, C. E. Close, F. T. O'Neill, and J. T. Sheridan, "Effects of absorption and inhibition during grating formation in photopolymer materials," *Journal of the Optical Society of America B*, vol. 23, no. 10, pp. 2079–2088, 2006.
- [16] M. R. Gleeson, J. V. Kelly, D. Sabol, C. E. Close, S. Liu, and J. T. Sheridan, "Modeling the photochemical effects present during holographic grating formation in photopolymer materials," *Journal of Applied Physics*, vol. 102, no. 2, Article ID 023108, 9 pages, 2007.
- [17] M. R. Gleeson, S. Liu, S. O'Duill, and J. T. Sheridan, "Examination of the photoinitiation processes in photopolymer materials," *Journal of Applied Physics*, vol. 104, no. 6, Article ID 064917, 8 pages, 2008.
- [18] S. Liu, M. R. Gleeson, D. Sabol, and J. T. Sheridan, "Extended model of the photoinitiation mechanisms in photopolymer materials," *Journal of Applied Physics*, vol. 106, no. 10, Article ID 104911, 10 pages, 2009.
- [19] S. Liu, M. R. Gleeson, J. Guo, and J. T. Sheridan, "Optical characterization of photopolymers materials: theoretical and experimental examination of primary radical generation," *Applied Physics B*, vol. 100, no. 3, pp. 559–569, 2010.
- [20] J. R. Lawrence, F. T. O'Neill, and J. T. Sheridan, "Photopolymer holographic recording material," *Optik*, vol. 112, no. 10, pp. 449–463, 2001.
- [21] A. Fimia, N. López, F. Mateos, R. Sastre, J. Pineda, and F. Amat-Guerri, "New photopolymer used as a holographic recording material," *Applied Optics*, vol. 32, no. 20, pp. 3706–3707, 1993.
- [22] M. D. Goodner and C. N. Bowman, "Modeling primary radical termination and its effects on autoacceleration in photopolymerization kinetics," *Macromolecules*, vol. 32, no. 20, pp. 6552–6559, 1999.
- [23] H. K. Mahabadi, "Effects of chain length dependence of termination rate constant on the kinetics of free-radical polymerization. 1. Evaluation of an analytical expression relating the apparent rate constant of termination to the number-average degree of polymerization," *Macromolecules*, vol. 18, no. 6, pp. 1319–1324, 1985.
- [24] G. Odian, *Principles of Polymerization*, John Wiley & Sons, New York, NY, USA, 4th edition, 1991.
- [25] M. R. Gleeson and J. T. Sheridan, "Nonlocal photopolymerization kinetics including multiple termination mechanisms and dark reactions. Part I. Modeling," *Journal of the Optical Society of America B*, vol. 26, no. 9, pp. 1736–1745, 2009.
- [26] M. R. Gleeson, S. Liu, R. R. McLeod, and J. T. Sheridan, "Non-local photopolymerization kinetics including multiple termination mechanisms and dark reactions. Part II. Experimental validation," *Journal of the Optical Society of America B*, vol. 26, no. 9, pp. 1746–1754, 2009.
- [27] M. R. Gleeson, S. Liu, J. Guo, and J. T. Sheridan, "Non-local photo-polymerization kinetics including multiple termination mechanisms and dark reactions: part III. Primary radical generation and inhibition," *Journal of the Optical Society of America B*, vol. 27, no. 9, pp. 1804–1812, 2010.
- [28] B. B. Bhowmik and P. Ganguly, "Photophysics of xanthene dyes in surfactant solution," *Spectrochimica Acta—Part A*, vol. 61, no. 9, pp. 1997–2003, 2005.
- [29] M. Izadifard, C. H. Langford, and G. Achari, "Photocatalytic dechlorination of PCB 138 using leuco-methylene blue and visible light; reaction conditions and mechanisms," *Journal of Hazardous Materials*, vol. 181, no. 1–3, pp. 393–398, 2010.
- [30] A. K. O'Brien and C. N. Bowman, "Modeling the effect of oxygen on photopolymerization kinetics," *Macromolecular Theory and Simulations*, vol. 15, no. 2, pp. 176–182, 2006.
- [31] J. T. Sheridan and J. R. Lawrence, "Nonlocal-response diffusion model of holographic recording in photopolymer," *Journal of the Optical Society of America A*, vol. 17, no. 6, pp. 1108–1114, 2000.
- [32] M. R. Gleeson, S. Liu, and J. T. Sheridan, "The production of primary radicals in photopolymers during holographic exposure," *Optik*, vol. 121, no. 24, pp. 2273–2275, 2010.
- [33] M. R. Gleeson and J. T. Sheridan, "A review of the modelling of free-radical photopolymerization in the formation of holographic gratings," *Journal of Optics A*, vol. 11, no. 2, Article ID 024008, 2009.
- [34] J. Guo, S. Liu, M. R. Gleeson, and J. T. Sheridan, "Study of photosensitizer diffusion in a photopolymer material for holographic applications," *Optical Engineering*, vol. 50, no. 1, Article ID 015801, 5 pages, 2011.

- [35] C. E. Close, M. R. Gleeson, and J. T. Sheridan, "Monomer diffusion rates in photopolymer material. Part I. Low spatial frequency holographic gratings," *Journal of the Optical Society of America B*, vol. 28, no. 4, pp. 658–666, 2011.
- [36] C. E. Close, M. R. Gleeson, D. A. Mooney, and J. T. Sheridan, "Monomer diffusion rates in photopolymer material. Part II. High-frequency gratings and bulk diffusion," *Journal of the Optical Society of America B*, vol. 28, no. 4, pp. 842–850, 2011.

Research Article

Coaxial Self-Trapping of White and Gray Regions of an Incandescent Field: A Bright Core with a Dark Cladding

Kailash Kasala and Kalaichelvi Saravanamuttu

Department of Chemistry and Chemical Biology, McMaster University, 1280 Main Street West, Hamilton, ON, Canada L8S 4M1

Correspondence should be addressed to Kalaichelvi Saravanamuttu, kalai@mcmaster.ca

Received 14 May 2012; Accepted 23 July 2012

Academic Editor: Michael R. Gleeson

Copyright © 2012 K. Kasala and K. Saravanamuttu. This is an open access article distributed under the Creative Commons Attribution License, which permits unrestricted use, distribution, and reproduction in any medium, provided the original work is properly cited.

We report the generation of a self-trapped incoherent hybrid beam comprising a dark-sheathed bright core. The hybrid beam originates from refractive index changes in a photocrosslinkable organosiloxane, which allow simultaneous and cooperative self-trapping of a gray ring with a white core embedded in a broad incandescent beam. The core narrowed and increased in intensity while the encircling gray ring decreased in intensity until rendered very dark. This dark sheath improves light confinement in the bright core and protects it from interactions with nearby self-trapped filaments. This is the first example of a self-trapped hybrid beam, which is moreover spatially and temporally incoherent.

1. Introduction

In this paper, we report that a new self-trapped spatially and temporally incoherent species—a hybrid beam—forms in a photocrosslinkable organosiloxane [1, 2]. This photopolymer, which undergoes free-radical polymerization and a corresponding increase in refractive index upon irradiation, can be classified as a self-focusing medium (Figure 1). The hybrid beam forms when an incandescent beam embedded with a gray ring propagates through the photopolymer. Refractive index changes (Δn) along the beam path lead to self-trapping of the white core into a narrow, intense bright beam. Simultaneously, the gray ring is depleted of intensity by the self-trapped bright core and self-traps into a very dark sheath. The decreased intensity and lack of divergence of the sheath is the signature of self-trapping dark beams [3].

Our finding is counter-intuitive because it shows for the first time that self-trapped bright and dark regions can coexist within the same optical field. Until now, self-trapped bright and dark beams could only be generated separately under the opposite conditions of self-focusing [4, 5] and self-defocusing [3], respectively. For example, self-trapped

bright incoherent beams can be generated in a photorefractive crystal under self-focusing conditions, in which Δn increases with intensity [4, 5]. By contrast, self-trapped dark incoherent beams must be generated under self-defocusing conditions [3]. Here, an incoherent beam bearing a dark depression (dip) propagating in an appropriately biased photorefractive crystal induces the greatest Δn along the path of the dip. The consequent defocusing of the bright background into the greater index (dark) regions counteracts the divergence of the dip and in this way, generates a self-trapped dark beam [3].

The hybrid beam in our study was created with incandescent light, which is incoherent in space and time. Self-trapping of a wavepacket with such poor correlation of phase and amplitude was experimentally discovered in 1997 [5]. The finding raised fundamental questions about the spatial correlation [6], shape [7], frequency distribution [8], and modulation instability (MI) [9] of incoherent white light. Self-trapping of white light was first demonstrated in a photorefractive crystal, which at very low intensities exhibits a noninstantaneous and saturable photoresponse [5]. These critical properties permit copropagation of the multiple

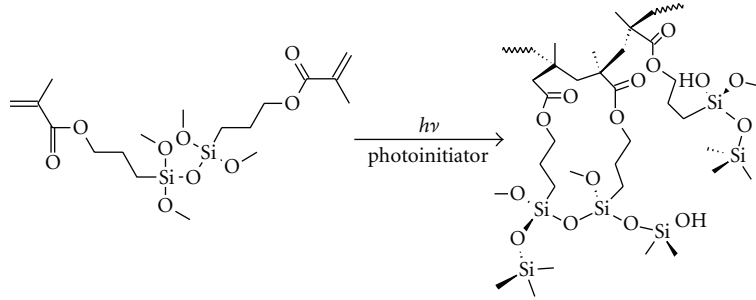


FIGURE 1: Methacrylate substituents in the organosiloxane photopolymer undergo photoinitiated free-radical polymerization. Chain formation leads to a local densification and in turn, an increase in refractive index [1].

modes of white light and time-average out its femtosecond phase fluctuations, respectively.

We have shown that such a saturable and noninstantaneous photoresponse is inherent to the organosiloxane photopolymer [2]. Spatial and temporal variations of Δn in the photopolymer can be described through [10]:

$$\Delta n(r, z, t) = \Delta n_s \left\{ 1 - \exp \left[-\frac{1}{U_0} \int_0^{t-r} |E(t)|^2 dt \right] \right\}, \quad (1)$$

where Δn_s is the maximum index change of 1.46 [1] (at saturation), U_0 is the critical exposure (total energy) required to initiate polymerisation, τ is the monomer radical lifetime (assumed to be negligible), and $|E(t)|^2$ is the square of the electric field amplitude of the incident optical field. We previously reported that the photoresponse of the polymer medium allowed self-trapping of individual incandescent light beams. Studies in this photopolymer also provided insight into the intensity-dependent dynamics, interactions [11], MI [12], and spontaneously formed lattices of self-trapped white beams [13]. We now find that the photopolymer permits simultaneous, coaxial propagation of a bright core and dark sheath as a hybrid beam.

In a typical experiment, a broad, collimated beam of white light (background beam) from a quartz-tungsten-halogen lamp (≈ 4 mW) was passed through an amplitude mask, which introduced a weakly dark (gray) ring (Figure 2(a)). The ring-embedded background beam was launched into a transparent cuvette containing an organosiloxane photopolymer gel, which was doped with a titanocene photoinitiator ($\lambda_{\max} = 393$ nm, 460 nm) to sensitise it to visible light [2]. At the entrance face (propagation distance (z) = 0.0 mm), the gray ring had an outer diameter (od) of 350 μm , while its white core had a FWHM diameter of 220 μm . The relative intensity of the ring was 44% while that of the core and background was 50%. The beam profile at $z = 6.0$ mm in the photopolymer was imaged with a CCD camera. At early times (when polymerization was negligible), the natural divergence of the background beam causes significant broadening of the ring and core with propagation from $z = 0.0$ mm to $z = 6.0$ mm. Based on the spatial correlation length (l_c) = 0.31 μm for the central wavelength (600 nm) of our incandescent source, the bright core can be calculated using $\theta \approx \lambda/\pi l_c^2$ to diverge to ~ 20 -fold its original width at $z = 6.00$ mm. The decrease in intensity due

to the extensive divergence of the core diminished its contrast with the gray ring to the extent that at $z = 6.0$ mm, the beam appeared effectively uniform with a relative intensity of $\sim 40\%$ (Figure 2(b)). This significant divergence, which erases any distinction between dark and bright regions of the optical field, is characteristic of incandescent light and originates from its random and rapid phase fluctuations [14].

Experimental results in Figure 2 show the evolution of the spatial intensity profile of the ring-bearing incandescent beam at $z = 6.0$ mm. 2D and 3D intensity profiles are shown; for clarity, both a top-down 3D view tracing the intensity increase of the white core and a bottom-up 3D view tracing the depletion of intensity from the gray ring are presented. Over time, polymerization and consequent refractive index changes (Δn) along the beam propagation path caused self-trapping of both the gray ring and its white core. At 36 s, self-trapping of the white core was indicated by a decrease in width to 141 μm and increase in relative intensity from 40% to 60%. Simultaneous self-trapping of the gray ring was evidenced through the emergence of a well-defined dark ring with od = 410 μm . Characteristic of self-trapped dark beams, the gray ring showed a decrease in relative intensity from 40% to 31% (Figure 2(c)). This dark-sheathed bright core propagated coaxially without significant divergence as a self-trapped hybrid beam.

Over time, the dark sheath of the hybrid beam continued to darken even as its core increased in intensity. The contrast between the sheath and core maximized at 72 s at relative intensities of 12% and 100%, respectively (Figure 2(e)). At this time, the core was only 105 μm wide, while the ring od was 440 μm . Although the core later decreased in intensity with a concomitant (slight) increase in width (characteristic of individual self-trapped white beams) [1], (Figures 2(f) and 2(g)) both the ring and core remained self-trapped. Figure 2(h) shows that at ~ 1200 s, the widths of the ring and core were 440 μm and 90 μm , respectively. This confirmed that the self-trapped hybrid beam was stable and nontransient.

To explain its mechanism of formation, we first reason that self-trapping of the core of the hybrid beam follows the same process as self-trapping of an individual white beam in the photopolymer [1]. The latter was extensively studied and described elsewhere [1]. Briefly, the core induces

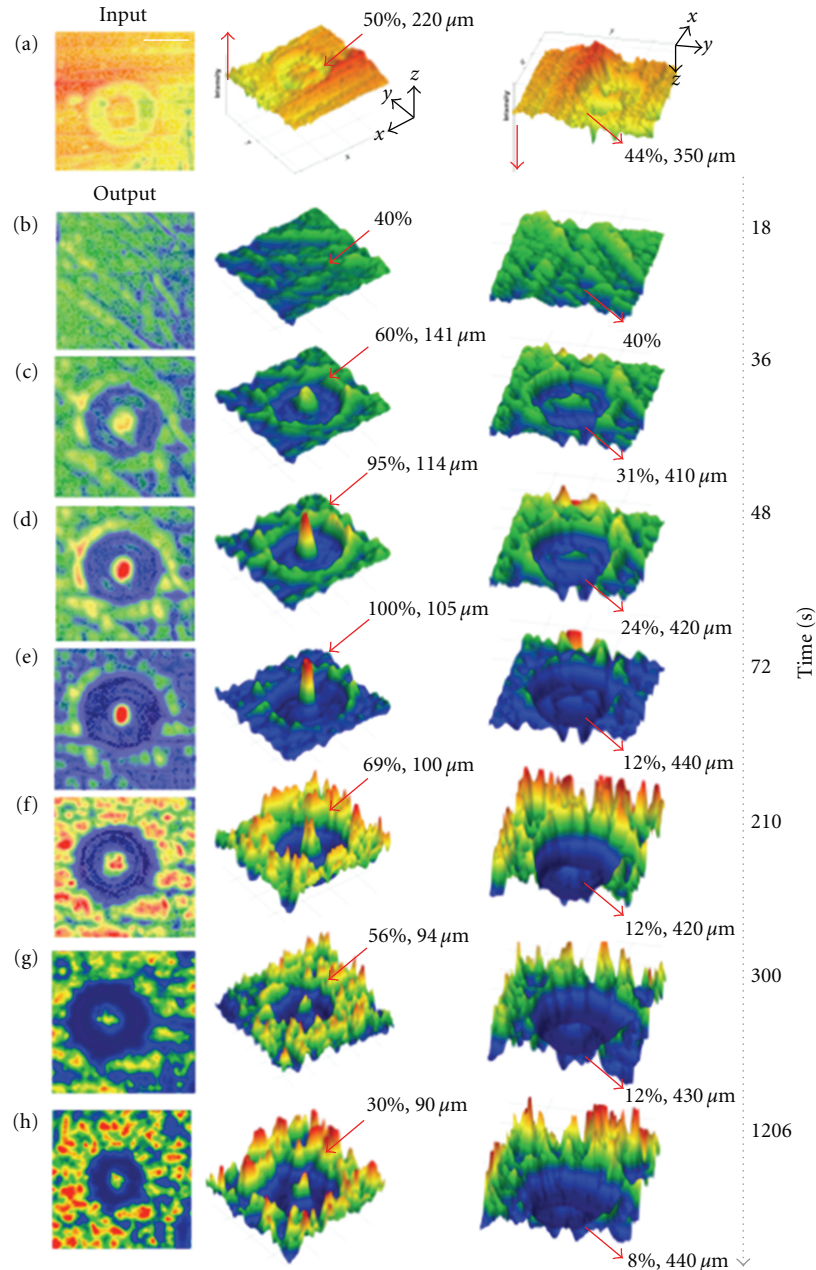


FIGURE 2: 2D and 3D spatial intensity profiles of the gray ring-embedded beam at $z = 0.0$ mm and (b–f) its evolution at $z = 6.0$ mm. For clarity, both top-down and bottom-up perspectives of 3D profiles are included. In (a), the scale bar = $250 \mu\text{m}$ and applies to (b–h). The spectral colour scale corresponds to relative intensities of 0% (blue) to 100% (red) and is the same in (a–g); for clarity, the scale was magnified by approximately $\times 2$ in (g). Intensities and widths of the ring and core are indicated.

noninstantaneous and saturable refractive index changes along its propagation path. This results in a multimode waveguide, which permits self-consistent propagation and self-trapping of the core as observed in Figure 2. Temporal plots in Figures 3(a) and 3(b) trace the decrease in width and increase in intensity of the self-trapping core. Notably, these plots follow the same trend that was previously observed for an individual self-trapped incandescent beam. This includes the slight increase in width and decrease in intensity at late times when Δn of the self-induced waveguide approaches saturation [1]. However, the white core remains self-trapped

and never reverts to its original diverged form over long times (>1200 s) (Figure 2).

The critical difference in the current study is that the same conditions that cause self-trapping and an increase in intensity of the core elicit self-trapping and a decrease in intensity of the gray ring. To explain this dichotomy, we consider that according to (1), the most intense regions of the optical field (i.e., the bright core and background beam) induce the greatest values of Δn in the photopolymer. These bright regions, which have the same initial intensity at $z = 0.0$ mm, must initiate comparable rates of

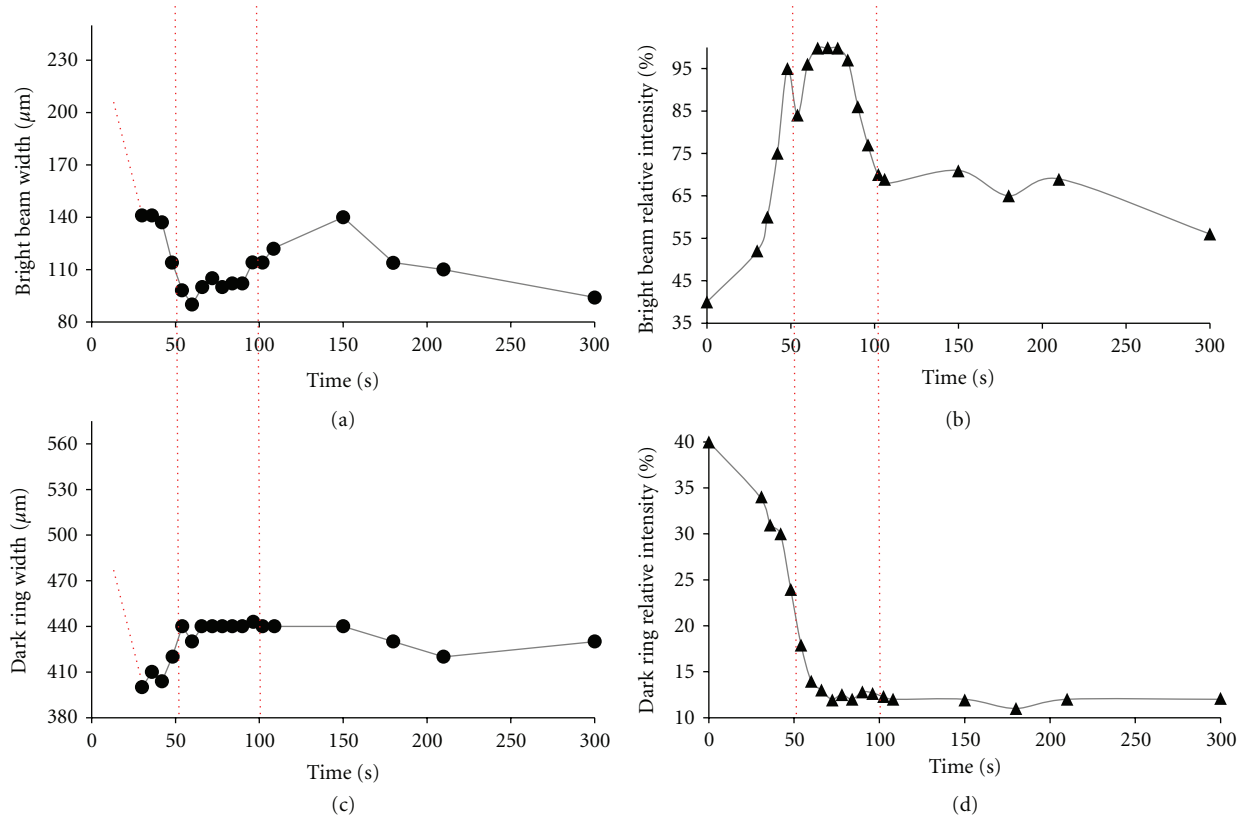


FIGURE 3: Temporal plots of width and relative intensity of the white core (a, b) and gray ring (c, d) of the self-trapped hybrid beam. Dotted lines indicate initial widths of ring and core could not be determined due to the significant divergence of the incandescent beam. Vertical dotted lines are provided as guides to the eye to compare time scales between the different plots.

polymerization. The positive Δn values induced in these regions are therefore similar and suppress the divergence of the core and background beam. While this can be directly observed as self-trapping of the core (Figure 2), similar changes to the background beam are not as evident. This is because the background illuminates nearly the entire photopolymer sample and changes to its boundaries cannot be easily detected (*vide infra*). However, as the core and the background now propagate without divergence, the embedded gray ring is essentially “held” in focus all along the propagation axis. No longer divergent, the ring effectively self-traps and becomes visible at $z = 6.0$ mm (Figure 2(c)).

The mechanism described above is confirmed by comparing the temporal variation in the widths of the core and gray ring (Figures 3(a)–3(c)). The plots show that the ring and core self-trap simultaneously within the same time scale: in the first 30 s, the ring and core suffer the greatest decrease in width to $410 \mu\text{m}$ and $141 \mu\text{m}$, respectively. This is consistent with the notion that self-trapping and divergence-free propagation of the bright regions of the optical field causes concomitant self-trapping of the embedded gray ring.

During self-trapping, light intensity spontaneously flows from the gray ring to the core until maximum contrast is achieved between the two. The intensity transfer from the ring to the core is evident in their temporal plots of intensity (Figures 3(b) and 3(d)): at early times, the core increases in

intensity from 40% to 99% by depleting the ring of intensity during the same period from 40% to 12%. This results in the simultaneous formation of a self-trapped *bright* core and self-trapped *dark* ring (Figure 2). The intensity flow from the ring to the core originates from differences in their photoinduced refractive indices: according to (1), Δn in the photopolymer is intensity-dependent. Δn induced by the gray ring is therefore smaller than that induced by the white core. The resulting gradient in refractive index between the two regions triggers the flow of intensity from the lower-index ring to the higher-index core. As its intensity increases, the core induces even greater values of Δn and attracts additional intensity from the ring. A cycle is established in which the core continually grows in intensity by depleting the ring, which reaches a minimum intensity of 12% at 72 s (Figures 2(e) and 3(d)). Intensity transfer ceases when Δn of the core approaches saturation. At this time, similar to individual self-trapped white beams [1], the core intensity decreases together with a slight increase in its width (Figures 2(f) and 3(b)). While the ring shows a corresponding increase in width, it remains dark and does not undergo any further significant changes (Figures 2(f) and 3(d)).

Our findings indicate that the hybrid beam originates from simultaneous self-trapping and cooperative interactions of the gray ring and white core. Once the hybrid beam is formed, the background beam, which as mentioned

above also induces index changes, undergoes an entirely different type of nonlinear behaviour, modulation instability (MI) [12]. By 210 s, the uniform background spontaneously divided into multiple filaments (Figure 2(f)). The filaments, which are akin to individual self-trapped beams, were approximately $80\ \mu\text{m}$ wide with $\sim 74\%$ relative intensity. They originate from noise such as random, weak amplitude variations, which become amplified due to polymerization and render the beam unstable. The beam stabilizes by spontaneously dividing into multiple filaments [12]. We note that although they originate in the same medium under identical conditions, MI-induced filaments form at a later time (210 s) than the self-trapped bright core (36 s). This is because the dark ring serves as a low-index sheath, which enhances light confinement in the core. This in turn increases the rate and efficiency of self-trapping of the core relative to MI-induced filaments. Furthermore, although filaments immediately surrounding the dark rings were within interacting distance [11] with the self-trapped core (Figure 2(e)), no interactions (e.g., fusion) were observed. We previously showed that interactions between self-trapped white light beams rely on index changes induced by their overlapping optical fields [11]. In the current study, the smaller index of the dark sheath inhibits such overlap and protects the bright core from interactions.

In summary, this to our knowledge is the first report of a self-trapped hybrid beam, which moreover is generated with spatially and temporally incoherent light. The hybrid beam originates from the simultaneous and cooperative self-trapping of a gray ring and its bright core embedded in a broad incandescent beam. The core grows by depleting the ring of most of its intensity and rendering it very dark. Like the cladding of an optical fiber, the dark, low-index sheath enhances light confinement in the core and protects it from interactions. The hybrid beam opens entirely new opportunities to manipulate the confinement and interactions of self-trapped beams through designed introduction of gray and white regions in an optical field. Importantly, they would be accessible with other inexpensive and miniature incoherent light sources such as LEDs. Because of its spatial and temporal incoherence, the hybrid beam also raises intriguing questions about the coherence structure of the dark ring and its bright core.

Acknowledgments

Funding from Natural Sciences and Engineering Research Council of Canada, Canadian Foundation for Innovation, Ontario Institute of Technology and McMaster University is gratefully acknowledged. The authors thank CIBA for generous donation of IRGACURE-784.

References

- [1] K. Saravanamuttu, X. M. Du, S. I. Najafi, and M. P. Andrews, "Photoinduced structural relaxation and densification in sol-gel-derived nanocomposite thin films: implications for integrated optics device fabrication," *Canadian Journal of Chemistry*, vol. 76, no. 11, pp. 1717–1729, 1998.
- [2] J. Zhang and K. Saravanamuttu, "The dynamics of self-trapped beams of incoherent white light in a free-radical photopolymerizable medium," *Journal of the American Chemical Society*, vol. 128, no. 46, pp. 14913–14923, 2006.
- [3] Z. Chen, M. Mitchell, M. Segev, T. H. Coskun, and D. N. Christodoulides, "Self-trapping of dark incoherent light beams," *Science*, vol. 280, no. 5365, pp. 889–891, 1998.
- [4] M. Mitchell, Z. Chen, M.-F. Shih, and M. Segev, "Self-trapping of partially spatially incoherent light," *Physical Review Letters*, vol. 77, no. 3, pp. 490–493, 1996.
- [5] M. Mitchell and M. Segev, "Self-trapping of incoherent white light," *Nature*, vol. 387, no. 6636, pp. 880–883, 1997.
- [6] H. Buljan, A. Šiber, M. Soljačić, and M. Segev, "Propagation of incoherent "white" light and modulation instability in noninstantaneous nonlinear media," *Physical Review E*, vol. 66, no. 3, Article ID 035601, 4 pages, 2002.
- [7] H. Buljan, A. Šiber, M. Soljačić, T. Schwartz, M. Segev, and D. N. Christodoulides, "Incoherent white light solitons in logarithmically saturable noninstantaneous nonlinear media," *Physical Review E*, vol. 68, no. 3, part 2, Article ID 036607, 2003.
- [8] H. Buljan, M. Segev, M. Soljačić, N. K. Efremidis, and D. N. Christodoulides, "White-light solitons," *Optics Letters*, vol. 28, no. 14, pp. 1239–1241, 2003.
- [9] T. Schwartz, T. Carmon, H. Buljan, and M. Segev, "Spontaneous pattern formation with incoherent white light," *Physical Review Letters*, vol. 93, no. 22, Article ID 223901, 2004.
- [10] A. S. Kewitsch and A. Yariv, "Self-focusing and self-trapping of optical beams upon photopolymerization," *Optics Letters*, vol. 21, no. 1, pp. 24–26, 1996.
- [11] K. Kasala and K. Saravanamuttu, "An experimental study of the interactions of self-trapped white light beams in a photopolymer," *Applied Physics Letters*, vol. 93, no. 5, Article ID 051111, 3 pages, 2008.
- [12] I. B. Burgess, W. E. Shimmell, and K. Saravanamuttu, "Spontaneous pattern formation due to modulation instability of incoherent white light in a photopolymerizable medium," *Journal of the American Chemical Society*, vol. 129, no. 15, pp. 4738–4746, 2007.
- [13] I. B. Burgess, M. R. Ponte, and K. Saravanamuttu, "Spontaneous formation of 3-D optical and structural lattices from two orthogonal and mutually incoherent beams of white light propagating in a photopolymerisable material," *Journal of Materials Chemistry*, vol. 18, no. 35, pp. 4133–4139, 2008.
- [14] M. Born and E. Wolf, *Principles of Optics: Electromagnetic Theory of Propagation, Interference and Diffraction of Light*, University of Rochester, New York, NY, USA, 7th edition, 1999.

Research Article

Development of Laser-Produced Tin Plasma-Based EUV Light Source Technology for HVM EUV Lithography

Junichi Fujimoto,¹ Tsukasa Hori,² Tatsuya Yanagida,² and Hakaru Mizoguchi¹

¹ EUV Development Division, Gigaphoton Inc., 400 Oaza Yokokurashinden Oyama-shi, Tochigi-ken 323-8558, Japan

² EUV Development Division, Gigaphoton Inc., 3-25-1 Shinomiya Hiratsuka-shi, Kanagawa-ken 254-8555, Japan

Correspondence should be addressed to Junichi Fujimoto, junichi_fujimoto@gigaphoton.com

Received 10 May 2012; Accepted 20 June 2012

Academic Editor: Sergi Gallego

Copyright © 2012 Junichi Fujimoto et al. This is an open access article distributed under the Creative Commons Attribution License, which permits unrestricted use, distribution, and reproduction in any medium, provided the original work is properly cited.

Since 2002, we have been developing a carbon dioxide (CO₂) laser-produced tin (Sn) plasma (LPP) extreme ultraviolet (EUV) light source, which is the most promising solution because of the 13.5 nm wavelength high power (>200 W) light source for high volume manufacturing. EUV lithography is used for its high efficiency, power scalability, and spatial freedom around plasma. We believe that the LPP scheme is the most feasible candidate for the EUV light source for industrial use. We have several engineering data from our test tools, which include 93% Sn ionization rate, 98% Sn debris mitigation by a magnetic field, and 68% CO₂ laser energy absorption rate. The way of dispersion of Sn by prepulse laser is key to improve conversion efficiency (CE). We focus on prepulsed laser pulsed duration. When we have optimized pulse duration from nanosecond to picosecond, we have obtained maximum 4.7% CE (CO₂ laser to EUV; our previous data was 3.8%) at 2 mJ EUV pulse energy. Based on these data we are developing our first light source as our product: "GL200E." The latest data and the overview of EUV light source for the industrial EUV lithography are reviewed in this paper.

1. Introduction

Since 2002, Gigaphoton/Komatsu have been developing a laser plasma produced (LPP) extreme ultraviolet (EUV) light source based upon carbon dioxide (CO₂) laser-produced tin (Sn) plasma. The CO₂-Sn-LPP EUV light source is deemed to be the most promising solution, as the 13.5 nm wavelength high power (>200 W) light source for high volume manufacturing (HVM) EUV lithography (EUVL) [1–4], because of the high efficiency, power scalability, and spatial freedom around plasma. Therefore, we have chosen the LPP-EUV method. We believe that the CO₂-Sn-LPP scheme is the most feasible candidate for the EUV light source for HVM.

In order to meet the performance requirements for an EUV light source, we have focused on three enabling technologies:

- (1) high conversion efficiency (CE), efficiency from CO₂ laser to EUV light energy;

- (2) debris mitigation functionality, Sn debris mitigation from optical components;
- (3) CO₂ laser power usage, efficiency CO₂ laser energy into Sn.

We have investigated how Sn droplets under laser irradiation generate EUV light. Also investigated is Sn behavior, in vacuum environment, under irradiation of laser beams.

In this paper, we report on the present development status of our LPP light source for EUVL for HVM.

2. LPP EUV Light Source Equipment Configurations

The typical setup of an EUV light source system is shown in Figure 1.

Our EUV light source contains, four primary sections:

- (1) EUV vessel including droplet generator and collector mirror;

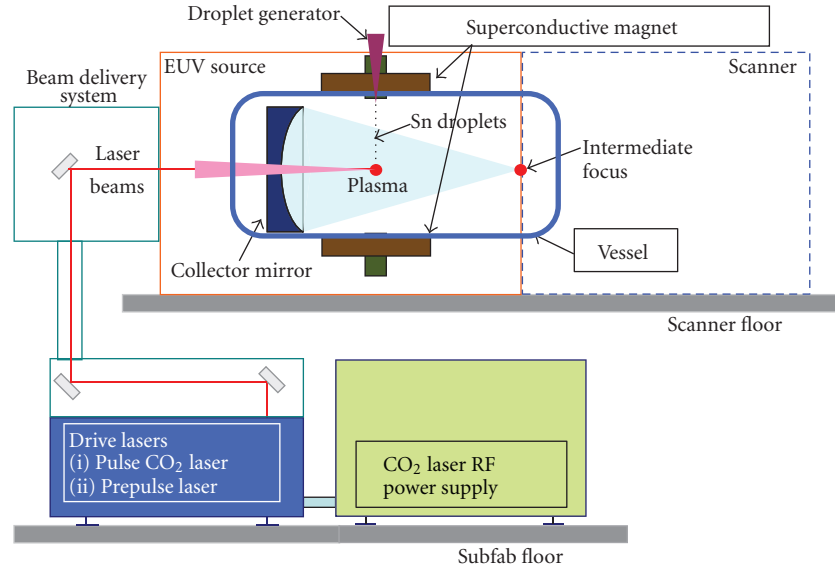


FIGURE 1: Typical layout of an LPP EUV light source.

- (2) superconductive magnets for tin debris mitigation;
- (3) plasma generation drive lasers, composed of prepulse laser and pulsed CO₂ laser;
- (4) CO₂ laser RF power supply system.

We are developing LPP-EUV light source based upon an experimental system. The small experimental light source tool is employed for Sn target shooting optimization. The features of this system are shown below. The GL200E proto system is used for system performance demonstration. Our target is to develop the GL200E system, which will be our first generation HVM EUV light source based upon the GL200E proto system.

2.1. Small Experimental Light Source Tool (Figure 2). We have investigated EUV plasma generation scheme with the use of the small experimental tool operated at the repetition rate of 10 Hz (maximum). Figure 2 shows the experimental setup for the basic investigation of EUV light generation and Sn debris mitigation [5–7].

The small experimental light source setup simulates the final system, except for the repetition rate of the driver laser and can be operated with and without magnetic field applied. It can simulate a 20 kW CO₂ laser with pulse energy of 200 mJ/pulse at low repetition rate of less than 10 Hz. The setup has various diagnostic features where Sn can be observed throughout the entire process from droplet generation to EUV plasma generation.

This tool is capable of simulating conditions of EUV light generation identical to those in GL200E, such as pulse duration, pulse energy of CO₂ laser, prepulse laser, Sn droplet size, and magnetic field environment with the only significant difference that it operates at a maximum repetition rate of 10 Hz. The tool's compactness makes it easier to measure results and optimize various plasma generation parameters.

The small experimental tool consists of various sub systems, including, a short-pulsed high-energy CO₂ laser, a prepulse laser, a Sn droplet generator, and a EUV vacuum vessel with a solenoid magnet. By using this tool, we are able to investigate EUV light emission under sequential prepulse laser and a CO₂ laser irradiation conditions. The development purpose for small experimental system is primarily debris mitigation analysis, Sn droplet and plasma formation and CO₂ laser energy consumption budget experiments.

2.2. GL200E Proto System (Figure 3). The prototype system of our first high volume manufacturing (HVM) EUV light source has a 100 kHz 20 kW CO₂ laser, 20 μm in diameter droplet generator, and magnetic field debris mitigation functionality.

The development purpose for the GL200E proto system is integration of all functionalities, testing and debugging based upon a HVM configured EUV light source. This system is planned to be integrated to a scanner system and to demonstrate actual lithographic performance. The target system specifications are shown in Table 1. The HVM system is required to balance many key performance aspects, such as: reliability, maintainability, footprint compactness and affordable operational cost.

3. Enabling Functions to Meet EUV Light Source Performance

There are some high level performance requirements necessary to be realized in order for LPP-EUV light source to be successful in the industry, high clean EUV power and EUV source reliability/availability for high volume continuous fab operation. In this section, we would like to discuss and demonstrate the basic enabling functionalities we are developing, in order to achieve the necessary performance.

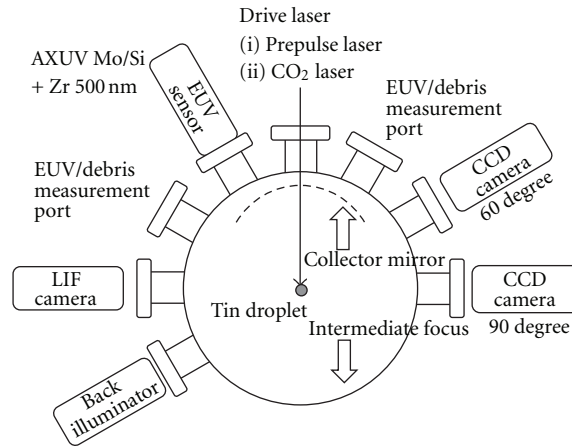


FIGURE 2: Diagram of small experimental tool.

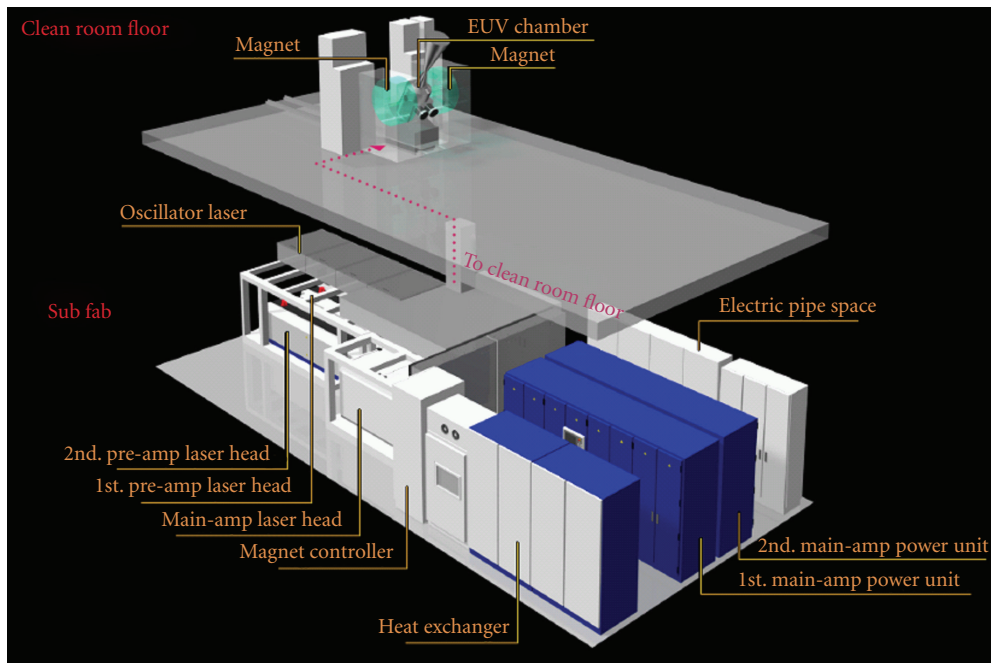


FIGURE 3: LPP EUV source system layout; Gigaphoton GL200E.

TABLE 1: Target specification of EUV source, GL200E for HVM.

Model number	Units	Gigaphoton GL200E
EUV clean power (at I/F)	W	250 (in-band; after filtering IR and DUV)
EUV pulse energy (at I/F)	mJ	~2.5
Max. rep. rate	kHz	~100
Max. CO ₂ laser system	kW	20 (100 kHz, 200 mJ/pulse)
Target material and shape		Liquid Sn droplet, spherical
Droplet size (diameter)	μm	10–30
Plasma creation scheme		Double-pulse laser shooting
Debris mitigation scheme		Hybrid: magnetic field guiding and chemical etching

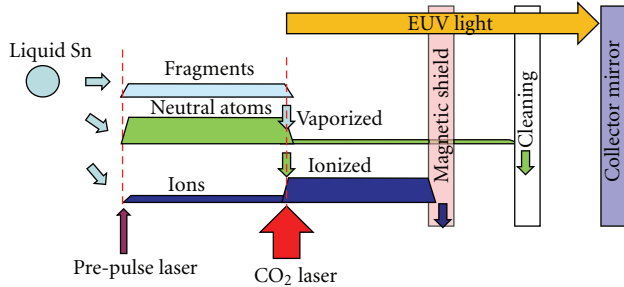


FIGURE 4: Droplet to Sn debris mitigation concept.

The basic enabling functionalities are:

- (1) Double pulse laser irradiation;
- (2) Sn debris mitigation by magnetic field.

Each function will be discussed at length in the following sections.

3.1. Double-Pulse Laser Irradiation. When a Sn droplet target is irradiated with a prepulse laser (wavelength $1.06\ \mu\text{m}$) beam and/or a CO_2 laser (wavelength $10.6\ \mu\text{m}$) beam, the Sn droplet in the vessel is converted into a plasma emitting EUV where several states of Sn exist simultaneously [6, 7]. Sn present during plasma generation is generally classified in three categories: fragments, neutral atoms, or ions. After emitting EUV light residues of the plasma are eventually scattered inside the vessel. To prevent the collector mirror from being contaminated, Sn debris needs to be trapped before being deposited onto the collector mirror surface or cleaned after deposition. This Sn-state scheme is shown in Figure 4.

To enhance EUV energy and to minimize Sn debris towards the collector mirror, the ionization of the Sn should be maximized in the laser irradiation processes. We believe that the shape of the Sn target is crucial [8–12]. To realize this, a double-laser irradiation process is utilized in our system. The theoretical [13] and experimental [14] data have clearly demonstrated the advantage of combining a laser beam at a wavelength of a CO_2 laser with Sn plasma to achieve high CE from driver laser pulse energy to EUV in-band energy [15].

The Sn fragments are generated during the prepulse irradiation. The Sn fragments are, at that moment, the majority of the Sn present. Fragments can reach a maximum of a few micrometers in diameter. The Sn fragments were measured by a shadowgraph method. Figure 5 shows the shadowgraphs of the fragments after the prepulse laser irradiation for the droplet with $20\ \mu\text{m}$ diameter. The droplet is irradiated by a prepulse laser originating from left hand side in the image. During laser irradiation, the Sn droplet is displaced away from the irradiation point while simultaneously expanding in diameter. Figure 5(e) shows the images after the prepulse laser irradiation without the main CO_2 laser irradiation. Figure 5(c) shows the images with the main CO_2 laser irradiation. Figure 5(d) is captured immediately after the EUV

light emission. When irradiation condition is optimized, the fragments have disappeared from the shadowgraph image.

The CE with the droplet target is measured. A CE of 3.5%, using $20\ \mu\text{m}$ diameter droplet and $200\ \text{mJ}$ CO_2 laser irradiation, has been demonstrated by optimizing the prepulse laser conditions as shown in Figure 6. We also have obtained greater than 3.7% CE, using $28\ \mu\text{m}$ droplet and $200\ \text{mJ}$ CO_2 laser energy irradiation. These data indicate that prepulse is very effective to enable high CE no dependence on droplet size in this range.

We have thus demonstrated the possibility to reduce the debris by use of a smaller $20\ \mu\text{m}$ diameter droplet target without degradation in CE. These basic studies, together with theoretical calculations, have contributed to the basic design and development of a high-power production machine capable for further EUV power scaling.

Figure 7 shows the clean EUV pulse energy (defined as “clean EUV” after filtering out of non-EUV band energy) obtained as a function of droplet size and CO_2 laser pulse energy using an optimal prepulse laser condition. Using the small experimental light source tool, and calculating based upon a targeted pulse repetition rate of $100\ \text{kHz}$, we have demonstrated using a $20\ \mu\text{m}$ droplet that $1.55\ \text{mJ}/\text{pulse}$ clean EUV pulse energy is achieved and therefore $>150\ \text{W}$ clean EUV power is possible. Further we demonstrated using a $40\ \mu\text{m}$ droplet that $2.52\ \text{mJ}$ clean EUV pulse energy is experimentally observed. Again, calculating for a $100\ \text{kHz}$ system, we can demonstrate that $>250\ \text{W}$ clean EUV power is achievable. It should be noted that with the use of the larger $40\ \mu\text{m}$ droplet, debris increased dramatically compared to the $20\ \mu\text{m}$ Sn droplet case. Therefore, in the future work, we will work further to optimize the $20\ \mu\text{m}$ Sn droplet experiment to target $>250\ \text{W}$ clean EUV power.

3.2. Sn Debris Mitigation by Magnetic Field. Our Sn debris mitigation is a simple concept based upon making use of a magnetic field capturing and channeling charged Sn ions away from critical parts of the EUV source system. During the process of EUV plasma creation, obtaining the optimum ratio of the three Sn categories (fragments, neutral atoms, and ions) is important from a debris mitigation perspective. When our double-pulse irradiation scheme and small droplets are combined, the majority of Sn ions are able to be trapped as Sn^{n+} within the magnetic field. The ionization rate of Sn will be described below in this section.

In order to mitigate Sn debris, a pair of superconductive magnetic coils is arranged on opposite sides of the vessel. In reality, however, not all of the Sn atoms and ions can be trapped in the magnetic field. Accordingly, our system is also equipped with a chemical etching mechanism. This chemical etching mechanism is designed to mitigate any remaining Sn atoms that could not have been trapped in the magnetic field and can potentially be deposited on the collector mirror surface or other optically sensitive locations.

The amount and the distribution of the Sn neutral atoms after the prepulse laser irradiation in a certain magnetic field were observed with a laser induced fluorescence (LIF)

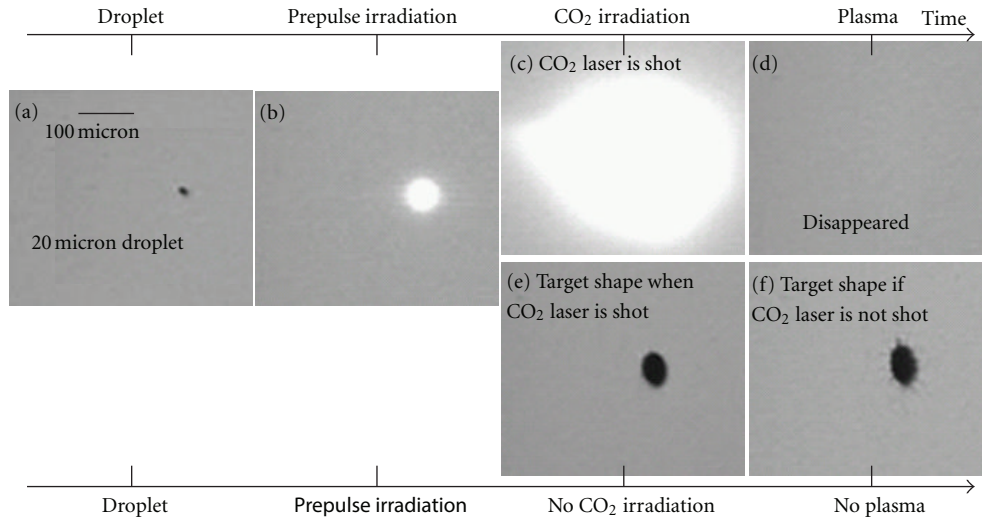


FIGURE 5: Shadowgraph images of Sn fragments.

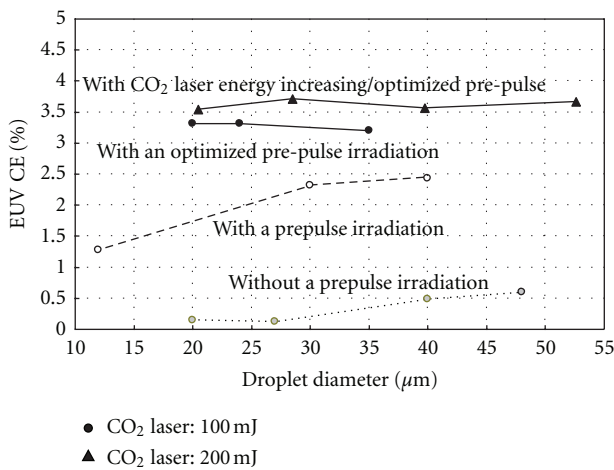


FIGURE 6: CE as a function of the droplet diameter.

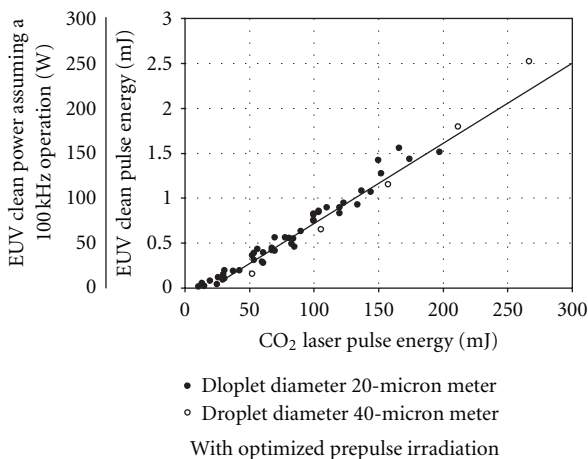


FIGURE 7: CE as a function of the CO₂ laser pulse energy.

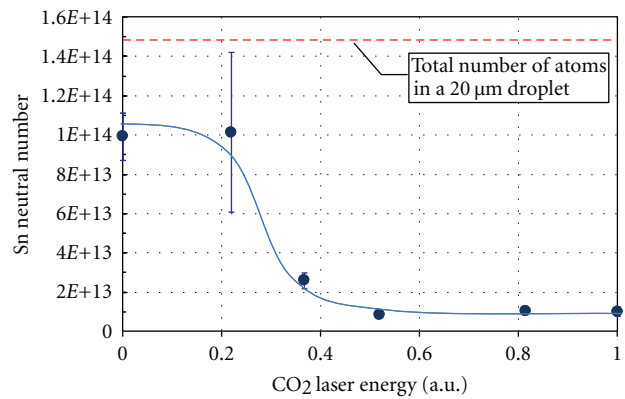


FIGURE 8: Sn neutral atoms versus CO₂ laser pulse energy.

experimental setup [16]. We conducted two experiments using the LIF metrology setup, with and without CO₂ laser irradiation, and then by comparing the two resultant signals, we are able to conclude 93% of the Sn atoms are ionized and 7% of the Sn atoms remain as neutral atoms. This ratio changes with CO₂ laser pulse energy, as shown in Figure 8 [7]. The experimental results indicate when above a certain threshold of CO₂ laser energy, almost all Sn atoms in the droplet are ionized. This is a very positive result, as it indicates that the Sn ionization rate remains constant when CO₂ irradiation energy exceeds a definable minimum energy level.

We measured the ion distribution with the faraday cup measurement [16] with and without a magnetic field. Two faraday cups are set at the position of the collector mirror, where a cup is located in a direction perpendicular to the direction of the magnetic field. The other cup is located where the magnetic flux converges. Based upon the assumption that the average valence of the Sn ion is two, we calculated the distribution and the collection rate of the ions

in the magnetic field. We tested with several magnetic field conditions. Figure 9 also indicates that the Sn ions are collected along the magnetic flux as the magnetic field is enhanced. The collection rate of the ions exceeds 98% under some magnetic field conditions.

The overall results are summarized; we have observed 30% fragments, 67% neutral atoms, and 3% ions from a 20 μm Sn droplet with only prepulse laser irradiation. After irradiate CO₂ laser, 0% of fragments, 7% of neutral atoms, and 93% of ions were observed.

3.3. CO₂ Laser Energy Consumption Budget. In the previous sections, we discussed Sn behavior during EUV light generation. From the drive laser point of view, we now turn to a discussion of energy transfer from CO₂ laser energy into Sn droplets. In an LPP EUV source, the CO₂ laser energy is either absorbed in the plasma, reflected from the plasma, or transmitted through the plasma. The reflected energy of the CO₂ laser can further be divided into three subcomponents: (a) reflection back into the CO₂ laser, (b) reflection onto the collector mirror, and (c) reflection onto the surrounding vessel wall. Figure 10 graphically shows the defined areas. In order to make an efficient system, it is preferred to maximize the absorbed energy into the Sn and minimize the reflected and (d) transmitted energy. Reducing the reflected energy back into the CO₂ laser will also reduce self-oscillation of the CO₂ laser which could limit the maximum power a drive laser could operate and damage components in the laser system. The energy distribution is measured in a plane parallel to the CO₂ laser entrance and for calculation purposes the reflected energy is assumed to scatter rotationally symmetric.

Figure 11 summarizes the results of CO₂ laser energy distribution with varying prepulse laser energy (pulse duration 10 nsec.). The CO₂ laser absorption ratio and CE increase with increasing prepulse energy. These results demonstrate that higher prepulse pulse energy is very effective to maximize CO₂ laser energy absorption into the Sn plasma and minimize transmission and reflection effects. And as expected, another positive aspect of increased prepulse pulse energy is increased absorption leading to improved CE [17].

CO₂ laser energy power distributions, under optimized conditions, are summarized 68% absorption, 26.6% reflected, and 5.4% transmitted CO₂ laser energy power. The 26.6% reflected power is further broken down to 3.9% back reflection into the CO₂ laser, 4.6% towards the collector mirror, and 18.1% reflected to the vessel walls. In the case of no prepulse irradiation, the transmission energy is significantly larger as Sn droplet size (20 μm) and CO₂ laser spot size (300 μm) are not matched. Optimal prepulse conditions therefore better match the physical sizes of the Sn mist to the CO₂ beam waist providing very high EUV transmissions with relatively low prepulse energies.

4. Optimization of Prepulse Laser Irradiation Conditions

4.1. Sn Target Formation Difference by Pulse Duration of Prepulse Laser. In the previous sections, we have shown

the prepulse is key to improve CE and our previous report has indicated higher prepulse energy supports higher CE [17]. However, the prepulse laser power is limited due to size and cost in the system. To improve the CE, we focus on the pulse duration of prepulse laser. Given that the pulse energy is the same, higher peak intensity is obtained with shorter pulse duration than with longer pulse duration. In this study, we conducted experiments using the two setups of the prepulse laser with different pulse durations and comparable pulse energy output. The one has nanosecond (nsec) pulse duration; the other has picosecond (psec) pulse duration. The maximum output of both laser setups is around 2.5 mJ. Table 2 shows the major experimental conditions on the small experimental light source tool that we have reported in the previous sections.

We have conducted tests with the two setups of prepulse laser energy pulse durations. We have compared the following phenomena:

- (i) transient phenomena of Sn target shape formations (Table 3);
- (ii) CE study by delay time dependency between prepulse laser and CO₂ laser with deferent prepulse laser energy (Figure 12 and Figure 13);
- (iii) target size expansion speed by prepulse laser energy at different laser pulse duration (Figure 15).

Table 3 shows the comparison of target shape formation in psec and nsec prepulse lasers. The pictures of two different delay time are shown to observe how target shape changes as time goes on. The targets were observed at 90 degree from the lasers irradiation angle. The target will be irradiated with CO₂ laser beam when it is expanding around 300 μm . However, it should be noted that this experiment was conducted without the CO₂ laser irradiation because we wanted to see the behavior of target shape change. The delay time between the prepulse laser irradiation and the CO₂ laser irradiation is indicated in the same scale in this paper.

Table 4 is summarized major difference of shape formation between the two pulse durations from the pictures of Table 3. Generally, on psec condition, the Sn target expansion speed is fast and fine while the expansion is slow and coarse on nsec condition.

4.2. CE versus Pulse Duration of Prepulse Laser. Figures 12 and 13 show CE difference by delay time dependency between the prepulse laser and the CO₂ laser with different prepulse laser energies. When the Sn target is expanding by prepulse laser irradiation, the shape and fragment size are also changing. These phenomena should affect CE.

Figure 12 shows the case of nsec prepulse laser. When we use nsec prepulse laser, we have obtained maximum 3.4% CE at 2.7 mJ pulse energy. The higher CE was obtained with higher laser pulse energy. The change in CE trend is not very significant with delay time change.

Figure 13 shows the case of the psec prepulse laser, we have obtained 4.7% CE at 2 mJ pulse energy. The higher CE was obtained with higher laser pulse energy. The delay time at highest CE is at 2.5 times faster than nsec prepulse duration.

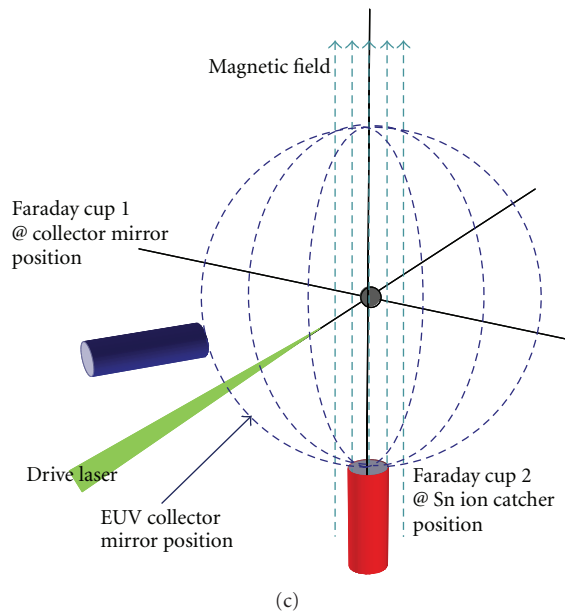
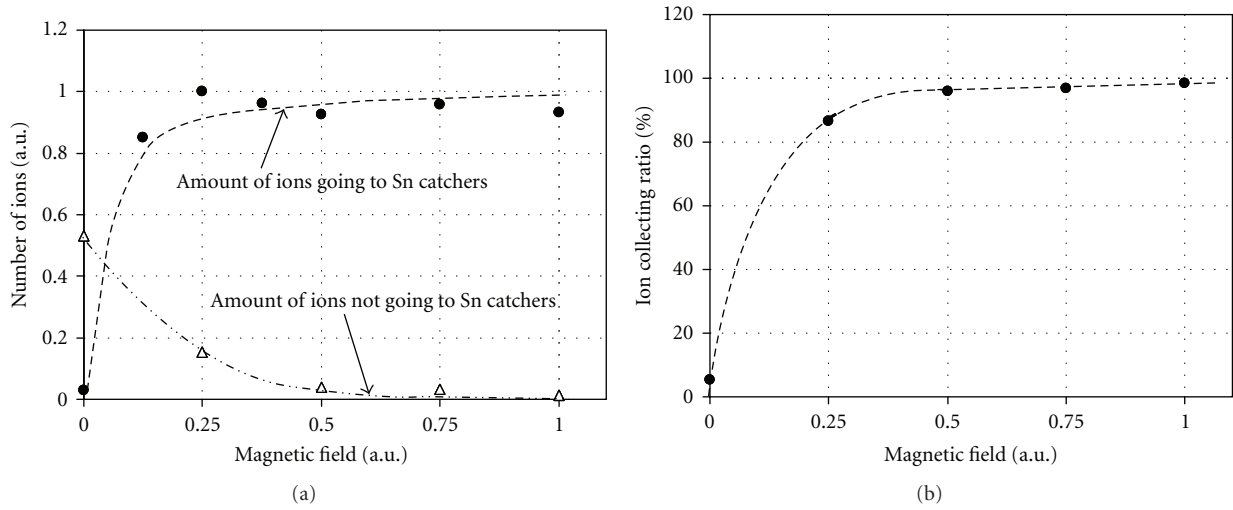


FIGURE 9: Sn ions collection rate versus magnetic field strength.

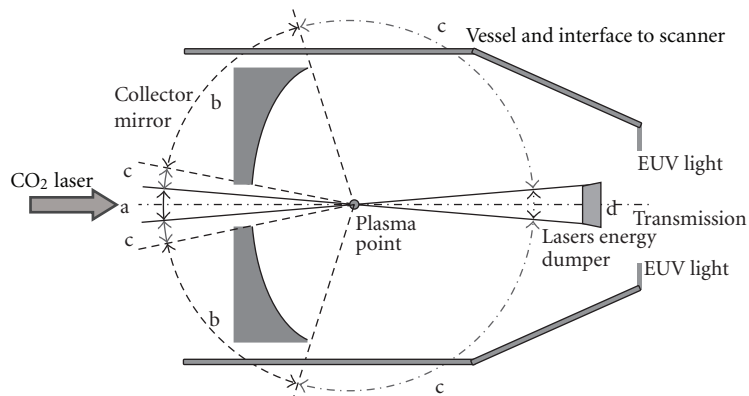


FIGURE 10: Category of reflected CO₂ laser energy; (a) reflection back into the CO₂ laser, (b) reflection onto the collector mirror, (c) reflection onto the surrounding vessel wall, and (d) transmitted energy.

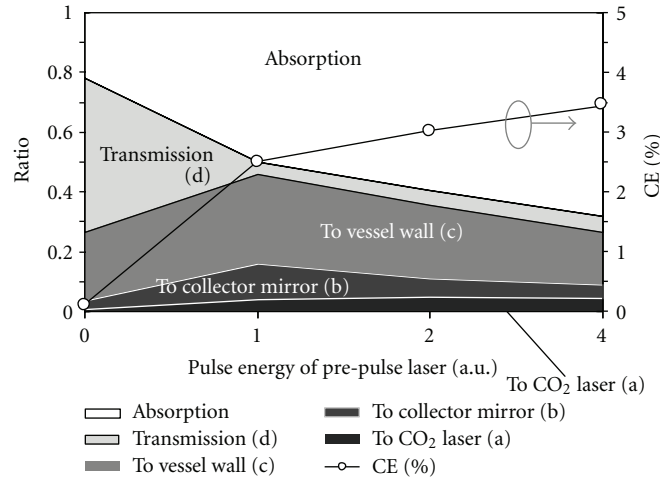


FIGURE 11: CO₂ laser energy distribution results versus prepulse condition laser energy.

TABLE 2: Major condition of small experimental light source.

		Unit	Setup 1	Value	Setup 2	
Sn droplet	Diameter	μm		21		
	Type of laser			YAG laser		
Pre pulse laser	Wave length	nm		1064		
	Pulse width	sec.	10 pico		10 nano	
	Pulse energy	mJ for 10 nsec.			max. 2.7	
		mJ for 10 psec.			max. 2.0	
CO ₂ laser	Pulse width	nsec (FWHM)		15		
	Pulse energy	mJ		0–150		
	Spot size	$\mu\text{m} (l/e^2)$		300		
	Plasma point			Beam waist of CO ₂ laser		
Laser pulse repetition rate		Hz		2		

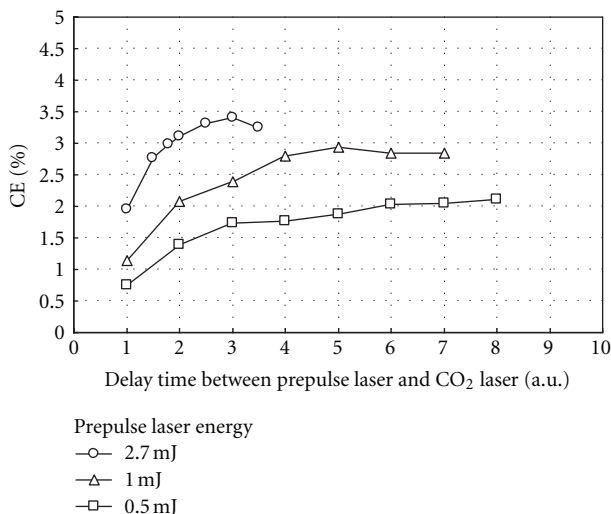


FIGURE 12: CE comparison with laser irradiation delay time between nsec prepulse & CO₂ laser.

The change in CE trend is precipitous with the delay time when the prepulse energy is not less than 0.5 mJ. These results suggest that target expansion speed is faster than psec, but size of Sn fragments are finer than nsec.

Figure 14 shows the relation between the CE and the prepulse energy on each pulse duration of prepulse laser.

The CE on 10 psec prepulse laser improves around 30 to 50% from the case of 10 nsec prepulse even though the prepulse laser energy is lower than nsec prepulse. The delay time of each point are optimized.

The speed of target expansion can be measured from the shadow graph pictures of the target as we have showed in the previous section. Figure 15 shows the comparison of the typical target expansion speed at nsec and psec pulse duration of prepulse laser. The speed of target expansion is increased with prepulse laser energy. The speed of psec pulse is about 4 to 5 times faster than that of nsec pulse. The almost maximum CEs on psec prepulse are obtained at 0.5 mJ or more of prepulse energy as shown in Figure 13.

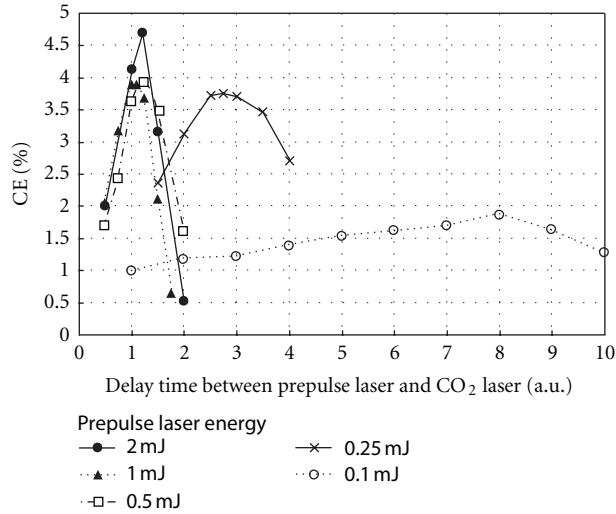


FIGURE 13: CE comparison with laser irradiation delay time between psec prepulse and CO₂ laser.

TABLE 3: Transient phenomena of Sn target shape with different prepulse laser pulse durations.

	Units				
Pulse duration	Sec	10 pico		10 nano	
Pulse energy	mJ	2		2.7	
Delay time between pre-pulse laser and CO ₂ laser	au.	1	2	1	2
Target shape 90 deg view					

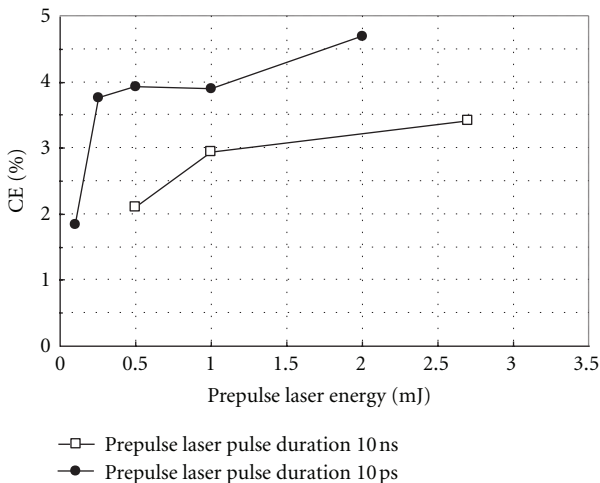


FIGURE 14: CE comparison between nsec and psec prepulse lasers.

When we look the target expansion speed, the change rates of speed are also saturated at 0.5 mJ or more of prepulse energy. The target size of these conditions is around 300–450 μm in diameter, which almost matches or a little bit larger them the CO₂ laser beam spot size (around 300–400 μm in diameter).

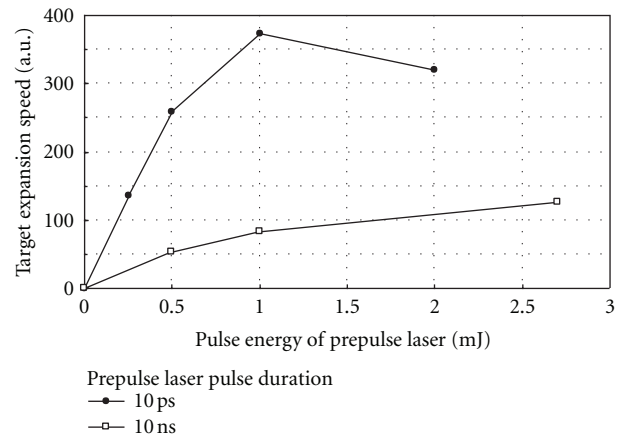


FIGURE 15: target expansion speed comparison between psec and nsec prepulse lasers.

5. Summary

We have investigated the EUV plasma generation scheme by use of a small experimental light source tool which operates at less than 10 Hz. We have proposed a double-laser pulse irradiation method to generate Sn plasma efficiently. We

TABLE 4: Characteristics of target formation between psec and nsec.

	Units		
Pulse duration	Sec.	10 pico	10 nano
Pulse energy	mJ	2.0	2.7
Delay time between pre pulse laser and CO ₂ laser	au.	1 and 2	1 and 2
Characteristic of target formation		√ Shape of laser side: dome shape of opposite side: dish	√ Shape of laser side: dish Shape of opposite side: dish
		√ Target formation scheme; shift to opposite side of lasers incident	√ Target formation scheme: shift to opposite side of lasers incident
		translation speed: slow	translation speed: fast
		Target expansion speed in diameter: fast Dispersion of target: fine	Target expansion speed in diameter: slow Dispersion of target: coarse

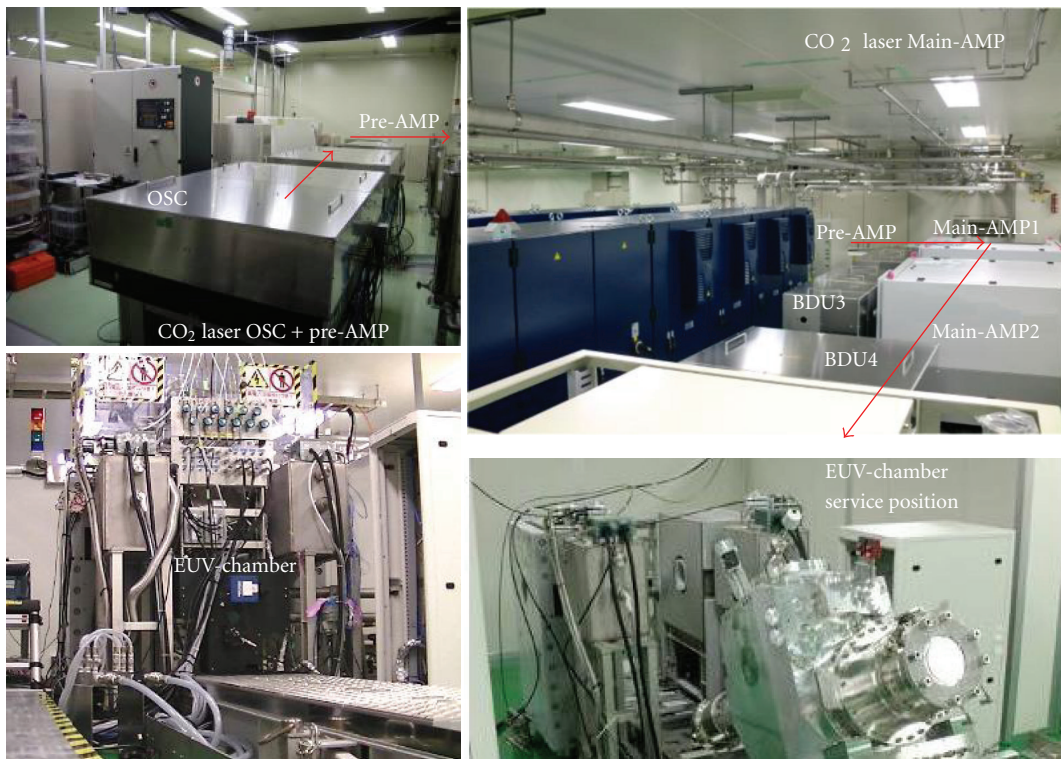


FIGURE 16: Picture of LPP-EUV light source system; Gigaphoton GL200E.

have obtained 93% Sn ionization rate when the droplets are irradiated with double-laser pulses under proper CO₂ laser pulse conditions. Also the CO₂ laser absorption ratio is up to 68%, reflected CO₂ laser energy back into the CO₂ laser is 3.9%.

When we have optimized the prepulse laser pulse duration, we obtained maximum 4.7% CE at 2 mJ prepulse laser energy and with 10 psec pulse duration. The pulse duration of prepulse laser was 10 nsec previously; CE was 3.8% at a maximum. These results indicate, there is plenty room for improvement on CE and the prepulse laser output condition to design HVM LPP-EUV source. The efficiency improvement is very important, because it impacts power

consumptions, heat load management, system size, and the cost of the whole system.

Based on these engineering results from the small experimental light source tool, we are continuing our development of our first generation EUV light source for HVM: "Gigaphoton GL200E." This system implements the following original concepts:

- (1) highly efficient Sn plasma generation driven by pulsed CO₂ laser;
- (2) double-pulse irradiation scheme for Sn plasma generation;

- (3) Sn debris mitigation by a magnetic field and small Sn droplet size (20 μm);
- (4) hybrid CO₂ laser system using a combination of a short pulse oscillator and commercial cw-CO₂ amplifiers [18, 19].

The design concepts are also reported. These data indicate that our LPP-EUV light source with the magnetic field debris mitigation system will be integrated to the HVM EUVL source system in the near future (Figure 16).

Acknowledgment

This work was partly supported by the New Energy and Industrial Technology Development Organization (NEDO), Japan.

References

- [1] H. Mizoguchi, T. Abe, Y. Watanabe et al., "1st generation laser-produced plasma source system for HVM EUV lithography," in *Proceedings of the SEMATECH Extreme Ultraviolet (EUV) Lithography Symposium*, Kobe, Japan, 2010.
- [2] H. Mizoguchi, T. Abe, Y. Watanabe et al., "1st generation laser-produced plasma source system for HVM EUV lithography," in *Extreme Ultraviolet (EUV) Lithography*, vol. 7636 of *Proceedings of SPIE*, 2010.
- [3] H. Mizoguchi, T. Abe, Y. Watanabe et al., "100W 1st generation laser-produced plasma light source system for HVM EUV lithography," in *Extreme Ultraviolet (EUV) Lithography II*, vol. 7969 of *Proceedings of SPIE*, 2011.
- [4] J. Fujimoto, T. Suzuki, H. Nakarai et al., "Development of LPP-EUV Source for HVM EUVL," in *Proceedings of the International Symposium on Extreme Ultraviolet (EUV) Lithography*, 2011.
- [5] T. Hori, T. Yanagida, T. Yabu et al., "Investigation on high conversion efficiency and Tin debris mitigation for laser produced plasma EUV light source," in *Proceedings of the SEMATECH Extreme Ultraviolet (EUV) Lithography Symposium*, Kobe, JAPAN, 2010.
- [6] T. Yanagida, H. Nagano, Y. Wada et al., "Characterization and optimization of tin particle mitigation and EUV conversion efficiency in a laser produced plasma EUV light source," in *Extreme Ultraviolet (EUV) Lithography II*, vol. 7969 of *Proceedings of SPIE*, 2011.
- [7] J. Fujimoto, T. Abe, S. Tanaka et al., "Laser-Produced Plasma based EUV light source technology for HVM EUV lithography," *Journal of Micro/Nanolithography MEMS, and MOEMS*, vol. 11, no. 2, 2012.
- [8] P. Dunne, G. O'Sullivan, and D. O'Reilly, "Prepulse-enhanced narrow bandwidth soft x-ray emission from a low debris, subnanosecond, laser plasma source," *Applied Physics Letters*, vol. 76, no. 1, pp. 34–36, 2000.
- [9] S. Fujioka, H. Nishimura, K. Nishihara et al., "Opacity effect on extreme ultraviolet radiation from laser-produced tin plasmas," *Physical Review Letters*, vol. 95, no. 23, Article ID 235004, 4 pages, 2005.
- [10] T. Higashiguchi, K. Kawasaki, W. Sasaki, and S. Kubodera, "Enhancement of extreme ultraviolet emission from a lithium plasma by use of dual laser pulses," *Applied Physics Letters*, vol. 88, no. 16, Article ID 161502, 2006.
- [11] T. Higashiguchi, M. Kaku, M. Katto, and S. Kubodera, "Suppression of suprathermal ions from a colloidal microjet target containing Sn O₂ nanoparticles by using double laser pulses," *Applied Physics Letters*, vol. 91, no. 15, Article ID 151503, 2007.
- [12] K. Nishihara, A. Sunahara, A. Sasaki et al., "Plasma physics and radiation hydrodynamics in developing," *Physics of Plasmas*, vol. 15, no. 5, Article ID 056708, 2008.
- [13] K. Nishihara, A. Sasaki, A. Sunahara, and T. Nishikawa, *EUV Sources for Lithography*, Edited by V. Bakshi, chapter 11, SPIE, Bellingham, Wash, USA, 2005.
- [14] H. Tanaka, A. Matsumoto, K. Akinaga, A. Takahashi, and T. Okada, "Comparative study on emission characteristics of extreme ultraviolet radiation from CO₂ and Nd:YAG laser-produced tin plasmas," *Applied Physics Letters*, vol. 87, no. 4, Article ID 041503, 3 pages, 2005.
- [15] H. Hoshino, T. Sukanuma, T. Asayama et al., "LPP EUV light source employing high power CO₂ laser," in *Emerging Lithographic Technologies XII*, vol. 6921 of *Proceedings of SPIE*, 2008.
- [16] Y. Ueno, H. Hoshino, T. Ariga et al., "Characterization of various Sn targets with respect to debris and fast ion generation," in *Emerging Lithographic Technologies XI*, vol. 6517 of *Proceedings of SPIE*, 2007.
- [17] J. Fujimoto, T. Hori, T. Yanagida et al., "Development of laser-produced plasma based EUV light source technology for HVM EUV lithography," in *Extreme Ultraviolet (EUV) Lithography III*, vol. 8322 of *Proceedings of SPIE*, 2012.
- [18] J. Fujimoto, T. Ohta, K. M. Nowak et al., "Development of the reliable 20 kW class pulsed carbon dioxide laser system for LPP EUV light source," in *Extreme Ultraviolet (EUV) Lithography II*, vol. 7969 of *Proceedings of SPIE*, 2011.
- [19] T. Ohta, K. M. Nowak, T. Sukanuma et al., "Development of the reliable 20 kW class pulsed carbon dioxide laser system for LPP EUV light source," in *Extreme Ultraviolet (EUV) Lithography II*, vol. 8322 of *Proceedings of SPIE*, 2012.

Research Article

Design and Analysis of a THz Metamaterial Structure with High Refractive Index at Two Frequencies

Zan Lu,¹ Bruno Camps-Raga,² and N. E. Islam¹

¹Electrical and Computer Engineering Department, University of Missouri, Columbia, MO 65201, USA

²MR: comp GmbH, Fuchs Pass 21, 46282 Gelsenkirchen, Germany

Correspondence should be addressed to N. E. Islam, islamn@missouri.edu

Received 25 April 2012; Accepted 11 July 2012

Academic Editor: Yasuo Tomita

Copyright © 2012 Zan Lu et al. This is an open access article distributed under the Creative Commons Attribution License, which permits unrestricted use, distribution, and reproduction in any medium, provided the original work is properly cited.

The concept of a single frequency band, single high-refractive-index metamaterial has been extended and applied in the design of dual frequency band, dual high-refractive-index metamaterials in the THz regime. The structure design consists of twenty five unit cells with a surface area of 250 μm by 250 μm and a thickness of 5 μm . Each cell has metallic structures embedded in a polyimide substrate. The return loss (S-parameter) analysis shows two strong electric responses at two frequency ranges, and the extracted constitutive parameters suggested high values of simultaneous dielectric constant and permeability at these frequencies. Results retrieved from the S-parameters also show high refractive index values. A first peak refractive index of 61.83 was observed at a resonant frequency of 0.384 THz, and another peak refractive index of 19.2 was observed at the resonant frequency 1.416 THz. Analysis show that higher refractive index at the second resonance frequency band is achievable through redesign of the structures, and modifications could lead to a single structure with multiple frequency, multiple high-refractive-index metamaterials that can be put to practical use.

1. Introduction

In recent years, metamaterials have been designed to operate in a broad frequency range, including the microwave [1], terahertz [2], and the infrared [3] regimes. Material design parameters include high refractive index [4], extraordinary optical transmission [5], negative refractive index, permittivity, and permeability values [6–9]. Characterizing the structure responses has been made easier because of the well-known properties of the embedded metallic (e.g., Cu, Au) designs. In the THz regime, Singh and his colleagues have studied the material characteristics extensively [10–16], including optically thin metamaterials [10], effects on resonance due to (i) material permittivity [11] and (ii) nearest neighbor interactions [13]. Metamaterials in the THz regime are of interest because of their applications [17].

In the past few years, great advances in the development of high-refractive-index metamaterials in the THz regime have been reported. Structures such as metallic wires [18], metallic films with cut slit [19], and specific designed

“I” shape structure [20] have been designed and used in experiments and their performance as high-refractive-index material analyzed.

However, almost all metamaterial structures designed for high-refractive-index do so at a single frequency band. Since potential applications in the THz regime could require wideband, it would be desirable, for practical usage, to have a multiband high refractive index metamaterials. Thus, the focus of research for many is the design of multi-THz, high-refractive-index metamaterials. Design of two resonant frequencies in a metamaterial structure has been reported earlier [21, 22], but the high refractive index needed for the applications was not shown. In this paper, we report on the development of a metamaterial structure that can have two or more wide bands with high-refractive-index value in the THz regime. With this brief introduction, the rest of the paper is divided as follows: in Section 2, the theory on designing the structure is described, while Section 3 shows the simulation and the design effort. The results are analyzed in Section 4, while we conclude in Section 5.

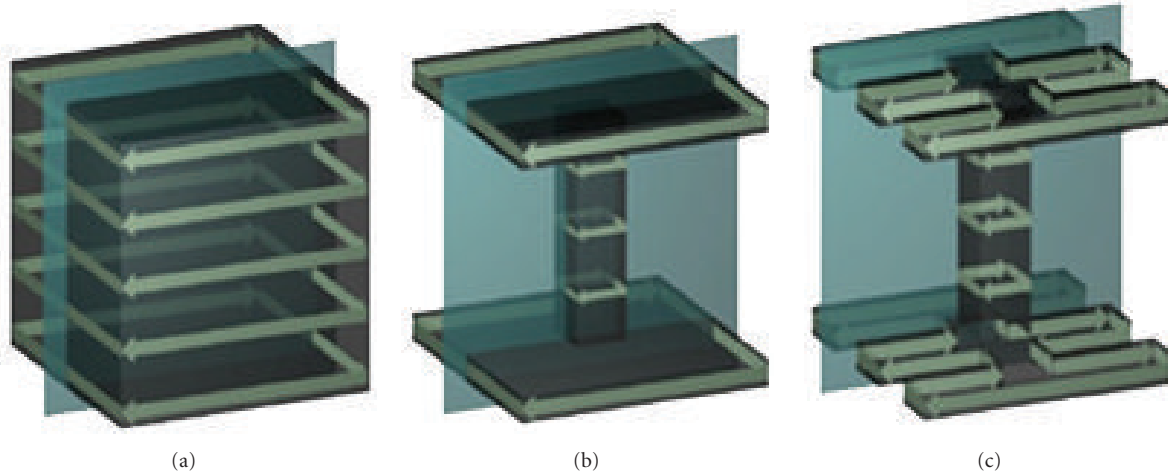


FIGURE 1: Current distribution when magnetic field is applied to the structure, from [23].

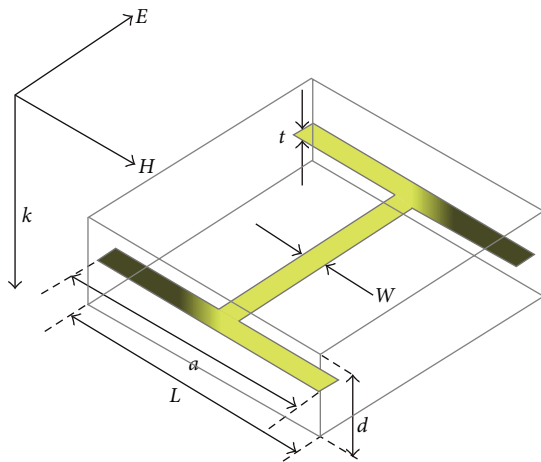


FIGURE 2: Schematic plot of the single "T" shape structure, from [20].

2. Background

The refractive index n is related to a material's relative permittivity and the relative permeability ϵ_r and μ_r , through the relationship $n = \sqrt{\epsilon_r \times \mu_r}$. To achieve a higher-refractive-index value in a metamaterial design, the dielectric constant and the permeability need to be enhanced at the same time. A high dielectric constant value can be achieved through an electric resonance that results from a strong capacitive response, as indicated in a previous work [18, 19]. However, such designs may also have a strong diamagnetic response induced by the current loop on the surface of the structure that is normal to the electric field, thus making the effective permeability of the metamaterial relatively small ($u \ll 1$). A reduction of the diamagnetic effect in the structure can be achieved through interactions with a propagating electromagnetic wave, by reducing the area subtended by the current loop that is parallel to the magnetic field to decrease the magnetic dipole moment to the maximum

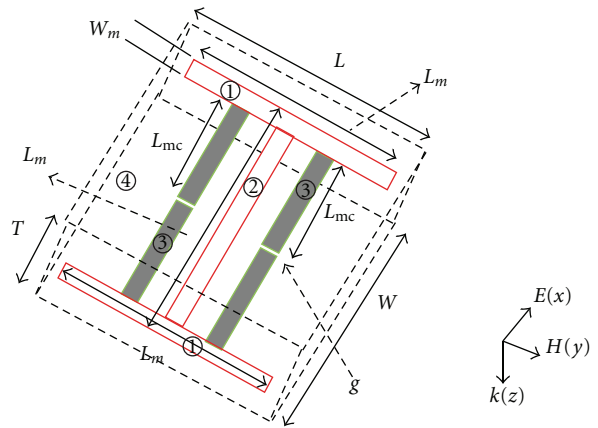


FIGURE 3: Schematic plot of the single-unit cell design.

extent possible. In this way, the strong capacitive response is maintained while the diamagnetic response is suppressed in the structure. Shin and his research utilized the principle of diamagnetic response suppression in producing a high-refractive-index value [23].

Figures 1(a)–1(c) show the configuration used by Shin in suppressing the diamagnetic effect of the structure. Figure 1(a) shows a metallic cube-like structure exposed to the magnetic field with a large area surrounded by the current loops induced on the surface of the structure, while Figure 1(b) shows the modified structure with a bar connecting the top and bottom panel to decrease the area surrounded by the induced current loop. In Figure 1(c), it shows an even improved structure with cut slits on the top and bottom panel of the structure to reduce the area surrounded by the current loop while maintaining the electric charge. According to the fringe-field effect [24, 25], the total surface charge on the top and bottom panel remains the same as the one without cut slits. As a result, the electric response remains the same while the diamagnetic response

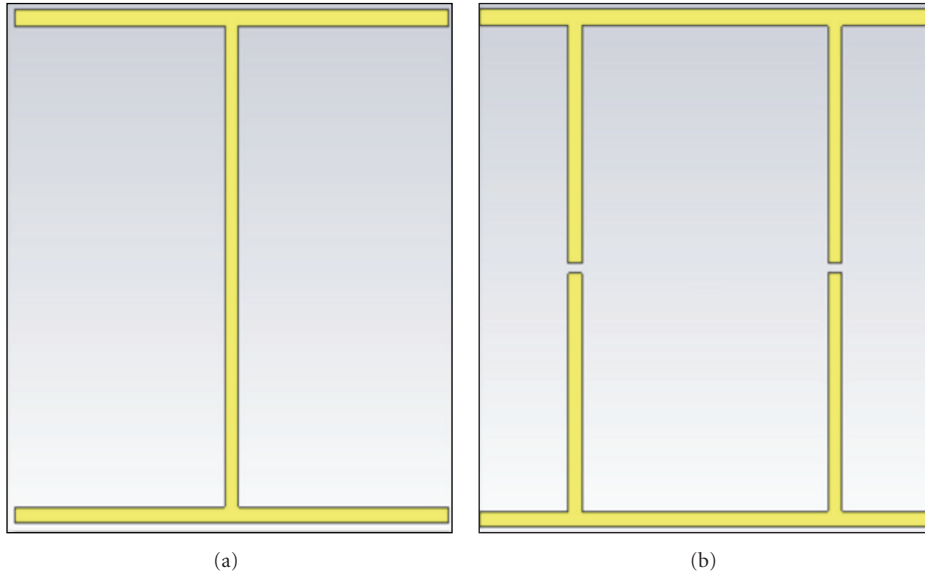


FIGURE 4: Schematic plot of the single band structures. (a) is the “I” shape structure with a lower resonant frequency band, and (b) is the cut wire structure with a higher resonant frequency band.

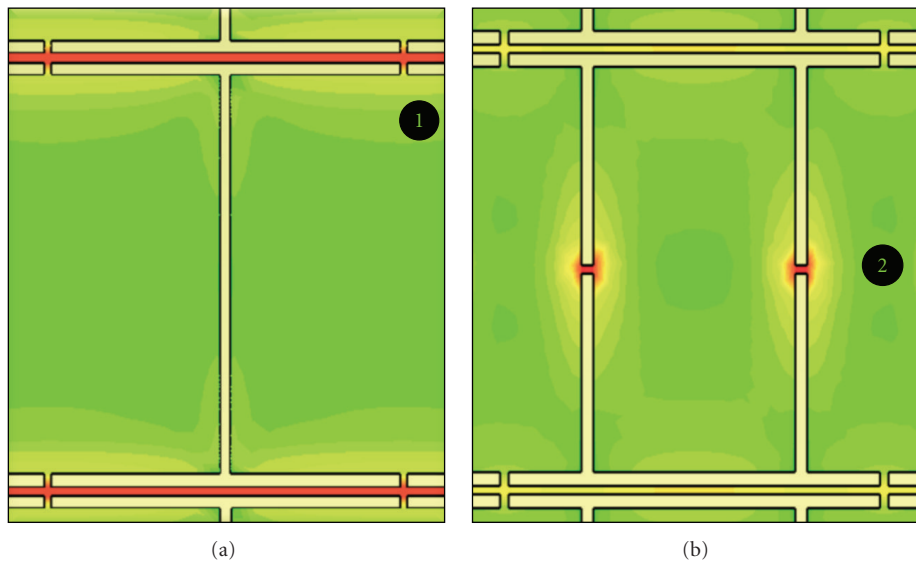


FIGURE 5: Normal of the electric field distribution on the single band structures. (a) is the field distribution on the “I” shape structure, and (b) is the field distribution on the cut wire structure.

is reduced when the area parallel to the magnetic field as produced in Figure 1(a) is made smaller by etching the surfaces as shown in Figure 1(c).

Another “I” shape structure in the terahertz frequency range that shows ultrahigh electric resonant value and low diamagnetic response was introduced by Choi recently [20] and is shown in Figure 2. This structure has high refractive index optimized from Shin’s work [23].

However, all such structures designed so far exhibit high refractive index at a single THz frequency band. Thus, there is a need to design a dual or multiband metamaterial structure with high refractive index at each band, such that

a single structure can be tuned to a specific application, if necessary. In this paper, we design and discuss such a metamaterial structure that has multiband, high-refractive-index values [26]. Our research builds on and integrates previous work discussed earlier.

3. Design and Simulation

Figure 3 shows the unit structure of the proposed metamaterial that produces high refractive index at each frequency band. Like the previously described single-band high-refractive-index material, this structure is also the result of

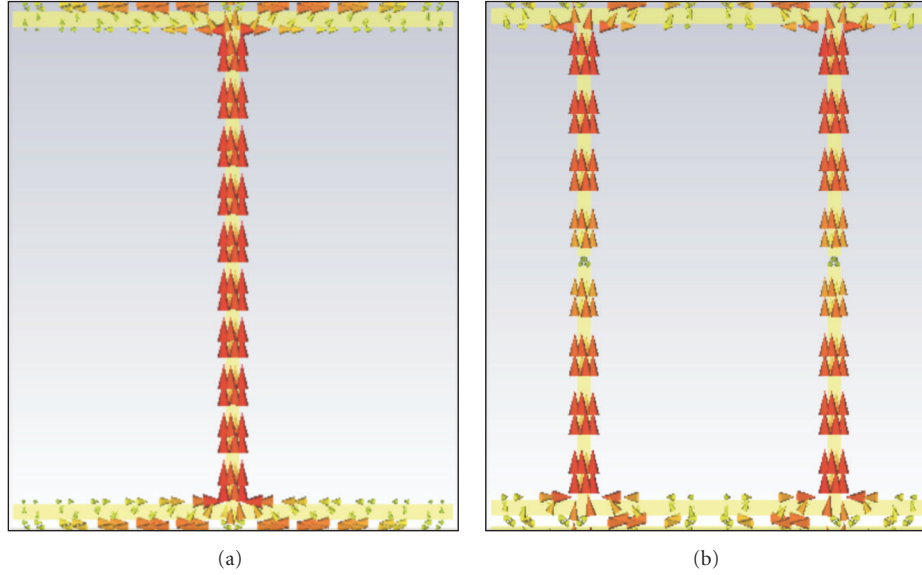


FIGURE 6: Surface current distribution of the single band structures. (a) shows the current distribution of the single “I” shape structure, and (b) shows the current distribution of the cut wire structures.

TABLE 1: Dimensions and components of the designed structure.

Location	Length	Width	Thickness
(1) Top and bottom bar, Au	$L_m = 49 \text{ um}$	$W_m = 1.5 \text{ um}$	0.1 um
(2) Center bar, Au	$L_m - 2 \times W_m = 46 \text{ um}$	$W_m = 1.5 \text{ um}$	0.1 um
(3) Cut wires, Au	$g = L - W; L_{mc} = (46 - g)/2$	$W_m = 1.5 \text{ um}$	0.1 um
(4) Substrate, polyimide	$L = 50 \text{ um}$	$W = 49 \text{ um}$	5 um

a number of iterations in the simulation effort that finally resulted in the configuration shown here.

The metallic structure (gold) is embedded in the center of a substrate made with polyimide. The thickness of the embedded metallic structure is 0.1 um, and the width of the metal is kept at 1.5 um in order to reduce the diamagnetic effect caused by the magnetic dipole that results from the current loop surrounding the structure. Table 1 details the dimensions associated with of the unit cell shown in Figure 3. Commercial software, the CST Microwave Studio, was used to simulate the effects of electromagnetic wave interactions with the metamaterial. The background and boundary conditions of the unit cell were set up properly to make the wave propagate and polarize in the desired direction. In the simulation, two waveguide ports were used to generate and receive the polarized THz wave, which is incident normally on the substrate along the z -direction with the electric field in the x -direction parallel to the metallic structure and magnetic field in the y -direction. It should be noted that the properties of the THz material could be affected at oblique incidence [24] and are not studied here.

3.1. Individual Structure Simulation. Since the modified design for dual frequency response presented here combines two separate high-refractive-index single frequency metamaterial designs, the response mechanism of the modified design can be best understood when the single frequency

structures are analyzed first. Figures 4(a) and 4(b) show the two high refractive index, single frequency structures. In both these designs, the metallic structures are embedded in polyimide foam and have five by five unit cells. The dimensions of both the structures are kept the same so that a reasonable comparison of their characteristics is possible.

When exposed to the electromagnetic field, surface charges accumulate on the top and bottom bar in the y -direction, which will then induce surface current along the center bar and the cut wires, as shown in Figures 6(a) and 6(b) and capacitors developed between the units in structure of Figure 5(a), while similar capacitors developed between the gaps of the two split bars in Figure 5(b). These capacitive resonances are reflected as two electric responses. Figures 5(a) and 5(b) show the induced electric resonance areas, marked as in Figure 5(a) and in Figure 5(b) with red color indicating the highest level of the induced electric field. This will be evident in the transmission plot and the extracted permittivity and permeability plot later.

These electric responses are also evident from the surface current distribution on the metallic structure. Figure 6(a) shows a strong current induced along the centers bar of the structure, resulting in the capacitive response between the gaps which induces the electric resonances. On the other hand, Figure 6(b) shows two induced surface current on the two sets of cut wires along the same direction. The two capacitive responses in the gaps couple with each other to

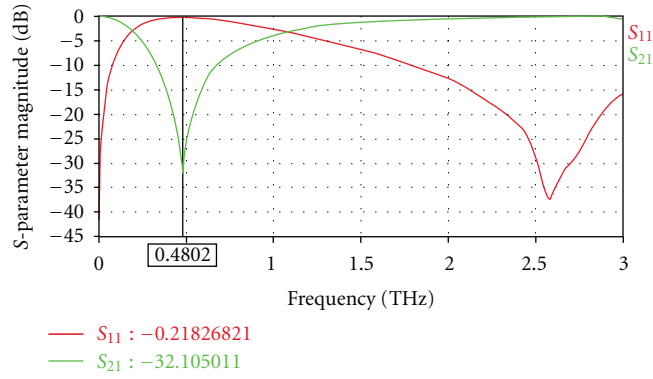


FIGURE 7: Transmission and reflection of the “I” shape structure. The resonant frequency is around 0.48 THz.

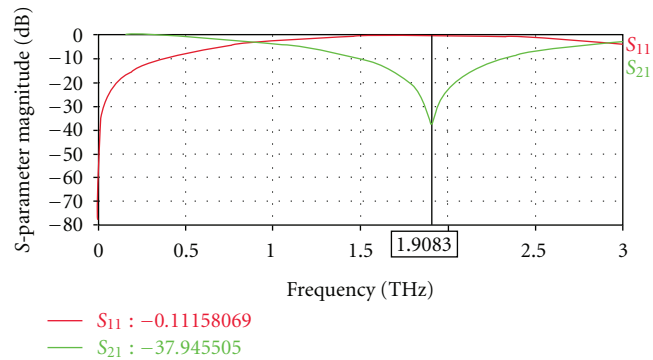


FIGURE 8: Transmission and reflection of the cut wire structure. The resonant frequency is around 1.9 THz.

provide a strong electric resonance, which is even stronger than the single-bar resonance. The resonance of the two structures is displayed in the plot of the transmittance in Figure 7. The lowest value of the transmission indicates the resonant frequency of the structure.

The resonance frequency band for structures in Figures 5(a) and 5(b) can be determined from the transmittance and reflectance plots of the structures, as shown in Figures 7 and 8. For the structure in Figure 5(a), the resonant frequency lies near 0.48 THz where the transmission reaches -32dB , while structure in Figure 5(b) has a resonant frequency at near 1.9 THz where transmission reaches -38dB . The second resonant frequency exhibits lower and broader electric response than the first one (Figure 8). We consider that the current distribution on the two sets of split cut wires and the corresponding capacitive response contribute the most to the second resonant frequency of the structure. The difference between the two plots indicates that it might have more broad use within the second resonant frequency band, which is even broader than the first resonant frequency band.

3.2. *Combined Structure Simulation.* The combined structure is shown in Figure 9, where the dimensions are the same as the single band structure simulated in the previous section.

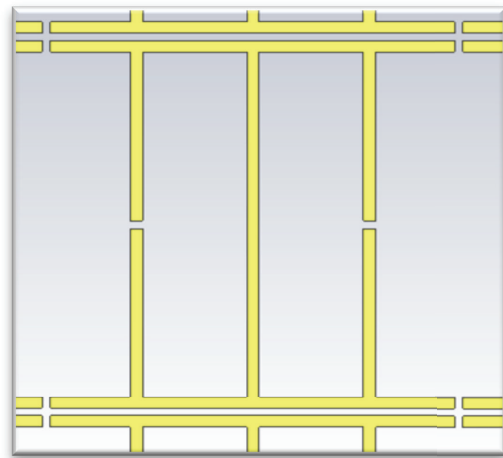


FIGURE 9: Schematic plot of the new design with dual band of resonant frequency.

Figure 10 is the transmittance and reflectance of the simulated combined structure. As known, the lowest point of the two transmissions reflects the strongest point of the resonance. The result clearly exhibits two strong resonant frequencies with a lower value of 0.416 THz and another one at a higher frequency of 2.046 THz.

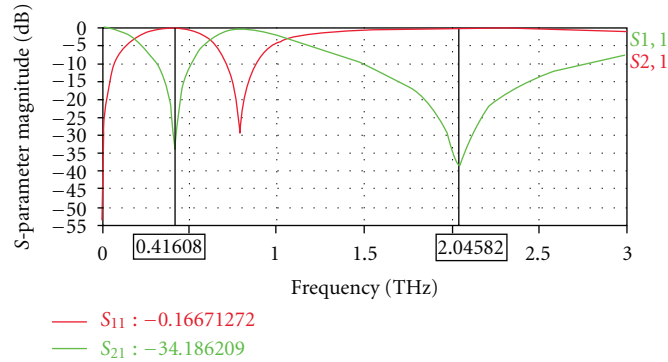


FIGURE 10: Transmission and reflection of the designed dual band metamaterial.

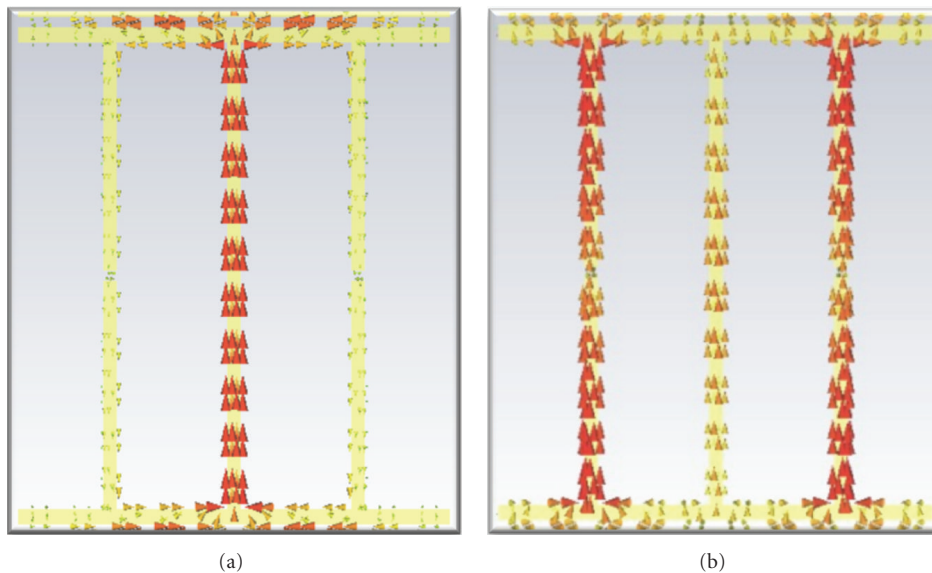


FIGURE 11: Current distribution at different resonant frequencies. The left figure indicates the lower resonant frequency with strong current distribution in the center bar. The figure on the right indicates the higher resonant frequency with current distribution mostly on the cut wires.

Here, the resonant frequencies of the combined structure have shifted a little as compared to the two individual structures shown earlier. The shift in the resonant peak frequency could be attributed to the coupling of the two surface currents induced in the modified structure at two resonance frequencies.

The structure in Figure 11(a) shows the current distribution at a resonant frequency of 0.416 THz. In this case, the electric response is mainly due to the strong current induced in the center bar. The structure in Figure 11(b) shows a current distribution at a higher resonance frequency of 2.046 THz. Here, the majority of the current is distributed on the side cut wires. These current distribution plots at different frequencies clearly show not only onset of two resonance frequencies for the modified structure, but also the fact that due to the presence of charges in the structures, there is a shift in the resonance frequencies when the original structure had only one embedded metallic structure in the dielectric. The final step in our analysis is to demonstrate the high-refractive-index values in the two

resonant frequencies for the proposed modified structure. We only compare the two cases: the “I” shape (Figure 5(a)) structure and the new modified structure as shown in Figure 9.

4. High-Refractive-Index Analysis

The intrinsic properties of the metamaterial structures can be retrieved by using the scattering parameters S_{11} and S_{21} and a method previously used by Smith and so forth [26]. The effective permittivity and the effective permeability for the comparison in both cases are extracted from the S-parameters, which are shown in the plot as the transmission and reflection of the simulated structure. Figures 7 and 10 show the S-parameter for the single frequency band structure (Figure 5(a)) and the dual frequency band modified structure (Figure 9), respectively.

In the first case of the “I” shape structure, a strong electric response and a high value of relative permeability are evident due to a strong coupling between the metallic

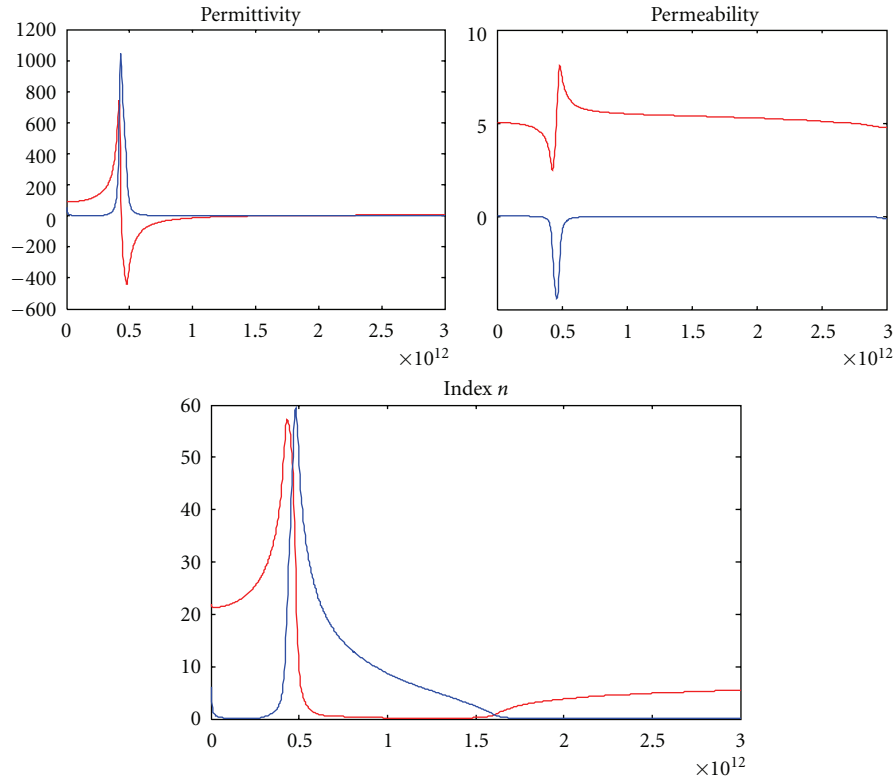


FIGURE 12: The upper left and right are the permittivity and permeability of the single frequency band metamaterial. The lower figure is the extracted refractive index of the metamaterial.

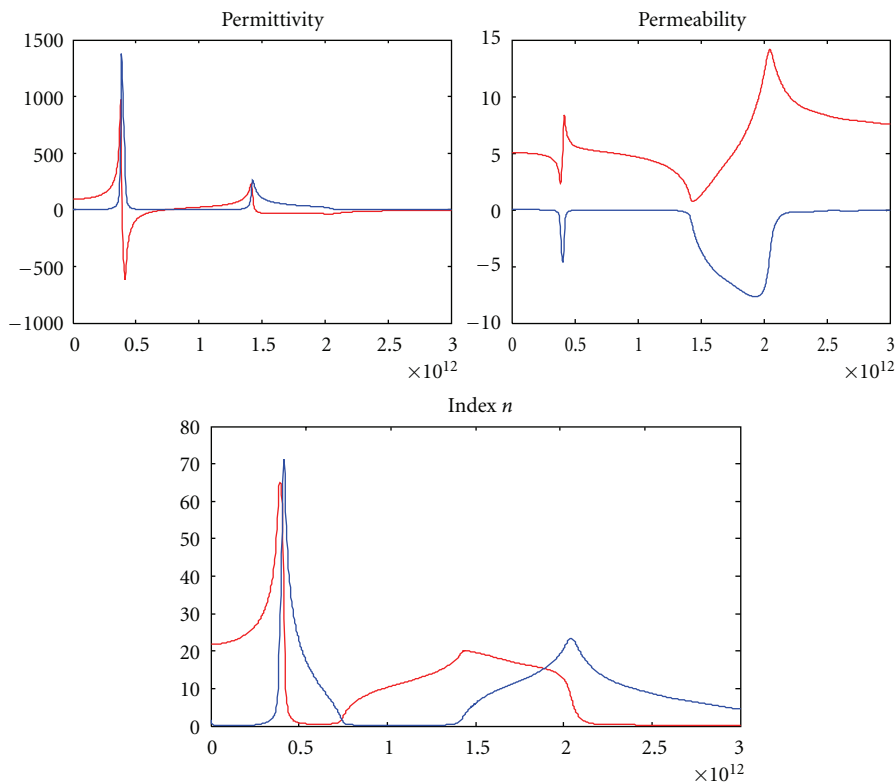


FIGURE 13: The upper left and right are the permittivity and permeability of the dual frequency band metamaterial. The lower figure is the extracted refractive index of the metamaterial.

units and the small area surrounded by the current loop parallel to the magnetic field. Figure 12 shows the retrieved permittivity and permeability of the “I” shape structure, where the relative permittivity reaches a high value of 715.1 at the frequency of 0.42 THz, and the relative permeability is 2.646 at the same frequency. The corresponding refractive index reaches 53.42 at this frequency. The result on one hand approves the research and theory of the early design [19], while on the other hand, it provides the comparison with the dual resonant structure in the resonant frequency band and the refractive index value.

Compared with the single frequency band structure in the first case, there exists, significant difference in the resonant frequency and the intrinsic parameters in the second case of the dual band frequency structure. As seen in Figure 13, there are two resonance peaks in the operating frequency range which results in two relative permittivity peak values of the 802.6 and 227 at 0.384 THz and 1.416 THz, respectively. The corresponding relative permeability at these frequencies is 2.381 and 1.153. Thus, the refractive index at 0.384 THz is 61.83 and 19.2 at 1.416 THz.

The first resonant frequency proves an enhancement in the relative permittivity due to the coupling effects between the center bar and the cut wires and a small decrease in the relative permeability due to the enlarged area of surface surrounded by the current loops. However, the second electric and magnetic resonances in the operating frequency appear to be not as strong as the first one in this design. The reason for the weak second resonant frequency band could be due to the fact that at this higher frequency a homogenous medium approximation would fail and thus would result in the elimination of the same direction-induced surface current on the cut wire. Since the second resonant frequency as we see is mainly decided by the cut wires, the same direction current loop on the cut wires eliminates the electric and magnetic response and results in a smaller capacitive resonance and a smaller relative permeability compared to those with the first resonant frequency.

As is evident from Figure 13, the second refractive index value is in the broadband range. Since the property of the metamaterial depends mostly on the geometry and the arrangement of the structure, we believe that the dimensions of the structure can be modified to get a stronger resonance at the desired frequency.

Finally, as discussed earlier in Section 2 and extensively by Shin et al. [23], the structure design suppresses the strong diamagnetic response of the structure, and extracted, effective permeability for the structure is more than the expected value, since inhomogeneity of the structure was not considered for parameter extraction [27], and the figures do not represent the exact profile.

5. Conclusion

A high-refractive-index metamaterial structure with dual frequency band was designed through simulation and analysis. Results show that the metamaterial, designed with gold structures embedded with polyimide film, effectively exhibits a high refractive index at two frequency bands.

In the second frequency band, the high refractive index is of relatively smaller value than the main effective band. It is expected that through modifications in geometry and design, improvement in the electric and magnetic resonant frequency and the refractive index value can be enhanced for the second frequency band.

The methodology applied in this study could be applied to structures to design high-refractive-index metamaterials at multifrequency. Since polyimide has good flexibility and isolation property, the designed structure can be used in a variety of applications.

References

- [1] M. C. K. Wiltshire, J. B. Pendry, I. R. Young, D. J. Larkman, D. J. Gilderdale, and J. V. Hajnal, “Microstructured magnetic materials for rf flux guides in magnetic resonance imaging,” *Science*, vol. 291, no. 5505, pp. 849–851, 2001.
- [2] T. J. Yen, W. J. Padilla, N. Fang et al., “Terahertz magnetic response from artificial materials,” *Science*, vol. 303, no. 5663, pp. 1494–1496, 2004.
- [3] S. Zhang, W. Fan, N. C. Panoiu, K. J. Malloy, R. M. Osgood, and S. R. J. Brueck, “Experimental demonstration of near-infrared negative-index metamaterials,” *Physical Review Letters*, vol. 95, no. 13, Article ID 137404, 4 pages, 2005.
- [4] J. T. Shen, P. B. Catrysse, and S. Fan, “Mechanism for designing metallic metamaterials with a high index of refraction,” *Physical Review Letters*, vol. 94, no. 19, Article ID 197401, 4 pages, 2005.
- [5] T. W. Ebbesen, H. J. Lezec, H. F. Ghaemi, T. Thio, and P. A. Wolff, “Extraordinary optical transmission through sub-wavelength hole arrays,” *Nature*, vol. 391, no. 6668, pp. 667–669, 1998.
- [6] J. B. Pendry, A. J. Holden, D. J. Robbins, and W. J. Stewart, “Magnetism from conductors and enhanced nonlinear phenomena,” *IEEE Transactions on Microwave Theory and Techniques*, vol. 47, no. 11, pp. 2075–2084, 1999.
- [7] D. R. Smith and N. Kroll, “Negative refractive index in left-handed materials,” *Physical Review Letters*, vol. 85, no. 14, pp. 2933–2936, 2000.
- [8] S. O’Brien and J. B. Pendry, “Magnetic activity at infrared frequencies in structured metallic photonic crystals,” *Journal of Physics Condensed Matter*, vol. 14, no. 25, pp. 6383–6394, 2002.
- [9] F. J. Rachford, D. L. Smith, P. F. Loschialpo, and D. W. Forester, “Calculations and measurements of wire and/or split-ring negative index media,” *Physical Review E*, vol. 66, no. 3, Article ID 036613, 5 pages, 2002.
- [10] R. Singh, E. Smirnova, A. J. Taylor, J. F. O’Hara, and W. Zhang, “Optically thin terahertz metamaterials,” *Optics Express*, vol. 16, no. 9, pp. 6537–6543, 2008.
- [11] R. Singh, A. K. Azad, J. F. O’Hara, A. J. Taylor, and W. Zhang, “Effect of metal permittivity on resonant properties of terahertz metamaterials,” *Optics Letters*, vol. 33, no. 13, pp. 1506–1508, 2008.
- [12] R. Singh, E. Plum, C. Menzel et al., “Terahertz metamaterial with asymmetric transmission,” *Physical Review B*, vol. 80, no. 15, Article ID 153104, 4 pages, 2009.
- [13] R. Singh, C. Rockstuhl, F. Lederer, and W. Zhang, “The impact of nearest neighbor interaction on the resonances in terahertz metamaterials,” *Applied Physics Letters*, vol. 94, no. 2, Article ID 021116, 3 pages, 2009.

- [14] R. Singh, A. A. I. Al-Naib, M. Koch, and W. Zhang, "Sharp Fano resonances in THz metamaterials," *Optics Express*, vol. 19, no. 7, pp. 6312–6319, 2011.
- [15] R. Singh, X. Lu, J. Gu, Z. Tian, and W. Zhang, "Random terahertz metamaterials," *Journal of Optics A*, vol. 12, no. 1, Article ID 015101, 2010.
- [16] R. Singh, E. Plum, W. Zhang, and N. I. Zheludev, "Highly tunable optical activity in planar achiral terahertz metamaterials," *Optics Express*, vol. 18, no. 13, pp. 13425–13430, 2010.
- [17] Z. Shi and W. Robert Boyd, "Slow-light Fourier transform interferometer," *Physical Review Letters*, vol. 99, no. 24, Article ID 240801, 4 pages, 2007.
- [18] X. Wei, H. Shi, X. Dong, Y. Lu, and C. Du, "A high refractive index metamaterial at visible frequencies formed by stacked cut-wire plasmonic structures," *Applied Physics Letters*, vol. 97, no. 1, Article ID 011904, 3 pages, 2010.
- [19] A. Pimenov and A. Loidl, "Experimental demonstration of artificial dielectrics with a high index of refraction," *Physical Review B*, vol. 74, no. 19, Article ID 193102, 3 pages, 2006.
- [20] M. Choi, S. H. Lee, Y. Kim et al., "A terahertz metamaterial with unnaturally high refractive index," *Nature*, vol. 470, no. 7334, pp. 369–373, 2011.
- [21] Y. Yuan, C. Bingham, T. Tyler et al., "A dual-resonant terahertz metamaterial based on single-particle electric-field-coupled resonators," *Applied Physics Letters*, vol. 93, no. 19, Article ID 191110, 3 pages, 2008.
- [22] Y. Yuan, C. Bingham, T. Tyler et al., "Dual-band planar electric metamaterial in the terahertz regime," *Optics Express*, vol. 16, no. 13, pp. 9746–9752, 2008.
- [23] J. Shin, J. T. Shen, and S. Fan, "Three-dimensional metamaterials with an ultrahigh effective refractive index over a broad bandwidth," *Physical Review Letters*, vol. 102, no. 9, Article ID 093903, 4 pages, 2009.
- [24] C. Menzel, R. Singh, C. Rockstuhl, W. Zhang, and F. Lederer, "Effective properties of terahertz double split-ring resonators at oblique incidence," *Journal of the Optical Society of America B*, vol. 26, no. 12, pp. B143–B147, 2009.
- [25] Z. Lu, B. Camps-Ragas, and N. E. Islam, "Design and analysis of multiband high refractive index metamaterials," in *IEEE International Symposium on Antennas and Propagation and USNC-URSI National Radio Science Meeting*, IEEE Conference Proceedings, pp. 8–14, Chicago, Ill, USA, July 2012.
- [26] D. R. Smith, S. Schultz, P. Markoš, and C. M. Soukoulis, "Determination of effective permittivity and permeability of metamaterials from reflection and transmission coefficients," *Physical Review B*, vol. 65, no. 19, Article ID 195104, 5 pages, 2002.
- [27] D. R. Smith, D. C. Vier, T. Koschny, and C. M. Soukoulis, "Electromagnetic parameter retrieval from inhomogeneous metamaterials," *Physical Review E*, vol. 71, no. 3, Article ID 036617, 11 pages, 2005.

Research Article

Closed-Aperture Z-Scan Analysis for Nonlinear Media with Saturable Absorption and Simultaneous Third- and Fifth-Order Nonlinear Refraction

Xiangming Liu^{1,2} and Yasuo Tomita¹

¹Department of Engineering Science, The University of Electro-Communications, 1-5-1 Chofugaoka, Chofu, Tokyo 182-8585, Japan

²Research Institute for Electronic Science, Hokkaido University, Souseitou, Kita 21, Nishi 10, Kita-ku, Sapporo 001-0021, Japan

Correspondence should be addressed to Xiangming Liu, liuxm@es.hokudai.ac.jp

Received 11 May 2012; Accepted 9 July 2012

Academic Editor: Michael R. Gleeson

Copyright © 2012 X. Liu and Y. Tomita. This is an open access article distributed under the Creative Commons Attribution License, which permits unrestricted use, distribution, and reproduction in any medium, provided the original work is properly cited.

We present a theory of open- and closed-aperture Gaussian beam Z-scan for nonlinear optical materials with saturable absorption and high-order nonlinear refraction. We show that an approximate expression for a transmitted intensity through the nonlinear optical material is possible by means of the Adomian's decomposition method and the thin film approximation. The theory is applied to semiconductor CdSe quantum dot-polymer nanocomposite films. It is shown that the theory well explains measured results of open- and closed-aperture transmittances in the Z-scan setup. It is also shown that the nanocomposite film possesses simultaneous third- and fifth-order nonlinear refraction as well as saturable absorption of a homogeneously broadened type.

1. Introduction

A Z-scan technique originally developed by Sheik-Bahae et al. [1] has been widely used for characterizing the nonlinear optical properties of various nonlinear optical materials whose nonlinear optical responses include nonlinear absorption and nonlinear refraction. Nonlinear absorption may be classified into four types (1) two-photon absorption (TPA), (2) multiphoton absorption, (3) saturable absorption (SA), and (4) reverse SA. Nonlinear refraction includes the third- and higher-order nonlinear refraction as well as cascaded second-order nonlinear refraction. The original Z-scan theory treats nonlinear optical materials having either the third-order nonlinear refraction with TPA or the fifth-order nonlinear refraction without TPA. Later, the theory was extended to the open-aperture Z-scan theories for nonlinear optical materials having multiphoton absorption [2], simultaneous TPA and three-photon absorption [3], and SA [4]. In addition, Z-scan analyses for nonlinear optical materials having simultaneous third- and fifth-order nonlinear refraction with or without TPA [5–9] were reported previously. These extensions are important for materials characterization and device design of, for example, optical limiters

and all-optical photonic devices using third- and high-order nonlinear optical effects. However, no Z-scan theory has been reported so far for nonlinear optical materials having both SA and simultaneous third and fifth-order nonlinear refraction. Such a new nonlinear optical phenomenon has been indeed observed in our recently developed inorganic-organic nanocomposites, semiconductor CdSe quantum-dot- (QD-) polymer nanocomposite films [10, 11]. This new class of inorganic-organic nanocomposite material is capable of optically constructing multidimensional and functional (e.g., nonlinear) photonic lattice structures by the so-called holographic assembly of nanoparticles [12]. Indeed, we recently demonstrated holographic assembly of semiconductor CdSe QDs in photopolymer for constructing volume Bragg grating structures with diffraction efficiency near 100% [10]. This composite material has potential nonlinear optical applications such as optical switching/limiting, signal/image processing, and nonlinear photonic crystals [13, 14].

The electronic states of QDs are strongly influenced by the quantum confinement effect when the radius of QDs is smaller than approximately three times of the exciton Bohr radius [15]. The band gap (E_g) of QDs increases with

decreasing their size and the quantum confinement effect can strongly enhance the third-order optical nonlinearity [16, 17]. The II-VI bulk semiconductor CdSe has the direct band gap $E_g = 1.74$ eV at 300 K and has the exciton Bohr radius of 5.6 nm [17]. Therefore, the strong quantum confinement effect of CdSe QDs plays an important role in a large enhancement of the optical nonlinearity as compared with that of the bulk CdSe. Most of past studies with semiconductor QDs reported the third-order optical nonlinearity with and without TPA, although high-order optical nonlinearities in CdS_xSe_{1-x} QDs doped glasses [18–20] and colloidal CdTe QDs [21] were also reported. Saturation of the cubic Kerr nonlinearity due to high-order nonlinearities prominently at high optical intensities provides interesting nonlinear phenomena such as the formation of stable multidimensional optical solitons, but it sometimes causes a detrimental effect [22]. Therefore, it is necessary to characterize the third- and, if any, high-order optical nonlinearities in nanocomposite materials.

In this paper, we present a theory of the open and closed-aperture Gaussian beam Z-scan for nonlinear optical materials with both SA and simultaneous third- and fifth-order nonlinear refraction. We show that an approximate expression for a transmitted intensity through a nonlinear optical material possessing SA can be found by means of the Adomian's decomposition method [23]. The theory is applied to semiconductor CdSe QD-polymer nanocomposite films. It is shown that the theory well explains measured results of open- and closed-aperture transmittances in the Z-scan setup. It is also shown that the nanocomposite film possesses simultaneous third- and fifth-order nonlinear refraction as well as SA of a homogeneously broadened type.

2. Theory

Consider a single transverse mode Gaussian beam propagating along the z direction in a thin nonlinear medium of thickness L with SA of a homogeneously broadened type. In this case the intensity-dependent absorption coefficient $\alpha(I)$ is given by

$$\alpha(I) = \frac{\alpha_0}{1 + I/I_s}, \quad (1)$$

where α_0 is the linear absorption coefficient and I_s is the saturable intensity. Note that the intensity I is a function of the radial distance r from the beam axis, time t , the propagation distance z from the Gaussian beam spot, and the local distance z' ($0 \leq z' \leq L$) measured from the entrance surface of the medium can be decomposed by means of the Adomian's decomposition method [23] and is given in a polynomial form as [4]

$$I(r, z, z', t) = I_{\text{in}} \left[1 + \sum_{n=1}^{\infty} \frac{(-\alpha_0 z')^n}{n!} \frac{g_n(\eta)}{(1 + \eta)^{2n-1}} \right], \quad (2)$$

where $\eta = I_{\text{in}}/I_s$ in which the incident intensity I_{in} is given by

$$I_{\text{in}}(r, z, t) = \frac{I_0(t)}{1 + (z/z_0)^2} \exp \left[-\frac{2r^2}{w^2(z)} \right], \quad (3)$$

with $I_0(t)$ being the on-axis input intensity in the medium at the beam focus, which contains the temporal intensity envelope peaked at $t = 0$, and $w^2(z) = w_0^2(1 + z^2/z_0^2)$. Here, w_0 is the beam waist radius and z_0 is the diffraction length given by $kw_0^2/2$ with k being the wavenumber of the incident beam. We therefore note that η is a function of z, r , and t . The first eight terms of $g_n(\eta)$ in (2), which are numerically confirmed to approximately represent a solution given by (2) with a high accuracy, are given by

$$\begin{aligned} g_1(\eta) &= 1, \\ g_2(\eta) &= 1, \\ g_3(\eta) &= 1 - 2\eta, \\ g_4(\eta) &= 1 - 8\eta + 6\eta^2, \\ g_5(\eta) &= 1 - 22\eta + 58\eta^2 - 24\eta^3, \\ g_6(\eta) &= 1 - 52\eta + 328\eta^2 - 444\eta^3 + 120\eta^4, \\ g_7(\eta) &= 1 - 114\eta + 1452\eta^2 - 4400\eta^3 + 3708\eta^4 - 720\eta^5, \\ g_8(\eta) &= 1 - 240\eta + 5610\eta^2 - 32120\eta^3 + 58140\eta^4 \\ &\quad - 33984\eta^5 + 5040\eta^6. \end{aligned} \quad (4)$$

When the third- and fifth-order nonlinear refraction is taken into account (these contributions are sufficient for our experiment with semiconductor CdSe QD-polymer nanocomposite films as is shown later), the nonlinear phase shift $\Delta\phi$ under the thin film and slowly varying envelope approximations is found from the following differential equation [6, 9]:

$$\frac{d\Delta\phi}{dz'} = k\Delta n(I) = k(n_2 + n_4 I), \quad (5)$$

where n_2 and n_4 are the third- and fifth-order nonlinear refraction coefficients, respectively. Integration of (5) yields to the nonlinear phase shift given by

$$\begin{aligned} \Delta\phi(r, z, t) &= kn_2 \int_0^L I(r, z, z', t) dz' + kn_4 \int_0^L I^2(r, z, z', t) dz' \\ &= \Delta\phi^{(3)}(r, z, t) + \Delta\phi^{(5)}(r, z, t), \end{aligned} \quad (6)$$

where the third- and fifth-order nonlinear phase shifts, $\Delta\phi^{(3)}(r, z, t)$ and $\Delta\phi^{(5)}(r, z, t)$ are expressed as

$$\begin{aligned} \Delta\phi^{(3)}(r, z, t) &= n_2 k L I_{\text{in}} A^{(3)}(r, z, t), \\ \Delta\phi^{(5)}(r, z, t) &= n_4 k L (I_{\text{in}})^2 A^{(5)}(r, z, t), \end{aligned} \quad (7)$$

in which

$$A^{(3)}(r, z, t) = \left[1 + \sum_{n=1}^{\infty} \frac{(-\alpha_0 L)^{n+1}}{(n+1)!} \frac{g_n(\eta)}{(1+\eta)^{2n-1}} \right], \quad (8a)$$

$$A^{(5)}(r, z, t) = \left[1 + 2 \sum_{n=1}^{\infty} \frac{(-\alpha_0 L)^{n+1}}{(n+1)!} \frac{g_n(\eta)}{(1+\eta)^{2n-1}} + \sum_{m=1}^{\infty} \sum_{n=1}^{\infty} \frac{(-\alpha_0 L)^{n+m+1}}{(m+n+1)m!n!} \frac{g_m(\eta)g_n(\eta)}{(1+\eta)^{2m+2n-2}} \right]. \quad (8b)$$

The electric field $E_e(r, z, t)$ at the exit surface of the medium that experiences the nonlinear phase shift is given by

$$E_e(r, z, t) = \sqrt{I(r, z, L, t)} \exp[i\Delta\phi(r, z, t)]. \quad (9)$$

The expansion of the exponential term on the right-hand side of (9) in a Taylor series yields to

$$e^{i\Delta\phi(r, z, t)} = \sum_{m=0}^{\infty} \frac{[i \sum_{n=1}^2 \phi^{(2n+1)}(r, z, t)]^m}{m!} \cong \sum_{m=0}^{\infty} \frac{\{i \sum_{n=1}^2 \Delta\varphi^{(2n+1)}(z, t) \exp[-(2nr^2)/(w^2(z))]\}^m}{m!}, \quad (10)$$

where

$$\Delta\varphi^{(2n+1)}(z, t) = n_{2n} k L [I^{\text{in}}(0, z, t)]^n A^{(2n+1)}(0, z, t). \quad (11)$$

In the second equation on the right-hand side of (10), the approximation is made such that (8a) and (8b) are evaluated at $r = 0$. Since $|\Delta\phi^{(3)}| \gg |\Delta\phi^{(5)}|$ in practice, the quadratic and higher-order terms in $\Delta\phi^{(5)}$ for the expansion of (10) may be neglected. Then, using the treatment by Tsigaridas et al. [6] with the Gaussian decomposition method [1], the electric field of the transmitted Gaussian beam at the distance d from the medium exit plane is expressed as

$$E_a(r, z, t) = \sqrt{I(0, z, L, t)} \sum_{m=1}^{\infty} \left\{ \frac{[i\Delta\varphi^{(3)}(z, t)]^m}{m!} E^{(m3)}(r, d) + \frac{mi^m}{m!} [\Delta\varphi^{(3)}(z, t)]^{m-1} \times \Delta\varphi^{(5)}(z, t) E^{(m5)}(r, d) \right\}, \quad (12)$$

where the electric field of each individual Gaussian beam propagated at the distance d is given by

$$E^{(m3,5)}(r, d) = F^{(m3,5)} \frac{w_0^{(m3,5)}}{w^{(m3,5)}(d)} \exp\left[-\left(\frac{r}{w^{(m3,5)}(d)}\right)^2\right] \times \exp\left(-\frac{ikr^2}{2R^{(m3,5)}(d)}\right) \times \exp\left[-ik(z+d) + i(\theta^{(m3,5)}(d) + \gamma^{(m3,5)})\right]. \quad (13)$$

In (13),

$$w_0^{(m3,5)} = \left(\frac{2z_R^{(m3,5)}}{k}\right)^{1/2},$$

$$w^{(m3,5)}(d) = w_0^{(m3,5)} \left[1 + \left(\frac{D^{(m3,5)} + d}{z_R^{(m3,5)}}\right)^2 \right]^{1/2},$$

$$R^{(m3,5)}(d) = (D^{(m3,5)} + d) \left[1 + \left(\frac{z_R^{(m3,5)}}{D^{(m3,5)} + d}\right)^2 \right], \quad (14)$$

$$\theta^{(m3,5)}(d) = \tan^{-1}\left(\frac{D^{(m3,5)} + d}{z_R^{(m3,5)}}\right),$$

$$F^{(m3,5)} = \left[1 + \left(\frac{D^{(m3,5)}}{z_R^{(m3,5)}}\right)^2 \right]^{1/2},$$

$$\gamma^{(m3,5)} = \tan^{-1}\left(\frac{z}{z_R^{(m3,5)}}\right) - \tan^{-1}\left(\frac{D^{(m3,5)}}{z_R^{(m3,5)}}\right),$$

where

$$z_R^{(m3,5)} = \frac{A^{(m3,5)} R^2(z)}{(A^{(m3,5)})^2 + R^2(z)}, \quad (15)$$

$$D^{(m3,5)} = \frac{(A^{(m3,5)})^2 R(z)}{(A^{(m3,5)})^2 + R^2(z)},$$

in which

$$A^{(m3)} = \frac{k}{2} \frac{w^2(z)}{2m+1},$$

$$A^{(m5)} = \frac{k}{2} \frac{w^2(z)}{2m+3}, \quad (16)$$

$$R(z) = z \left[1 + \left(\frac{z_0}{z}\right)^2 \right].$$

Note that the physical meanings of the parameters shown above are described in [6]. The normalized Z-scan transmittance $T(z)$ [1] is defined as

$$T(z) = \frac{\int_{-\infty}^{\infty} P_T(z, t) dt}{S \int_{-\infty}^{\infty} P_i(t) dt}, \quad (17)$$

where the transmitted power $P_T(z, t)$ through the aperture is given by

$$P_T(z, t) = 2\pi \int_0^{r_a} |E_a(r, z, t)|^2 r dr, \quad (18)$$

the input power $P_i(t)$ is expressed as $\pi\omega_0^2 I_0(t)/2$, and the linear transmittance of the aperture S is given by $1 - \exp(-2r_a^2/w_a^2)$ with r_a and w_a being the aperture radius and the Gaussian beam radius at the aperture, respectively. Note that although we have described the theory for SA of a homogeneously broadened type given by (1), it is also possible to analyze this problem for SA of an inhomogeneously broadened type.

In what follows, we show numerical calculations for $T(z)$ of the closed-aperture Z-scan for a nonlinear medium possessing both SA of a homogeneously broadened type and the simultaneous third- and fifth-order nonlinear refraction. Figure 1 shows $T(z)$ with n_2 and n_4 having the same signs for negative (positive) value for n_2 as shown in Figure 1(a) (Figure 1(b)), where the third- and fifth-order nonlinear phase shifts at the temporally and spatially peak input intensity $I_0(0)$ are defined as $\Delta\phi_0^{(3)} = n_2 k L I_0(0)$ and $\Delta\phi_0^{(5)} = n_4 k L I_0(0)^2$, respectively. It can be seen from Figures 1(a) and 1(b) that, unlike the pure third-order case, the peak-to-valley (or the valley-to-peak) configuration becomes asymmetric and its peak-to-valley difference in $T(z)$ increases with an increase in $|\Delta\phi_0^{(5)}|$ because n_2 and n_4 have the same signs. It can also be seen that the fifth-order effect separates the valley more than the peak. The single peak and valley configuration is always maintained although the symmetry of the configuration is opposite each other for $n_2 > 0$ and $n_2 < 0$. The deviation of the valley from unity is larger than that of the peak with an increase in $|\Delta\phi_0^{(5)}|$. The peak and valley tend to approach to the beam waist position ($z = 0$) with an increase in $|\Delta\phi_0^{(5)}|$ as seen in Figures 1(a) and 1(b).

Figure 2 presents $T(z)$ with $\Delta\phi_0^{(3)}$ and $\Delta\phi_0^{(5)}$ having the opposite signs for negative (positive) value for n_2 as shown in Figure 2(a) (Figure 2(b)). It can be seen from Figures 2(a) and 2(b) that the peak-to-valley (or the valley-to-peak) configuration becomes asymmetric and its peak-to-valley difference in $T(z)$ decreases with an increase in $|\Delta\phi_0^{(5)}|$ because n_2 and n_4 have the opposite signs. It can also be seen that the fifth-order effect separates the valley more than the peak as similar to the case of the same signs of n_2 and n_4 . The single peak and valley configuration is always maintained although the symmetry of the configuration is opposite each other. This trend is also the same as the case of the same signs of n_2 and n_4 for $n_2 > 0$ and $n_2 < 0$. The peak and valley tend to separate from the beam waist position ($z = 0$) with an increase in $|\Delta\phi_0^{(5)}|$ as seen in Figures 2(a) and 2(b). This trend is opposite to the case of the same signs of n_2 and n_4 shown in Figures 1(a) and 1(b).

Peak-to-valley differences in $T(z)$, ΔT_{p-v} , are plotted as a function of $I_0(0)/I_s$ in Figure 3 for different values of $\Delta\phi_0^{(5)}$ when $T(z)$ maintains the single peak and valley configuration. It can be seen that ΔT_{p-v} with $n_2 = -5.0 \times 10^{-3} \text{ cm}^2/\text{GW}$ and $n_4 = -1.0 \times 10^{-3} \text{ cm}^4/\text{GW}^2$ increases

faster than the case of the pure third-order effect without the influence of the fifth-order effect with an increase in $I_0(0)/I_s$. On the other hand, the fifth-order effect results in a slow increase of ΔT_{p-v} as $I_0(0)/I_s$ increases with $n_2 = -5.0 \times 10^{-3} \text{ cm}^2/\text{GW}$ and $n_4 = 1.0 \times 10^{-3} \text{ cm}^4/\text{GW}^2$.

A dependence of the normalized transmittance on S is shown in Figure 4. The calculation was made with $\Delta\phi_0^{(3)} = -0.5$ and $\Delta\phi_0^{(5)} = 0.1$ and at $I_0(0)/I_s = 0.33$. It can be seen that the peaks and valleys of $T(z)$ decrease as S increases. It means that the closed-aperture Z-scan is highly sensitive when S is small as reported in [1].

3. Application to Semiconductor Quantum Dot-Polymer Nanocomposites

3.1. Sample Preparation. CdSe QDs (the average core size of 3 nm) were synthesized by the aqueous synthetic method and then extracted into an ionic liquid monomer. Detailed descriptions of preparation for the CdSe QD-monomer syrup were given in [10]. The syrup was cast on a glass plate loaded with a 10- μm spacer and was covered with another glass plate. For our Z-scan measurement, this uncured film sample was exposed to a green LED to prepare a uniformly cured polymer nanocomposite film sample having the quantum-confined electron-hole transition at $\sim 480 \text{ nm}$.

3.2. Experimental Setup. A conventional Z-scan technique [1] was employed to evaluate nonlinear absorption and nonlinear refraction of our uniformly cured polymer nanocomposite film samples. We used a frequency-doubled, passively and actively mode-locked Nd:YAG laser (Continuum, YG601) with the FWHM pulse width of 35 ps at a wavelength of 532 nm and at a repetition rate of 10 Hz. The incident laser beam was divided into two beams. One laser beam was taken as a reference, while the other one was focused onto the film sample by a 200 mm convex lens to a spot with its beam waist radius $\sim 32 \mu\text{m}$. A film sample was moved along the beam propagation direction (z -axis) by a computer-controlled moving stage. An aperture and a detector were placed at a distance far away from a film sample. Linear transmittance of the aperture S was set to be 0.06 in the closed-aperture Z-scan setup. Individual transmitted pulses at a given pulse energy within $\pm 10\%$ were selected and averaged to obtain one data point.

3.3. Experimental Results. Typical open-aperture Z-scan results for a film sample with 0.91 vol.% CdSe QDs at $I_0 = 0.6, 1.2,$ and $1.8 \text{ GW}/\text{cm}^2$ are shown in Figures 5(a), 5(b), and 5(c). It can be seen that $T(z)$ is peaked at the beam focus. Since no nonlinear absorption was observed in a neat polymer film without CdSe QDs, the observed data was caused by the optical nonlinearity of CdSe QDs. The open Z-scan model with SA of a homogeneously broadened type [4] can clearly fit the data better than with TPA [1] having a negative TPA coefficient β . We note that the model with SA of an inhomogeneously broadened type could not fit well with the closed-aperture Z-scan data (not shown here). Figure 5(d) shows transmittance change $\Delta T(0)$ at $z = 0$ as a function

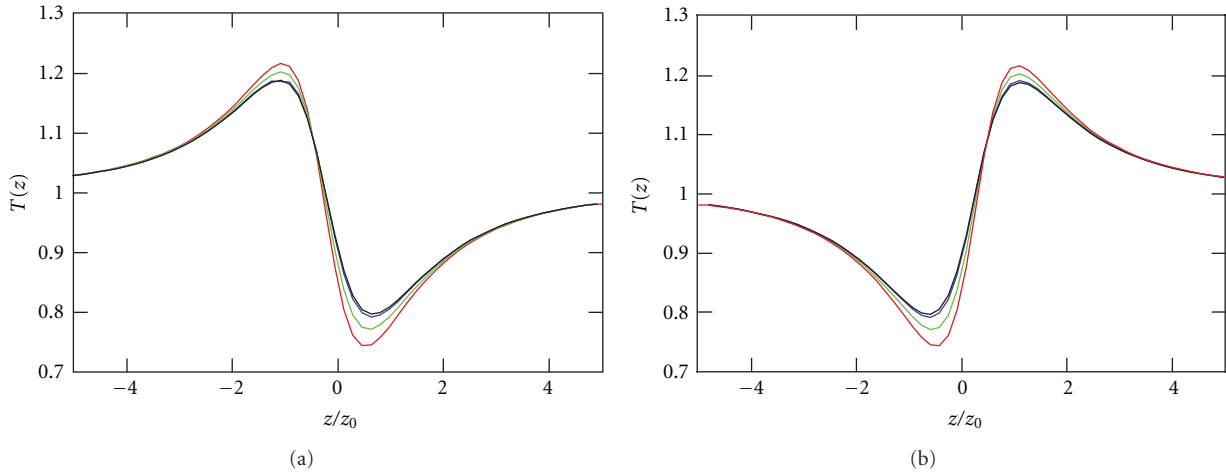


FIGURE 1: Normalized transmittances $T(z)$ with $S = 0.05$ and $I_s = 0.3 \text{ GW/cm}^2$ for (a) $\Delta\phi_0^{(3)} = -0.3\pi$ and $\Delta\phi_0^{(5)} < 0$ and (b) $\Delta\phi_0^{(3)} = 0.3\pi$ and $\Delta\phi_0^{(5)} > 0$. Solid curves in black, blue, green, and red correspond to $|\Delta\phi_0^{(5)}| = 0, 0.01\pi, 0.05\pi$ and 0.1π , respectively.

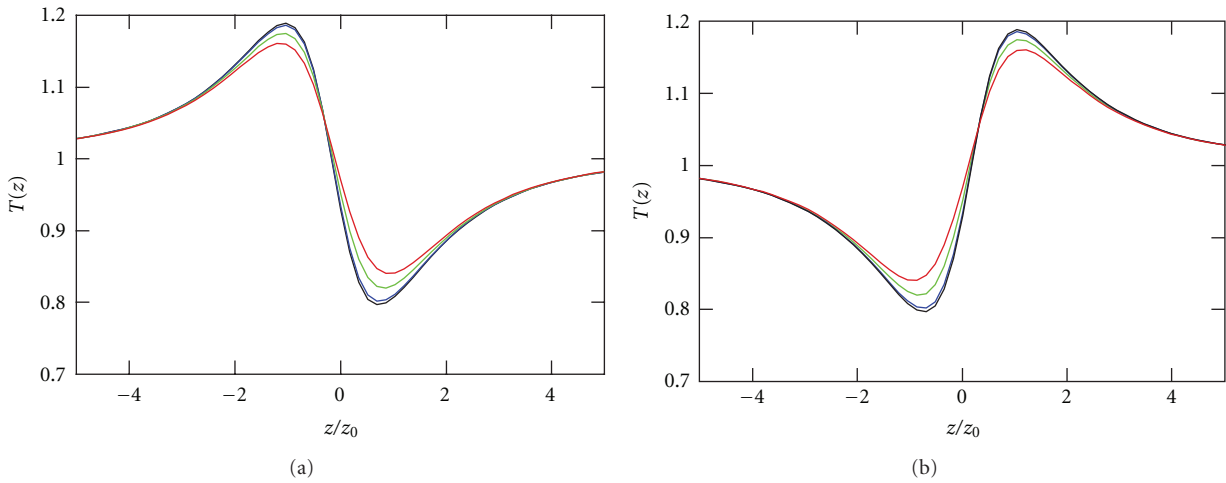


FIGURE 2: Normalized transmittances $T(z)$ with $S = 0.05$ and $I_s = 0.3 \text{ GW/cm}^2$ for (a) $\Delta\phi_0^{(3)} = -0.3\pi$ and $\Delta\phi_0^{(5)} > 0$ and (b) $\Delta\phi_0^{(3)} = 0.3\pi$ and $\Delta\phi_0^{(5)} < 0$. Solid curves in black, blue, green, and red correspond to $|\Delta\phi_0^{(5)}| = 0, 0.01\pi, 0.05\pi$ and 0.1π , respectively.

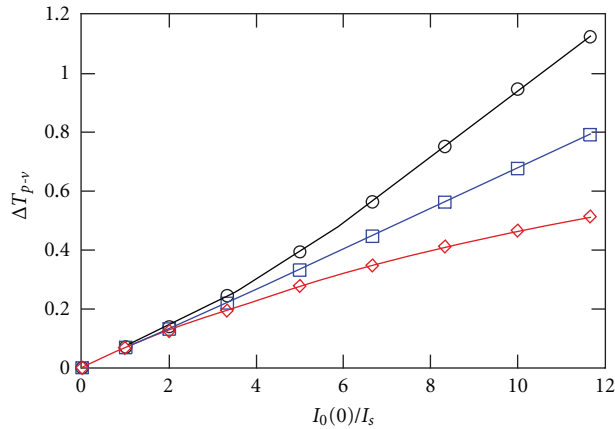


FIGURE 3: ΔT_{p-v} versus $I_0(0)/I_s$ for $S = 0.05$ and $I_s = 0.3 \text{ GW/cm}^2$ for $n_2 = -5.0 \times 10^{-3} \text{ cm}^2/\text{GW}$ and $n_4 = 0$ (\square), 1.0×10^{-3} (\diamond) and -1.0×10^{-3} (\circ) cm^4/GW^2 . The solid curves are a guide to the eyes.

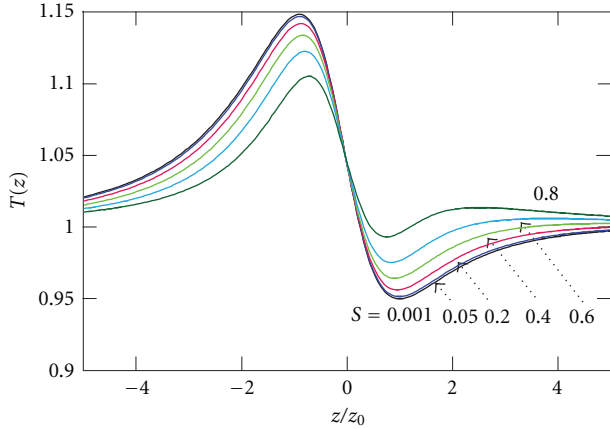


FIGURE 4: Normalized transmittances $T(z)$ for different aperture size S with $\Delta\phi_0^{(3)} = -0.5$ and $\Delta\phi_0^{(5)} = 0.1$ and at $I_0(0)/I_s = 0.33$.

of I_0 . It can be seen that the SA model gives the best fit value for I_s to be 0.54 GW/cm^2 , which is consistent with that ($0.53 \pm 0.06 \text{ GW/cm}^2$) estimated from Figures 5(a)–5(c). It follows that the saturable absorption observed in our film sample is well described by SA of a homogeneously broadened type. This result implies excellent size uniformity of CdSe QDs in our sample as confirmed by a transmission electron microscope image of CdSe QDs [11]. We consider that the physical origin of the light-induced transparency is caused by transient bleaching of the CdSe QDs [24].

Figure 6 shows the closed-aperture Z-scan result for the same film sample as that shown in Figure 5 at $I_0 = 1.8 \text{ GW/cm}^2$, which is fitted by our closed-aperture Z-scan model without and with the fifth-order nonlinear refraction in the absence of nonlinear absorption (Figure 6(a)) and in the presence of saturable absorption (Figure 6(b)). It can be clearly seen from Figures 6(a) and 6(b) that the film sample exhibits the simultaneous third- and fifth-order nonlinear refraction as well as saturable absorption.

Figures 7(a), 7(b), and 7(c) show the closed-aperture Z-scan results at several levels of intensities for the same film sample as that shown in Figure 5. It can be seen that the Z-scan data exhibit the peak-and-valley configuration, indicating the negative nonlinear refraction. It is well known that ΔT_{p-v} is proportional to I_0 for a Kerr material [1]. However, we found that $\Delta T_{p-v}/I_0$ for our film sample approximately had a linear dependence of I_0 (see Figure 7(d)), indicating that the third-order effect was not the sole contribution to the observed optical nonlinearity. The fifth-order contribution to $T(z)$ as well as SA should be taken into account in the analysis of the closed-aperture Z-scan data.

Based on our model given in Section 2, we performed the curve fitting of the present theoretical model with I_s , together with n_2 and n_4 as fitting parameters, to the data. The best-fit values for n_2 and n_4 were found to be $(-4.0 \pm 0.6) \times 10^{-3} \text{ cm}^2/\text{GW}$ and $(1.5 \pm 0.4) \times 10^{-3} \text{ cm}^4/\text{GW}^2$, respectively. For comparison, a theoretical fitting curve in which only third- and fifth-order nonlinear refraction is taken into

account (without nonlinear absorption) is also shown in Figure 7. Poor fit with the data is obvious, showing the need for the inclusion of nonlinear absorption (i.e., SA in our case).

The magnitude of the obtained n_2 for the film sample with 0.91 vol.% (3.6 wt%) CdSe QDs is approximately two orders of magnitude larger than that ($-1.45 \times 10^{-5} \text{ cm}^2/\text{GW}$) of a bulk CdSe at 1064 nm [25] and is approximately one order of magnitude larger than that ($4.3 \times 10^{-4} \text{ cm}^2/\text{GW}$) at 794 nm for a polymer CR39 composite film with 1.5 wt% CdSe QDs [26]. Generally, electronic and thermal effects mainly contribute to the optical nonlinearities. However, the thermal contribution to the observed optical nonlinearities of the film sample was negligible in our experiment using a picosecond laser at a low repetition rate and therefore the dominating nonlinear response is attributed to the electronic origin as was also confirmed by degenerating multiwave mixing (DMWM) [11]. We also found from a dependence of n_4 on the concentration of CdSe QDs that the observed fifth-order nonlinearity had contributions mainly from the intrinsic fifth-order optical nonlinearity and partly from macroscopic and microscopic cascaded fifth-order optical nonlinearities [11, 27]. The occurrence of the intrinsic fifth-order optical nonlinearity is attributed to TPA-induced free carriers in bulk semiconductors [25]. In our case, however, it may originate from the state filling effect in CdSe QDs.

4. Conclusion

We have developed a closed-aperture Z-scan theory for nonlinear optical materials with SA of a homogeneously broadened type and with simultaneous third- and fifth-order nonlinear refraction. The shape and symmetry of the closed-aperture Z-scan transmittance are strongly influenced by the relative sign and magnitude of the fifth-order optical nonlinearity with respect to the third-order one. Because the light-induced transparency takes place due to SA, the peak (the valley) increases (decreases) in the closed-aperture Z-scan transmittance. The theoretical model has been applied to characterize the nonlinear optical properties of our newly developed uniformly cured CdSe QD-polymer nanocomposites. We have shown that the films exhibit SA as well as the negative third-order and the positive fifth-order nonlinear refraction. Such coexistence of the third- and fifth-order optical nonlinearities has also been confirmed by our recent DMWM measurements [11]. Finally, it should be stressed that the Z-scan theory presented in this paper is proved to be useful for characterizing the nonlinear optical properties of novel QD-polymer nanocomposite materials capable of constructing nonlinear photonic crystal structures by holographic patterning. In addition, the observed large nonlinear refraction and induced transparency as well as the capability of holographic nanoparticle assembling make QD-polymer nanocomposite materials promising for nonlinear photonics applications (e.g., optical switching, limiting, and signal processing) by use of holographic Bragg grating structures that provide the electromagnetic nonlinear feedback mechanism.

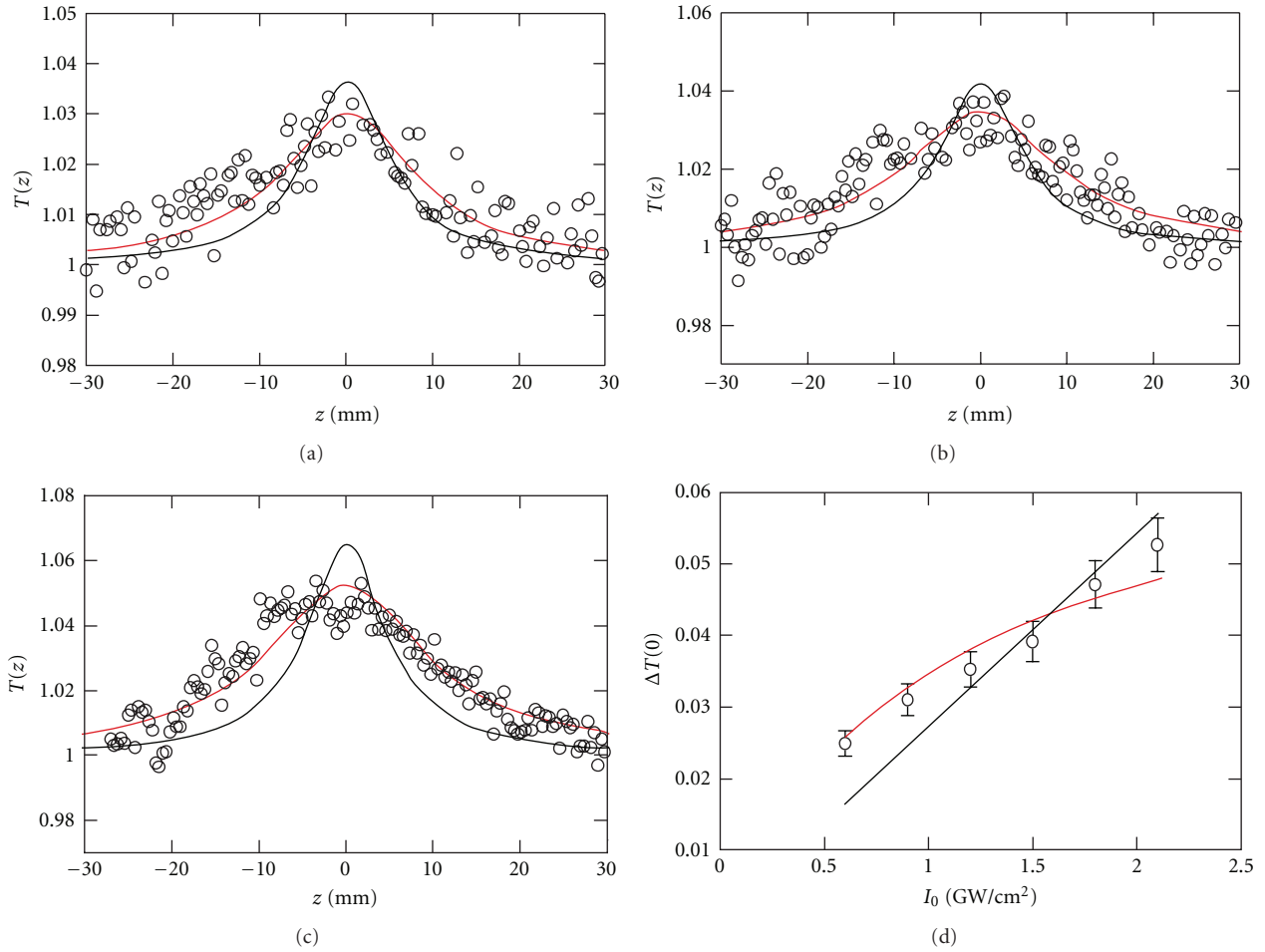


FIGURE 5: (a) Open-aperture Z-scan $T(z)$ at $I_0 =$ (a) 0.6, (b) 1.2, and (c) 1.8 GW/cm^2 for a film sample with 0.91 vol.% CdSe QDs. (b) Transmittance change $\Delta T(0)$ at $z = 0$ as a function of input intensity I_0 . The best fittings correspond to the SA (red) and TPA (black) models, respectively.

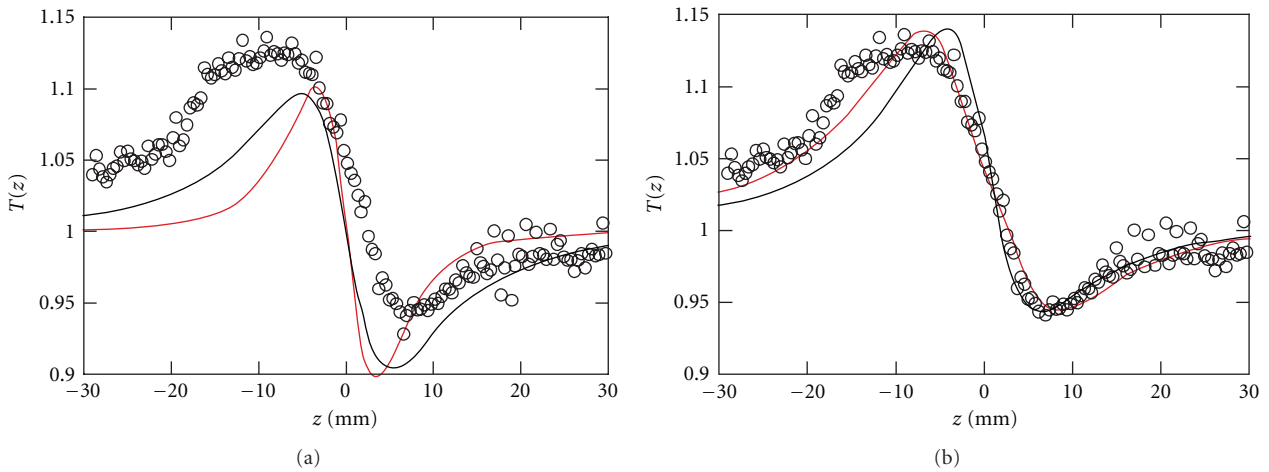


FIGURE 6: Closed-aperture Z-scan $T(z)$ at $I_0 = 1.8$ GW/cm^2 for the same film sample as that shown in Figure 5. In Figure 6(a), solid curves correspond to the least-squares fit of the theoretical formulae for a medium possessing the third-order nonlinear refraction without (black) and with (red) the fifth-order nonlinear refraction in the absence of saturable absorption of a homogeneously broadened type. In Figure 6(b), solid curves correspond to the least-squares fit for a medium possessing the third-order nonlinear refraction without (black) and with (red) the fifth-order nonlinear refraction in the presence of saturable absorption of a homogeneously broadened type.

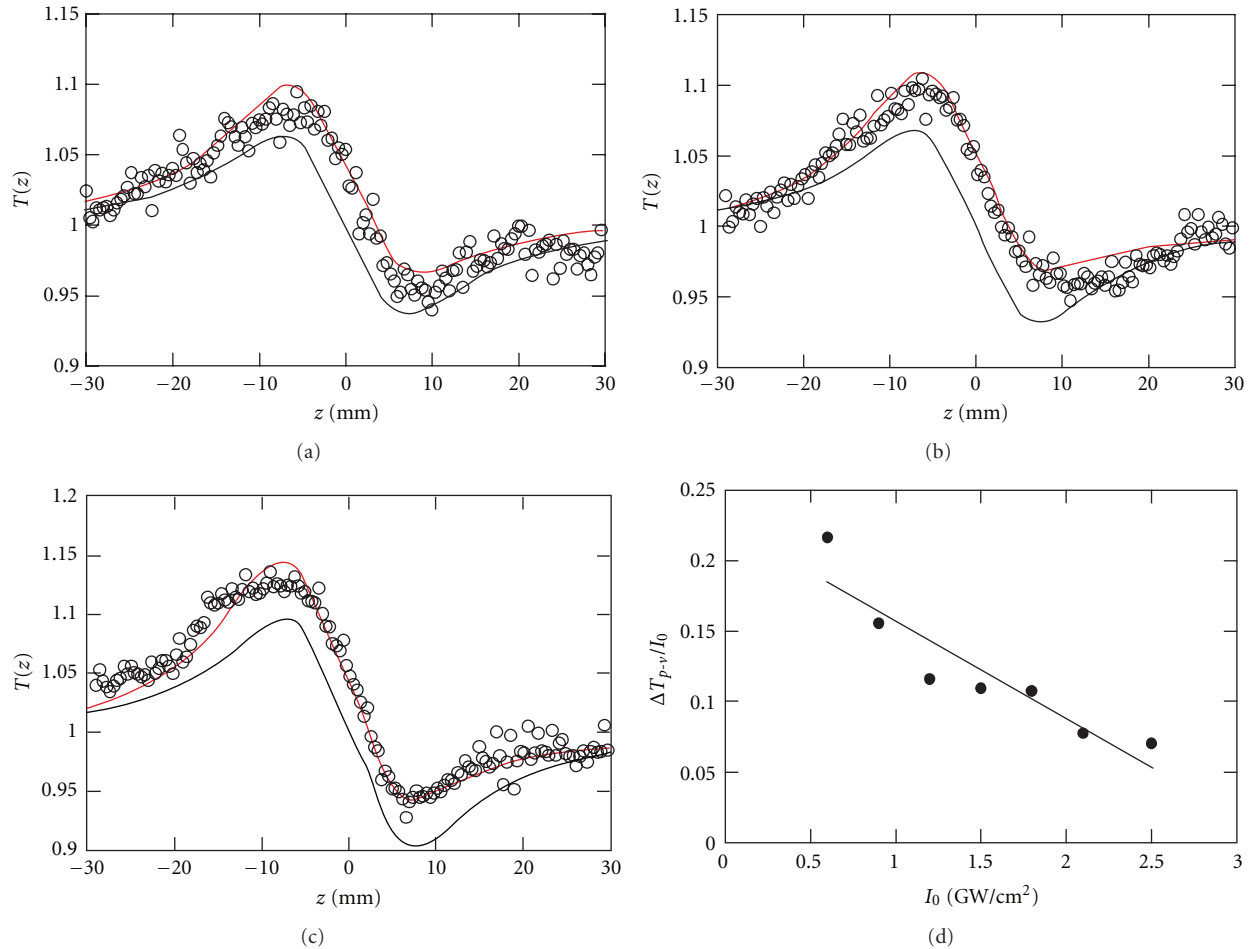


FIGURE 7: Closed-aperture Z-scan $T(z)$ at $I_0 =$ (a) 0.6, (b) 1.2, and (c) 1.8 GW/cm² for the same film sample as that shown in Figure 5. Solid curves correspond to the least-squares fit of the theoretical formulae for the closed-aperture Z-scan with (red) and without (black) saturable absorption of a homogeneously broadened type. The best-fit values for n_2 and n_4 are $(-4.0 \pm 0.6) \times 10^{-3}$ cm²/GW and $(1.5 \pm 0.4) \times 10^{-3}$ cm⁴/GW², respectively. (d) $\Delta T_{p-v}/I_0$ as a function of input intensity I_0 . The solid line is the least-squares linear fit to the data.

Acknowledgment

This work was supported by the Ministry of Education, Culture, Sports, Science, and Technology of Japan under Grant no. 20360030.

References

- [1] M. Sheik-Bahae, A. A. Said, T. H. Wei, D. J. Hagan, and E. W. Van Stryland, "Sensitive measurement of optical nonlinearities using a single beam," *IEEE Journal of Quantum Electronics*, vol. 26, no. 4, pp. 760–769, 1990.
- [2] R. L. Sutherland, *Handbook of Nonlinear Optics*, Marcel Dekker, New York, NY, USA, 2nd edition, 2003.
- [3] B. Gu, J. Wang, J. Chen, Y. X. Fan, J. Ding, and H. T. Wang, "Z-scan theory for material with two- and three-photon absorption," *Optics Express*, vol. 13, no. 23, pp. 9230–9234, 2005.
- [4] B. Gu, Y. X. Fan, J. Wang et al., "Characterization of saturable absorbers using an open-aperture Gaussian-beam Z scan," *Physical Review A*, vol. 73, no. 6, Article ID 065803, 2006.
- [5] G. Tsigaridas, M. Fakis, I. Polyzos, M. Tsibouri, P. Persephonis, and V. Giannetas, "Z-scan analysis for near-Gaussian beams through Hermite-Gaussian decomposition," *Journal of the Optical Society of America B*, vol. 20, no. 4, pp. 670–676, 2003.
- [6] G. Tsigaridas, M. Fakis, I. Polyzos, P. Persephonis, and V. Giannetas, "Z-scan analysis for high order nonlinearities through Gaussian decomposition," *Optics Communications*, vol. 225, no. 4–6, pp. 253–268, 2003.
- [7] Z. Liu, W. Zang, J. Tian, W. Zhou, C. Zhang, and G. Zhang, "Analysis of Z-scan of thick media with high-order nonlinearity by variational approach," *Optics Communications*, vol. 219, no. 1–6, pp. 411–419, 2003.
- [8] B. Gu, X. C. Peng, T. Jia, J. P. Ding, J. L. He, and H. T. Wang, "Determinations of third- and fifth-order nonlinearities by the use of the top-hat-beam Z scan: theory and experiment," *Journal of the Optical Society of America B*, vol. 22, no. 2, pp. 446–452, 2005.
- [9] B. Gu, J. Chen, Y. X. Fan, J. Ding, and H. T. Wang, "Theory of Gaussian beam Z scan with simultaneous third- and fifth-order nonlinear refraction based on a Gaussian decomposition method," *Journal of the Optical Society of America B*, vol. 22, no. 12, pp. 2651–2659, 2005.
- [10] X. Liu, Y. Tomita, J. Oshima et al., "Holographic assembly of semiconductor CdSe quantum dots in polymer for volume Bragg grating structures with diffraction efficiency near

- 100%," *Applied Physics Letters*, vol. 95, no. 26, Article ID 261109, 2009.
- [11] X. Liu, Y. Tomita, J. Oshima, T. Nakashima, and T. Kawai, "High-order nonlinear optical response of a polymer nanocomposite film incorporating semiconductor CdSe quantum dots," *Optics Express*, vol. 20, pp. 13457–13469, 2012.
- [12] Y. Tomita, N. Suzuki, and K. Chikama, "Holographic manipulation of nanoparticle distribution morphology in nanoparticle-dispersed photopolymers," *Optics Letters*, vol. 30, no. 8, pp. 839–841, 2005.
- [13] Y. Tomita, "Holographic manipulation of nanoparticle-distribution morphology in photopolymers and its applications to volume holographic recording and nonlinear photonic crystals," in *Proceedings of the OSA Trends in Optics and Photonics Series (TOPS '05)*, vol. 99, pp. 274–280, July 2005.
- [14] R. E. Slusher and B. J. Eggleton, *Nonlinear Photonic Crystals*, Springer, Berlin, Germany, 2003.
- [15] Y. Kayanuma, "Quantum-size effects of interacting electrons and holes in semiconductor microcrystals with spherical shape," *Physical Review B*, vol. 38, no. 14, pp. 9797–9805, 1988.
- [16] S. Schmitt-Rink, D. A. B. Miller, and D. S. Chemla, "Theory of the linear and nonlinear optical properties of semiconductor microcrystallites," *Physical Review B*, vol. 35, no. 15, pp. 8113–8125, 1987.
- [17] G. Banfi, V. Degiorgio, and D. Ricard, "Nonlinear optical properties of semiconductor nanocrystals," *Advances in Physics*, vol. 47, no. 3, pp. 447–510, 1998.
- [18] L. H. Acioli, A. S. L. Gomes, and J. R. R. Leite, "Measurement of high-order optical nonlinear susceptibilities in semiconductor-doped glasses," *Applied Physics Letters*, vol. 53, no. 19, pp. 1788–1790, 1988.
- [19] G. Banfi, V. Degiorgio, and H. M. Tan, "Optical nonlinearity of semiconductor-doped glasses at frequencies below the band gap: the role of free carriers," *Journal of the Optical Society of America B*, vol. 12, no. 4, pp. 621–628, 1995.
- [20] K. S. Bindra and A. K. Kar, "Role of femtosecond pulses in distinguishing third- and fifth-order nonlinearity for semiconductor-doped glasses," *Applied Physics Letters*, vol. 79, no. 23, pp. 3761–3763, 2001.
- [21] I. Dancus, V. I. Vlad, A. Petris, N. Gaponik, V. Lesnyak, and A. Eychmüller, "Saturated near-resonant refractive optical nonlinearity in CdTe quantum dots," *Optics Letters*, vol. 35, no. 7, pp. 1079–1081, 2010.
- [22] Y. F. Chen, K. Beckwitt, F. W. Wise, B. G. Aitken, J. S. Sanghera, and I. D. Aggarwal, "Measurement of fifth- and seventh-order nonlinearities of glasses," *Journal of the Optical Society of America B*, vol. 23, no. 2, pp. 347–352, 2006.
- [23] G. Adomian, "A review of the decomposition method in applied mathematics," *Journal of Mathematical Analysis and Applications*, vol. 135, no. 2, pp. 501–544, 1988.
- [24] C. Burda, S. Link, T. C. Green, and M. A. El-Sayed, "New transient absorption observed in the spectrum of colloidal CdSe nanoparticles pumped with high-power femtosecond pulses," *Journal of Physical Chemistry B*, vol. 103, no. 49, pp. 10775–10780, 1999.
- [25] M. Sheik-Bahae, D. C. Hutchings, D. J. Hagan, and E. W. Van Stryland, "Dispersion of bound electronic nonlinear refraction in solids," *IEEE Journal of Quantum Electronics*, vol. 27, no. 6, pp. 1296–1309, 1991.
- [26] C. Gan, Y. Zhang, S. W. Liu, Y. Wang, and M. Xiao, "Linear and nonlinear optical refractions of CR39 composite with CdSe nanocrystals," *Optical Materials*, vol. 30, no. 9, pp. 1440–1445, 2008.
- [27] K. Dolgaleva, H. Shin, and R. W. Boyd, "Observation of a microscopic cascaded contribution to the fifth-order nonlinear susceptibility," *Physical Review Letters*, vol. 103, no. 11, Article ID 113902, 2009.

Review Article

Zero Spatial Frequency Limit: Method to Characterize Photopolymers as Optical Recording Material

**Sergi Gallego,^{1,2} Andrés Márquez,^{1,2} Manuel Ortuño,^{1,2}
Cristian Neipp,^{1,2} Inmaculada Pascual,^{2,3} and Augusto Beléndez^{1,2}**

¹ *Departamento de Física, Ingeniería de Sistemas y Teoría de la Señal, Universidad de Alicante, Apartado 99, 03080 Alicante, Spain*

² *Instituto Universitario de Física Aplicada a las Ciencias y las Tecnologías, Universidad de Alicante, Apartado 99, 03080 Alicante, Spain*

³ *Departamento de Óptica, Farmacología y Anatomía, Universidad de Alicante, Apartado 99, 03080 Alicante, Spain*

Correspondence should be addressed to Sergi Gallego, sergigir@gmail.com

Received 3 May 2012; Accepted 14 June 2012

Academic Editor: Michael R. Gleeson

Copyright © 2012 Sergi Gallego et al. This is an open access article distributed under the Creative Commons Attribution License, which permits unrestricted use, distribution, and reproduction in any medium, provided the original work is properly cited.

Photopolymers are useful for different holographic applications such as holographic data storage or diffractive optical elements. However, due to the presence of two different phenomena, polymer formation and monomer diffusion, it is difficult to characterize each parameter independently. We propose a direct method based on zero spatial frequency recording, to eliminate the diffusion influence, and on interferometric techniques, both in transmission and in reflection, to obtain quantitative values of shrinkage, polymerization rate, polymer refractive index and relation between intensity and polymerization, and so forth. This method has been implemented in the Holography and Optical Processing Group from the University of Alicante to characterize different photopolymers. In this paper, we present a compilation of the results obtained with this method for different photopolymers and we compare their characteristics.

1. Introduction

Photopolymers are useful for different applications due to the refractive index variations and relief profiles generated [1–8]. There are many types of photopolymers that may be differentiated by the type of binder, since this component determines to a great extent the choice of monomer, dye, and initiator used in the photopolymer. Normally, these materials are used in holographic applications, where high values of spatial frequencies are recorded. In these range of frequencies many processes are involved in the hologram formation, such as species diffusion, nonlocal polymerization (due to the finite size of polymer chains), shrinkage or swelling (volume changes), and others [9–13]. Therefore, analyzing the behaviour of a photopolymer as an optical storage medium is a complicate task. In this sense, the variations in the estimation of the monomer diffusion affect significantly the values obtained for other material parameters, making difficult to calculate them separately. In particular, it is interesting to analyze the material behavior at very low spatial

frequencies, since at these frequencies monomer diffusion does not play an important role [14] and even disappears at the zero spatial frequency limit [15–17].

Zero spatial frequency limit analysis is a method based on an interferometer that has been successfully applied in the phase-shift versus applied voltage characterization of liquid-crystal displays (LCDs) [18]. In the limit of zero frequency recording, that is, uniform exposure of the photosensitive layer, no diffusion processes are produced [15–17] and we can determined directly many parameters (as opposed to holographic characterization, the data obtained in this case are directly related to the physical properties of the material without the need of nonlinear fitting of multiparametric models) and these values can be used in diffusion models to predict the exact holographic material behavior [12, 13]. The measuring of refractive index variation and the changes in the thickness, in noncover-plated samples only (where the light is reflected directly from the material), can be directly observed in real time. Some other parameters that can be measured are polymerization rate, polymer refractive index

and relation between polymerization and recording intensity, and so forth. Interferometric measurements are applied to calculate the phase shift between transmitted and reflected beams. Measuring the phase variation of the reflected beam on the zone where polymerization takes place, we obtain direct information about the changes in the material thickness, and analyzing the phase changes in the transmitted beam in the same area we obtain information about changes in the refractive index and thickness together. The interferometric method proposed has been applied with success to characterize some materials. In this work we present a review and new comparison between different photopolymers. In this paper we present a compilation of the results obtained with this method for different photopolymers presented in the following references [15–17] with some new experiments and we compare their characteristics. At first we present the results obtained for some materials with polyvinyl alcohol (PVA) as a binder. One of them has Acrylamide (AA) as a main monomer. This photopolymer have been studied for many groups in many different cases [19–23]. Nevertheless, AA has an undesirable feature, the toxicity of AA and its low environmental compatibility [24, 25]. Therefore, we have changed the AA by sodium acrylate, NaAO, in order to obtain a higher environmental compatibility. Then we present the study of the recovered this material at the zero spatial frequency limit. The shrinkage of recovered materials cannot be measured which is an important drawback in the characterization of this material with zero spatial frequency recording. Finally, we present how the zero spatial frequency recording can be applied successfully also to H-PDLC materials.

2. Materials and Experimental Setup

The zero spatial frequency method (Figures 1(a) and 1(b)) is based on an interferometer that has been successfully applied in the phase-shift versus applied voltage characterization of liquid-crystal displays (LCDs) [18]. It shows good precision, and, due to its quasi-common-path architecture, is a robust setup, less sensitive to changing environmental conditions, and simpler to construct than Mach-Zehnder type interferometers. The setup has two arms with an angular separation of 14° , one to expose the recording material, whereas the second arm is the interferometer used to measure, in real time, the phase-shift. The recording material is perpendicularly oriented with respect to the interferometer axis in order to simplify the analysis of the interferometric results: at an oblique incidence we should take into account both the Fresnel coefficients at the interface and the increase of distance in the propagation across the layer.

In the first arm, the exposure beam provided by a solid-state Nd:YVO₄ Verdi laser with a wavelength of 532 nm (at this wavelength the dye presents the maximum absorption) is expanded and collimated using a spatial filter and a lens, obtaining a beam with 1 cm of radius. A wave plate and a neutral filter (attenuator) are added before the spatial filter to control the orientation and the intensity of the linearly polarized beam produced by the laser Nd:YVO₄. A polarizer

(P), with its transmission axis oriented along the vertical of the lab, is introduced to produce a beam with TE polarization incident onto the recording material. This incident beam forms an angle of 14° with respect to the photopolymer layer.

In the second arm we use a He-Ne laser to generate the interferences pattern, since the photopolymer does not present any absorption at 633 nm. We introduce a grating with a spatial frequency of 4 lines/mm to generate a series of diffracted orders; we block all the orders except +1 and -1. One of the two orders impinges on the exposed zone (illuminated by the Nd:YVO₄ laser, 532 nm) and the other one impinges on the nonexposed zone. The distance between the two orders is more than 1 cm, so as to eliminate the influence of the monomer diffusion in the polymerization process. Afterwards the orders are brought to interfere and from the interference pattern we may obtain the evolution in the material due to polymerization (diffusion is not present).

In Figure 1(a), once the two orders have propagated throughout the photopolymer, a lens is used to make them interfere. A microscope objective is used to amplify the interference pattern onto a CCD camera. This pattern is captured in real time as a function of exposure at specific time intervals, then is digitized and transferred to a personal computer [15]. We note that there may appear reflection gratings generated by Fresnel boundary reflections. However the recording of these undesired reflection gratings probably is highly attenuated due to the following reasons: the last boundary reflection between glass and air is weak and in addition, due to the nonlocal effect, the size of polymer chains prevents the recording of these high spatial frequencies.

In Figure 1(b) once the two orders are reflected by the photopolymer, we place a lens to make them interfere. A microscope objective is used to amplify the interference pattern onto a CCD camera. This pattern is captured at specific exposure time intervals, and then it is digitized and transferred to a personal computer. The reflections from the back surface are eliminated using a black film on the back surface [16].

Once the interference pattern has been stored, we can measure the shift with respect to the initial pattern obtained for the unexposed layer. To increase the accuracy in this calculation, we cross-correlate the different interference patterns with the initial one. The cross-correlation produces a clear peak [15–17]. The location of this peak for each correlated interference pattern with respect to the center of the image is equal to the shift in the fringe pattern. A full fringe shift is equal to a 2π radians variation in the phase shift. In this experiment, as we are using a reflection interferometer, the phase shift is directly related to the thickness variation of the material [16]. Depending on the sense of movement of the fringes (indicated by the arrow in the Figure 1) we can deduce if the exposed zone is shrinking or swelling with respect to the nonexposed one. In the case of the photopolymer studied in this paper we obtained that the exposed zone shrinks with respect to the nonexposed area.

When PVA is used as a binder the monomer must be water soluble, it must not evaporate during the preparation of layers (drying process) and it has to react through

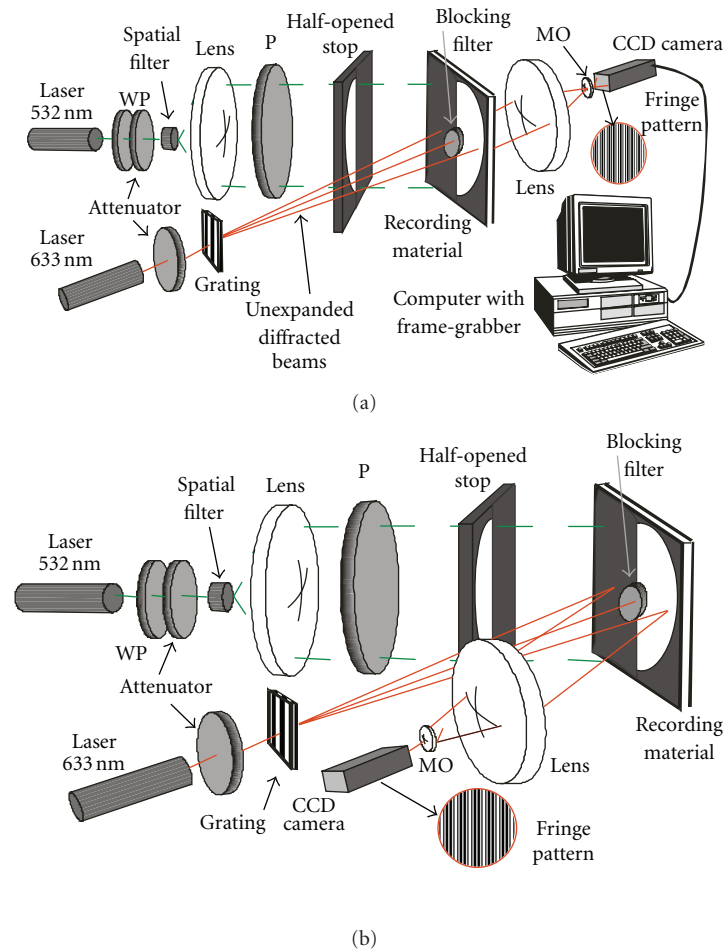


FIGURE 1: Experimental setup for zero spatial frequency analysis. P is polarizer, WP is wave plate, MO is microscope objective. (a) Transmission analysis. (b) Reflection analysis.

a radical chain mechanism. As mentioned above the toxicity of sodium acrylate (NaAO) is lower than that of AA [17]. Moreover, different triethanolamine (TEA) concentrations are normally used to obtain different material properties (TEA is a liquid at ambient temperature and plays an important role in the monomer and polymer diffusion during the polymerization process too).

The less toxic component of PVA/AA standard photopolymer is the dye, yellowish Eosin (YE), nevertheless to obtain a real environmental compatibility we have tested a less toxic dye [23, 24]. In the new photopolymer we use the sodium salt 5'-riboflavin monophosphate (PRF) as dye, bearing in mind that this substance is water soluble and exists in the environment, so it is not likely to cause environmental problems.

The solutions, whose compositions can be seen in Table 1, with water as solvent, and PVA as binder ($M_w = 130000$ a.m.u., hydrolysis degree = 87.7%) are deposited, using the force of gravity over a glass. The glass surface measures 30×40 cm² and left inside a dark chamber where humidity and temperature are controlled (relative humidity = 40–45%, $T = 21$ – 23°C) [17]. When large part of

the water has evaporated (about 48 hours), the layer has enough mechanical resistance and it can be cut without deformation. As crosslinker we have used N, N'-methylene-bis-acrylamide (BMA) to study the mixture with NaAO. The presence of BMA in the formulation of biophotopol [25] is optional and not essential to the main features of the photopolymer. Furthermore, the toxicity of BMA is clearly lower than AA. In this work we have characterized five new compositions. We have tested photopolymers with different TEA concentrations, with different concentrations of BMA, and different dyes. Composition A is directly derived from the previous works where biophotopol composition is optimized to achieve thick layers (around 1 mm thick). Since we have found weak modulation of layer type A, we have introduced BMA as crosslinker in compositions B and C. To increase the differences between exposed and nonexposed zones we have also introduced more NaAO in compositions B and D. To substitute YE we have presented composition E. The standard compositions used in previous works are compositions F and G (PVA/AA-based materials without and with crosslinker). The thickness of the samples is around (100 μm) and the intensity at 532 nm used is 1 mW/cm².

TABLE 1: Solution compositions and thicknesses.

Composition type	A	B	C	D	E	F	G
NaAO (g)	0.75	1.5	0.75	1.5	0.75	—	—
H ₂ O (mL)	12.5	12.5	12.5	12.5	12.5	14.5	14.5
TEA (mL)	1.25	1.5	1.5	3	3	1.25	2.3
PVA (mL) (15% w/v)	12.5	12.5	12.5	12.5	12.5	12.5	12.5
YE (0.8% w/v) (mL)	0.6	0.6	0.6	0.6	—	0.6	0.6
PRF (g)	—	—	—	—	0.14	—	—
BMA (g)	—	0.1	0.2	—	—	—	0.25
AA (g)	—	—	—	—	—	0.96	0.84
Thickness ± 4 (μm)	105	100	97	107	106	100	102

TABLE 2: Chemical compositions of H-PDLCs layers analyzed.

	C1	C2	C3	C4	C5
DPHPA	1.4 g	1.5 g	1.6 g	1.8 g	2 g
NMDETA	0.4 mL				
NVP	0.1 mL				
YE _t	1 mg				
LC BL087	0.6 mL	0.5 mL	0.4 mL	0.2 mL	

In these materials the absence of cover plate will lead to two types of cross membrane diffusion taking place: oxygen across the boundary [26] and water in and/or out (due to heating or absorption).

The H-PDLC photopolymer is composed of dipentaerythritol penta/hexa-acrylate (DPHPA) as monomer and binder, N-vinylpyrrolidone (NVP) as crosslinker, ethyl eosin (YE_t) as dye, and N-methyl diethanolamine (NMDETA) as radical generator. These components were mixed under red light where the material is not sensitive and under a temperature of 40°C to solve properly all the components, specially the crystal liquid molecules (LC BL087 provided by Merck). The solution (100 mL) was sonicated in an ultrasonic bath, heated, mixed with a magnetic mixer, and deposited between two glass plates each 2 mm thick. The H-PDLCs layers have thickness around 12 μm in order to apply the electric field and to align the crystal liquid molecules, thus obtain the switchable holographic gratings. In the samples analyzed in this work we have used spacing of 106 μm to increase the phase shift and see properly the different behaviours reducing the error in our calculations [15]. We focus our attention on the characterization of the chemical composition; we do not make switchable gratings. In Table 2 we described the composition of different layers analyzed at zero spatial frequencies. These compositions are designed to keep the liquid volume constant. In the five compositions we analyzed the influence of the liquid crystal in the polymerization process.

In order to calculate an approximate value for the refractive index, we will assume that when exposition has finished, all the monomer has been polymerized. In this sense, it is important to obtain a precise estimation of the initial volume fraction of the monomer present in the layer [13, 27, 28]. This volume fraction it is more complicate to calculate in

TABLE 3: Initial monomer volume fraction for PVA compositions analyzed.

Composition type	A	B	C	D	F	G
Initial monomer volume fraction	0.13	0.15	0.25	0.17	0.20	0.22

noncover-plated PVA materials, because PVA water absorption from the environment depends on the humidity. The water presence can be estimated if we measure the quantity of water evaporated during the drying process. It is interesting to note that after the drying process only very small portion of the initial water remains inside the layer. In our case, 48 hours after the layer deposition, the initial monomer volume fraction reaches the values presented in Table 3.

Once we have introduced the volume fractions, it is easy obtain the volume fraction for each component, $\phi^{(i)}$. Using the values of the refractive index, n_i , of each compound together with the Lorentz-Lorenz equation [27, 28], the refractive index of the layer before recording can be calculated, n_0 :

$$\frac{n_0^2 - 1}{n_0^2 + 2} = \sum_{i=1}^k \frac{n_i^2 - 1}{n_i^2 + 2} \phi^{(i)}. \quad (1)$$

These values were checked using Abbe refractometer (Model AYA-15) measurements and are presented in Table 4. As can be deduced from Table 4, in compositions C1 and C2 the liquid crystal volume fraction is higher than 20%. That can avoid huge variations in the refractive index at zero spatial frequency recording. n_0 is the average refractive index of the layer before the exposure. For zero spatial frequency analysis applied to H-PDLC, liquid crystal plays a similar role than binder in PVA materials; therefore, it does not participate in the chemical reactions.

3. Theoretical Treatment of Experimental Data

The phase shift in the reflection measurements, $\Delta\Phi_{\text{Shr}}$, is directly related to thickness variation during exposition at the zero spatial frequency limit. In this case, the thickness variations of the material (Δd) can be expressed as follows:

$$\Delta d = \frac{\Delta\Phi_{\text{Shr}} \lambda \cos \alpha}{4\pi}, \quad (2)$$

TABLE 4: Initial volume fractions and refractive indices, n .

	C1	C2	C3	C4	C5	n
DPHPA	0.5241	0.5649	0.6061	0.6899	0.7758	1.4900
NMDETA	0.1729	0.1739	0.1750	0.1771	0.1792	1.4694
NVP	0.0433	0.0435	0.0437	0.0443	0.0448	1.5110
YEt	0.0002	0.0002	0.0002	0.0002	0.0002	1.7700
LC BL087	0.2594	0.2175	0.1750	0.0885	0	1.5460
n_0	1.5016	1.4993	1.4969	1.4922	1.4873	

where λ is the wavelength, 633 nm in our case, and α is the angle inside the material. At zero spatial frequency limit, when diffusion does not take place, the decreasing of the monomer concentration, $\phi^{(m)}$, depends on the recording intensity, I , the dependency of the polymerization on intensity, γ , the initial monomer concentration, and the polymerization reaction constant, K_R [12]:

$$\phi^{(m)}(t) = \phi_0^{(m)} e^{-I^\gamma K_R t}, \quad (3)$$

where $\phi^{(m)}$ is the initial monomer concentration in volume fraction.

The model used in this paper is simple and based on the classical model proposed by Zhao and Moroulis [12]. The aim of the paper is to propose and demonstrate a simple diffractive and interferometric method to calculate the first approximation of the polymerization rate and monomer diffusion. It is important to note that the gradient of monomer concentration in depth due to the dye absorption analyzed in previous works [29, 30] has been disregarded in this first approximation to the problem. In this sense it is important to mention the contributions of Sheridan et al. to clarify all the parameters involved in the polymerization process such as the influence of oxygen inhibiting [26], the effects of the dye kinetics, and polymer chain initiation, propagation, and termination [31–33] that can be studied using real zero analysis in future works. In any case the parameters obtained using the presented methodology produce good results when introduced in simple models as it is shown in references [34, 35]. Following the same steps presented in [15–17] we can obtain the polymerization rate as a function of the experimental values of the phase shift during recording, PS , and the phase of saturation, PS_∞ :

$$\ln\left(1 - \frac{PS(t)}{PS_\infty}\right) = -I^\gamma K_R t = -F_R t. \quad (4)$$

Parameter, γ (which governs the relation between recording intensity and polymerization rate, see (3)), can be associated to the viscosity of photopolymer system. In this sense values of γ around 0.5 are associated to high fluid systems and for very dry systems values are near to 1 [12, 17]. To calculate this parameter the material can be exposed with some different intensities.

Furthermore, if the quantities of different compounds are known, it is possible to obtain the polymer refractive index using Lorentz-Lorenz equation [28]. To make the calculus more accurate it is possible to measure the exact concentration of each component at the end of zero spatial frequency

recording by additional methods. In any case, interesting information can be extracted solving the following equation for some particular cases:

$$\frac{n_p^2 - 1}{n_p^2 + 2} = \frac{1}{\phi_f^{(p)}} \left[\frac{n_f^2 - 1}{n_f^2 + 2} - \sum \frac{n_i^2 - 1}{n_i^2 + 2} \phi_f^{(i)} \right], \quad (5)$$

where n_f is the final refractive index of the layer, n_p is the refractive index of the polymer formed during exposition, n_i is the refractive index of chemical compound i , and $\phi_f^{(i)}$ is the final volume fraction for compound i . In the cases analyzed in this work, due to the high value of dye concentration, the samples show high absorption (the initial transmittances are around 1%). In addition, at the end of exposing process we detected a weak presence of dye. Thus we assume that in the exposed zones all the components, except the binder (in the case of PVA/AA and PVA/NaAO) or liquid crystal (in PEA photopolymer), are polymerized. In this sense, radical polymerization models could be used to know the exact concentration of monomer and dye after illumination [31–33]. With this assumption (5) can be reduced to:

$$\frac{n_p^2 - 1}{n_p^2 + 2} = \frac{1}{\phi_f^{(p)}} \left[\frac{n_f^2 - 1}{n_f^2 + 2} - \frac{n_C^2 - 1}{n_C^2 + 2} \phi^{(C)} \right], \quad (6)$$

where n_C and $\phi^{(C)}$ are the refractive index and volume fraction of the constant component, binder in PVA materials, and liquid crystal in H-DPLC.

4. Results and Discussion

In this section we present the experimental data obtained for different material compositions and different thicknesses using both experimental setups for PVA photopolymers and only transmission analysis for H-DPLC.

4.1. PVA Photopolymers. In transmission analysis we can observe the effects of the refractive index changes and thickness variation during polymerization. The results for the new five compositions are presented in Figure 2. As can be seen the changes in the phase between exposed and nonexposed zones for compositions A and E are very weak (around 60°), therefore the refractive index variation and polymerization rate are small. It is important to note that the absorption of PRF is clearly lower than YE.

As the velocity of the reaction is very slow, after 1000 s the material continues changing in compositions A, E, and D (compositions without crosslinker). Compositions B and C (compositions with crosslinker) present very similar behavior in transmission analysis. In these compositions after 400 s the reaction stops and the layers are in saturation state (where the phase shift does not change with the illumination). Using composition G (AA+BMA) the highest values of phase shift are obtained due to presence of the crosslinker.

In Figure 3, we have presented the results obtained in reflection analysis for NaAO-based compositions (A, B, C, D, and E). We can observe that the maximum shrinkage is around 3% for compositions B, C, and D. This shrinkage is

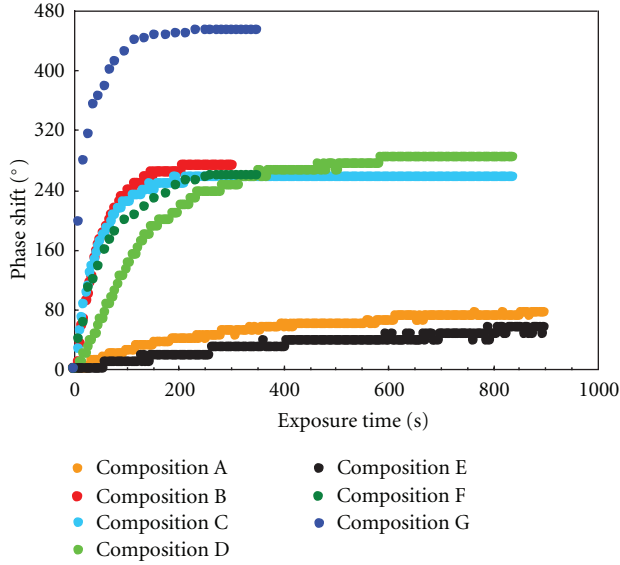


FIGURE 2: Phase shift as a function of the exposure time in transmission experiments for photopolymer compositions A, B, C, D, and E Biophotopol-derived compositions and F- and G- (PVA/AA) based materials.

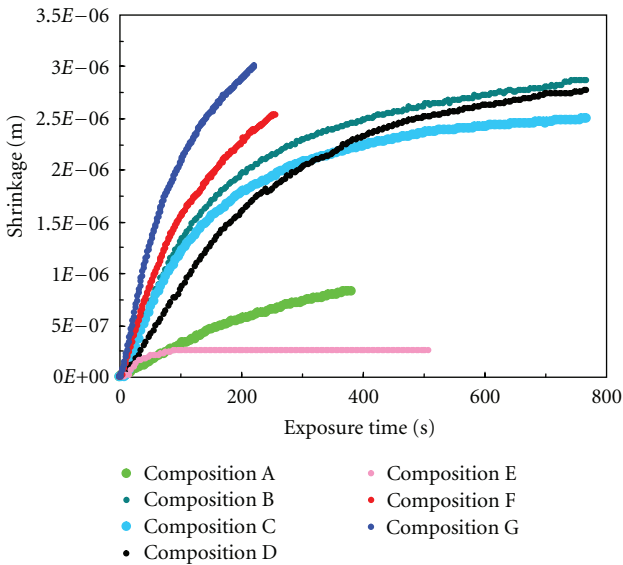


FIGURE 3: Shrinkages as a function of the exposure time for photopolymer compositions A, B, C, D, E, and F in reflection experiments.

large enough to store reflection diffractive elements using the relief variations [35]. On the other hand to use these materials as holographic memories the shrinkage should be reduced. As can be deduced from this and last figures compositions B, C, and D present similar behavior. The composition E, with PRF as a dye, the shrinkage is around $0.25\ \mu\text{m}$, nevertheless we cannot extract any significant information because the dye crystallizes during exposition.

In Figure 4 we depicted the results for some compositions obtained by the fitting based on (4). The results show us different values of F_R for each composition and in Table 5.

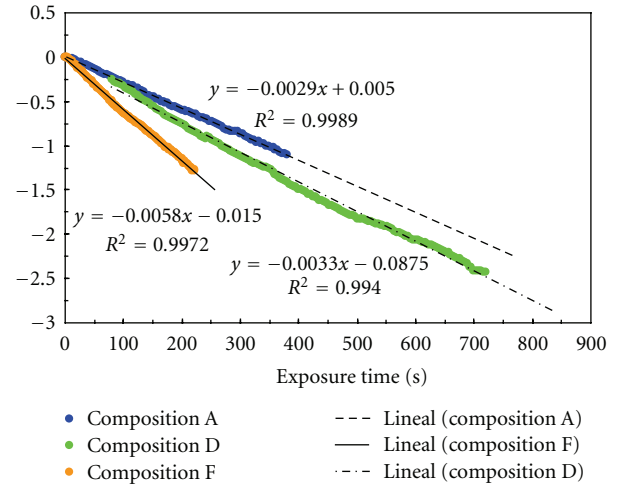


FIGURE 4: Fittings derived from (4) based on reflection experiments.

TABLE 5: Initial volume fractions and refractive indexes, n .

Composition type	A	B	C	D	F	G
$F_R \times 10^{-3} \text{ (s}^{-1}\text{)}$	3.2	3.6	4.1	3.3	5.8	7.0
R^2	0.999	0.993	0.992	0.994	0.997	0.994

The correlation value of the fittings, R^2 , indicates the good agreement between theory and experiments. In addition the compositions A and D present similar values of F_R because the only variation is the monomer concentration. For composition G (AA+BMA) we measured the highest values of phase shift are obtained due to presence of the crosslinker. Maybe for holographic recording there are some small changes in F_R values, because the experimental conditions present some differences such as the moving of monomers. Nevertheless we believe that using real zero spatial frequency a good estimation of the order of magnitude of F_R can be obtain. The validity of these values has been confirmed in recent papers [35], where the values of zero spatial frequency were used to predict the formation of relief optical elements on the photopolymer surface.

To calculate the value of γ in PVA/NaAO materials we exposed the material to two different exposure intensities 0.5 and $1\ \text{mW/cm}^2$ for composition type A and we calculated the polymerization rate value in each experiment using (4). The comparative result between the two exposures intensities are presented in Figure 5. With these data it is easy to obtain the value of γ . In our case the value obtained is 0.48 . This value is in good agreement with the value of 0.5 , usually assumed for photopolymers with low viscosity [12, 17]. It is important to note that for low values of the parameter γ the nonlinearity is increased.

It is obvious that the phase shift obtained depends directly of the photopolymer thickness. In [15] this method was applied to characterize layers thicker than $0.5\ \text{mm}$ able to store high quantity of data pages [5]. Results provided by (6) are presented in Table 6 (we have omitted composition G due to its different behavior). These values for n_p are important when they are compared with the monomers ones; that is,

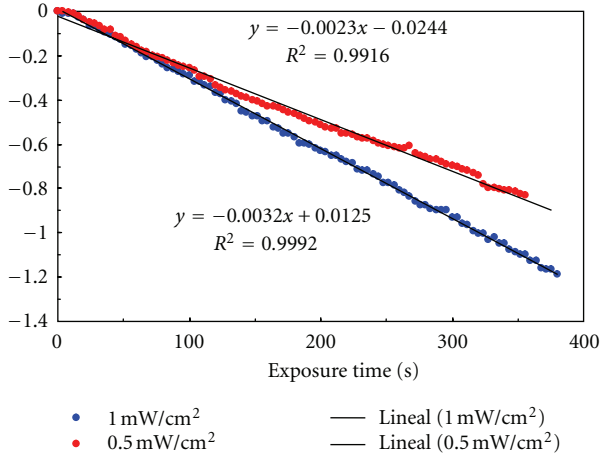


FIGURE 5: Fittings derived from (4) based for different exposure intensities (0.5 mW/cm^2 and 1 mW/cm^2).

TABLE 6: Fitted polymer refractive index.

Composition type	A	B	C	D	E
n_p	1.578	1.603	1.585	1.595	1.583

the refractive index of acrylamide is clearly lower than the NaAO refractive index [17]. To determinate these values we have followed the steps indicated in [15–17]. Furthermore we want to remark that the main important point is to compare n_m with n_p and these parameters with the value of the refractive index of the binder, n_b (5). In this sense the importance of crosslinker to increase n_p has been demonstrated using the zero frequency technique. To obtain a better analysis of the data presented in Table 6 it is important to note that the refractive index of NaOA is 1.565 [17].

4.2. H-DPLC Photopolymers. In order to obtain information about the effect of incorporating CL in the photopolymerizable solution using real zero frequency recording, the phase shift between illuminated and nonilluminated zones for compositions C1, C2, C3, C4, and C5 is shown in Figure 6. As can be seen in this figure, the presence of CL molecules produces a decrease in phase shift. The values of n_p obtained for C5, C4, C3, and C5 (without LC) using (6) are 1.492, 1.492, 1.495, 1.496, and 1.496, respectively. Therefore we can conclude that incorporation of LC molecules results in only a small change in polymer refractive index. As zero spatial frequency recording prevents diffusion of liquid crystalline molecules into dark regions and of monomers to bright regions, the uniform concentration of LC throughout the whole layer makes it difficult for the refractive index to change.

Following the steps described previously and using (4), it is possible to obtain the polymerization rate for each composition. The values obtained are represented in Table 7. As can be seen in this figure the correlation parameter indicates that there is agreement between experimental data and theoretical behaviour. From the analysis of Table 7 the high values of the polymerization rates obtained can be deduced. These values

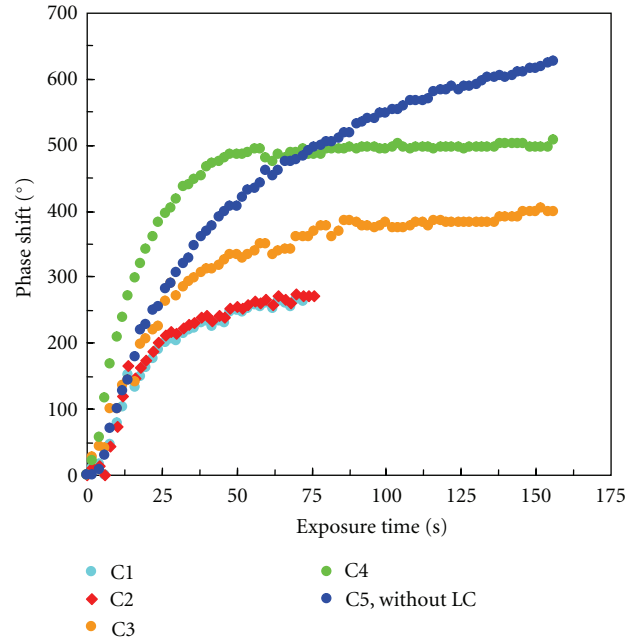


FIGURE 6: Behavior of photopolymers C1, C2, C3, C4, and C5 at the zero spatial frequency limit in transmission.

TABLE 7: Initial volume fractions and refractive indexes, n .

Composition type	C1	C2	C3	C4	C5
$F_R \times 10^{-2} (\text{s}^{-1})$	4.38	4.86	3.56	5.50	4.54
R^2	0.984	0.986	0.977	0.997	0.994

are 10 times higher than the ones obtained for PVA materials analyzed in Table 5, due to the multifunctional monomer used in H-PDLC materials. To fit accurately the polymerization rate in these materials the temperature is a fundamental parameter. In general, in Table 7 we can detect a decrease in the polymerization when high values of LC concentration are included in the composition. The exception is the C3 with very low polymerization rate and correlation parameter. As can be seen the curve grows very quickly from 0 to 50 s and then the phase shifts increases slowly, as if the residual monomer polymerizes with difficulties, maybe produced by Trommsdorff effect [36] and the cooling of the layer.

5. Conclusions

Using zero frequency recording we characterized different types of photopolymers with and without liquid crystal molecules, cover plating, crosslinker, and so forth. Using this method we were able to analyze polymerization separately from the diffusion and thus discuss the influence of the different components such as liquid crystal molecules, crosslinker, and so forth on grating formation. We also presented some simple models using interferometric methods to fit the polymerization rate, the refractive index of polymers and the relation between exposure intensity on polymerization. We

have shown how this method can be used to obtain photopolymer layers with desired properties. Finally we think that this method can be applied to fit some of the multitude of parameters that take place in the light absorption in photopolymers materials. All these parameters should be taking into account in order to design holographic diffusion model to predict the behavior of these photopolymers. In our opinion the viability of these three types of photopolymers for diffractive and holographic application has been demonstrated.

Acknowledgments

This work was supported by the Ministerio de Ciencia e Innovación of Spain under Projects FIS2011-29803-C02-01 and FIS2011-29803-C02-02 and by the Generalitat Valenciana of Spain under Project PROMETEO/2011/021.

References

- [1] J. Neumann, K. S. Wiekling, and D. Kip, "Direct laser writing of surface reliefs in dry, self-developing photopolymer films," *Applied Optics*, vol. 38, no. 25, pp. 5418–5421, 1999.
- [2] X. T. Li, A. Natansohn, and P. Rochon, "Photoinduced liquid crystal alignment based on a surface relief grating in an assembled cell," *Applied Physics Letters*, vol. 74, no. 25, pp. 3791–3793, 1999.
- [3] A. Márquez, S. Gallego, M. Ortuño et al., "Generation of diffractive optical elements onto a photopolymer using a liquid crystal display," in *Optical Modelling and Design*, vol. 7717, 77170D of *Proceedings of the SPIE*, Brussels, Belgium, April 2010.
- [4] M. D. Lechner, "Photopolymers for optical memories and waveguides," *Electronic Properties of Polymers and Related Compounds*, vol. 63, pp. 301–308, 1985.
- [5] H. J. Coufal, D. Psaltis, and G. T. Sincerbox, *Holographic Data Storage*, Springer Series in Optical Sciences, Springer, Berlin, Germany, 2000.
- [6] A. Márquez, C. Neipp, A. Beléndez, S. Gallego, M. Ortuño, and I. Pascual, "Edge-enhanced imaging with polyvinyl alcohol/acrylamide photopolymer gratings," *Optics Letters*, vol. 28, no. 17, pp. 1510–1512, 2003.
- [7] G. Manivannan and R. A. Lessard, "Trends in holographic recording materials," *Trends in Polymer Science*, vol. 2, pp. 282–290, 1994.
- [8] K. Curtis, L. Dhar, L. Murphy, and A. Hill, *Future Developments, in Holographic Data Storage: From Theory to Practical Systems*, John Wiley & Sons, 2010.
- [9] J. T. Sheridan and J. R. Lawrence, "Nonlocal-response diffusion model of holographic recording in photopolymer," *Journal of the Optical Society of America A*, vol. 17, no. 6, pp. 1108–1114, 2000.
- [10] M. R. Gleeson, S. Liu, and J. T. Sheridan, "The production of primary radicals in photopolymers during holographic exposure," *Optik*, vol. 121, no. 24, pp. 2273–2275, 2010.
- [11] I. Naydenova, E. Mihaylova, S. Martin, and V. Toal, "Holographic patterning of acrylamide-based photopolymer surface," *Optics Express*, vol. 13, no. 13, pp. 4878–4889, 2005.
- [12] G. Zhao and P. Moroulis, "Extension of diffusion model of holographic photopolymer," *Optics Communications*, vol. 15, pp. 528–532, 1995.
- [13] J. V. Kelly, M. R. Gleeson, C. E. Close et al., "Temporal analysis of grating formation in photopolymer using the nonlocal polymerization-driven diffusion model," *Optics Express*, vol. 13, no. 18, pp. 6990–7004, 2005.
- [14] S. Gallego, A. Márquez, D. Méndez, S. Marini, A. Beléndez, and I. Pascual, "Spatial-phase-modulation-based study of polyvinyl-alcohol/acrylamide photopolymers in the low spatial frequency range," *Applied Optics*, vol. 48, no. 22, pp. 4403–4413, 2009.
- [15] S. Gallego, A. Márquez, D. Méndez et al., "Real-time interferometric characterization of a polyvinyl alcohol based photopolymer at the zero spatial frequency limit," *Applied Optics*, vol. 46, no. 30, pp. 7506–7512, 2007.
- [16] S. Gallego, A. Márquez, D. Méndez et al., "Analysis of PVA/AA based photopolymers at the zero spatial frequency limit using interferometric methods," *Applied Optics*, vol. 47, no. 14, pp. 2557–2563, 2008.
- [17] S. Gallego, A. Márquez, M. Ortuño, S. Marini, and J. Francés, "High environmental compatibility photopolymers compared to PVA/AA based materials at zero spatial frequency limit," *Optical Materials*, vol. 33, no. 3, pp. 531–537, 2011.
- [18] A.J. Bergeron, F. Gauvin, D. Gagnon, H. Gingras, H. H. Arsenault, and M. Doucet, "Phase calibration and applications of a liquid crystal spatial light modulator," *Applied Optics*, vol. 34, pp. 5133–5139, 1995.
- [19] S. Calixto, "Dry polymer for holographic recording," *Applied Optics*, vol. 26, pp. 3904–3909, 1987.
- [20] S. Blaya, R. Mallavia, L. Carretero, A. Fimia, and R. F. Madrigal, "Highly sensitive photopolymerizable dry film for use in real time holography," *Applied Physics Letters*, vol. 73, no. 12, pp. 1628–1630, 1998.
- [21] S. Martin, P. E. Leclere, Y. L. M. Renotte, V. Toal, and Y. F. Lion, "Characterization of an acrylamide-based dry photopolymer holographic recording material," *Optical Engineering*, vol. 33, p. 3942, 1994.
- [22] M. Ortuño, S. Gallego, C. García, C. Neipp, A. Beléndez, and I. Pascual, "Optimization of a 1 mm thick PVA/acrylamide recording material to obtain holographic memories: method of preparation and holographic properties," *Applied Physics B*, vol. 76, no. 8, pp. 851–857, 2003.
- [23] F. T. O'Neill, A. J. Carr, S. M. Daniels et al., "Refractive elements produced in photopolymer layers," *Journal of Materials Science*, vol. 40, no. 15, pp. 4129–4132, 2005.
- [24] M. Friedman, "Chemistry, biochemistry, and safety of acrylamide. A review," *Journal of Agricultural and Food Chemistry*, vol. 51, no. 16, pp. 4504–4526, 2003.
- [25] M. Ortuño, E. Fernández, S. Gallego, A. Beléndez, and I. Pascual, "New photopolymer holographic recording material with sustainable design," *Optics Express*, vol. 15, no. 19, pp. 12425–12435, 2007.
- [26] M. R. Gleeson, J. V. Kelly, C. E. Close, F. T. O'Neill, and J. T. Sheridan, "Effects of absorption and inhibition during grating formation in photopolymer materials," *Journal of the Optical Society of America B*, vol. 23, no. 10, pp. 2079–2088, 2006.
- [27] S. Gallego, *Modelización del comportamiento holográfico de un fotopolímero de polivinilalcohol/acrilamida [Ph.D. thesis]*, University of Alicante, 2005.
- [28] M. Born and E. Wolf, *Principles of Optics*, Pergamon Press, Oxford, UK, 1980.
- [29] S. Gallego, C. Neipp, M. Ortuño, A. Beléndez, E. Fernández, and I. Pascual, "Analysis of monomer diffusion in depth in photopolymer materials," *Optics Communications*, vol. 274, no. 1, pp. 43–49, 2007.

- [30] S. Gallego, M. Ortuño, C. Neipp et al., “3-dimensional characterization of thick grating formation in PVA/AA based photopolymer,” *Optics Express*, vol. 14, no. 12, pp. 5121–5128, 2006.
- [31] S. Liu, M. R. Gleeson, J. Guo, and J. T. Sheridan, “Optical characterization of photopolymers materials: theoretical and experimental examination of primary radical generation,” *Applied Physics B*, vol. 100, pp. 559–569, 2010.
- [32] D. Sabol, M. R. Gleeson, S. Liu, and J. T. Sheridan, “Photoinitiation study of Irgacure 784 in an epoxy resin photopolymer,” *Journal of Applied Physics*, vol. 107, no. 5, Article ID 053113, 2010.
- [33] S. Liu, M. R. Gleeson, J. Guo, and J. T. Sheridan, “High intensity response of photopolymer materials for holographic grating formation,” *Macromolecules*, vol. 43, no. 22, pp. 9462–9472, 2010.
- [34] S. Gallego, A. Márquez, M. Ortuño et al., “Surface relief model for photopolymers without cover plating,” *Optics Express*, vol. 19, no. 11, pp. 10896–10906, 2011.
- [35] S. Gallego, A. Márquez, M. Ortuño, J. Francés, I. Pascual, and A. Beléndez, “Relief diffracted elements recorded on absorbent photopolymers,” *Optics Express*, vol. 20, pp. 11218–11231, 2012.
- [36] J. V. Kelly, F. T. O’Neill, J. T. Sheridan, C. Neipp, S. Gallego, and M. Ortuno, “Holographic photopolymer materials: non-local polymerization-driven diffusion under nonideal kinetic conditions,” *Journal of the Optical Society of America B*, vol. 22, no. 2, pp. 407–416, 2005.

Review Article

A Review of the Optimisation of Photopolymer Materials for Holographic Data Storage

Jinxin Guo,¹ Michael R. Gleeson,² and John T. Sheridan¹

¹ School of Electrical, Electronic and Communications Engineering, College of Engineering and Architecture, Communications and Optoelectronic Research Centre, The SFI-Strategic Research Cluster in Solar Energy Conversion, University College Dublin, Belfield, Dublin 4, Ireland

² Department of Computer Science, National University of Ireland Maynooth, Maynooth Co. Kildare, Ireland

Correspondence should be addressed to John T. Sheridan, john.sheridan@ucd.ie

Received 25 April 2012; Accepted 4 May 2012

Academic Editor: Sergi Gallego

Copyright © 2012 Jinxin Guo et al. This is an open access article distributed under the Creative Commons Attribution License, which permits unrestricted use, distribution, and reproduction in any medium, provided the original work is properly cited.

Photopolymers are very interesting as optically sensitive recording media due to the fact that they are inexpensive, self-processing materials with the ability to capture low-loss, high-fidelity volume recordings of 3D illuminating patterns. We have prepared this paper in part in order to enable the recognition of outstanding issues, which limit in particular the data storage capacity in holographic data storage media. In an attempt to further develop the data storage capacity and quality of the information stored, that is, the material sensitivity and resolution, a deeper understanding of such materials in order to improve them has become ever more crucial. In this paper a brief review of the optimisation of photopolymer materials for holographic data storage (HDS) applications is described. The key contributions of each work examined and many of the suggestions made for the improvement of the different photopolymer material discussed are presented.

1. Introduction

Despite improvement to a range of standard storage media, such as solid state memory/magnetic tape [1], there is an every growing need to increase the capabilities and flexibility of data storage systems. To succeed further in the data storage market, optical storage technology must compete effectively against magnetic tape on all fronts: cost, capacity, and data transfer rate [2]. One great potential optical method uses a holographic approach, where recorded data are distributed throughout the volume of a thick medium. Photopolymer materials are being actively studied for practical applications such as Holographic Data Storage (HDS), hybrid optoelectronics, photo embossing, including the manufacture of refractive and diffractive optical elements, and the self-trapping of light [3–9]. Their versatility, ease of use, and self-processing ability give them many advantages over more traditional materials such as silver halide and DCG [10, 11]. The necessity for development and optimization of a photopolymer system, with higher storage capability and stability, has

been recognized, and they have recently received significant attention.

In this paper, we review recent attempts to more fully understand what is needed to optimise the performance of photopolymer materials for HDS applications. Specifically we aim to discuss the evolution of our understanding of what takes place inside these materials and what happens during and after holographic recording, with the objective of further improving the performance of such materials.

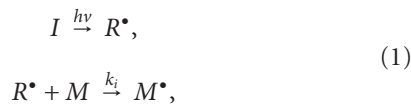
The paper is structured as follows. In Section 2, we briefly review the photochemical processes generally occurring during the fabrication of refractive index structures in free-radical photopolymerisation material systems. In Section 3, a description of some typical measurements performed in order to optically characterise photopolymer materials is presented. In Section 4, we begin by briefly discussing a range of different photopolymer materials, which are currently being developed for potential use as HDS media. Then an overview of optimisation of photopolymer materials in the literature is presented. A brief conclusion is given in Section 5.

A discussion of several issues, which limit the performance of such materials and some potential improvements, is presented.

2. Photochemical Processes

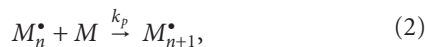
In typical free radical photopolymerization systems, the kinetic model describing what takes place involves five main processes: (I) initiation, (II) propagation, (III) termination, (IV) inhibition, and (V) chain transfer, each of which may involve several physicochemical reactions. We discuss the major chemical reactions taking place in each process below [12–16].

(I) *Initiation.* During illumination, the reaction between the photosensitiser and the electron donor (coinitiator) leads to the production of initiator radicals, R^\bullet , which can react with the monomers to produce chain initiators, M^\bullet [14]:



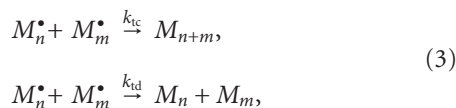
where I is the initiator, $h\nu$ indicates the energy absorbed from a photon, k_i is the chain initiation kinetic constant, and M represents a monomer molecule.

(II) *Propagation.* The chain initiator, M_1^\bullet , will attach itself to another monomer molecule, M , by addition to the C=C bond yielding a growing polymer radical with an active tip. Through propagation the polymer chain grows [11, 12]:



where k_p is the rate constant of propagation and M_n^\bullet and M_{n+1}^\bullet are the growing macroradical chains of n and $(n + 1)$ repeat monomeric units ($n \geq 1$).

(III) *Termination.* Termination can occur in three ways. Two of these, disproportionation and combination, involve two growing macroradicals interacting, that is, the bimolecular termination mechanism:



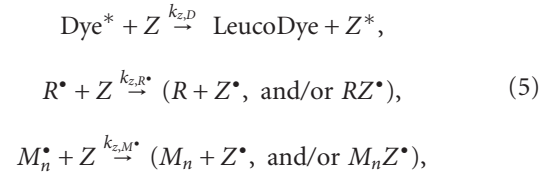
where k_{ic} and k_{id} are the rate constants of combination and disproportionation termination, respectively. M_n, M_m , and M_{n+m} represent terminated chains which have no radical tip, that is, a dead polymer chain.

A third possible termination mechanism involves primary radical termination [14, 17]:



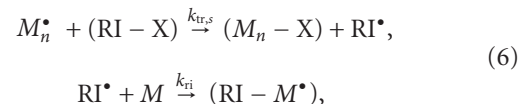
where k_{tp} is the rate constant of primary radical termination. In this step, a growing macro-radical chain reacts with a primary radical (initiator radical) leading once again to the production of inactive or dead polymer chains [14].

(IV) *Inhibition.* Inhibitors are chemicals which react with the initiating and propagating radical species by rapidly removing or scavenging these radicals. Polymerization is completely halted until they are all consumed [13]. Several possible inhibitor reaction mechanisms are listed below:



where Z is the inhibitor species, for example, oxygen, Dye^* is the excited photosensitiser, Z^\bullet is the concentration of singlet oxygen [13, 16–18], and $k_{z,D}$, k_{z,M^\bullet} , and k_{z,R^\bullet} are the rate constants of inhibition of the photosensitiser, the macroradicals, and the primary radicals, respectively. Inhibition leads to a dead band at the start exposure, that is, no initial grating formation during exposure. The effects of inhibitors are especially significant when lower exposure energies are used, for example, when large areas must be exposed or short pulses must be used [14].

(V) *Chain Transfer Mechanism.* In many polymerization systems, the average polymer weight is observed to be lower than predicted by the chain transfer reaction [13, 19–21]. Generally, the chain transfer process causes the premature termination of a growing macro-radical chain and arises because of the presence of a chain transfer agent (CTA) [13]. Due to this reaction, a new radical is produced which is referred as a reinitiator. This reinitiator reacts with a monomer molecule to initiate a new growing macro-radical chain. The chain transfer reactions can be written as



where RI-X is the chain transfer agent, $-\text{X}$ is the atom or species transferred, and RI^\bullet is the reinitiator which has a radical tip. $k_{\text{tr,S}}$ and k_{ri} are the transfer rate constant to chain-transfer agent and the re-initiation rate constant, respectively. Due to the premature termination reaction with the chain transfer agent, RI-X , the propagating polymer chains will stop growing earlier than they would have if the CTA was not present. We assume that the free radical RI-M^\bullet produced can be treated as acting chemically identical to a chain initiator M^\bullet . Therefore the reinitiator, RI^\bullet , simply initiates a new growing chain with a radical tip M^\bullet . Thus, while the polymer chains are shortened, the amount of monomer polymerized and the rate of polymerization can remain high.

In the above we have presented the main photochemical processes which take place in general free-radical photopolymerisation materials. However, the processes may vary in complexity and significance in different photopolymer systems. Furthermore, Figure 1 illustrates simple 1D grating formation process in such a photopolymer material. It can be seen from the schematic that polymerisation occurs most

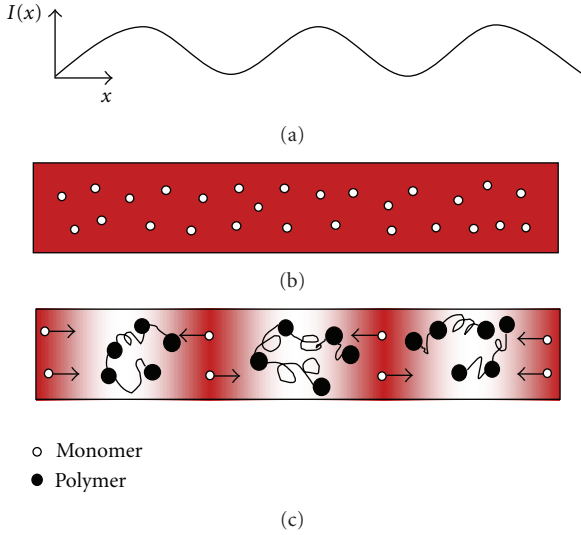


FIGURE 1: Grating formation in photopolymer where (a) represents the sinusoidal illuminating intensity distribution at the plate; (b) represents the photopolymer layer before recording; (c) represents the photopolymer layer during recording.

strongly in the bright regions of high exposure due to the sinusoidal illuminating intensity pattern. As monomer is consumed in these regions due to polymerisation, a monomer concentration gradient is created. In the weakly illuminated regions, the excess monomer diffuses into the brighter regions in order to eliminate the resulting concentration gradient. This is illustrated in Figure 1(c). As a result, a sinusoidal polymer concentration distribution is formed. Assuming all the monomer is converted to polymer by the end of the recording process, the spatial variation in the permittivity of the material will be related to the polymer concentration distribution. Thus a permanent modulation of the layer permittivity is generated; that is, a volume refractive index grating structure is produced.

3. Holographic Setup and Measurements

In order to optically characterise holographic recording materials, the gratings fabricated are often modeled using Kogelnik's two-wave coupled-wave theory [22]. In 1981, Moharam and Gaylord [23] presented a rigorous coupled-wave approach, which included the second derivatives and boundary diffraction, to obtain a stable algorithm for thick material layers. More rigorous models have been developed, see Syms [24], based on the electromagnetic theory, in order to explore more accurately what happens in volume (thick) hologram. Comparing with the simple coupled wave theory, such models can involve the use of complex computational techniques but deal with more complicated grating structures. Kogelnik's two-wave coupled-wave theory is both simple and practical and describes the efficiency with which thick holograms can diffract incident light. Analytic expressions for both the angular and wavelength dependence of sinusoidal grating diffraction efficiency as the incident light

deviates from the Bragg condition are available. Thus the dependence of the diffraction efficiency, $\eta(t)$, on a number of grating parameters is known. For a lossless, unslanted transmission geometry grating replayed on Bragg with TE-polarized probe light [22], that $\eta(t)$ is described by the following equation:

$$\eta(t) = \frac{I_D(t)}{I_{in}} = \sin^2\left(\frac{\pi d n_1(t)}{\lambda \cos \theta}\right), \quad (7)$$

where I_{in} and $I_D(t)$ are the incident and diffracted probe beam intensities, respectively, d is the grating thickness, θ and λ represent the Bragg angle and wavelength of the incident probe beam inside the grating layer, and $n_1(t)$ is the amplitude of the first harmonic time-dependent refractive index modulation. We note that in deriving (7), all boundary reflections have been neglected. This equation can be rearranged to give a convenient expression for the temporally varying refractive index modulation, $n_1(t)$, as follows:

$$n_1(t) = \frac{\lambda \sin^{-1}\left(\sqrt{\eta(t)}\right) \cos \theta}{\pi d}. \quad (8)$$

By monitoring the amount of light diffracted from a weak probe beam during exposure, $I_D(t)$, growth curves of refractive index modulation against exposure time can be extracted. In most of the literature, reviewed below, such growth curves are used to monitor grating formation. A typical experimental setup used to obtain such growth curves is presented in Figure 2 [25].

During the recording process, the evolution of the grating in real time is monitored. One of the main advantages of many photopolymer materials is that they are self-processing and thus nonlatent [22], and therefore the diffractive scattering properties are immediately available as the grating is being formed. This allows the evolution of the grating to be monitored during exposure by replaying the grating as it is being recorded using a probe laser with a wavelength which lies outside the absorption spectrum of the photosensitizer used. This ensures that the probing does not affect the fabrication process. Using the setup as showed in Figure 2, it is possible to monitor the grating formation (growth curve) by recording the intensity of the diffracted beam, $I_D(t)$, to estimate $n_1(t)$ using (8). The angular response of the grating can also be obtained by introducing a rotation stage into the setup. The resulting system allows the recording of grating arrays, and appropriate processing of the measured intensity data allows other grating parameter values to be extracted, that is, grating thickness and nonuniformities [22, 26].

4. Photopolymer Materials and Optimisations

Photopolymers generally consist of a monomer, a photosensitive dye, and an initiator. They can either be liquid or dry layer systems. The dry photopolymers usually contain a polymeric binder in addition to the other components in order to produce dry photopolymer layers. Several photopolymer materials, which have received attention during HDS media studies, are now discussed.

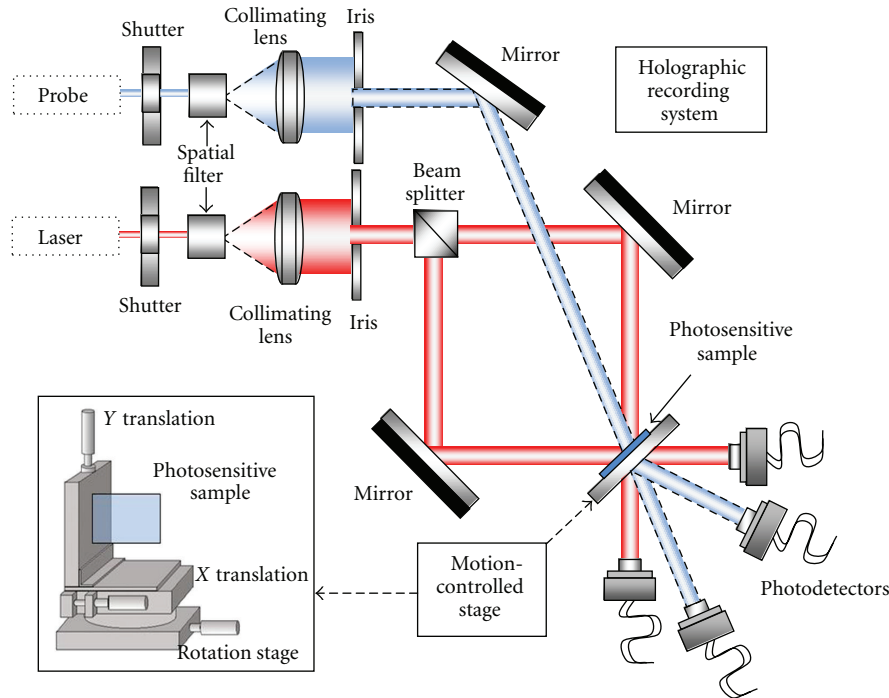


FIGURE 2: Typical experimental setup to record unslanted volume transmission holographic gratings with a recording wavelength of $\lambda = 633$ nm and a probing wavelength of $\lambda = 430$ nm.

Photopolymers were first introduced as a holographic recording material by Close et al. in 1969 [27]. This liquid state material consisted of a mixture of acrylamide and metal acrylate monomers and a photocatalyst, methylene blue. Sadlej and Smolinska [28] improved the original system proposed by Close by including a polyvinyl alcohol (PVA) binder which allowed the production of dry photopolymer layers. In the 1980s, Calixto [29] continued the work on acrylamide-based systems. The material contained acrylamide monomer, TEA as an electron donor, methylene blue photosensitizer, and PVA as a binder. Blaya et al. [30] improved the sensitivity of the acrylamide material for recording at 633 nm by changing the cross-linker, N,N' -(1,2-Dihydroxyethylene)bisacrylamide. A hybrid material containing acrylamide and acrylic acid as monomers was proposed by Zhao et al. [31]. The material uses methylene blue as the photosensitizer, TEA and *p*-toluenesulfonic acid as sensitizers, and gelatin as a binder.

Trentler et al. [32] developed an epoxy resin photopolymer material with a solid matrix, which is formed *in situ* as the epoxy cures at room temperature. The unreacted vinyl monomers within the material are subsequently photopolymerized during hologram recording. One of the key features of this type of material is the separation of the epoxy and vinyl polymerizations. This separation allows for a large index contrast to be developed in holograms when components are optimized. This material is functional in thick formats (several millimetres), which enables narrow angular bandwidth and high diffraction efficiency. A dynamic range ($M/\#$) up to 13 has been measured in these materials.

Eich et al. [33] introduced a type of photopolymer material with liquid crystals, which offered a completely different method for optical data storage. Following this work, various functionalized systems, with liquid crystals and/or optical chromophores, commonly referred in the literature as photoaddressable polymers (PAPs), were developed. Zilker et al. [34] improved these types of materials by introducing a new concept, donor-acceptor substitutions, which lead to an increase of the interaction between azo and mesogen groups. A refractive index modulation up to 0.2 has been obtained in these materials.

While materials above have received much attention in the literature, attempts have also been made to improve the refractive index modulation of a photopolymerizable medium by introducing diffusible high refractive index species, such as titania nanoparticles, into the regular photopolymerisable layers. The refractive index modulation in such materials is comparable to those for holographic polymer-dispersed liquid crystals [35]. This type of approach also offers one possible way to suppress the effects of polymer shrinkage, which occur due to volumetric changes during photopolymerisation process [35].

In 1998, Blaya et al. [36] investigated the effects of the addition of a cross-linking agent (N,N' -methylenebisacrylamide) to a photopolymerisable matrix for HDS. A nonlinear response of the material with regard to the storage intensity was observed. Diffraction efficiency of around 88% was obtained with energy exposure of 12 mJ/cm². At that time, the sensitivity of this material approached that of commercial films without the use of postprocessing, which was necessary

in other materials. Later in 1998, the effects of the exposing intensity, the thickness, and the variation of the concentration of each component were experimentally examined by Blaya et al. [37]. Diffraction efficiencies of 80%, with energetic sensitivities of 40 mJ/cm², were obtained in photosensitive films of a 35 μm thickness at a spatial frequency of 1000 lines/mm.

In 1999, Mallavia et al. [38] developed a photopolymerizable system composed of a xanthene dye and N-methyldiethanolamine (MDEA) as photoinitiator with a monomer mixture of 2-hydroxyethyl methacrylate (HEMA) and pentaerythritol triacrylate (PETA). The best results reported were diffraction efficiencies over 40% with energetic exposures of 800 mJ/cm², with a decrease of inhibition time when high concentrations of PETA (>67%) were used.

At the same time, Fimia et al. [39] reported a new aqueous photopolymer containing the monomers acrylamide, N,N'-methylenebisacrylamide and zinc acrylate, the initiators 4,6-dimethyl-2,5-diformylphenylfluorescein (2ISF) and methylene blue (MB), and the coinitiator sodium p-toluenesulphinate. This formulation enhanced the high-energy sensitivity at 514 or 633 nm, compared to that of the same mixture but with only one of the two dyes. Maximum diffraction efficiencies of 15–20% for 15–60 mJ/cm² were reached, due to the combined action of the cationic and anionic dyes as visible photoinitiators. The enhancement observed, which arose due to the developer mixture in photographic emulsions, suggested that such mixture could be of potential utility when recording multifunctional diffractive systems.

In 2000, Karpov et al. [40] proposed a theoretical model for hologram recording in photoformers (polymer aggregates with polymerization diffusion mechanism of refractive index modulation and/or absorption coefficient modulation). This method is derived from the rate equations, which describe the sequence of chemical transformations in the photoformer under illumination using an appropriate wavelength and power. A set of equations which take into account the nonlinear diffusion and the multicomponent diffusion (monomer, polymer, holes) effects is presented. This model is then fitted to experimental data in an attempt to estimate the kinetics involved during photopolymerization, such as the polymer chain termination order and diffusivity.

In 2001, O'Neill et al. [41] examined the use of an aerosol sealant (varnish) to seal the photopolymer holographic recording material from the environment. Application of the sealant was found to produce some deterioration in the optical quality of the resulting holographic optical elements (HOEs). It was also shown to produce an increased lifetime of the active material (prerecording), an increase in the diffraction efficiency from the resulting diffraction gratings recorded, and improved HOE shelf life. While some of the material characteristics were improved by the introduction of the varnish layer, an increase diffuse scatter was observed during the recording layers producing. This technique was chosen to replace coverplating as it was found to be a cheaper and simpler way to seal the photopolymer recording material from the environment. The coverplating material in general leads to better humidity stability and more stable long-term diffraction efficiency.

In 2002, in work reported by Yao et al. [42], an acrylamide-based polymeric film was optimised and characterised for holographic recording. Diffraction efficiencies of 55%, with the energetic sensitivity of 60 mJ/cm², were obtained in the photosensitive films of 150 μm thickness with a spatial frequency of 2750 lines/mm. The paper indicated that each component had an optimal concentration and that it is not the case that the higher the concentration, the better the holographic recording characteristics. The effects of several components' concentrations were examined experimentally in this work.

In the same year, Suzuki et al. [35] demonstrated stable holographic storage in the green with high diffraction efficiency and recording sensitivity in TiO₂ nanoparticle-dispersed methacrylate photopolymer films. It was shown that the diffraction efficiency as well as the recording sensitivity significantly increases with increasing nanoparticle concentration. It was also found that volumetric shrinkage during holographic exposure is noticeably suppressed by their inclusion. A fractional change of 2.9% in thickness was estimated. A refractive index modulation of 5.1×10^{-3} with sensitivity $S = 1.8 \times 10^{-3} \text{ cm}^2/\text{J}$ in this material was reported.

In 2003, Tomita and Nishibiraki [43] extended the results in [35] reporting a more than one-order-of-magnitude improvement in holographic recording sensitivities in the green by doping pyrromethene dyes into SiO₂ nanoparticle-dispersed methacrylate photopolymer films. Holographic recording dynamics were measured for several dye concentrations and writing intensities. It was found that there exists an optimum recording intensity for a given dye concentration to maximize the strength of a permanent (fixed) volume hologram. It was shown that the doped dye concentrations lower than 0.1 wt% were preferable when the thickness of sample layer is 50 μm. The sample with 0.05 wt% of dye doped increased sensitivity S and dynamic sensitivity S^* that were 9 and 12 times the values, 4.2×10^{-4} and $1.2 \times 10^{-4} \text{ cm}^2/\text{J}$, for undoped sample.

Later in the same year, Blaya et al. [44] also reported a photopolymerisable dry polymeric film based on pyrromethene dye. This new composition was based on three components: poly-(methylmethacrylate) (PMMA) as a binder, 2-hydroxyethylmethacrylate (HEMA) as a monomer and 1,3,5,7,8-pentamethyl-2,6-diethylpyrromethene-, difluoroborate as photoinitiator. Diffraction efficiencies near 60% were obtained with exposures of $\approx 1 \text{ J}/\text{cm}^2$ in 500 μm thick layers. The properties of the material were also examined when the concentration of monomer and the exposing intensity were changed. Good results were obtained for low exposure intensities, which imply that this material could be used for low power applications.

Ortuno et al. [45] developed a method of preparing layers of a polyvinyl alcohol/acrylamide-based photopolymer approximately 1 mm thick. Optimization of this material made it possible to obtain diffraction efficiencies up to 70% and energetic sensitivity of 50 mJ/cm². In order to increase the final thickness of the layer, the PVA concentration in the initial solution was increased; because of this, a greater amount of water is retained by the PVA in the dry layer.

In 2004, Cho et al. [46] reported that both the diffraction efficiency and morphology of holographic gratings were improved by combining ring-opening polymerizable epoxides with radical polymerizable conventional acrylate systems. By adding epoxide materials, the grating spacing was increased when compared with the case where only acrylate was used. The effects were especially notable for cyclohexane oxide derivatives. The diffraction efficiency was the highest, and nanoscale phase-separated liquid crystal domains were the most clearly formed using siloxane-containing cyclohexane oxide group, due to both their incompatibility with other components and fast curing. Their addition to ordinary vinyl polymerization system also reduced the volume shrinkage. However, specific values regarding the diffraction efficiencies and shrinkage obtained were not presented in this work.

In 2005, McLeod et al. [47] showed that with the addition of a reflecting head and a confocal pinhole, a standard optical drive can read and write many layers of microholographic tracks in a rapidly rotating, homogeneous holographic photopolymer disk. The analysis revealed that the index change available for each layer is the total possible change over the number of layers, analogous to results for page-based holographic multiplexing. The experiment demonstrated that photopolymer materials specifically developed for page-based holographic storage could potentially be used in a modified traditional optical drive to achieve performance comparable with page-based holographic storage but at a reduced write/read system complexity. In comparison with page-based holographic storage, the rapid-disk rotation of the bit-based storage permits faster access time, and the total addressable storage space was shown to be as large as page-based systems at comparable operating points. The analysis was experimentally validated at 532 nm by writing and reading 12 layers of microholograms in a 125 μm photopolymer disk continuously rotating at 3600 rpm. The experimental results predicted a capacity limit of 140 Gbytes in a millimeter-thick disk or over 1 Tbyte in a system using the wavelength and numerical aperture of Blu-Ray technique.

Kelly et al. [48] proposed an extension to the nonlocal polymerization-driven diffusion model (NPDD) model [49, 50] to account for the temporal response associated with polymer chain growth. This was achieved by including an exponential temporal material response along with the nonlocal spatial material response function. Previously, all temporal effects were assumed to be instantaneous and were neglected. Using RCWA and the Lorentz-Lorenz expression, the temporal evolution of refractive index modulation was determined during and after illumination. Comparisons were then made between the theory and experiment for two models. In the first, the dominant termination mechanism was assumed to be bimolecular, while in the second, primary termination was assumed to be dominant. Material parameters were then extracted based on best fits to the experimental data for both models. For the two models examined, values for the diffusion coefficient were found to be of the order, $D \sim 10^{-11} \text{ cm}^2 \text{ s}^{-1}$, the nonlocal spatial response parameter was found to be $\sqrt{\sigma} \approx 60 \text{ nm}$, and the nonlocal temporal response parameter was found to be $\tau_n \sim 0.1 \text{ s}$. The best fits,

that is, higher correlation, to the experimental data were achieved assuming the primary termination model.

O'Neill et al. [51] examined the temporal evolution of the optically induced surface relief pattern in acrylamide-based holographic recording materials during and after exposure to intense light. In this work, they examined the effects of coherent exposure energy and mask pattern on the final surface relief pattern. The temporal evolution of the exposed spot was estimated. The 44 μm thick photopolymer layer was exposed using a 24 mJ/cm^2 beam. It clearly showed that there is an initial shrinkage, $\sim 0.34 \mu\text{m}$, followed by a period during which swelling occurs. The resulting profile was a pedestal $\sim 1.2 \mu\text{m}$ in height. The effects of varying the exposure energy on the resulting temporal behavior of the central height were also examined. The height parameter was defined as the difference between the edge and the center of the exposure. The material variation increases with increasing intensity as was expected. From an examination of the effects of exposing the layer with both single-beam and double-beam (holographic) illumination, it was found that although the swelling is less for the two-beam recording, it is still appreciable. The layers examined were 47 and 50 μm thick for the double-beam and single-beam exposures, respectively. The exposure energy in both cases was $\sim 240 \text{ mJ}/\text{cm}^2$. This result has implications for holographic recording in this material as shrinkage/swelling of the material can result in Bragg detuning effects, which are important for slanted gratings recording. This study also showed that it is possible to use the volume change in holographic recording materials to produce patterned surfaces.

In 2006, Wei et al. [52] presented a dual-channel holographic recording technique and its corresponding memory scheme using a cationic ring-opening photopolymer. In this dual-channel technique, a pair of holograms is recorded simultaneously with two orthogonal polarization channels in the common volume of the material and is reconstructed concurrently with negligible interchannel crosstalk. A holographic memory system with equal diffraction intensities (in each page) was developed by combining the dual-channel technique with a speckle shift multiplexing method. In addition, this system used only one 4- f optical head to transfer the pair of data pages with orthogonal polarization. This simultaneous use of the two channels provided a compact system with a fast data transfer rate in both the recording and reading processes.

In the same year, Tomita et al. [53] reported the use of hyperbranched polymers (HBPs), acting as mobile organic nanoparticles, dispersed in methacrylate photopolymers for highly efficient volume holographic recording. Two types of reduced HBPs, hyperbranched poly (ethyl methacrylate) (HPEMA) and hyperbranched polystyrene (HPS), having the average size of 10 nm were synthesized. This type of material provided diffraction efficiency near 100% at a recording intensity of 100 mW in the green (532 nm) recording. An approximately 60% reduction in the fractional volume change was obtained compared to the undoped material sample; that is, there was substantial polymerization-shrinkage suppression in this photopolymer system.

John et al. [54] developed a new erasable photopolymerisable recording media based on poly (vinyl alcohol) and vinyl acetate (PVA and VAc) sensitized with methylene blue. The PVA-VAc ratio was optimised at 2 : 1. Diffraction efficiency of 6.3% was obtained without any fixing at a dye concentration of 9.3×10^{-4} mol/L and an exposure of 750 mJ/cm². The material is attractive on account of its reusability. The recorded gratings were found to remain in the material for 24 hours with a continuous fall in diffraction efficiency. In order to examine the reusability of the MBPVA/VAc system, gratings were again recorded on the same area of the same film after 24 hours, that is, after the absorption spectra showed complete recovery. Their results showed that the MBPVA/VAc system could be reused 24 times. Being an inexpensive, nontoxic material with high environmental stability and good optical clarity, this material is of some interest for rewritable holographic data storage.

Fernandez et al. [55] reported a combination of two multiplexing methods, that is, peristrophic and angular multiplexing, for hologram recording in the acrylamide-based photopolymer material layers. In order to obtain holograms with higher and more uniform diffraction efficiency in thick material layers, an optimised exposure schedule method was used during the recordings. A dynamic range of $M\# = 8.7$, with an angular selectivity of 0.5° , was obtained. Mean diffraction efficiencies of 1.8% were also obtained from 60 holograms recorded.

In 2007, in order to enhance the material's energetic sensitivity, Jeong et al. [56] introduced an epoxy-resin cross-linked matrix into an acrylamide-based photopolymer material. Diffraction efficiency near 92% and an energetic sensitivity of 11.7×10^{-3} cm²/J were achieved by the additions of epoxy-resin-based matrix. Value of volume shrinkage of 0.67% was also obtained. It was found that the epoxy-resin-based cross-link photopolymer with low cross-linking density, which could significantly enhance the energetic sensitivity without reducing both the diffraction efficiency and dimensional stability.

Ling et al. [57] used a triangle prism tilted at 13.7° to the axis within the focus of a lens, in order to reduce the depth variation of recording intensity in thick (1 mm) polyvinyl alcohol/acrylamide (PVA/acrylamide) photopolymer layers. A mean diffraction efficiency of 9.5% was obtained for the modulated recording lights. From the results, the larger dynamic range, $M\# = 9.2$, was obtained as a result of decreasing the attenuation in depth of light of the material.

Li et al. [58] demonstrated three-dimensional erasable bit optical data storage in a quantum-dot doped photopolymer under two-photon excitation using a near infrared femtosecond pulsed laser beam. It was shown that the photorefractive polymer, consisting of poly(vinyl carbazole), ethyl carbazole, 4-(dimethylaminobenzylidene)-malononitrile, and CdS quantum dots (QDs), exhibited changes not only in refractive index but also in fluorescence. It was found that, after incorporating CdS QDs with a sulfur-rich surface, the rewritable recording range of the sample was more than 200% that of the sample without QDs. Such a photosensitivity provided a multimode readout mechanism, which could

be potentially applied in multilayered 3D erasable bit optical data storage.

Krul et al. [59] modified a photosensitive system based on polymethylmethacrylate (PMMA) by the additions of radical copolymerisation of methylmethacrylate (MMA) with acrylic acid (AA). This enhanced the adhesion to soda-lime glass substrate, thus also improving the heat and thermal stability of the resulting holographic gratings. Polymer films deposited from samples of the copolymer of MMA with AA containing 9,10-phenanthrenequinone additives were used as a photosensitive material for the recording of holographic gratings. Their results demonstrated that the system of copolymer of MMA with AA was more stable and only showed some deterioration at 200°C. However, even in this case it was possible to measure the DE, which then fell to zero within 350 minutes. Therefore it was found possible to generate gratings that are thermally stable up to 200°C using this modified PMMA material.

The effective optical thickness of the material layer, d_{eff} , determines the width of the central lobe in the off-Bragg response of the gratings recorded, and this parameter therefore governs the angular separation needed between two consecutive holograms so that they may be read separately with low crosstalk during read out. Gallego et al. [60] proposed a new method to record many angularly multiplexed holograms, having similar diffraction efficiency values by taking into account the different effective optical thickness of each hologram. The method therefore predicts the exposure times required to obtain maximum storage capacity. AA/PVA-based photopolymer material was studied in order to analyse the different dependence of the effective optical thickness on the number of holograms multiplexed.

Temperature changes during the recording process can have a profound influence on the hologram medium: (1) the exposing amount of energy to eliminate inhibiting by oxygen is altered; (2) the material sensitivity and $M/\#$ are varied; (3) the average refractive index changes and on-Bragg replay angle variations are found; (5) changes are founded in the monomer diffusion speed during the recording process. In 2008, Toishi et al. [61] proposed a compensation method to suppress the effects of temperature change. Through a description of how these parameters affect actual recording properties, methods to compensate for and thus avoid these problems were presented: (1) tuning of the preexposure energy; (2) using the proper recording schedule for a given temperature; (3) tuning the recording angle and wavelength; (5) recording each hologram at high speed. These methods then could be employed by actively detecting the medium temperature during recording. It was also found that the changes of the diffusion coefficient and the polymerization rate primarily affected parameters such as $M/\#$, the medium recording sensitivity, the preexposure time, and the transmission rate.

Khan et al. [62] reported an efficient and solventless processing technique for the fabrication of millimeter-thick, high-quality optical films for holographic storage based on a nondiffusion crosslinked photopolymer material. This was achieved by incorporation of crosslinkable Dewar benzene derivatives, which allowed the production of thick films

that exhibit no diffuse light scattering and low absorption cross-section at the desired recording wavelength. A variety of photochemical reactions can be utilized to achieve such refractive index modulation. However, very few reactions exhibit quantum yields greater than unity, that is, where one photon of light triggers numerous chemical reactions. This nonlinearity and efficiency are essential for the high sensitivity and ultrafast recording speeds required for commercial holographic data storage. In examining other photochemical reactions with quantum yields greater than unity, the isomerization of Dewar benzene was noteworthy due to its very high quantum yield (>100 in solution). Additionally, isomerization of Dewar benzene gave rise to a large change in the electronic structure of the molecule and was therefore anticipated to result in high refractive index modulation upon photoisomerization. Utilizing 1 mm thick films of the described recording medium, diffraction efficiencies of up to 100% at a recording intensity of $\sim 6 \text{ mW/cm}^2$ and $M/\# > 6$ were obtained. This work suggested that Dewar benzene systems may be attractive candidates for write-once-read-many (WORM) disk-based holographic memory devices.

In 2008, Matushevich et al. [63] further developed the material reported in [59] to investigate the contribution of the absorption and phase gratings to the total diffraction efficiency of volume holographic gratings, written in glass-like polymer recording materials, based on poly(methylmethacrylate) and a thermostable derivative (copolymer with acrylic acid) with distributed phenanthrenequinone (PQ-PMMA). Absorption by the recording media decreased following illumination and increased by heating. The maximal diffraction efficiency was 2% (0.5%) for absorption type gratings and 32% (22.5%) for phase gratings in PMMA+AA (PMMA). Refractive index modulations in the range 10^{-4} – 10^{-3} were observed during recording. During heating the diffraction efficiency of the absorption grating could reach 4% for PMMA, while for absorption grating in PMMA+AA it was 0.3%. The total diffraction efficiency in saturation was about 10% for both material samples.

McLeod et al. [64] demonstrated a three-dimensional optical data storage system in an initially homogenous volume by first recording a reflection grating in a holographic photopolymer. The volume data storage method used a single read/write head locked, in radius and depth, to a pre-fabricated volume servopattern. In addition, the power in the writing focus did not depend on depth, and the reflection efficiency of the bits was independent of the precise writing mechanism. Difficulties associated with the use of two opposing read/write heads were overcome by separating the holograms from the write mechanism so that a single-head optical drive could both read and write from one side of the disk. Superposition of two or three of such gratings, with slightly different k -vectors, created a track and layer structure that specialized servodetection optics can use to lock the focus to these deeply buried tracks. Writing was accomplished by locally modifying the reflectivity of the preexisting hologram. This modification could take the form of ablation, inelastic deformation via heating at the focus, or erasure via linear or two-photon continued polymerization in the

previously unexposed fringes of the hologram. Moreover, by fabricating the precision grating in the factory, the drive does not require vibration isolation or a highly coherent laser, both hallmarks of traditional holographic data storage. This work suggested the strong possibility of TByte capacity in submillimeter thickness disks of diameter 120 mm.

Gallego et al. [65] reported on the different values of shrinkages or swelling of photopolymer layer by using a reflection interferometer. Furthermore, these variations were shown to depend on the spatial frequencies of the gratings stored in the materials. Using this technique they measured the variations of the layer refractive index and estimated the polymer refractive index. Their results suggested that at higher spatial frequencies, monomer diffusion from the dark zones to the bright ones, together with surface tension effects, could considerably affect the material volume changes. In particular, molecular migration (mass transport) reduced shrinkage. Values of shrinkage of around 2% (without crosslinker) and 3% (with crosslinker) were obtained. This reduction was observed to increase with the spatial frequency and with the monomer diffusion velocity.

Tomita et al. [66] examined thermal distortions of volume holograms recorded in (meth)acrylate photopolymers doped with SiO_2 or ZrO_2 nanoparticles. A holographic method was used to evaluate the temperature-induced Bragg-angle detuning of the recorded volume holograms as a result of thermally induced refractive index and dimensional changes. It was shown that thermal distortions could be suppressed by reducing both the thermo-optic coefficients dn/dT and the out-of-plane linear coefficient of thermal expansion, by the addition of inorganic nanoparticles to the photopolymer. A reduction in the out-of-plane thermal expansion by approximately a factor of 2 was observed. Such an improvement, besides both extending the range of operating temperatures (the increase in Δn) and suppressing polymerization-related shrinkage, suggested the value of nanoparticle-polymer composite materials not only for holographic data storage but also for other photonic applications, that is, for diffractive optical element fabrication, in optical interconnects, for narrowband optical filters, and for using displays.

One of the key predictions of the NPDD model [49, 50] is that a reduction in the extent of the nonlocal effects within a material will improve its high spatial frequency response. In the work presented in 2008 by Gleeson et al. [67], the spatial frequency response of an acrylamide/polyvinyl alcohol-based photopolymer was improved through the addition of a chain transfer agent (CTA), sodium formate. The CTA has the effect of decreasing the average length of the polyacrylamide (PA) chains formed, thus reducing the nonlocal response parameter, σ while maintaining a high rate of polymerisation. In addition, this work indicated that the chain transfer kinetic effects introduced by the CTA, which contribute to the increased localization of the polymerization, include (a) an increase in the concentration of the monomer radicals available for bimolecular termination and/or (b) the effects of less than 100% efficiency in the reinitiation process. A significant reduction in the nonlocal parameter, from 63 to 50 nm, was obtained.

Kelly et al. [68] proposed an algorithm, using a more rigorous NPDD formulation, to determine an appropriate holographic data storage recording schedule based on the physical properties of the recording medium's properties. The predictions of the algorithm and the inverse-square scaling law of holographic diffraction were examined experimentally, for a peristrophic multiplexing scheme. The scaling law was shown to significantly break down for low numbers of high diffraction efficiency gratings. Using the algorithm, a good correlation between the theoretically predicted and experimentally achieved exposure schedules was found. The largest discrepancy in all cases occurs for the final exposure, where the reduced monomer concentration available, and possible grating nonuniformities, strongly affects the exposure schedule time. The examinations showed that for multiple high diffraction efficiency gratings the scaling relationship, between the numbers of gratings recorded, broke down but that this could be explained using Kogelnik's model.

In 2009, Choi et al. [69] proposed a new free radical polymerization holographic recording medium, based on low shrink cyclic allylic sulfides (LS-CASs) ring-opening monomers. For comparison, the LS-CAS monomer was replaced with 4-bromostyrene. In ring-opening systems, a covalent bond is broken within the molecule for every covalent bond formed between the molecules. The result is the paradoxical situation of there being no net bond formation during the polymerization, and therefore ring-opening monomers typically display at least half the shrinkage of a conventional monomer of the same molecular weight. In this material system, 6-methyl-3-methylene-1,5-dithiacyclooctane was used as monomer. The percentage of volume shrinkage is measured to be 0.02%, with refractive index contrast of $(1.01 \pm 0.5) \times 10^{-3}$. This result indicated that a fivefold decrease in the volume shrinkage compared to 4-bromostyrene monomer system.

Orlic et al. [70] examined different classes of organic photosensitive materials in order to optimise the interaction between the material and the surrounding read/write optoelectronic system. Both cationic ring-opening and free radical polymerization systems were investigated. Localised recording of small volume reflection holographic elements, that is, microgratings, enabled testing of a variety of exposure conditions with a single record, allowing rapid optimisation of the exposure conditions. For the purpose of testing and investigating different photosensitive polymer materials, a laboratory system was developed that allows for high flexibility in their optical characterization experiments. While the microlocalised recording setup was designed for recording/readout at the optical resolution limit, the media tester comprises objective lenses having lower numerical apertures, and it was designed to operate with microgratings larger than a few hundred nanometers. Methods of investigation include spatial, spectral, and temporal measurements of the reflection diffraction efficiency at the individual recorded microgratings. In this way, an optimised exposure scheduling was achieved. The results confirmed that careful investigation and optimisation of the exposure scheduling is necessary in order to best use a specific photopolymer material.

Lin et al. [71] fabricated two photopolymer samples, Irgacure 784 doped poly(methyl methacrylate) (PMMA) and Irgacure 784 doped epoxy resin, using a two-step thermopolymerization procedure. Comparing the experimental results for Irgacure 784/PMMA to those produced using PQ/PMMA, the $M\#$ was improved by a factor of 1.9, and the sensitivity has been improved by a factor of 10. These experimental results revealed that Irgacure 784 molecules are efficient in increasing the holographic recording sensitivity at 532 nm. By adding acrylamide (AA) and 2-hydroxyethyl methacrylate (HEMA) monomers, together with photosensitive DI and Irgacure 784 to form the doping solution, and then using diglycidyl ether (BADGE) and *N*-(2-Aminoethyl)-3-aminopropyl-trimethoxysilane (3ABTS) together to form a polymer matrix solution, they fabricated Irgacure 784 doped epoxy resin photopolymer. It was found that the $M\#$ and sensitivity of the Irgacure 784 doped epoxy resin are 5.49 and $26.65 \text{ cm}^2 \text{ J}^{-1}$, respectively. The $M\#$ was around 1.7 times larger, whereas the sensitivity was about 350 times higher than that of Irgacure 784/PMMA sample. These results suggested that epoxy-resin matrix-based photopolymer system provides an effective way to improve the holographic recording characteristics for volume data storage.

To improve the temperature tolerance of holographic data storage systems, Tanaka [72] proposed a compensation method adjusting the wavelengths and incident directions of the recording and reading beams. The reading temperature tolerance of a photopolymer medium recorded at 25°C and the tolerance of the recording and reading temperature are calculated using the compensation method. Typically, the reading tolerance is from -20.0 to $+26.0$ K, and the recording and reading tolerance is ± 10.0 K. This suggested that, to widen the tolerance, it was effective to increase the coefficient of thermal expansion (CTE) of the substrate or to decrease the CTE of the photopolymer, thereby reducing the difference of the CTEs.

In 2009, Kim and Chung [73] optimised a photopolymer system made from complex compositions of binder, photoacid generator (PAG), and sensitiser involving the cationic ring-opening polymerization of 1,3-bis[2-(3-7-oxabicyclo-[4.1.0]heptyl)]-tetramethyldisiloxane in the presence of polydimethylsiloxane, with four epoxide moieties as a comonomer. It was found that when diffractive efficiency values were compared quantitatively, in order to analyse the effect of the binder on holographic photopolymerisation, the diffractive efficiency was affected by the viscosity of the mixture. Extremely low diffractive efficiency values were observed when the immiscible dimethyl silicone was used as a binder. The optimal conditions were also given in this work as a binder viscosity between 250 to 390 cP, and binder, PAG, and sensitiser content of 75–125 wt%, >6 wt%, and 0.05 wt% compared to the total monomer mixture, respectively. This work suggested that a chemical, which is miscible with the monomer mixture, should be chosen as the binder when carrying out further studies to improve this photopolymer system.

All multilayer optical data storage methods, in which bits are written in an initially homogeneous material, are constrained by the imaging system phase aberrations that

decrease the Strehl ratio (SR) as the number of layers and the index perturbation (due to each bit stored) are increased. Due to the complexities of accurately modelling the signal in such systems (e.g., due to consumption of the materials dynamic range out of focus exposures) and noise (e.g., due to wavefront variance), many studies of 3D data storage in homogeneous media were carried out experimentally. Without suitable relationships indicating how a particular experimental result can be extrapolated, comparison of different technological approaches is difficult. In 2009, McLeod [74] carried out an investigation to establish the capacity limitation on storage density with sufficient generality so that it can be applied independently of the particular system: (i) write mechanism, (ii) modulation code, (iii) nonlinearity of the material response, (iv) details of the lens, and (v) the disk geometry. The resulting equations for the Strehl ratio (SR) of a spot focused through the disk are quite simple and independent of the specific storage mechanism. Importantly, they revealed several interesting scaling relationships. Such scalings, even though derived via a number of approximations, provide a valuable method to evaluate and optimise next-generation optical storage methods. It is noted that the observed noise on the microholographic signal does not appear to be due to changes in the induced wavefront aberration and thus must arise due to other qualities of the material or optical system.

Gallego et al. [75] examined the influence of diffusion in polyvinyl-alcohol/acrylamide at very low spatial frequencies, that is, for spatial frequencies between 2 and 6 lines/mm, and also the dark evolution of the grating shape. They demonstrated the influence of the spatial frequency on the magnitude and sign of the material volume variations. In this work, they indicated that if the diffusion phenomena were well predicted, it was possible to achieve diffractive gratings with very high values of diffraction efficiency in the first order (near 35%). These results are a significant preliminary step to build diffractive elements with stable properties using PVA/AA-based photopolymers.

Liu et al [76] reported on the fabrication of centimeter-size transmission Bragg grating structure in semiconductor CdSe quantum dots dispersed in 50 μm thick photopolymer films. This was done by holographic assembly of CdSe quantum dots in a photopolymerisable monomer blend. This single-step holographic method, involving the so-called holographic assembly of nanoparticles in polymer, does not require a shadow mask and can fabricate centimeter-size multidimensional photonic lattice structures. Periodic patterning of CdSe quantum dots in polymer was confirmed by a fluorescence microscope and confocal Raman imaging. Because of the high refractive index of CdSe QDs and their high thermal mobility, the diffraction efficiency from the grating of period 1 μm was close to 100% in the green with 0.34 vol% CdSe quantum dots, giving a refractive index modulation as large as 5.1×10^{-3} at a recording intensity of 100 mW/cm².

In 2010, Gleeson et al. [16] further developed the non-local photopolymerization-driven diffusion (NPDD) model to more accurately model the effects of (i) time-varying primary radical production, (ii) the rate of removal of

photosensitizer, and (iii) inhibition. For the first time, the spatial and temporal variations in primary radical generation were included. These extensions provide a more physically comprehensive theoretical representation of the processes, which occur during free radical photopolymerization. The model was also extended to incorporate the effect of oxygen diffusion from outside the material layer by including a rate of oxygen replenishment from the surrounding environment. This allowed accurate modelling of the inhibition effects, which dominate the start of grating growth. This work provided a comprehensive approach to analyse and optimise the photopolymer materials under low intensity condition.

Omura et al. [77] further developed their nanoparticle-polymer composite material by optimising the concentration of ZrO₂ nanoparticles at a wavelength of 404 nm. The dependence of the polymerization kinetics on the concentrations of initiator and ZrO₂ nanoparticles in acrylate monomer was examined using a photodifferential scanning calorimeter. The optimum concentration of ZrO₂ nanoparticles to maximise the polymerization rate was identified. The diffraction and scattering properties of transmission volume gratings were also investigated. Refractive index modulations and the material recording sensitivities as high as 8×10^{-3} and 9000 cm²/J were demonstrated at the optimum ZrO₂ nanoparticle concentration of 35 vol.% and at a recording intensity of 5 mW/cm². The occurrence of the maximum photopolymerisation rate later during conversion accelerates the mutual diffusion of monomer molecules and nanoparticles during recording. This results in an increase in Δn_{sat} . It was also observed that the sensitivity dramatically increases at the shorter wavelengths, for example, 404 nm, being approximately seven times higher than that at 532 nm at a recording intensity of 10 mW/cm².

Later in that year, Hata and Tomita [78] proposed a novel nanoparticle-polymer composite to further suppress shrinkage of their material using of the thiol-ene step-growth polymerization mechanism. Due to crosslinked thiol-ene, polymerisation proceeds very rapidly but will not reach the gel point until high functional group conversions take place, that is, reaching the gelation point later during conversion in the mixtures accelerates the mutual diffusion and phase separation of the monomer molecules and nanoparticles during recording. This will again result in an increase in Δn_{sat} and the material sensitivity. It was shown that the polymerisation shrinkage can be reduced as low as 0.3% for a nanoparticle concentration of 35 vol.%, giving a maximum refractive index modulation and material sensitivity of 8×10^{-3} and 1014 cm/J, respectively, when recording in the green. These results provide a significant and noticeable advance in the development of holographic data storage materials.

Guo et al. [79] examined the photosensitiser diffusion effects of erythrosine B (EB) in an acrylamide/polyvinyl alcohol (AA/PVA) material. This was achieved using simple experimental techniques and use of a 2D diffusion model. The rate of EB diffusion, $D \approx 6.27 \times 10^{-12}$ cm²/s, was estimated. In the literature [80–82], the rate of diffusion of the acrylamide monomer (AA) in such photopolymer layers has been reported to be in the range $\sim 10^{-11}$ – 10^{-10} cm²/s.

The molecular weight of EB is 879.86 g/mol while that of AA is 71.08 g/mol. While molecular weight alone does not determine the rate of diffusion, it would be reasonable to expect EB to diffuse more slowly than AA. The results indicated that EB diffuses an order of magnitude slower than the AA monomer.

Sabol et al. [83] then reported a detailed study on the photoinitiation process of the photosensitizer, Irgacure 784, used in the epoxy-resin-based photopolymer. Irgacure 784 is a type of the titanocene photoinitiator which has the property that it does not require a coinitiator to produce the free radical. In this work, the photochemical reactions of Irgacure 784 involved are thoroughly discussed. Importantly, the experimental results reportedly verify that multiple different absorbers are simultaneously present in the layer at different stages during the exposure.

In 2011, Hata et al. [84] introduced the thiol-ene monomers into silica nanoparticle-polymer composites and examined the photopolymerisation kinetics and volume holographic recording characteristics. Real-time Fourier transform spectroscopy and photocalorimetry were used to characterize the visible light curing kinetics containing a secondary dithiol (with high self-life stability and low odor) and a triene with rigid structure and high electron density. It was shown that while the nanoparticle-(thiol-ene) polymer composites exhibit high transparency, values of Δn_{sat} and S as large as 1×10^{-2} and $1615 \text{ cm}^2/\text{J}$ were achieved. The polymerisation shrinkage was reduced to the value as low as 0.4%, as a result of delaying the gelation point in conversion by introducing the thiol-ene monomers. These values were within the acceptable range of values for holographic data storage media (i.e., $\Delta n_{\text{sat}} = 5 \times 10^{-3}$, $S = 500 \text{ cm}^2/\text{J}$ and 0.5% shrinkage). It was also shown that because of the dispersion of the inorganic silica nanoparticles and the use of the triene monomer, (having the rigid structure of the triazine functional group), the thermal stability of the recorded holograms is much improved compared to that of those previously reported in earlier nanoparticle-polymer composites using organic nanoparticles and primary mercaptopropionate trithiol/allyl ether triene monomers [53, 78].

Further research to the properties of the stoichiometric thiol-to-ene and nanoparticle-(thiol-ene) polymer composites was presented by Hata and Tomita [85] later in the same year. The impact of the stoichiometric thiol-ene ratio on the properties of photopolymerisation was estimated. It was found that the thiol-ene stoichiometry strongly influences the dynamics of the thiol and ene functional group conversions and therefore the polymerisation rate, R_p , for samples with silica nanoparticle dispersion. It was also found that α_c , which is the value of time-dependent relative conversion α at the peak value of R_p , increases with increasing stoichiometric ratios of thiol-to-ene functional groups, r . This work indicated that while Δn_{sat} and S are maximized at $r = 1$, out-of-plane fractional thickness change, σ , can be reduced by increasing r . It was also shown that there exists a negative correlation between α_c and σ . It suggested that such a correlation must also be presented in other holographic photopolymer systems, and that can be used as part of the material design strategy for holographic applications.

Certain photorefractive processes, as is the case for photopolymerisation, involve mass transport. As a consequence, not only the optical but also the neutron refractive index may be changed in these cases [86]. The light-induced change of the refractive index for neutrons in materials (the photo-neutron-refractive effect) has been exploited to produce diffraction gratings for neutrons by structuring suitable recording materials using holography [87]. The reduction in size of the grating modulation with position, that is, within the layer depth due to the absorption during the recording process, becomes an issue at grating thicknesses of about 100 microns and larger. This limits the achievable diffraction efficiency for neutrons. In an attempt to overcome this problem, the Pendellosung interference effect in holographic gratings was examined by Klepp et al. [88] in 2011. Diffraction experiments with holographic gratings recorded in SiO_2 nanoparticle-polymer composites were carried out with slow neutrons. The influence of parameters, such as the nanoparticle concentration, grating thickness, and grating spacing, on the neutron-optical properties of such materials was tested. It was shown that the difficulty of obtaining sufficiently larger thicknesses can be overcome by exploiting the Pendellosung interference effect. This was done by tilting the grating around an axis parallel to the grating vector to increase the effective thickness of the gratings. Using this method, high peak reflectivity of 83% was achieved and reached for a neutron wavelength of 3.76 nm. Such results, besides extending the range of passive neutron optical elements available, have also provided evidence for the superiority of the Beta-value method over Kogelnik's K -vector closure method [89, 90].

In work by Vayalamkuzhi et al. [91], a panchromatic silver-doped poly (vinyl alcohol)/acrylamide photopolymer system was developed. In the presence of Ag^+ , diffraction efficiency of 70% in transmission gratings was recorded using both Ar^+ and Nd:YAG lasers. This offers the possibility of using the developed photopolymer system as a panchromatic recording medium. Such material developments have important applications in the fields of true-color display holography, holographic storage, and holographic optical elements.

The microholographic approach relies on submicron-sized reflection gratings recorded in layer at different depths to encode the digital data stored. In 2011, Orlic et al. [92] presented an optical write/read system for high density optical data storage in 3D. This design of their optical system for high-density microholographic storage was based on a single-beam path, using a retroreflecting configuration. The combined performance of these two components, that is, a retroreflector and confocal filter, was a key feature of the system. They demonstrated resolution-limited volume recording in photopolymer materials sensitive in the green and violet spectral ranges. The optimum exposure condition was identified as a compromise between the requirements of strong volume localization and sufficiently high diffraction efficiency. Microgratings with widths of 306 nm at 532 nm and 197 nm at 405 nm were recorded. These results were the smallest volume microholograms ever recorded up to that time. Photopolymer materials used in this work

were cationic ring-opening polymerization (CROP) systems developed by Aprilis [93]. The work indicated the potential of the technique for volumetric optical structuring, data storage, and encryption applications.

Following on from the work by Ortuño et al. [94] in 2007, on the development of a nontoxic photopolymer, Gallego et al. [95] further developed a new environmental sustainable photopolymer, by introducing a sodium acrylate (NaAO) into AA/PVA-based photopolymer material as a substitute for acrylamide-based photopolymers in the manufacture of diffractive optical elements. Diffraction efficiencies of ~40% were achieved for planar gratings. They estimated the NaAO diffusion rate inside the photopolymer, and the values obtained were 10 times smaller than those in the case of the widely studied PVA/AA photopolymer. Therefore the PVA/NaAO photopolymer should be used when slow diffusion is required. The influence of TEA on monomer diffusion inside the material and on the polymerisation rate was also examined. The results suggested that the concentration of this component, that is, NaAO, can be carefully adjusted in order to obtain photopolymers with desired dynamic properties.

Following this work [95], later in the same year, Gallego et al. [96] reported on other possibilities to achieve thin photopolymer layers with lower environmental impact. Using direct measurements of the phase shift and the shrinkage of photopolymeric layers based on PVA/NaAO material (for five different chemical compositions), they estimated several different material parameters. They obtained values of the shrinkage between 1% and 3% in the layers analysed. Although the results for shrinkage were too high for holographic memory applications, these values are promising for use in obtaining relief structures for liquid crystal applications. From comparison of the results to those for typical PVA/AA-based materials, it was shown that sodium acrylate provides less toxic photopolymer thin layers suitable for very low spatial frequency applications. It was also suggested that, in order to achieve “greener” layers [94], the incorporation of sodium salt 5'-riboflavin monophosphate (PRF) as a dye should be pursued.

Clearly, when attempting to improve a photopolymer material's performance for a given application, an understanding of the photochemical and photophysical processes, which occur during photopolymerisation, is extremely important. In 2011, Gleeson et al. [97] demonstrated how NPDD-based modelling of the mechanisms which occur in photopolymers during and after exposure has led to the development of a tool, which can be used to predict the behaviour of many distinct types of material for a wide range of recording conditions. They reported on work to the extended their NPDD model, in order to clearly quantify some of the trends, which the model predicts, and thus be able to analyse their implications for attempts to improve photopolymer material performance. The results are of practical importance when attempting to optimise the performance of a photopolymer material. As the many types of monomer have diverse chemical and structural characteristics, knowledge of these characteristics is necessary. For example, when choosing a monomer, an informed choice can

yield specific improvements in material performance. One of the implications of the predictions of the NPDD model is that utilising a monomer with a large propagation rate constant and low bimolecular termination rate will produce a higher refractive index modulation, Δn_{sat} . However, it is also desirable to have a monomer with high mobility, that is, a fast diffusion rate, in order to increase the dynamic range of the photopolymer and to maximise the index modulation achievable. One of the results highlighted in this work is that if the propagation rate is too large or the bimolecular termination rate is too small, the optimum refractive index modulation will not be obtained. These deleterious effects are compounded further by increased material viscosity as a result of polymerisation. In this work a qualitative understanding of trends is given for quantitative predictability.

Gleeson et al. [98] reported results for an impressive new acrylate-based photopolymer material developed by Bayer Material Science (BMS). The material was examined using various optical techniques and then characterised using the NPDD model. Refractive index modulation up to $\Delta n_{\text{sat}} = 8 \times 10^{-3}$ and a very low nonlocal parameter value of 9.2 nm were estimated. A comparison between AA/PVA-based and BMS materials shows that the BMS material has (i) a substantially faster response of the refractive index modulation with respect to the recording dosage, especially at lower power densities; (ii) three times higher refractive index modulation achievable; (iii) six times smaller nonlocal response parameter, (representing the spatial spread of the reactive chain ends of the formed polymer coils during photopolymerisation), indicating a much higher resolution, that is, little dropoff in material response up to 5000 lines/mm; (iv) an improved performance at high spatial frequencies permitting high diffraction efficiency reflection holograms to be recorded. This material demonstrated the capabilities of a new class of photopolymer, which importantly can be produced on an industrial scale as large area plastic films, offering high index modulation, full colour recording, high light sensitivity, and environmental stability.

The NPDD model has been extended to include the kinetics of chain transfer and reinitiation, in order to analyse the effects of various chain transfer agents on the system kinetics and to study their use in reducing the average polymer chain length [67], in free-radical-based photopolymer materials. Guo et al. [99, 100] studied AA/PVA-based photopolymer material containing chain transfer agents. The effects of two different types of chain transfer agent, that is, Sodium Formate (HCOONa) and 1-Mercapto-2-Propanol ($\text{CH}_3\text{CH}(\text{OH})\text{CH}_2\text{SH}$), were compared. The validity of the extended NPDD model [99, 100] was examined by applying it to fit the resulting experimental data. It is confirmed that the average polymer chain length formed is reduced by the addition of the chain transfer agents, as they reduce the nonlocal response of the materials. The most effective material combination used resulted in a reduction in the nonlocal parameter, from 61 nm to 41 nm. Comparing the two types of transfer agents, the results achieved using 1-mercapto-2-propanol were shown to be better than those using sodium formate. These CTAs produced improved high spatial frequency material response, giving up to ~28%

increase in the refractive index modulation achieved at 3000 line/mm.

5. Conclusions

An overview of reported work on the optimisation of photopolymer materials is presented, and several types of photopolymers are discussed. We have emphasised in this review those materials used as holographic data storage (HDS) media. Even limiting our review to papers explicitly dealing with such photopolymer materials, it is clear that there have been impressive developments in the field of photopolymer material research since photopolymers were first studied as a holographic recording media in 1969 [27]. As described various types of photopolymer for use with a range of read/write technologies have been developed. Increased material sensitivities, resolutions, diffraction efficiencies, and material stabilities have been reported. Such improvements include (i) two-photon absorption techniques to store and retrieve information in the volume of the material layer [58]; (ii) the introduction of nanoparticles to reduce polymerisation shrinkage [35]; (iii) the introduction of thermally curable matrix networks suitable for mass production [32, 98]; (iv) the introduction of chain transfer agents to improve the high spatial frequency performance of the materials [67, 99, 100]; (v) the introduction of quantum dots to improve the materials' refractive index modulation and fluorescence [58, 76]; (vi) the introduction of PMMA-based photopolymer materials to increase the thermal stability [59]. Clearly many promising materials, providing high storage capacities, are being developed for the next generation optical data storage media.

Photopolymer materials offer many advantages; however, there still exists several detrimental effects encountered in those materials as they are being optimised for commercial applications. What this paper clearly leads us to conclude is that it is important to build up a physically comprehensive model, which can be used to predict the behaviours of these materials, in order to improve their performance and reduce the effects that limit their commercial use. In order to achieve this comprehensive model, a number of effects must be included; these are (a) multicomponent diffusion; (b) viscosity effects; (c) shrinkage; (d) inhibition; (e) mass transport effects; (f) spatially nonlocal polymer chain growth; (g) spatial/temporal primary radical (photokinetic) behaviours; (h) thermal effects. As this model develops, it will provide a more rigorous and informed basis for predicting the behaviours of photopolymer materials and will indicate useful trends in performance, which can be used for material optimisation [97, 101].

Acknowledgments

One of the authors (J. Guo) currently holds an IRCSET Government of Ireland Postgraduate Scholarship in Science, Engineering and Technology, while another author (M. Gleeson) currently holds a Government of Ireland Postdoctoral Scholarship in Science, Engineering and Technology, also

granted by the Irish Research Council for Science, Engineering and Technology. The authors would also like to acknowledge the support of Enterprise Ireland and Science Foundation Ireland under the National Development Fund.

References

- [1] <http://www.insic.org/>.
- [2] D. Sarid and B. H. Schechtman, "A roadmap for optical data storage application," *Optics and Photonics News*, vol. 18, no. 5, pp. 32–37, 2007.
- [3] Aprilis 2007, <http://www.hedgewood.com/>.
- [4] InPhase Technologies 2007, <http://www.inphase-technologies.com/>, Tapestry Media.
- [5] K. Curtis, L. Dhar, L. Murphy, and A. Hill, "Future developments," in *Holographic Data Storage: From Theory to Practical Systems*, Wiley, New York, NY, USA, 2010.
- [6] H. J. Coufal, D. Psaltis, and G. T. Sincerbox, *Holographic Data Storage*, Springer, New York, NY, USA, 2000.
- [7] C. Ye and R. R. McLeod, "GRIN lens and lens array fabrication with diffusion-driven photopolymer," *Optics Letters*, vol. 33, no. 22, pp. 2575–2577, 2008.
- [8] A. Sato, M. Scepanovic, and R. K. Kostuk, "Holographic edge-illuminated polymer Bragg gratings for dense wavelength division optical filters at 1550 nm," *Applied Optics*, vol. 42, no. 5, pp. 778–784, 2003.
- [9] A. B. Villafranca and K. Saravanamuttu, "Diffraction rings due to spatial self-phase modulation in a photopolymerizable medium," *Journal of Optics A*, vol. 11, no. 12, Article ID 125202, 2009.
- [10] G. Manivannan and R. A. Lessard, "Trends in holographic recording materials," *Trends in Polymer Science*, vol. 2, pp. 282–290, 1994.
- [11] J. R. Lawrence, F. T. O'Neill, and J. T. Sheridan, "Photopolymer holographic recording material," *Optik*, vol. 112, no. 10, pp. 449–463, 2001.
- [12] F. K. Bruder and E. Thomas, "Materials in optical data storage," *International Journal of Materials Research*, vol. 101, no. 2, pp. 199–215, 2010.
- [13] G. Odian, *Principles of Polymerization*, Wiley, New York, NY, USA, 4th edition, 1991.
- [14] M. R. Gleeson and J. T. Sheridan, "Nonlocal photopolymerization kinetics including multiple termination mechanisms and dark reactions. Part I. Modeling," *Journal of the Optical Society of America B*, vol. 26, no. 9, pp. 1736–1745, 2009.
- [15] M. R. Gleeson, S. Liu, R. R. McLeod, and J. T. Sheridan, "Nonlocal photopolymerization kinetics including multiple termination mechanisms and dark reactions. Part II. Experimental validation," *Journal of the Optical Society of America B*, vol. 26, no. 9, pp. 1746–1754, 2009.
- [16] M. R. Gleeson, S. Liu, J. Guo, and J. T. Sheridan, "Non-local photo-polymerization kinetics including multiple termination mechanisms and dark reactions: part III. Primary radical generation and inhibition," *Journal of the Optical Society of America B*, vol. 27, no. 9, pp. 1804–1812, 2010.
- [17] S. Liu, M. R. Gleeson, J. Guo, and J. T. Sheridan, "Optical characterization of photopolymers materials: theoretical and experimental examination of primary radical generation," *Applied Physics B*, pp. 1–11, 2010.
- [18] A. Fimia, N. Lopez, F. Mateos, R. Sastre, J. Pineda, and F. Amat-Guerri, "Elimination of oxygen inhibition in photopolymer systems used as holographic recording materials," *Journal of Modern Optics*, vol. 40, no. 4, pp. 699–706, 1993.

- [19] F. R. Mayo, "Chain transfer in the polymerization of styrene: the reaction of solvents with free radicals," *Journal of the American Chemical Society*, pp. 2324–2329, 1943.
- [20] M. Fevola, R. Hester, and C. McCormack, "Molecular weight control of polyacrylamide with sodium formate as a chain-transfer agent: characterization via size exclusion chromatography/multi-angle laser light scattering and determination of chain-transfer constant," *Journal of Polymer Science A*, vol. 41, no. 4, pp. 560–568, 2003.
- [21] F. Karasu, N. Arsu, and Y. Yagci, "2-mercapto thioxanthone as a chain transfer agent in free-radical polymerization: a versatile route to incorporate thioxanthone moieties into polymer chain-ends," *Journal of Applied Polymer Science*, vol. 103, no. 6, pp. 3766–3770, 2007.
- [22] H. Kogelnik, "Coupled wave theory for thick holographic gratings," *Bell System Technical Journal*, vol. 48, no. 9, pp. 2909–2947, 1969.
- [23] M. G. Moharam and T. K. Gaylord, "Rigorous coupled-wave analysis of planar-grating diffraction," *Journal of the Optical Society of America*, vol. 71, no. 7, pp. 811–818, 1981.
- [24] R. R. A. Syms, *Practical Volume Holography*, Clarendon, Oxford, Miss, USA, 1990.
- [25] M. R. Gleeson and J. T. Sheridan, "A review of the modelling of free-radical photopolymerization in the formation of holographic gratings," *Journal of Optics A*, vol. 11, no. 2, Article ID 024008, 2009.
- [26] F. T. O'Neill, J. R. Lawrence, and J. T. Sheridan, "Automated recording and testing of holographic optical element arrays," *Optik*, vol. 111, no. 10, pp. 459–467, 2000.
- [27] D. H. Close, A. D. Jacobson, J. D. Margerum, R. G. Brault, and F. J. McClung, "Hologram recording on photopolymer materials," *Applied Physics Letters*, vol. 14, no. 5, pp. 159–160, 1969.
- [28] N. Sadlej and B. Smolinska, "Stable photo-sensitive polymer layers for holography," *Optics and Laser Technology*, vol. 7, no. 4, pp. 175–179, 1975.
- [29] S. Calixto, "Dry polymer for holographic recording," *Applied Optics*, vol. 26, pp. 3904–3909, 1987.
- [30] S. Blaya, R. Mallavia, L. Carretero, A. Fimia, and R. F. Madrigal, "Highly sensitive photopolymerizable dry film for use in real time holography," *Applied Physics Letters*, vol. 73, no. 12, pp. 1628–1630, 1998.
- [31] F. Zhao, E. E. E. Frietman, and X. Li, "Novel type of red sensitive photo-polymer system for optical storage," in *Proceedings of the 1998 Conference on Advanced Optical Memories and Interfaces to Computer Storage*, pp. 317–321, July 1998.
- [32] T. J. Trentler, J. E. Boyd, and V. L. Colvin, "Epoxy resin photopolymer composites for volume holography," *Chemistry of Materials*, vol. 12, no. 5, pp. 1431–1438, 2000.
- [33] M. Eich, J. H. Wendorff, B. Reck, and H. Ringsdorf, "Reversible digital and holographic optical storage in polymeric liquid crystals," *Macromolecular Rapid Communications*, vol. 8, no. 1, pp. 59–63, 1987.
- [34] S. J. Zilker, M. R. Huber, T. Bieringer, and D. Haarer, "Holographic recording in amorphous side-chain polymers: a comparison of two different design philosophies," *Applied Physics B*, vol. 68, no. 5, pp. 893–897, 1999.
- [35] N. Suzuki, Y. Tomita, and T. Kojima, "Holographic recording in TiO₂ nanoparticle-dispersed methacrylate photopolymer films," *Applied Physics Letters*, vol. 81, no. 22, pp. 4121–4123, 2002.
- [36] S. Blaya, L. Carretero, A. Fimia et al., "Optimal composition of an acrylamide and N,N'-methylenebisacrylamide holographic recording material," *Journal of Modern Optics*, vol. 45, no. 12, pp. 2573–2584, 1998.
- [37] S. Blaya, L. Carretero, R. Mallavia et al., "Optimization of an acrylamide-based dry film used for holographic recording," *Applied Optics*, vol. 37, no. 32, pp. 7604–7610, 1998.
- [38] R. Mallavia, A. Fimia, S. Blaya et al., "A mixture of mono-, bi- and trifunctional acrylates with eosine O-benzoyl- α -oxoimine: advances in holographic copolymerizable composition," *Journal of Modern Optics*, vol. 46, no. 4, pp. 559–566, 1999.
- [39] A. Fimia, F. Mateos, R. Mallavia et al., "High-energy sensitivity enhancement in panchromatic photopolymers for holography using a mixture of visible-light photoinitiators," *Journal of Modern Optics*, vol. 46, no. 7, pp. 1091–1098, 1999.
- [40] G. M. Karpov, V. V. Obukhovskiy, T. N. Smirnova, and V. V. Lemeshko, "Spatial transfer of matter as a method of holographic recording in photoformers," *Optics Communications*, vol. 174, no. 5–6, pp. 391–404, 2000.
- [41] F. T. O'Neill, J. R. Lawrence, and J. T. Sheridan, "Improvement of holographic recording material using aerosol sealant," *Journal of Optics A*, vol. 3, no. 1, pp. 20–25, 2001.
- [42] H. Yao, M. Huang, Z. Chen, L. Hou, and F. Gan, "Optimization of two-monomer-based photopolymer used for holographic recording," *Materials Letters*, vol. 56, no. 1–2, pp. 3–8, 2002.
- [43] Y. Tomita and H. Nishibiraki, "Improvement of holographic recording sensitivities in the green in SiO₂ nanoparticle-dispersed methacrylate photopolymers doped with pyrromethene dyes," *Applied Physics Letters*, vol. 83, no. 3, pp. 410–412, 2003.
- [44] S. Blaya, P. Acebal, L. Carretero, and A. Fimia, "Pyromethene-HEMA-based photopolymerizable holographic recording material," *Optics Communications*, vol. 228, no. 1–3, pp. 55–61, 2003.
- [45] M. Ortuno, S. Gallego, C. Garcia, C. Neipp, A. Belendez, and I. Pascual, "Optimization of a 1 mm thick PVA/acrylamide recording material to obtain holographic memories: method of preparation and holographic properties," *Applied Physics B*, vol. 76, no. 8, pp. 851–857, 2003.
- [46] Y. H. Cho, M. He, B. K. Kim, and Y. Kawakami, "Improvement of holographic performance by novel photopolymer systems with siloxane-containing epoxides," *Science and Technology of Advanced Materials*, vol. 5, no. 3, pp. 319–323, 2004.
- [47] R. R. McLeod, A. J. Daiber, M. E. McDonald et al., "Micro-holographic multilayer optical disk data storage," *Applied Optics*, vol. 44, no. 16, pp. 3197–3207, 2005.
- [48] J. V. Kelly, M. R. Gleeson, C. E. Close et al., "Temporal analysis of grating formation in photopolymer using the nonlocal polymerization-driven diffusion model," *Optics Express*, vol. 13, no. 18, pp. 6990–7004, 2005.
- [49] J. T. Sheridan and J. R. Lawrence, "Nonlocal-response diffusion model of holographic recording in photopolymer," *Journal of the Optical Society of America A: Optics and Image Science, and Vision*, vol. 17, no. 6, pp. 1108–1114, 2000.
- [50] J. R. Lawrence, F. T. O'Neill, and J. T. Sheridan, "Adjusted intensity nonlocal diffusion model of photopolymer grating formation," *Journal of the Optical Society of America B*, vol. 19, no. 4, pp. 621–629, 2002.
- [51] F. T. O'Neill, A. J. Carr, S. M. Daniels et al., "Refractive elements produced in photopolymer layers," *Journal of Materials Science*, vol. 40, no. 15, pp. 4129–4132, 2005.
- [52] H. Wei, L. Cao, Z. Xu, Q. He, G. Jin, and C. Gu, "Orthogonal polarization dual-channel holographic memory in cationic ring-opening photopolymer," *Optics Express*, vol. 14, no. 12, pp. 5135–5142, 2006.

- [53] Y. Tomita, K. Furushima, K. Ochi et al., "Organic nanoparticle (hyperbranched polymer)-dispersed photopolymers for volume holographic storage," *Applied Physics Letters*, vol. 88, no. 7, 2006.
- [54] B. M. John, M. Ushamani, R. Joseph, K. Sreekumar, and C. S. Kartha, "Reusable recording medium based on MBPVA and vinyl acetate," *Journal of Modern Optics*, vol. 53, no. 3, pp. 343–355, 2006.
- [55] E. Fernandez, C. Garcia, I. Pascual, M. Ortuno, S. Gallego, and A. Belendez, "Optimization of a thick polyvinyl alcohol-acrylamide photopolymer for data storage using a combination of angular and peristrophic holographic multiplexing," *Applied Optics*, vol. 45, no. 29, pp. 7661–7666, 2006.
- [56] Y. C. Jeong, S. Lee, and J. K. Park, "Holographic diffraction gratings with enhanced sensitivity based on epoxy-resin photopolymers," *Optics Express*, vol. 15, no. 4, pp. 1497–1504, 2007.
- [57] F. R. Ling, B. H. Tong, S. J. Jiang, B. Wang, and Y. L. Zhang, "Optimization of holographic storage with modulated recording beams in a thick polyvinyl alcohol/acrylamide photopolymer," *Journal of the Optical Society of America A*, vol. 24, no. 7, pp. 1945–1949, 2007.
- [58] X. Li, C. Bullen, J. W. M. Chon, R. A. Evans, and M. Gu, "Two-photon-induced three-dimensional optical data storage in CdS quantum-dot doped photopolymer," *Applied Physics Letters*, vol. 90, no. 16, Article ID 161116, 2007.
- [59] L. P. Krul, V. Matusevich, D. Hoff et al., "Modified polymethylmethacrylate as a base for thermostable optical recording media," *Optics Express*, vol. 15, no. 14, pp. 8543–8549, 2007.
- [60] S. Gallego, M.F. Ortuno, C. Neipp, E. Fernandez, A. Belendez, and I. Pascual, "Improved maximum uniformity and capacity of multiple holograms recorded in absorbent photopolymers," *Optics Express*, vol. 15, no. 15, pp. 9308–9319, 2007.
- [61] M. Toishi, T. Tanaka, and K. Watanabe, "Analysis of temperature change effects on hologram recording and a compensation method," *Optical Review*, vol. 15, no. 1, pp. 11–18, 2008.
- [62] A. Khan, G. D. Stucky, and C. J. Hawker, "High-performance, nondiffusive crosslinked polymers for holographic data storage," *Advanced Materials*, vol. 20, no. 20, pp. 3937–3941, 2008.
- [63] V. Matusevich, A. Matusevich, R. Kowarschik, Y. I. Matusevich, and L. P. Krul, "Holographic volume absorption grating in glass-like polymer recording material," *Optics Express*, vol. 16, no. 3, pp. 1552–1558, 2008.
- [64] R. R. McLeod, A. J. Daiber, T. Honda et al., "Three-dimensional optical disk data storage via the localized alteration of a format hologram," *Applied Optics*, vol. 47, no. 14, pp. 2696–2707, 2008.
- [65] S. Gallego, A. Marquez, D. Mendez et al., "Analysis of PVA/AA based photopolymers at the zero spatial frequency limit using interferometric methods," *Applied Optics*, vol. 47, no. 14, pp. 2557–2563, 2008.
- [66] Y. Tomita, T. Nakamura, and A. Tago, "Improved thermal stability of volume holograms recorded in nanoparticle-polymer composite films," *Optics Letters*, vol. 33, no. 15, pp. 1750–1752, 2008.
- [67] M. R. Gleeson, D. Sabol, S. Liu, C. E. Close, J. V. Kelly, and J. T. Sheridan, "Improvement of the spatial frequency response of photopolymer materials by modifying polymer chain length," *Journal of the Optical Society of America B*, vol. 25, no. 3, pp. 396–406, 2008.
- [68] J. V. Kelly, M. R. Gleeson, C. E. Close, and J. T. Sheridan, "Optimized scheduling for holographic data storage," *Journal of Optics A*, vol. 10, no. 11, Article ID 115203, 2008.
- [69] K. Choi, J. W. M. Chon, M. Gu, N. Malic, and R. A. Evans, "Low-distortion holographic data storage media using free-radical ring-opening polymerization," *Advanced Functional Materials*, vol. 19, no. 22, pp. 3560–3566, 2009.
- [70] S. Orlic, E. Dietz, T. Feid, S. Frohmann, and C. Mueller, "Optical investigation of photopolymer systems for micro-holographic storage," *Journal of Optics A*, vol. 11, no. 2, Article ID 024014, 2009.
- [71] S. H. Lin, Y. N. Hsiao, and K. Y. Hsu, "Preparation and characterization of Irgacure 784 doped photopolymers for holographic data storage at 532 nm," *Journal of Optics A*, vol. 11, no. 2, Article ID 024012, 2009.
- [72] T. Tanaka, "Recording and reading temperature tolerance in holographic data storage, in relation to the anisotropic thermal expansion of a photopolymer medium," *Optics Express*, vol. 17, no. 16, pp. 14132–14142, 2009.
- [73] D. Kim and D. W. Chung, "Study on the optimization of cationic ring opening polymerization of silicone-based epoxy monomers for holographic photopolymers," *Macromolecular Research*, vol. 17, no. 9, pp. 651–657, 2009.
- [74] R. R. McLeod, "Impact of phase aberrations caused by multi-layer optical data storage in weakly inhomogeneous media," *Journal of the Optical Society of America B*, vol. 26, no. 2, pp. 308–317, 2009.
- [75] S. Gallego, A. Marquez, S. Marini, E. Fernandez, M. Ortuno, and I. Pascual, "In dark analysis of PVA/AA materials at very low spatial frequencies: phase modulation evolution and diffusion estimation," *Optics Express*, vol. 17, no. 20, pp. 18279–18291, 2009.
- [76] X. Liu, Y. Tomita, J. Oshima et al., "Holographic assembly of semiconductor CdSe quantum dots in polymer for volume Bragg grating structures with diffraction efficiency near 100%," *Applied Physics Letters*, vol. 95, no. 26, Article ID 261109, 2009.
- [77] K. Omura and Y. Tomita, "Photopolymerization kinetics and volume holographic recording in ZrO₂ nanoparticle-polymer composites at 404 nm," *Journal of Applied Physics*, vol. 107, no. 2, Article ID 023107, 2010.
- [78] E. Hata and Y. Tomita, "Order-of-magnitude polymerization-shrinkage suppression of volume gratings recorded in nanoparticle-polymer composites," *Optics Letters*, vol. 35, no. 3, pp. 396–398, 2010.
- [79] J. Guo, S. Liu, M. R. Gleeson, and J. T. Sheridan, "Study of photosensitizer diffusion in a photopolymer material for holographic applications," *Optical Engineering*, vol. 50, no. 1, Article ID 015801, 2011.
- [80] D. J. Lougnot, P. Jost, and L. Lavielle, "Polymers for holographic recording: VI. Some basic ideas for modelling the kinetics of the recording process," *Pure and Applied Optics*, vol. 6, no. 2, pp. 225–245, 1997.
- [81] C. E. Close, M. R. Gleeson, and J. T. Sheridan, "Monomer diffusion rates in photopolymer material. Part I. Low spatial frequency holographic gratings," *Journal of the Optical Society of America B*, vol. 28, no. 4, pp. 658–666, 2011.
- [82] C. E. Close, M. R. Gleeson, D. A. Mooney, and J. T. Sheridan, "Monomer diffusion rates in photopolymer material. Part II. High-frequency gratings and bulk diffusion," *Journal of the Optical Society of America B*, vol. 28, no. 4, pp. 842–850, 2011.
- [83] D. Sabol, M. R. Gleeson, S. Liu, and J. T. Sheridan, "Photo-initiation study of Irgacure 784 in an epoxy resin photopolymer," *Journal of Applied Physics*, vol. 107, no. 5, Article ID 053113, 2010.

- [84] E. Hata, K. Mitsube, K. Momose, and Y. Tomita, "Holographic nanoparticle-polymer composites based on step-growth thiol-ene photopolymerization," *Optical Materials Express*, vol. 1, no. 2, pp. 207–222, 2011.
- [85] E. Hata and Y. Tomita, "Stoichiometric thiol-to-ene ratio dependences of refractive index modulation and shrinkage of volume gratings recorded in photopolymerizable nanoparticle-polymer composites based on step-growth polymerization," *Optical Materials Express*, vol. 1, no. 6, pp. 1113–1120, 2011.
- [86] R. A. Rupp, J. Hehmann, R. Matull, and K. Ibel, "Neutron diffraction from photoinduced gratings in a PMMA matrix," *Physical Review Letters*, vol. 64, no. 3, pp. 301–302, 1990.
- [87] M. Fally, "The photo-neutronrefractive effect," *Applied Physics B*, vol. 75, no. 4-5, pp. 405–426, 2002.
- [88] J. Klepp, C. Pruner, Y. Tomita et al., "Diffraction of slow neutrons by holographic SiO₂ nanoparticle-polymer composite gratings," *Physical Review A*, vol. 84, no. 1, Article ID 013621, 2011.
- [89] M. Fally, J. Klepp, and Y. Tomita, "An experimental study to discriminate between the validity of diffraction theories for off-Bragg replay," *Applied Physics B*. In press.
- [90] J. T. Sheridan, "A comparison of diffraction theories for off-Bragg replay," *Journal of Modern Optics*, vol. 39, no. 8, pp. 1709–1718, 1992.
- [91] P. Vayalamkuzhi, R. Joseph, K. Sreekumar, and C. S. Kartha, "Investigation on the panchromaticity of silver-doped poly(vinyl alcohol)/acrylamide photopolymer," *Applied Optics*, vol. 50, no. 18, pp. 2886–2891, 2011.
- [92] S. Orlic, E. Dietz, S. Frohmann, and J. Rass, "Resolution-limited optical recording in 3D," *Optics Express*, vol. 19, no. 17, pp. 16096–16105, 2011.
- [93] D. A. Waldman, C. J. Butler, and D. H. Raguin, "CROP holographic storage media for optical data storage at greater than 100 bits/ μm^2 ," in *Proceedings of the SPIE on Organic Holographic Materials and Applications*, vol. 5216, pp. 10–25, August 2003.
- [94] M. Ortuño, E. Fernández, S. Gallego, A. Beléndez, and I. Pascual, "New photopolymer holographic recording material with sustainable design," *Optics Express*, vol. 15, no. 19, pp. 12425–12435, 2007.
- [95] S. Gallego, A. Marquez, M. Ortuno, S. Marini, I. Pascual, and A. Belendez, "Monomer diffusion in sustainable photopolymers for diffractive optics applications," *Optical Materials*, vol. 33, no. 11, pp. 1626–1629, 2011.
- [96] S. Gallego, A. Marquez, M. Ortuno, S. Marini, and J. Frances, "High environmental compatibility photopolymers compared to PVA/AA based materials at zero spatial frequency limit," *Optical Materials*, vol. 33, no. 3, pp. 531–537, 2011.
- [97] M. R. Gleeson, J. Guo, and J. T. Sheridan, "Optimisation of photopolymers for holographic applications using the Non-local photopolymerization driven diffusion model," *Optics Express*, vol. 19, no. 23, pp. 22423–22436, 2011.
- [98] M. R. Gleeson, J. T. Sheridan, F. K. Bruder et al., "Comparison of a new self developing photopolymer with AA/PVA based photopolymer utilizing the NPDD model," *Optics Express*, vol. 19, no. 27, pp. 26325–26342, 2011.
- [99] J. Guo, M. R. Gleeson, S. Liu, and J. T. Sheridan, "Non-local spatial frequency response of photopolymer materials containing chain transfer agents: part I. Theoretical modelling," *Journal of Optics*, vol. 13, no. 9, Article ID 095601, 2011.
- [100] J. Guo, M. R. Gleeson, S. Liu, and J. T. Sheridan, "Non-local spatial frequency response of photopolymer materials containing chain transfer agents: part II. Experimental results," *Journal of Optics*, vol. 13, no. 9, Article ID 095602, 2011.
- [101] M. R. Gleeson, J. Guo, and J. T. Sheridan, "Recent developments in non-local photopolymerisation driven diffusion model," in *Proceedings of the SPIE*, pp. 8429–8448, Brussels, Belgium, 2012.